

**EFFECT OF ATOMIZER SCALE AND FLUID  
PROPERTIES ON ATOMIZATION  
MECHANISMS AND SPRAY  
CHARACTERISTICS**

by

Travis Waind

A dissertation submitted to the faculty of  
The University of Utah  
in partial fulfillment of the requirements for the degree of

Doctor of Philosophy

Department of Chemical Engineering

The University of Utah

December 2015

Copyright © Travis Waind 2015

All Rights Reserved

# The University of Utah Graduate School

## STATEMENT OF DISSERTATION APPROVAL

The dissertation of Travis Waind  
has been approved by the following supervisory committee members:

<u>Kevin Whitty</u>	, Chair	<u>2015/05/05</u> Date Approved
<u>Terry Ring</u>	, Member	<u>2015/05/05</u> Date Approved
<u>Mikhail Skliar</u>	, Member	<u>2015/05/05</u> Date Approved
<u>Jeremy Thornock</u>	, Member	<u>2015/05/05</u> Date Approved
<u>Kevin Davis</u>	, Member	<u>2015/05/05</u> Date Approved

and by Milind Deo, Chair/Dean of  
the Department/College/School of Chemical Engineering

and by David B. Kieda, Dean of The Graduate School.

## ABSTRACT

Atomization is chaos. The breakup of liquid structures by a gas encompasses such a wide range of possible configurations that a definitive mechanism describing breakup in any and all situations is an impossibility. However, when focus is applied, trends can be teased out of experimental data that seem to appropriately describe the action undertaken.

These studies sought to better understand atomization, specifically coaxial, two-stream, airblast (or air-assist) atomization in which a central liquid jet is broken up by an annular, high-velocity gas stream. The studies enclosed focused on identifying the effect of changing the atomizer's scale on atomization. While most (but not all) atomization studies only focus on the resulting far-field drop diameters, these studies placed the focus largely on the intermediate structures, in the form of the intact liquid jet (ILJ), while also quantifying the resulting drop diameters. The location and shape of the ILJ constantly change, and on its surface, wavelengths were seen to form and grow, which have been correlated to the resulting drop diameters in previous studies. The studies enclosed herein are unique in that they attempt to apply and explain exiting mechanism-based breakup mechanisms to regimes, fluids, and geometry changes not yet evaluated in the literature. Existing correlations were compared to the experimental data for a range of atomizer geometries, and when they were found lacking, Buckingham-II theorem was used to develop new correlations for predicting behavior. Additionally, the method developed for the calculation of these parameters for other image sets is included, allowing for easy comparison and value verification.

A small-scale, coaxial atomization system was used to atomize water and two silicone oils with air. The atomizers used in these studies had the same general geometry type, but had varying sizes, allowing for the effect of both scale and geometry to be evaluated. These studies quantified instability development and growth along with the resulting spray characteristics, allowing for correlations to be made between the two data sets as the more recent mechanism-based atomization models do. Existing mechanism-based models from the literature are compared to the experimental results, as these existing models have not been evaluated significantly with changing atomizer geometry, high-viscosity fluids, and high flow regimes as was done here. Additionally, two experimental campaigns were undertaken

with atomizers used to operate the University of Utah's PDU-scale (process development unit) entrained flow gasifier. The first campaign showed the effect of gas velocity, atomizer load (total flow), and gas-liquid impingement angle on the qualitative cold-flow atomizer performance. These trends are then tied to behavior of the entrained flow gasifier, showing the existence of a minimum required degree of atomization to avoid substantial losses in fuel conversion and efficiency in a gasifier. The second campaign showed the effect of gas flow, liquid flow, and fluid on the quantitative cold-flow atomizer performance. While in the literature, changing fluid properties of Newtonian fluids are shown to have a relatively linear response on atomizer performance, the behavior of non-Newtonian fluids was shown to be much more complex and difficult to predict. The correlations developed for the small-scale atomizers are applied to the micro-hole atomizers and found to be erroneous for the change in atomizer geometry. Buckingham-II theorem is then used to develop correlations to predict the spray Sauter mean diameter for the micro-hole atomizers.

Slurry-fed combustion and gasification systems are but one industrial implementation of atomization. Atomization plays important roles in numerous other industries, and despite decades of study, it is not well understood. This document serves to shed some light on a few small, specific subsets of the topic.

For my family and friends.

“I know nothing, and I’m overjoyed.”

– Bonnie “Prince” Billy

“The best thing to get out of grad school is yourself.”

– Mike Bockelie

“An expert is a man who has made all the mistakes which can be made in a very narrow field.”

– Niels Bohr

“That’s going to be a slushy ride to the airport.”

– Mike Burton

“Does the white whale actually symbolize the unknowability and meaninglessness of human existence? No, it’s just a %#!\$ing fish.”

– Ron Swanson

# CONTENTS

<b>ABSTRACT</b> .....	<b>iii</b>
<b>LIST OF FIGURES</b> .....	<b>ix</b>
<b>LIST OF TABLES</b> .....	<b>xvi</b>
<b>NOTATION AND SYMBOLS</b> .....	<b>xvii</b>
<b>ACKNOWLEDGEMENTS</b> .....	<b>xix</b>
<b>1. INTRODUCTION</b> .....	<b>1</b>
1.1 Gasificaton .....	1
1.1.1 Fundamentals .....	2
1.1.2 Benefits and Opportunities .....	3
1.2 Atomization .....	5
1.2.1 Pressure Atomization .....	6
1.2.2 Air-Assist/Airblast Atomization .....	8
1.2.3 Opportunities .....	9
1.3 Objectives .....	10
1.4 Organization of the Dissertation .....	11
<b>2. LITERATURE REVIEW</b> .....	<b>16</b>
2.1 Atomization .....	17
2.1.1 ILJ Length .....	20
2.1.2 ILJ Pendular Behavior .....	21
2.1.3 Spray/Cone Angle .....	21
2.1.4 Shedding (or Wave) Frequency .....	22
2.1.5 Surface Wavelengths .....	22
2.1.6 Scaling .....	23
2.2 Stability Analysis .....	24
2.2.1 Existing Studies .....	24
2.2.2 Breakup Mechanisms .....	28
2.2.3 Atomization Regimes and Morphology .....	29
2.3 Gasificaton .....	31
<b>3. EXPERIMENTAL METHODS</b> .....	<b>39</b>
3.1 Small-Scale Atomizer Testing .....	39
3.1.1 Equipment and Conditions .....	40
3.1.2 Image Processing .....	41
3.2 Pilot-Scale Atomizer Testing .....	42
3.2.1 Injector Design .....	42
3.2.2 Cold-Flow Testing .....	45

3.3	Entrained Flow Gasifier	47
<b>4.</b>	<b>SMALL-SCALE ATOMIZER TESTING</b>	<b>57</b>
4.1	Morphology	57
4.2	Intact Liquid Jet Characteristics	58
4.2.1	Average ILJ Length	58
4.2.2	ILJ Length Oscillations	60
4.2.3	Pendular Behavior	61
4.2.4	Surface Oscillation	64
4.2.5	Wavelengths	67
4.3	Spray-Representative Drop Diameters	68
4.3.1	Buckingham-II Theorem Application	68
4.3.2	Geometric Mean Drop Diameter	70
4.3.3	Drop Size Distribution	73
4.3.4	Spray Sauter Mean Diameter	73
4.3.5	Characteristic Drop Correlations	75
4.4	Comparing Instabilities and the Resulting Spray	76
4.5	Conclusions	76
<b>5.</b>	<b>ATOMIZER DESIGN SCOPING</b>	<b>108</b>
5.1	Introduction	108
5.2	Theory	109
5.3	Results	109
5.3.1	Cold-Flow Testing	109
5.3.2	Entrained-Flow Gasifier Reactor Operation	112
5.4	Conclusions	114
<b>6.</b>	<b>ITERATING PILOT-SCALE ATOMIZERS</b>	<b>121</b>
6.1	Introduction	121
6.2	Theory	121
6.3	Results	122
6.3.1	Rheology	122
6.3.2	Patternator	123
6.3.3	PSV Results	125
6.3.4	High-Speed Imaging Results	129
6.4	Conclusions	134
<b>7.</b>	<b>CONCLUSIONS</b>	<b>155</b>
7.1	Main Conclusions	155
7.2	Surface Tension vs. Viscosity Effect	156
7.3	Hypothesized Mechanism(s) Observed	157
7.4	Future Work	158
	<b>REFERENCES</b>	<b>159</b>

## LIST OF FIGURES

1.1	Sequential breakdown of processes occurring to solid fuel in a gasifier © [16].	12
1.2	Steps occurring to a solid fuel particle entering a gasifier © [16]. . . . .	12
1.3	Theoretical (a) and real (b) breakup in the Rayleigh-Plateau regime, reproduced from Lefebvre [34]. . . . .	13
1.4	Breakup regimes of a liquid jet issued into a stagnant gas, reproduced from Dumouchel [32]. . . . .	14
2.1	Graphical illustration of analysis performed on image sets. . . . .	32
2.2	Kelvin-Helmholtz (or primary) instability wavelength, reproduced from Varga [33].	33
2.3	Rayleigh-Taylor instability wavelength manifestation one. © [40] The wavelength is seen to manifest in the radial direction, away from the center axis of the spray. . . . .	33
2.4	Rayleigh-Taylor instability wavelength manifestation two © [41]. The wavelength is seen to manifest in the azimuthal direction, around the circumference of the liquid jet. . . . .	34
2.5	Faragó and Chigier's breakup regimes, reproduced from Faragó and Chigier [94].	34
2.6	Lasheras and Hopfinger's breakup regimes © [82]. . . . .	35
2.7	Rayleigh-type breakup morphology, reproduced from Faragó and Chigier [94].	35
2.8	Membrane-type breakup morphology © [41]. . . . .	35
2.9	Fiber-type breakup morphology © [41]. . . . .	36
2.10	Superpulsating submode breakup morphology. . . . .	36
3.1	Atomizer schematic. . . . .	49
3.2	Above is a rough schematic of the coal-water slurry injector used for EFG testing at the University of Utah. The diagram on the left shows an overall view of the injector, while the diagram on the right shows some detail of inside the injector. . . . .	49
3.3	Schematic of the 45° nozzle that was used for testing. The angle is measured with the vertical as a reference. . . . .	50
3.4	Atomizer design iterations. . . . .	51
3.5	Old atomizer design showing a nonconcentric spray. . . . .	52
3.6	Above is the set-up of the cold-flow testing that was done on the injector. The injector was suspended on scaffolding so the water spray could be seen. . . . .	52

3.7	The AR-500 viscometer. . . . .	53
3.8	The patternator. . . . .	53
3.9	PSV equipment and injector alignment. . . . .	54
3.10	Schematic of the University of Utah’s entrained flow gasifier © [112]. . . . .	55
4.1	Morphological breakup regimes of Lasheras and Hopfinger © [82]. . . . .	78
4.2	L2G1 water. . . . .	78
4.3	L2G1 Silicone Oil A. . . . .	79
4.4	L2G1 Silicone Oil B. . . . .	79
4.5	L4G4 water. . . . .	80
4.6	L4G4 Silicone Oil A. . . . .	80
4.7	L4G4 Silicone Oil B. . . . .	81
4.8	$M$ versus the ILJ length. Filled markers represent Silicone Oil A. All data. . .	81
4.9	$M$ versus the ILJ length. Filled markers represent Silicone Oil A. Scale-able atomizers only. All have $A_g/A_l \approx 6$ . Dashed lines indicate similar tests and serve to better identify geometric trends between conditions. . . . .	82
4.10	$M$ versus the ILJ length. Filled markers represent Silicone Oil A. Constant $d_0$ by marker edge color, changing $b$ . Dashed lines indicate similar tests and serve to better identify geometric trends between conditions. . . . .	82
4.11	$M$ versus the ILJ length. Filled markers represent Silicone Oil A. Constant $b$ by marker edge color, changing $d_0$ . Dashed lines indicate similar tests and serve to better identify geometric trends between conditions. . . . .	83
4.12	$M$ versus the $d_0$ -normalized ILJ length. Filled markers represent Silicone Oil A. Dashed line represents the prediction of Lasheras et al. [39], shown in Equation 4.1. $x$ ’s represent the predictions of Zhao et al. [73], shown in Equation 4.2. . .	83
4.13	$M$ versus the ILJ length oscillation frequency. Filled markers represent Silicone Oil A. All data. . . . .	84
4.14	$M$ versus the ILJ length oscillation frequency. Filled markers represent Silicone Oil A. Scale-able atomizers only. All have $A_g/A_l \approx 6$ . Dashed lines indicate similar tests and serve to better identify geometric trends between conditions. . . . .	84
4.15	$M$ versus the ILJ length oscillation frequency. Filled markers represent Silicone Oil A. Constant $b$ by marker edge color, changing $d_0$ . Dashed lines indicate similar tests and serve to better identify geometric trends between conditions. . . . .	85
4.16	$M$ versus the ILJ length oscillation amplitude. Filled markers represent Silicone Oil A. All data. . . . .	85
4.17	$M$ versus the ILJ length oscillation amplitude. Filled markers represent Silicone Oil A. All data. . . . .	86
4.18	$M$ versus the ILJ angle oscillation frequency. Filled markers represent Silicone Oil A. All data. . . . .	86

4.19	$M$ versus the ILJ angle oscillation frequency. Filled markers represent Silicone Oil A. Constant $b$ by marker edge color, changing $d_0$ . Dashed lines indicate similar tests and serve to better identify geometric trends between conditions.	87
4.20	$M$ versus the ILJ angle oscillation amplitude. Filled markers represent Silicone Oil A. All data.	87
4.21	$M$ versus the ILJ angle oscillation amplitude. Filled markers represent Silicone Oil A. Constant $d_0$ by marker edge color, changing $b$ . Dashed lines indicate similar tests and serve to better identify geometric trends between conditions.	88
4.22	$M$ versus the ILJ angle oscillation amplitude. Filled markers represent Silicone Oil A. Constant $b$ by marker edge color, changing $d_0$ . Dashed lines indicate similar tests and serve to better identify geometric trends between conditions.	88
4.23	Average Strouhal number as a function of $M$ .	89
4.24	ILJ surface oscillation frequency (SO <sub>f</sub> ) as a function of distance past the atomizer. Atomizer L3G2. Column one and two (from left to right) are water tests (subfigures a, b, e, f, i, j, m, n), column three is Silicone Oil A (subfigures c, g, k, o), and column four is Silicone Oil B (subfigures d, h, l, p). From top to bottom, gas velocity is increased, corresponding to an increase in $M$ .	90
4.25	ILJ surface oscillation amplitude (SO <sub>a</sub> ) as a function of distance past the atomizer. Atomizer L3G2. Column one and two (from left to right) are water tests (subfigures a, b, e, f, i, j, m, n), column three is Silicone Oil A (subfigures c, g, k, o), and column four is Silicone Oil B (subfigures d, h, l, p). From top to bottom, gas velocity is increased, corresponding to an increase in $M$ .	91
4.26	$Re_{g,hd}$ versus the ILJ surface oscillation frequency. Light-filled markers represent Silicone Oil A. Dark-filled markers represent Silicone Oil B. All data.	92
4.27	$Re_{g,hd}$ versus the ILJ surface oscillation frequency. Light-filled markers represent Silicone Oil A. Dark-filled markers represent Silicone Oil B. Scale-able atomizers only. All have $A_g/A_t \approx 6$ . Dashed lines indicate similar tests and serve to better identify geometric trends between conditions.	92
4.28	$Re_{g,hd}$ versus the ILJ surface oscillation frequency. Light-filled markers represent Silicone Oil A. Dark-filled markers represent Silicone Oil B. Constant $d_0$ by marker edge color, changing $b$ . Dashed lines indicate similar tests and serve to better identify geometric trends between conditions.	93
4.29	Measured versus calculated ILJ surface oscillation frequencies.	93
4.30	$Re_{g,hd}$ versus the primary wavelength. Light-filled markers represent Silicone Oil A. Dark-filled markers represent Silicone Oil B. All data.	94
4.31	$Re_{g,hd}$ versus the primary wavelength. Light-filled markers represent Silicone Oil A. Dark-filled markers represent Silicone Oil B. Scale-able atomizers only. All have $A_g/A_t \approx 6$ . Dashed lines indicate similar tests and serve to better identify geometric trends between conditions.	94
4.32	$Re_{g,hd}$ versus the primary wavelength. Light-filled markers represent Silicone Oil A. Dark-filled markers represent Silicone Oil B. Constant $d_0$ by marker edge color, changing $b$ . Dashed lines indicate similar tests and serve to better identify geometric trends between conditions.	95

4.33	Measured versus calculated ILJ surface primary wavelengths. . . . .	95
4.34	Drop diameter distribution comparison to a log-normal distribution. Water, L1G1-1, $Re_g = 1,637$ . . . . .	96
4.35	Drop diameter distribution comparison to a log-normal distribution. Water, L1G1-2, $Re_g = 1,638$ . . . . .	96
4.36	Drop diameter distribution comparison to a log-normal distribution. Water, L4G4-1, $Re_g = 12,022$ . . . . .	97
4.37	Drop diameter distribution comparison to a log-normal distribution. Water, L4G4-2, $Re_g = 12,022$ . . . . .	97
4.38	$Re_{g,hd}$ versus the geometric mean drop diameter. Filled markers represent Silicone Oil A. All data. Dashed lines indicate similar tests and serve to better identify geometric trends between conditions. . . . .	98
4.39	$Re_{g,hd}$ versus the geometric mean drop diameter. Filled markers represent Silicone Oil A. Scale-able atomizers only. All have $A_g/A_l \approx 6$ . Dashed lines indicate similar tests and serve to better identify geometric trends between conditions. . . . .	98
4.40	$Re_{g,hd}$ versus the geometric mean drop diameter. Filled markers represent Silicone Oil A. Constant $d_0$ by marker edge color, changing $b$ . Dashed lines indicate similar tests and serve to better identify geometric trends between conditions. . . . .	99
4.41	$Re_{g,hd}$ versus the geometric mean drop diameter. Filled markers represent Silicone Oil A. Constant $b$ by marker edge color, changing $d_0$ . Dashed lines indicate similar tests and serve to better identify geometric trends between conditions. . . . .	99
4.42	Downstream Silicone Oil A spray of L2G1 for $M = 11.5$ . . . . .	100
4.43	$Re_{g,hd}$ versus the geometric standard deviation of the drop diameter. Filled markers represent Silicone Oil A. All data. Dashed lines indicate similar tests and serve to better identify geometric trends between conditions. . . . .	100
4.44	$Re_{g,hd}$ versus the geometric standard deviation of the drop diameter. Filled markers represent Silicone Oil A. Scale-able atomizers only. All have $A_g/A_l \approx 6$ . Dashed lines indicate similar tests and serve to better identify geometric trends between conditions. . . . .	101
4.45	$Re_{g,hd}$ versus the geometric standard deviation of the drop diameter. Filled markers represent Silicone Oil A. Constant $d_0$ by marker edge color, changing $b$ . Dashed lines indicate similar tests and serve to better identify geometric trends between conditions. . . . .	101
4.46	$Re_{g,hd}$ versus the geometric standard deviation of the drop diameter. Filled markers represent Silicone Oil A. Constant $b$ by marker edge color, changing $d_0$ . Dashed lines indicate similar tests and serve to better identify geometric trends between conditions. . . . .	102
4.47	$Re_{g,hd}$ versus the spray Sauter mean diameter. Filled markers represent Silicone Oil A. All data. Dashed lines indicate similar tests and serve to better identify geometric trends between conditions. . . . .	102

4.48	$Re_{g,hd}$ versus the spray Sauter mean diameter. Filled markers represent Silicone Oil A. Scale-able atomizers only. All have $A_g/A_l \approx 6$ . Dashed lines indicate similar tests and serve to better identify geometric trends between conditions.	103
4.49	$Re_{g,hd}$ versus the spray Sauter mean diameter. Filled markers represent Silicone Oil A. Constant $d_0$ by marker edge color, changing $b$ . Dashed lines indicate similar tests and serve to better identify geometric trends between conditions.	103
4.50	$Re_{g,hd}$ versus the spray Sauter mean diameter. Filled markers represent Silicone Oil A. Constant $b$ by marker edge color, changing $d_0$ . Dashed lines indicate similar tests and serve to better identify geometric trends between conditions.	104
4.51	Measured drop SMDs versus calculated drop SMDs. Solid black line represents the one-to-one, where the measured and calculated values are identical. . . . .	105
4.52	$\mu_{dd}$ correlation comparison to measured values. Solid black line represents the one-to-one, where the measured and calculated values are identical. . . . .	106
4.53	$\sigma_{dd}$ correlation comparison to measured values. Solid black line represents the one-to-one, where the measured and calculated values are identical. . . . .	106
4.54	SMD correlation comparison to measured values. Solid black line represents the one-to-one, where the measured and calculated values are identical. . . . .	107
4.55	$b$ -normalized primary wavelength versus the $b$ -normalized spray Sauter mean diameter. Filled markers represent Silicone Oil A. . . . .	107
5.1	The injector on the left has the 65° nozzle. The injector in the middle has the 45° nozzle. The injector on the right has the 25° nozzle. Each green square represents an area that is approximately 1.27 cm (0.5 in) by 1.27 cm (0.5 in)..	116
5.2	Both injectors have the 45° nozzle. The injector on the left has a flow rate corresponding to an EFG system pressure of 1.7 bara (25 psia). The injector on the right has a flow rate corresponding to an EFG system pressure of 7.9 bara (115 psia). Both injectors are operating at a 2.8 bar (40 psi) air pressure drop. . . . .	116
5.3	Both injectors shown have the 65° nozzle. The injector on the left is operating at a 0.7 bar (10 psi) pressure drop, whereas the injector on the right is operating at a 3.5 bar (50 psi) pressure drop. Water and air flows are the same for both cases. . . . .	117
5.4	Oxygen pressure drop over the injector versus time. . . . .	117
5.5	Reactor temperature profiles during operation with the 45° nozzle at specific injector oxygen pressure drops. The thermocouples are number in order of their position from the top of the reaction zone, so TC1 is closest to the injector and TC5 is furthest away. The thermocouples are 29 cm (11 in) from the adjacent thermocouple. . . . .	118
5.6	Oxygen pressure drop over the injector during the second day of testing. . . . .	118
5.7	Reactor temperature profiles during operation with the 65° nozzle at specific injector oxygen pressure drops. The thermocouples are number in order of their position from the top of the reaction zone, so TC1 is closest to the injector and TC5 is furthest away. The thermocouples are 29 cm (11 in) from the adjacent thermocouple. . . . .	119

6.1 Particle size distribution for both the coal and petcoke evaluated. . . . .	136
6.2 Shear-dependent viscosity of various fuel slurries. . . . .	136
6.3 Patterning results of water. . . . .	137
6.4 Patterning results of 31_Coal (left) and 53_Coal (right). . . . .	138
6.5 Patterning results of 37_Petcoke (left) and 43_Petcoke (right). . . . .	139
6.6 Effect of gas and liquid flow on the average drop diameter along the spray's center axis. . . . .	140
6.7 Effect of gas and liquid flow on the average drop diameter along the spray's edge.	140
6.8 Drop diameter number distribution for all liquids and the 0.93 kg/hr air, 3.79e-2 m <sup>3</sup> /hr case. . . . .	141
6.9 Drop diameter number distribution for all liquids and the 0.65 kg/hr air, 4.54e-2 m <sup>3</sup> /hr case. . . . .	141
6.10 Effect of gas and liquid flow on the average spray direction along the center of the spray. . . . .	142
6.11 Effect of gas and liquid flow on the average spray direction along the edge of the spray. . . . .	142
6.12 Relation between spray direction and drop velocity for all liquids. Flow rates were 3.79e-2 m <sup>3</sup> /hr (12 gph) and 0.93 kg/hr, liquid and air, respectively. . . . .	143
6.13 Drop diameter distribution comparison to a log-normal distribution. Water, MH013, $u_g = 330$ m/s, $u_l = 0.35$ m/s. . . . .	144
6.14 Drop diameter distribution comparison to a log-normal distribution. Water, MH031, $u_g = 332$ m/s, $u_l = 0.35$ m/s. . . . .	144
6.15 Drop diameter distribution comparison to a log-normal distribution. Water, Atomizer S, $u_g = 332$ m/s, $u_l = 0.35$ m/s. . . . .	145
6.16 $Re_{g,hd}$ versus the spray SMD. $u_l = 0.35$ m/s. . . . .	145
6.17 Image of breakup for Atomizer S. $u_g = 344$ m/s, $u_l = 0.35$ m/s, and $Re_{g,hd} =$ 2, 236. . . . .	146
6.18 Image of breakup for Atomizer S. $u_g = 344$ m/s, $u_l = 0.35$ m/s, and $Re_{g,hd} =$ 3, 122. . . . .	146
6.19 $Re_l$ versus the spray SMD. $u_g = 313$ m/s for MH013. $u_g = 117$ m/s for MH031. $u_g = 332$ m/s for Atomizer S. . . . .	147
6.20 Image of breakup for Atomizer S. $u_g = 332$ m/s, $u_l = 0.03$ m/s, and $Re_{g,hd} =$ 1, 733. . . . .	147
6.21 Image of breakup for Atomizer S. $u_g = 332$ m/s, $u_l = 0.35$ m/s, and $Re_{g,hd} =$ 1, 690. . . . .	148
6.22 $Re_{g,hd}$ versus the geometric mean drop diameter, $\mu_{dd}$ . $u_l = 0.35$ m/s for all cases shown. . . . .	148
6.23 $Re_{g,hd}$ versus the geometric mean standard deviation of the drop diameter, $\sigma_{dd}$ . $u_l = 0.35$ m/s for all cases shown. . . . .	149

6.24	SMD correlation of Equation 4.14 compared to the measured SMD values for the micro-hole atomizers. Solid black line represents the one-to-one, where the measured and calculated values are identical. . . . .	149
6.25	$\mu_{dd}$ correlation of Equation 4.13 compared to the measured $\mu_{dd}$ for the micro-hole atomizers. Solid black line represents the one-to-one, where the measured and calculated values are identical. . . . .	150
6.26	$\sigma_{dd}$ correlation of Equation 4.15 compared to the measured $\sigma_{dd}$ for the micro-hole atomizers. Solid black line represents the one-to-one, where the measured and calculated values are identical. . . . .	150
6.27	SMD correlation of Equation 6.1 compared to the measured SMD values for the micro-hole atomizers. Solid black line represents the one-to-one, where the measured and calculated values are identical. . . . .	151
6.28	$\mu_{dd}$ correlation of Equation 6.2 compared to the measured $\mu_{dd}$ for the micro-hole atomizers. Solid black line represents the one-to-one, where the measured and calculated values are identical. . . . .	151
6.29	$\sigma_{dd}$ correlation of Equation 6.3 compared to the measured $\sigma_{dd}$ for the micro-hole atomizers. Solid black line represents the one-to-one, where the measured and calculated values are identical. . . . .	152

## LIST OF TABLES

1.1 Major gas-solid gasification reactions. . . . .	15
1.2 Major gas-gas reactions occurring in an entrained flow gasifier. . . . .	15
2.1 Identified trends with gas and liquid properties. . . . .	37
2.2 Identified trends with flows and geometry. . . . .	38
3.1 Atomizer dimensions. . . . .	56
3.2 Experimental conditions. . . . .	56
3.3 Fluid properties. . . . .	56
5.1 Syngas composition (mol %, dry, normalized nitrogen-free) from EFG testing on 8/18/10. . . . .	120
5.2 Syngas composition (mol %, dry, normalized nitrogen-free) from EFG testing on 8/19/10. . . . .	120
6.1 Description of the liquids being evaluated. . . . .	153
6.2 Atomizer dimensions. . . . .	154
6.3 Experimental conditions. . . . .	154

## NOTATION AND SYMBOLS

variable	description	units
$a$	inner tube wall thickness (See Figure 3.1)	$m$
$AFR$	air-to-fuel ratio	—
$A$	cross-sectional area	$m^2$
$AR$	angle ratio ( $\frac{globalsprayangle}{LLJangle}$ )	—
$b$	gap between inner and outer tubes (See Figure 3.1)	$m$
$c$	empirical coefficients	—
$d$	diameter	$m$
$f$	frequency	<i>Hertz</i>
$FR$	frequency ratio ( $\frac{surfaceoscillationfrequency}{dropcountoscillationfrequency}$ )	—
$I$	intensity	—
$l$	generalized system length scale placeholder	$m$
$M$	dynamic pressure ratio	—
$Oh$	Ohnesorge number	—
$Q$	flow rate	$\frac{m^3}{s}$
$Re$	Reynolds number	—
$SMD$	Saunter mean diameter	$m$
$St$	Strouhal number	—
$u$	velocity	$\frac{m}{s}$
$We$	Weber number	—
$\delta$	boundary layer thickness	$m$
$\lambda$	wavelength	$m$
$\mu$	viscosity	$Pa * s (\frac{kg}{s * m})$
$\nu$	kinematic viscosity ( $= \frac{\rho}{\mu}$ )	<i>Stokes</i> ( $\frac{m^2}{s}$ )
$\rho$	density	$\frac{kg}{m^3}$
$\sigma$	surface tension	$\frac{N}{m} (\frac{kg}{s^2})$

superscript    description

\*                      reference

subscript	description
$a, b, \dots$	coefficient index
$d$	drop
$C$	convective or critical
$i$	gas or liquid
$g$	gas
$l$	liquid
$R$	relative
0	central tube, inner
1	central tube, outer
2	outer tube, inner

acronym	description
ASU	air separation unit
CMOS	complementary metal-oxide semiconductor
ECUST	East China University of Science and Technology
EFG	entrained flow gasifier
EIA	Energy Information Agency
FIJI	FIJI Is Just ImageJ
FFT	fast Fourier transform
GC	gas chromatograph
HRSE	heat recovery steam generator
IGCC	integrated gasification combined cycle
ILJ	intact liquid jet
KHI	Kelvin-Helmholtz instability
LED	light emitting diode
NaN	not a number
NIH	National Institute of Health
OECD	Organization for Economic Co-operation and Development
PhD	doctor of philosophy
PSD	particle size distribution
PSV	particle shadow velocimetry
ROI	region of interest
RPI	Rayleigh-Plateau instability
RTI	Rayleigh-Taylor instability
TC	thermocouple
TIFF	tagged image file format
U.S.	United States

## ACKNOWLEDGEMENTS

I would like to thank a great many people for helping me get to this point, and like most things in life, there will inevitably be people that I forget to thank who should be thanked.

I would like to thank my advisor (Kevin Whitty) and my supervisory committee members (Terry Ring, Mikhail Skliar, Jeremy Thornock, and Kevin Davis). Each one of them significantly helped me along in one way or another at some point in this process, whether it was by showing some general enthusiasm for a result when I was burning out, arguing a point that was not valid and forcing me to better articulate my justification and reasoning, politely asking me how long I've been a graduate student, clarifying a problem when I've been focused on the wrong forces, or offering up their valuable time to just listen to me ramble about whatever tangential research problem I've decided to put thought into most recently. Academics have a reputation of being cold, self-serving, and uninviting. All members of my committee have starkly defied that persona on many occasions over my graduate career.

I cannot thank enough the various staff engineers in the university labs in which I worked, namely David Wagner, Dana Overacker, Andrew Fry, Ryan Okerlund, and Bob Cox. Additionally, I'd like to thank the machinists and welders who have put up with my general lack of knowledge on how to describe what I want: Dennis Romney and Steve from the Chemistry machine shop, Ron the welder, Dale Hoskins, Leonard Myers, Jack Treasure, Kory Watkins, and Andrew Fry (on occasion). Without the help of these people, I would be nowhere in the pursuit of this graduate degree. Despite my background as a farmer, I came in with little more than enthusiasm with regard to building things. These people made sure the mistakes that I made were far and few between, and mainly, kept me from hurting myself or others. I will always have fond memories of "Wu Tang Wednesdays", which quickly became everyday. Additionally, Eric Berg, Mike Burton, Chris Valenti, Mark "Country", Eric, and Carter Greene deserve thanks for helping (and sometimes leading) me with the various builds and ancillary tasks with which I was involved downtown and on campus. Jessica Earl deserves thanks for taking delight in surprising me at my desk, in the lab, or wherever I may be working when she happens to arrive back in town. Other than her help deciphering the GC data, she is a friend who has been there for me to vent to when life

seems overwhelming, and she is appreciated.

The group of students that I joined when arriving at the University of Utah helped me get back into class mode. I'm looking at Bernardo Castro, Preston Montalvo, Richard Baraki, Robert Krumm, Dadmehr Razeid, Scott Fayer, Chris Clayton, Trevor Stoddard, Daniel Sweeney, and David Ray Wagner. Suhui Li, Randy Pummill, Daniel Sweeney, David Ray Wagner, and Chris Clayton deserve thanks for bringing me into Dr. Whitty's research group. They were there to offer advice in research and in life.

The other students whom I met upon arrival to the University of Utah will be people with whom I am friends for life. They also provided much needed outlets from graduate school work at a time when I knew no one else in the area. Bernardo Castro, Preston Montalvo, Richard Baraki, Robert Krumm, Dadmehr Razeid, Scott Fayer, Trevor Stoddard, Daniel Sweeney, and David Ray Wagner were always more than happy to get a beer on the weekend, on a weekday night, or at Ed's after a particularly tough morning of classes (once Ed's could start serving beer at 11AM, of course). The skiing adventures with Daniel Sweeney, Richard Baraki, David Ray Wagner (on occasion), Elizabeth Lund (formerly), Yao Chen, and others are the types of events that only happen rarely in life. The friends I've made outside of academia deserve thanks. Richard Aaron Lee, Kim Raff, Bug Raff-Lee, Richard "Buddy" Tymchiasdoifjaogsda, Sara Crowder, Kendall Rathunde, Kate Montalvo, Carly Gillespie, Kyle Yurkovich, TJ and Corey Ersfeld, among others, have all offered up other paths in life that I likely would not have seen with my graduate-school tunnel vision.

My two sets of Utah parents deserve thanks: Trevor "Boots" Stoddard and Kandace Davis, and David and Geni Wagner. Both Trevor and Kandace independently offered fun alternatives to working all the time. They fed me more than the friendship contract stipulated, and were kind, genuine people. Of anyone in the state of Utah, David and Geni Wagner deserve the most thanks. They have truly taken me in as one of their own, and have seemingly been happy to do so, despite David's tough exoskeleton. They have helped me with issues that were unreasonable for me to ask of them and have asked nothing in return. David Ray Wagner deserves special thanks. The *Summer of Great Accomplishment* was no small task, and it could not have been achieved without his help. *The Game* was also great fun, and we will have to continue it at a future point in life.

My family deserves thanks. My brothers' prodding over the last 5.5 years along the lines of "When are you going to be done? Another year... year and a half?" worked wonders in the last few years of my graduate school experience. Their yearly ski trips have been something to which I look forward, despite feeling guilty about not working on my dissertation. We will

only continue the ski trips in coming years. My parents deserve thanks. Of likely anyone, they have had to put up with the largest quantity of my frustrations. They continually encourage me and point out things that are completely out of my control, that I likely have not realized. I cannot thank them enough.

# CHAPTER 1

## INTRODUCTION

The U.S. Energy Information Administration (EIA) forecasts that world coal consumption will increase from 139 quadrillion BTU in 2008 to 209 quadrillion BTU in 2035 [1]. Over the same period of time, the global population is expected to go from 6,709,621,000 to 8,618,768,000 [2]. In order to mitigate environmental issues while continuing to increase power production to meet the rising world population [2], current fuel sources must be used more efficiently.

Of the many technologies offering improved efficiency and reduced emissions, gasification is a leader. A benefit of gasification over combustion is that the syngas can be further manipulated to produce liquid fuels, chemicals, or electricity via an Integrated Gasification Combined Cycle (IGCC) facility. These facilities use gasification to produce syngas from a chosen fuel, combust syngas in a turbine to generate electricity, and generate steam from the combustion turbine flue gas to run an additional steam turbine. These facilities offer efficiencies around 40%. Gasification facilities offer great flexibility in both the fuel source and the product, often turning would-be waste streams such as slag (inorganic fuel elements that have melted in the high reactor temperature, and are subsequently frozen) into a revenue stream. They also allow for easier removal of all harmful emissions, easily meeting or exceeding the expectations and regulations [3, 4]. Gasification is not a silver bullet, but it offers a bridge to higher efficiency and lower emissions from conventional “dirty” and inexpensive fossil fuels.

### 1.1 Gasificaton

Gasification is the process of converting a carbonaceous feedstock (commonly solid) to synthesis gas or syngas (hence “gas”-ification) with a substoichiometric quantity of oxygen. The solid, carbonaceous fuel is typically coal, petroleum coke, wood, municipal solid waste, or other biomass types. Oftentimes, the solid fuel is mixed with water before being fed to a gasifier, as it both simplifies the feed system and provides the necessary water that

is used in the main gasification reactions. Syngas is a valuable gaseous fuel comprised mainly of hydrogen ( $\text{H}_2$ ), carbon monoxide ( $\text{CO}$ ), methane ( $\text{CH}_4$ ), and carbon dioxide ( $\text{CO}_2$ ). Syngas is formed in lieu of the conventional combustion products, water ( $\text{H}_2\text{O}$ ) and carbon dioxide ( $\text{CO}_2$ ), as a gasifier operates in a reducing, or oxygen-starved, manner. This shifts equilibrium towards  $\text{CO}$  instead of  $\text{CO}_2$  and  $\text{H}_2$  instead of  $\text{H}_2\text{O}$ .

### 1.1.1 Fundamentals

There are four main steps occurring to the solid fuel fed to an entrained flow gasifier that can be analyzed sequentially, but often occur in parallel in a gasifier. These steps are illustrated in Figure 1.1.

The first step, illustrated in Figure 1.1, is drying. Before the solid carbonaceous fuel can react with the gaseous environment in the gasifier, any coating water must be removed, or boiled away. This occurs relatively quickly in an entrained flow gasifier, as operating temperatures are much higher than other conventional gasifier types. Most times, it is advantageous to have solid fuel with a low moisture content, as reactions with solid carbon occur faster when there is no water to boil away first. In slurry-fed gasifiers, a slight efficiency loss is taken by the addition of water to the fuel. However, it makes the fuel much easier to feed as only a pump is needed, and it eliminates the need for any fuel preprocessing to remove excess water that may be necessary for a dry-feed system.

The second step is devolatilization, also known as pyrolysis or thermal decomposition. Devolatilization is largely dependent on the rate of heat transfer to the solid fuel particle. It is comprised of a complex series of physical and chemical steps resulting in the volatile species (essentially any nonpure carbon species) being emitted from the solid fuel particle as a gas. These volatile species then often react with the oxygen in the gas. This step is responsible for a significant portion of a particle's conversion.

The third step is the reaction of the remaining char with the various gas species. This step is often the most time-consuming step of them all, and in the high-temperature environment of an entrained flow gasifier, this step is very diffusion limited, meaning any increase in overall system mixing will facilitate complete reaction. In order to react with the solid carbon char, a given gas species has to diffuse to the particle's surface, diffuse within the particle's pores, react on the surface of the pore to form a product gas, diffuse out of the particle's pores, and diffuse away from the particle's surface. Four of the main gas-solid reactions are listed in Table 1.1. As gasification can be thought of as oxygen-starved combustion, and the net result of the occurring reactions will be endothermic, as shown in Table 1.1.

The fourth step is the processing of the remaining inorganic species of the solid fuel. Conventional combustion systems operate at lower temperature than a typical entrained flow gasifier, so these inorganic species form ash that gets carried away with the product gas stream. At the high operating temperatures of an entrained flow gasifier, the solid inorganic species melt to form slag, which then sticks to the walls of the gasifier, flows down, and is handled in a means that is dependent on the entrained flow gasifier type.

Another step that is not always included in this list is the equilibrium-reaching gas phase reactions that are always occurring during the previously discussed four steps. As mentioned previously, while these steps are often isolated and experimentally explored as if they occur sequentially, they are always occurring in parallel in a real gasifier. The components of the gas phase are always reacting with each other to reach an equilibrium. These simultaneous processes lead to difficulties in making predictions in these systems, as simple one-dimensional models only serve to provide leading order approximations, if that. Four of the main gas-gas reactions occurring in an entrained flow gasifier are shown in Table 1.2.

Of the six irreversible reactions listed in Table 1.1 and Table 1.2, four are exothermic (having a negative heat of reaction). Of those four exothermic reactions, three consume oxygen. As gasification is overall an oxygen-starved process, the oxygen will be completely consumed as soon as there is an opportunity presented. Additionally, at the high temperatures associated with entrained flow gasification, oxygen will react with nearly anything. This places most of the burden of conversion on the slower, endothermic gasification reactions listed in Table 1.1.

### 1.1.2 Benefits and Opportunities

Gasifiers are often the focal point of Integrated Gasification Combined Cycle (IGCC) systems, which incorporate an additional water/steam loop via a steam turbine and/or a heat recovery steam generator (HRSG) in order to reach efficiencies up to 43% [5,6]. Additionally, 88.5% of the gasifiers built in since 1952 or currently in planning or construction are entrained flow gasifiers [7], lending particular relevance to the work being done with the University of Utah's entrained flow gasifier [8–18]. These industrial gasifiers operate at pressures up to 8 MPa and temperatures up to 1650°C (approximately 3000°F) and higher [19].

Gasification offers improved emissions/pollutant control, increased efficiency, flexibility in feed source, and flexibility in the end product. A benefit of gasification over combustion is that the syngas can be further manipulated to produce liquid fuels, chemicals, or electricity. Removal of CO<sub>2</sub> becomes much easier with these systems for two reasons: the increased

pressure concentrates the targeted gas species and pure oxygen is typically fed, removing nitrogen as a diluent. These reactors can offer carbon conversion up to 98%.

IGCC facilities and gasification as a technology also have drawbacks. Any solid fuel used will have a certain percentage of inorganic mineral matter, referred to as ash in combustion systems. Depending on the operating temperature, ash can become sticky and form large deposits on boiler tubes. At the high operating temperatures common to entrained flow gasifiers, the ash becomes a liquid, called slag, and flows down the inner walls of the gasifier. Slag is extremely erosive and corrosive. Handling the production of slag often causes problems.

Capital cost is also a drawback of gasification facilities. Most conventional combustions systems cannot be retrofitted to run as a gasifier. For a gasifier to offer the best efficiency, it must be oxygen-blown, eliminating nitrogen as a heat sink and diluent. However, this requires large air separation units (ASUs) to provide the oxygen flow rate needed. The capital cost alone is often enough of a deterrent to rule-out an IGCC installation in the U.S. However, in China, India, and non-OECD countries, the rampant growth of coal use over the next 20 years would be better handled, with regard to the environment and energy efficiency, by the installation of a high-efficiency IGCC.

There are still opportunities for improvement with IGCC systems, and coal-based IGCC systems still cannot be considered fully commercial. One path to improvement lies in the atomizer design. The fuel to these reactors is commonly coal or petroleum coke mixed with water at upwards of 70% (by weight) solids. This slurried fuel is typically non-Newtonian and behaves much differently than water. For slurry-fed systems, complete carbon burnout requires thorough atomization resulting in small drops that provide a maximum surface area-to-volume ratio and facilitate quick heat and mass transfer [20]. All the steps shown in Figure 1.1 need to occur as quick as possible for complete carbon conversion to happen. Figure 1.2 shows a generalized EFG schematic along with the steps towards conversion. While it is generally understood that many small drops will allow for quicker mass and heat transfer than a large drop of equivalent volume, the ideal drop size, drop size distribution, spray pattern, and spray angle are not known for a given system [21, 22]. Ideally, insights into spray behavior can help explain performance of the gasifier.

The University of Utah operates a one ton/day slurry-fed, oxygen-blown, pressurized, entrained flow gasifier. These systems have many input variables that will effect operation (fuel type, fuel slurry solids loading, test conditions), but during operation, there are typically only two inputs that can be changed, oxygen feed rate and fuel feed rate. Some entrained flow

gasifier designs employ electric heaters to set general operating temperature of the system. However, many entrained flow gasifiers, including the one in operation at the University of Utah, use the heat of reaction to maintain the desired operating temperature. As such, it is not often that the feed rates can be changed to benefit operation, as they are often set to maintain a temperature. This leaves atomizer design as the sole knob to turn to improve operation.

The atomizer should be tuned, ideally on a fuel- and condition-basis, to preferentially place the flame and provide the fastest progression of Figure 1.2's steps as possible. If the flame from the atomizer is pushed too far into the reactor, a myriad of problems can occur including insufficient carbon conversion, as the fuel is likely not fully reacting until far down into the reaction zone. If the flame is kept too close to the atomizer, substantial degradation can and will occur, and the atomizer lifetime can be significantly less than what was expected, leading to downtime. Downtime and repairs can be expected from problems such as excessive refractory erosion, erratic syngas composition, overheating of the gasifier body, and others.

Atomizer performance is important for gasification. An efficient atomizer design will provide the proper atomization of a coal-water slurry mixture so that the fuel can completely devolatilize and react to form the gasification products. An efficient atomizer will also ensure the proper spatial and temporal distributions of fuel within the reaction zone to ensure stable operation and flame position for the system [23]. The ideal level of atomization and fuel distribution within a gasifier is not known.

## 1.2 Atomization

Atomization entails the breakup of a liquid mass into smaller liquid structures. This process generally occurs through one of two scenarios: the liquid breaks apart due to its own internal energy (kinetic or otherwise) or the liquid breaks apart due to the application of an external source of energy (such as a high-velocity gas stream or a mechanical device). While liquid viscosity typically offers only a stabilizing force, the surface tension can be either stabilizing or destabilizing (sometimes both, at different parts of the atomization process), depending on the situation. These liquid properties are typically what need to be overcome in order for breakup to occur. How the atomization process progresses and these forces are balanced or overcome depends largely on the mode of atomization occurring.

### 1.2.1 Pressure Atomization

When an atomization system consists solely of a pressure-drive liquid jet flowing into a stagnant gas, it is considered to be pressure atomization. This is likely the first “atomization” system encountered in history, as it is seemingly the simplest. Liquid flowing from an atomizer into a stagnant gas is inherently unstable. The instabilities are amplified and lead to breakup. Perhaps one of the first studies performed on such a system was by Plateau [24] in 1873, who showed that a cylindrical liquid column is unstable when its length is greater than its perimeter. Upon breakup, two drops are formed, having less surface energy than the original column.

In 1897, Rayleigh [25] examined the breakup of a nonviscous liquid surface. If a disturbance has a wavelength that is larger than the jet circumference, that disturbance will grow. The fastest growing disturbance was found to control the breakup of the jet, and Rayleigh’s results agreed with those of Plateau. Hence, the mode of breakup is commonly referred to as Rayleigh-Plateau breakup or capillary breakup. Under the regime of this Rayleigh-Plateau instability (RPI), surface tension acts as a destabilizing agent, which is uncommon. The RPI appears to pinch drops from the liquid column, and the resulting drops are predicted to have a diameter of  $1.89d_0$ . In reality, liquid jets have a nonnegligible viscosity, can be turbulent, and interact with the surrounding gaseous environment. However, in most cases, the results and predictions of Plateau and Rayleigh are good approximations. Figure 1.3 shows both the theoretically predicted drops and the actual drops.

In 1931, Weber [26] extended Rayleigh’s analysis to account for viscosity. Liquid viscosity has a stabilizing effect on breakup and tends to increase the size of the formed drops while reducing the breakup rate. Additionally, the phase interaction was shown to reduce the optimal wavelength for jet breakup, and in turn, the drop size. By increasing the relative velocity between the gas and the liquid phases, the distance at which breakup occurs is reduced. A study by Haenlein [27] in 1932 also explored the effect of gas-liquid interaction on atomization. As the liquid jet velocity (or the relative phase velocity) was increased, the phase interactions became more substantial, which led to larger wavelengths and oscillations.

In 1936, Ohnesorge [28] further explored the effect of liquid physical properties (surface tension, viscosity) on drop formation using dimensional analysis. He specifically evaluated the balance of inertial forces and viscous forces, which was defined by the jet Reynolds number. Three main breakup regimes were identified.

1. low-Reynolds number liquid jet flows which lead to drop sizes larger than the jet diameter

2. intermediate-Reynolds number liquid jet flows where breakup takes place through aerodynamically-enhanced jet oscillations producing a wide range of drop diameters
3. high-Reynolds number liquid jet flows where short wavelength instabilities dominate the breakup process and drops much smaller than the liquid jet diameter are produced

A different (and arguably more intuitive) method of delineating between liquid breakup regimes is by tracking the intact liquid jet (ILJ) length as a function of liquid jet velocity. Studies by Chigier and Reitz [29], Leroux et al. [30], Lin and Reitz [31], and Dumouchel [32] detail the theoretical underpinnings of these regimes. Five regimes manifest as the liquid velocity is increased from null. An illustration of these regimes can be seen in Figure 1.4.

The first regime is the dripping regime, shown in Figure 1.4-A, which corresponds to the situation where drops are directly emitted from the atomizer exit without a continuous liquid column being formed. The criteria defining the maximum liquid velocity for the existence of this regime is a function of the atomizer liquid jet diameter and the surface tension. The dripping regime has the smallest liquid jet velocity and has a negligible ILJ length.

Second is the Rayleigh regime, shown in Figure 1.4-B. In the Rayleigh regime, the liquid column is assumed to be disturbed by a single axisymmetric perturbation that has a wavelength of the same order of magnitude as the liquid jet diameter. Drops will detach from the liquid jet when the amplitude of the perturbation becomes equal to the jet radius. The Rayleigh regime is the manifestation of the RPI discussed previously. The Rayleigh regime represents a somewhat linear relationship between the liquid jet velocity and the ILJ length, as they are directly correlated.

Third is the first wind-induced regime, shown in Figure 1.4-C. In the first wind-induced regime, a dominant perturbation can still be identified on the liquid jet surface, but drop production is not as structured as that of the Rayleigh regime. The drops still are of the same order as the liquid jet diameter, but the main drops are slightly smaller and the drop size distribution becomes wider with the appearance of satellite drops between main drops. The first wind-induced regime is the manifestation of the phase interaction explored by Weber [26]. The first wind-induced regime shows a somewhat linear relationship between the liquid jet velocity and the ILJ length, but here, they are inversely correlated. As the liquid jet velocity is increased, the pinching off of drops occurs closer to the atomizer exit.

Fourth is the second wind-induced regime, shown in Figure 1.4-D. In the second wind-induced regime, the liquid jet is immediately perturbed as it exits the atomizer. These perturbations are amplified via a combination of liquid turbulence and aerodynamic interaction. The perturbations cover a wide range of length scales, which contribute to the

produced drop size distribution widening even further. Drops are seen being stripped from the surface of the liquid jet, and downstream, the remaining liquid core breaks into large ligaments that likely undergo secondary atomization. The mechanisms for breakup in the second wind-induced regime are not well understood. It is thought that the ILJ length increases slightly with increasing liquid jet velocity in this regime, but different atomizer geometries have shown the degree to which the ILJ length increases to change or the ILJ length to decrease with increasing liquid jet velocity [31].

The fifth and last regime is the atomization regime, shown in Figure 1.4-E. In the atomization regime, the liquid jet is completely disrupted immediately after exiting the atomizer. The diameters of the produced drops are significantly smaller than the liquid jet diameter. Here, turbulence and/or liquid cavitation can play a crucial role in the breakup process, and studies exploring the effect of atomizer exit geometry have indicated just that. Here, the ILJ length is negligible, as liquid breakup occurs immediately after exiting the atomizer.

The breakup and atomization of a low-velocity liquid jet by a coaxial, high-velocity, annular gas stream is fundamentally different from a high-velocity liquid jet injected into a stagnant gas. When the kinetic energy of the gas stream exceeds that of the liquid jet, the breakup is due to the transfer of kinetic energy from gas to liquid. This is why this type of atomization is commonly referred to as gas-assisted, or air-assist/airblast atomization. The gas used is commonly air, but the atomization mode in existence will hold with a change in the gas (such as using pure oxygen in combustion or gasification applications).

### 1.2.2 Air-Assist/Airblast Atomization

The studies enclosed herein only investigate air-assist/airblast atomization, namely where a co-flowing gas stream exists along with a liquid jet. As discussed previously, a slightly different atomization process involves the injection of a liquid jet into a stagnant gas, which is commonly described as pressure atomization (Section 1.2.1). The obvious difference between pressure atomization and air-assist/airblast atomization is the existence of a co-flowing gas stream, which affects the balance of stabilizing and destabilizing forces in a significant way.

A common reference used to distinguish between breakup regimes in air-assist/airblast atomization and pressure atomization is the relative velocity between the gas and liquid phases ( $u_R = |u_g - u_l|$ ). As such, it may be thought that the same fundamental breakup mechanisms exist for identical  $u_R$ , regardless of which phase's velocity is larger. This has been shown to not be the case. A fundamental difference exists in the scaling of the initial drops formed with the primary instability wavelength. For pressure atomization ( $u_l > u_g$ ),

the primary drop diameter is directly proportional to the primary instability wavelength. For air-assist/airblast atomization ( $u_g > u_l$ ), the primary drop diameter is significantly smaller than the primary instability wavelength, as a secondary instability is typically present to yield a smaller drop [33–35]. Additionally, for air-assist/airblast atomization, the energy transfer and interaction between the gas and liquid flows often leads to a pendular motion of the ILJ, which is not present for pressure atomization, and yields a different spatial drop distribution.

Conventional nomenclature defines two regions for external-mixing, coaxial atomization: the near-field and the far-field. The near-field is taken to encompass everything from the issuing of the liquid jet from the atomizer to the first stripping of drops or ligaments from the liquid jet, or primary atomization. As such, the near-field captures the formation and growth of instabilities that lead to breakup. The far-field is typically taken to encompass everything past primary atomization. Once a ligament or drop is stripped from the ILJ, it is considered to be in the far-field and may possibly undergo secondary atomization, which is the further breakup of a drop or ligament. While observations are made of the far-field, the focus of this work is on primary atomization and the near-field. More background and detail of air-assist/airblast atomization can be found in the literature review, Chapter 2.

### 1.2.3 Opportunities

Atomization is a topic that has been studied for 60+ years [36]. However, it is still far from being understood [22,37]. Despite the longevity of its study, atomization has yet to be scaled in a reliable way [22,37]. Any innovation in spray-drying operations, or atomization processes, typically requires large-scale testing that is often expensive [37]. This testing is often the result of an operator’s years of experience with a process providing some slight insight into how things could improve [37]. This is definitely a way to make improvements but does not lead to optimal operation [37]. Due to the ease of understanding, most experimentation is performed on low-viscosity liquids [22,37]. A large majority of these experiments are performed with small, bench- or lab-scale atomizers. By changing the flow rates, effects of the air-to-fuel ratio (AFR) and shear rate can be analyzed [22]. These are valuable experiments to show the basic relationships between physical properties and atomizer performance, but are difficult to use as a basis for improving upon the industrial-scale atomization of a non-Newtonian slurry [22,37]. In order to avoid the cost associated with large-scale testing, establishing effective methods of predicting industrial-scale behavior from bench-scale data would be extremely valuable [22,37]. Many properties (droplet size distribution, particle size distribution, spray pattern) can be determined on a small-scale. However, the optimal

ranges for these properties in a large-scale system are far from understood [22, 37].

Atomizers need to be more predictable as well [37] in order to better understand the systems in which they are utilized. In combustion systems, small droplets are preferred, whereas in spray drying systems, a narrow particle size distribution is desired [37]. Making structural or operating changes to an atomizer can cause a change in the spray pattern, yet this relationship is not established. The optimal spray pattern for a given system is not well understood [22]. The typical approach to scaling atomization is a dimensionless number approach, but this is not always an easy feat to accomplish, as it is often impossible to conserve all relevant dimensionless numbers [22]. Difficulty arises in accounting for length scale effects, pressure effects, slurry rheology, and non-Newtonian effects [22]. Large improvement on large-scale systems is to be had by accounting for the effect of atomizer geometry on system performance [38].

### 1.3 Objectives

The aim of this study is to offer some insight into the mechanisms and forces at work when attempting to scale an atomizer. The literature is ripe with studies exploring the effect of gas or liquid flow on resulting spray characteristics for a given atomizer geometry, but these studies in no way lead to an understanding of how atomizer geometry itself effects the resulting spray properties. As the target application here is a slurry-fed, entrained flow gasifier, the conditions and geometry explored will take values that are appropriate to those systems. However, the mechanisms of breakup are the same or similar for atomizers being used in a wide variety of other industries, and they can easily be applied elsewhere.

This project seeks to extend existing fundamental breakup mechanisms to different atomizer scales and different fluids (with different viscosities, surface tensions, etc.), while thoroughly detailing both the image processing method used (as this is a rare occurrence) and providing statistics on the measured instability characteristics (as this also is a rare occurrence). Additionally, characterization of pilot-scale gasifier atomizers has been performed in order to offer a guidebook to those designing atomizers for similar systems. Specific objectives of this research are the following.

- Determine the effect of the kinetic energy ratio on spray characteristics.
- Determine the effect of atomizer scale on spray characteristics and proposed mechanism applicability.
- Extend existing atomization mechanisms to unexplored fluids.

- Provide detailed statistics on observed instability characteristics.
- Determine the effect of atomizer design on qualitative performance in- and ex-situ gasifier.
- Develop and document an image processing method allowing for easy extraction of key breakup parameters.

## 1.4 Organization of the Dissertation

This dissertation follows a traditional format. Chapter 1 contains the introduction, while Chapter 2 contains a literature review. Chapter 3 details the various pieces of equipment and analytical techniques used in the included studies. Chapter 4 includes results from exploring the effect of atomizer scale on the atomization of water with air and silicone oil with air. Chapter 5 and Chapter 6 both include results from testing with the atomizers used for operating the University of Utah's pilot-scale entrained flow gasifier. A summary of the conclusions along with recommendations for future work exists in Chapter 7.

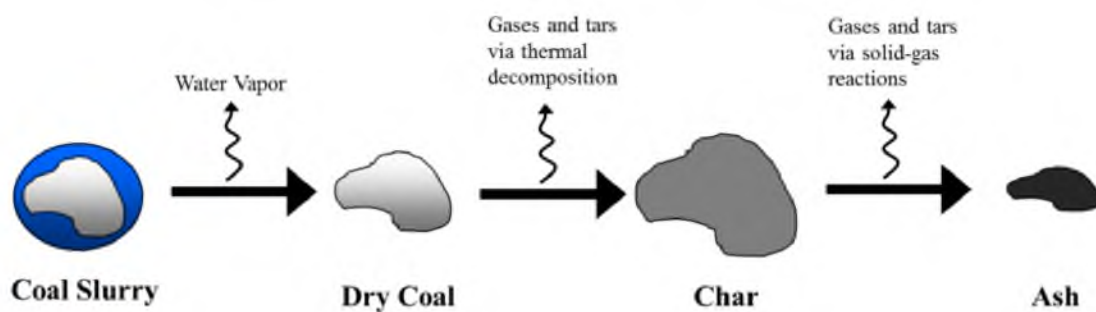


**Figure 1.1.** Sequential breakdown of processes occurring to solid fuel in a gasifier © [16].

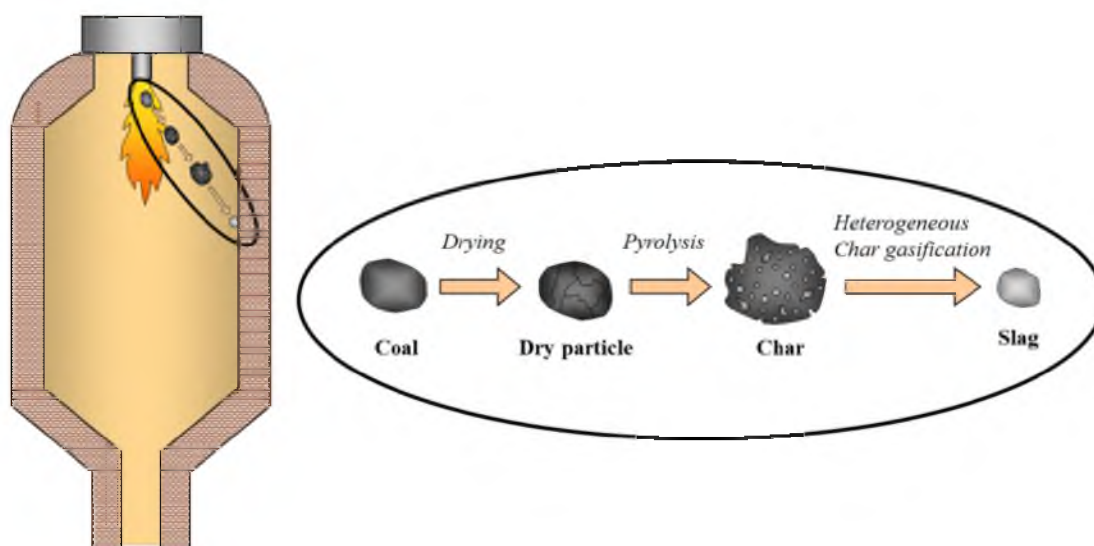


**Figure 1.2.** Steps occurring to a solid fuel particle entering a gasifier © [16].

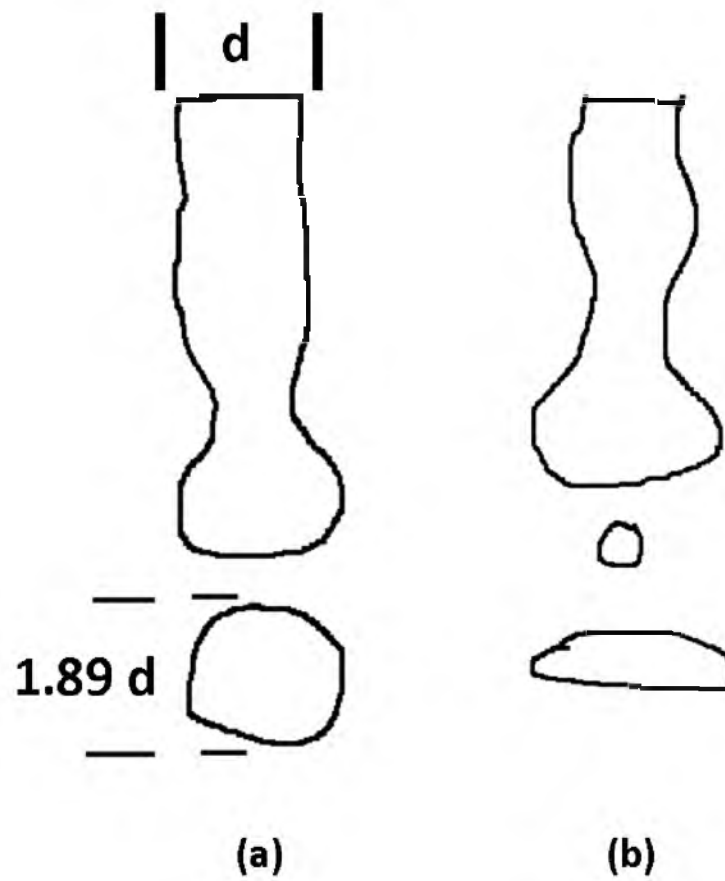


**Figure 1.3.** Theoretical (a) and real (b) breakup in the Rayleigh-Plateau regime, reproduced from Lefebvre [34].

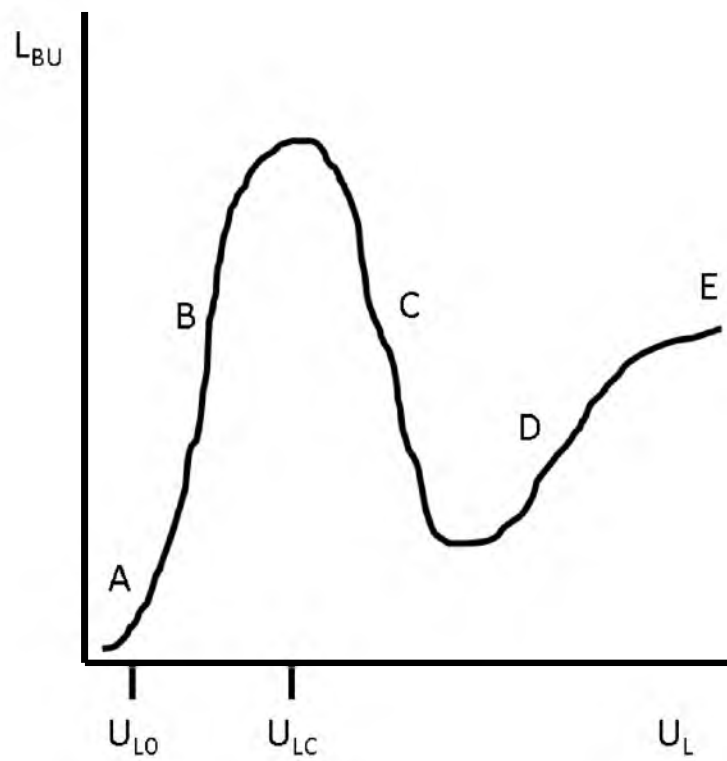


**Figure 1.4.** Breakup regimes of a liquid jet issued into a stagnant gas, reproduced from Dumouchel [32].

**Table 1.1.** Major gas-solid gasification reactions.

Reaction	Formula	Heat of Reaction ( $\frac{kJ}{mol}$ )
Char Oxidation	$C(s) + O_2(g) \rightarrow CO_2(g)$	-394
Steam Gasification	$C(s) + H_2O(g) \rightarrow CO(g) + H_2(g)$	+131
CO <sub>2</sub> Gasification	$C(s) + CO_2(g) \rightarrow 2CO(g)$	+172
Methanation	$C(s) + 2H_2(g) \rightarrow CH_4(g)$	-75

**Table 1.2.** Major gas-gas reactions occurring in an entrained flow gasifier.

Reaction	Formula	Heat of Reaction ( $\frac{kJ}{mol}$ )
Hydrogen Oxidation	$H_2(g) + \frac{1}{2}O_2 \rightarrow H_2O(g)$	-242
Carbon Monoxide Oxidation	$CO(g) + \frac{1}{2}O_2 \rightarrow CO_2(g)$	-283
Water-Gas Shift	$CO(g) + H_2O(g) \leftrightarrow CO_2(g) + H_2(g)$	-41
Methane Formation	$CO(g) + 3H_2(g) \leftrightarrow CH_4(g) + H_2O(g)$	-206

## CHAPTER 2

### LITERATURE REVIEW

As the main focus of these studies is atomization, the main theme to be identified here is the summation of work that explores various aspects of atomization (Section 2.1). Many studies exist exploring the effect of fluid properties, flow rates, slight geometry changes, and atomization methods. However, most (if not all) of these studies focus on one main atomizer geometry applied to a specific system. While this can lead to optimization of that given system within the bounds of the study, it does not allow optimization outside those constraints, mainly because the results are presented in the form of empirical equations as opposed to mechanism-based models that can be evaluated at multiple points of the atomization process.

The biggest push the author has been able to identify in recent atomization literature is the abandonment of empirical studies and the embrace of mechanism-based studies. These studies [39–41] hypothesize breakup mechanisms based upon the visualization of the breakup of the liquid jet, and the clear formation and growth of instabilities on the intact liquid jet (ILJ) surface, commonly referred to as the most important parameter characterizing the breakup region [42–44]. Using stability analysis, these studies are able to theoretically predict the fastest growing (or most unstable) wave numbers (for given flow conditions and fluid properties) on a gas-liquid interface [45–50], and thus offer a sound basis on which to predict the ILJ characteristics that influence near-field characteristics. These studies, the methods used, and brief method development are summarized in Section 2.2.

As the primary application and funding sources (at least during the author’s graduate student tenure) of this work involved the University of Utah’s gasification system, a brief summary of the existing literature pertaining to slurry-fed gasification, particularly any atomization-specific studies on such systems, is included here. While the number of entrained flow gasifiers in existence (and operation!) is increasing quite rapidly, the number of studies detailing the minutia of their operation is quite small. Any studies detailing operation of slurry-fed, entrained flow gasifiers are summarized as well (Section 2.3).

## 2.1 Atomization

Atomization is a complex, multiparameter, multiscale, and multiphase problem that becomes ever more elusive with the involvement of high velocity, viscosity, and density ratios [51]. It has been studied extensively at lower flow regimes, namely where the velocity ratios are lower, allowing for some of the fundamental physics to be deduced. As the flow regime increases and the respective phase velocity difference approaches  $O(10^2)$ , fundamental physics are more difficult to quantify, and studies tend to only present empirically-correlated results of the far-field spray characteristics. With the advent and proliferation of high-speed imaging capabilities, it has become significantly easier to visualize the phase interactions for higher flow regimes in the near-field of the spray, offering more theories into the mechanisms driving breakup [32]. Development of these theories and the deduction of the fundamental physics behind atomization at high flow regimes is important to numerous industries, such as liquid-fuel-fed gasification / combustion, pharmaceutical production, and metallurgy, among others [34, 52, 53].

Air-assist and airblast atomization are two of the more commonly used methods of atomization [34, 54]. These methods utilize the energy and momentum contained in a high-velocity gas flow (commonly in the form of an annular stream) to break apart a low-velocity liquid flow (commonly in the form of a central liquid jet). Some of the earliest air-assist/airblast atomization research performed was by Nukiyama and Takasawa [55–60], who looked at the effect of gas velocity on the spray Sauter mean diameter ( $SMD = \frac{\sum N_i d_i^3}{\sum N_i d_i^2}$ , where  $d_i$  is the drop diameter, and  $N_i$  is the number of drops per unit volume in size class  $i$ ) of gasoline, water, oils, and solutions of water and glycerol with air using a coaxial atomizer. They developed a correlation that spanned a viscosity range of 0.001 to 0.050  $Pa \cdot s$ , a surface tension range of 0.019 to 0.073  $N/m$ , and a density range of 700 to 1,200  $kg/m^3$ . This equation can be seen in Equation 2.1 [55–60].

$$SMD = \frac{0.585}{(u_g - u_l)} \left( \frac{\sigma}{\rho_l} \right)^{0.5} + 53 \left( \frac{\mu_l^2}{\sigma \rho_l} \right)^{0.225} \left( \frac{Q_l}{Q_g} \right)^{1.5} \quad (2.1)$$

In Equation 2.1,  $\sigma$  is the surface tension,  $u$  is the velocity,  $\rho$  is the density,  $\mu$  is the viscosity,  $Q$  is the volumetric flow, and the subscript  $i$  can be either  $g$  or  $l$  representing a gas or liquid property, respectively. It should be noted that Equation 2.1 is not dimensionally correct, and to make it dimensionally correct, a length scale raised to the 0.5 power is needed. This was considered by Nukiyama and Tanasawa [55–60], but they concluded that the liquid jet diameter or the annular air gap thickness (common system length scales) had little to no effect on the resulting mean drop size. Hence, it was kept out of Equation 2.1. The obtained

empirical equation, shown in Equation 2.1, suited a specific process; diving into the the underlying physics was not a priority.

A more recent study by Varga et al. [40] explored the atomization of water and ethanol with air using a coaxial atomizer. They developed a phenomenological breakup model that ties a final characteristic drop diameter to the system conditions via liquid instability wavelengths that develop. They developed a correlation that spanned a viscosity range of 0.001 to 0.0012  $Pa \cdot s$ , a surface tension range of 0.023 to 0.070  $N/m$ , and a density range of 791 to 998  $kg/m^3$ . This correlation is shown in Equation 2.2.

$$SMD \approx \frac{0.68\gamma^{1/2}(\rho_l\nu_g)^{1/4}\sigma^{1/2}}{\rho_g^{3/4}[u_g(1 + \sqrt{\rho_g/\rho_l}) - u_l]u_g^{1/4}} \quad (2.2)$$

In Equation 2.2,  $\gamma \approx 0.055m^{1/2}$  is a proportionality factor accounting for nozzle geometry [40]. It should be noted that Equation 2.2 does not include a dependence on the liquid jet diameter,  $d_0$ . It was shown by Varga et al. [40] that changing the liquid jet diameter by a factor of three resulted in no change in the resulting drop diameter. They showed that the drop diameter is a function of the gas boundary layer thickness at the nozzle exit.

An even more recent study by Aliseda et al. [61] explored the atomization of water, glycerol-water mixtures, an acetone / water / cellulose acetate / polyethylene glycol mixture, and two commercially available water-based suspensions with air using a coaxial atomizer. The non-Newtonian suspensions exhibited shear thinning behavior, and the viscosities measured at the highest shear rates for these fluids were used as inputs to their correlation. They developed a correlation that spanned a viscosity range of 0.00097 to 0.152  $Pa \cdot s$ , a surface tension range of 0.022 to 0.072  $N/m$ , and a density range of 800 to 1,220  $kg/m^3$ . This correlation is shown in Equation 2.3.

$$\frac{SMD}{d_0} = C_1(1 + m_r) \left(\frac{b}{d_0}\right)^{1/2} \left(\frac{\rho_l/\rho_g}{Re_{b,g}}\right)^{1/4} \frac{1}{\sqrt{We_{d_0}}} \left\{ 1 + C_2 \left(\frac{d_0}{b_g}\right)^{1/6} \left(\frac{Re_{b,g}}{\rho_l/\rho_g}\right)^{1/12} We_{d_0}^{1/6} Oh^{2/3} \right\} \quad (2.3)$$

In Equation 2.3,  $m_r$  is the liquid-to-gas mass flow ratio ( $m_r$ ),  $Re_{b,g}$  is the Reynolds number calculated with  $b$  as the length scale,  $We_{d_0}$  is the Weber number calculated with  $d_0$  as the length scale,  $C_1$  is a coefficient of  $O(1)$ , and  $C_2 = 1$ . While Equation 2.3 normalizes the SMD by the liquid jet diameter, Aliseda et al. [61] note that the drop diameter does not depend on the liquid jet diameter; it depends on the gas boundary layer thickness, as shown by Varga et al. [40]. Aliseda et al. [61] suggest that the length of the gas potential cone is

approximately  $6b$  and that for atomization to be efficient, the gas potential cone must be equal to or larger than the intact liquid jet length in order for primary atomization to be complete before the gas velocity begins to decrease. The limit can be defined by  $b\sqrt{M}/d_0 > 1$ . Additionally, for the primary instability to develop rapidly, the Reynolds number based upon the liquid shear layer must be large, according to  $Re_{\lambda_l} = (u_c - u_l)\lambda_l/\nu_l > 10$ .  $u_c$  is the convective velocity ( $u_c = \frac{\sqrt{\rho_l}u_l + \sqrt{\rho_g}u_g}{\rho_l + \rho_g}$ ).

While the Equation 2.1, Equation 2.2, and Equation 2.3 take on a similar form, they are different, particularly in the way they were developed. The studies of Nukiyama and Tanasawa are of the empirical type that has been referenced, while the studies of Varga et al. [40] and Aliseda et al. [61] were mechanistic. Equation 2.2 and Equation 2.3 essentially insert an intermediate step between the system inputs and a representative drop size. By measuring instability characteristics (such as wavelength size and surface oscillation), Varga et al. [40] and Aliseda et al. [61] were able to correlate the system inputs to those intermediate steps, and then correlate the intermediate steps to a representative drop size. An easy comparison can be made to the process of trying to predict a nonlinear trend with two data points as opposed to three. While three points may not completely capture the trend, it will do a better job than only using two points.

Many other empirical equations have been obtained that predict a characteristic drop diameter, often the SMD, from miscellaneous operating conditions, and many of these equations can be found in books by Lefebvre [62,63], Chigier [64], Bayvel and Orzechowski [54], Liu [65], Nasr et al. [66], or Ashgriz [53]. These are not summarized herein, as the goal of this work is to apply and verify the more recent mechanistic models. Table 2.1 and Table 2.2 show the trends identified in the literature for external-mixing, coaxial, two-stream atomizers (the kind explored here). These trends show how both the final spray characteristics and the intermediate measurements have been shown to change as function of fluid properties. The explored factors are the spray Sauter mean diameter (SMD), the intact liquid jet (ILJ) length, the ILJ breakup frequency, the ILJ surface oscillation (wave) frequency, the ILJ surface oscillation amplitude, and the spray angle. The ILJ length (also referred to as the core length, breakup length, potential cone length, etc.) is often identified as the most important parameter pertaining to external-mixing, coaxial, two-stream, air-assist (or airblast) atomization [42–44]. The ILJ also happens to be the main transition structure between the fluid injection and the resulting spray, so identifying its characteristics is important. The independent factors included in Table 2.1 and Table 2.2 are the liquid viscosity ( $\mu_l$ ), the liquid density ( $\rho_l$ ), the surface tension ( $\sigma$ ), the liquid velocity ( $u_l$ ), the

gas velocity ( $u_g$ ), liquid jet diameter ( $d_0$ ), the ambient pressure ( $P$ ), the liquid jet tube thickness ( $a$ ), and the gas-to-liquid cross-sectional area ratio ( $A_g/A_l$ ).

As characterization of transient near-field atomization is our goal, we seek to quantify both average and fluctuating components of the ILJ length, ILJ angle, primary wavelengths, ILJ surface oscillations, drop diameters, and drop count oscillations. Most of these measurements are illustrated in Figure 2.1.

Figure 2.1 shows a number of properties that fall under the category of near-field atomization characteristics. The top-left image in Figure 2.1 shows an image of the overall spray with a clear cone profile (likely full cone as opposed to hollow) visible. However, on a smaller time scale, the left-center image in Figure 2.1 is visible. There you can see the intact liquid jet, along with a number of recently formed drops. By processing the image, we are able to get a clear binary images of both the isolated intact liquid jet and the drops, shown on the middle-top and the bottom-top of Figure 2.1, respectively. From these images, a number of properties are quantified. From the ILJ, the length and angular position is quantified. Additionally, the surface of the ILJ is indexed. Any wavelengths present on the left or right side of the ILJ are quantified, and the location of the ILJ perimeter at every pixel-row in the image is quantified. From the drops, any isolated drop is quantified, along with the total number of drops present. This quantification is repeated over all images captured for a particular condition, commonly 10,000. As such, time series of all measurements can be established. The ILJ length versus time, the ILJ angle versus time, the ILJ surface position (at a given pixel-row) versus time, and the total number of drops versus time can all be analyzed. By applying Fourier transforms to time series such as these, we are able to determine dominant frequencies of oscillation of the various parameters. The static (average) and dynamic (oscillating) properties of the ILJ and near-field spray allow for an extremely thorough understanding of the forces at work in the system, and good comparison to existing literature becomes possible. As some of these static and dynamic properties have been explored before, the studies doing such exploration are summarized.

### 2.1.1 ILJ Length

Most cases evaluate the ILJ length for air-water systems [39, 42–44, 67–69], some look at other fluids [43, 44, 70], but none quantify the actual oscillations. Eroglu et al. [42], Engelbert et al. [67], Matas and Cartellier [68], and Zhao et al. [69] show that the ILJ length decreases as the liquid flow rate is decreased or the gas flow rate increased. Eroglu et al. [42] compared the ILJ lengths of two different atomizer geometries over a range of Weber numbers, finding no significant difference, but while the atomizers used were of the same scale, they were not

of the same design, employing a modification to the inner geometry. Porcheron et al. [43] showed that the ILJ length decreases with increasing gas density for constant liquid velocity and gas-to-liquid kinetic energy ratio. Leroux et al. [44] showed a slight increase in the ILJ length with a decrease in the liquid jet tube thickness. The postulated mechanism suggested by Leroux et al. [44], that increasing the liquid jet tube thickness increased the distance past the atomizer at which the gas and liquid flows reattach, was later shown by Tian et al. [71]. Zhao et al. [69] showed that the ILJ length will decrease as the liquid-to-gas cross-sectional area ratio is increased. Typically, only averaged ILJ length values are reported, and the basis of that average is often not given (number of images). Equations predicting the ILJ length tend to be of the form shown in Equation 2.4, normalized by a characteristic length scale of the system.

$$\frac{L}{l} \approx f(\dots) \quad (2.4)$$

### 2.1.2 ILJ Pendular Behavior

In addition to length oscillations, the ILJ moves from side to side much like the pendulum of a clock. Many studies have reported this behavior, but only a few have sought to quantify it. In order to characterize this motion, a compound pendulum model [72–76] is used, and a Strouhal ( $St$ ) number is defined for each condition. The Strouhal number, shown in Equation 2.5, represents the ratio between the transversal liquid velocity and axial liquid velocity.  $f$  is the dominant frequency as found by running the measured ILJ angle (subtended between the downward vertical and the liquid jet, as illustrated in Figure 2.1) through fast Fourier transform (FFT). Zhao et al. [72] and Carvalho et al. [75] found the Strouhal number to correlate with the square-root of  $M$ , as shown in Equation 2.5. Zhao et al. [72] found  $c_a = 0.17$  and  $c_b = 0.5$ , while Carvalho et al. [75] found  $c_a = 0.13$  and  $c_b = 0.38$ . Carvalho et al. [75] explored the case of a liquid film surrounded by co-flowing air streams, whereas Zhao et al. [72] explored the case of a liquid jet surrounded by an annular air stream, which likely accounts for the discrepancy in their reported coefficients.

$$St = \frac{fd_0}{u_t} \approx c_a M^{c_b} \quad (2.5)$$

### 2.1.3 Spray/Cone Angle

The absolutes of the ILJ oscillations partially define the cone angle of the spray, at least in the near-field. Boylu and Atesok [77] showed that the spray angle decreases as the

gas-to-liquid mass flow ratio is increased. Zheng et al. [78] showed that as the ambient pressure is increased, the spray angle increases. Daviault et al. [79] showed that increasing the liquid viscosity correlated with a decrease in the spray angle. Leroux et al. [44] proposed a relationship between the kinetic energy ratio and the spray angle. Using nine different atomizer geometries, Leroux et al. [44] showed that the spray angle initially increases before decreasing as  $M$  is increased.

#### 2.1.4 Shedding (or Wave) Frequency

The shedding frequency has been reported by a number of studies, again, typically only for low viscosity, Newtonian fluids [39, 41, 71, 80–82]. Most studies show that the frequency increases with increasing liquid velocity and increasing gas velocity, although the effect of the gas velocity has more effect [39, 80, 81]. The highest frequencies reported in these studies is roughly 4 kHz [39, 41, 71].

Eroglu and Chigier [80] reported that the frequency first decreases and then increases with increasing distance from the atomizer, whereas Tian et al. [71] suggest that the shedding frequency is constant along the entire length of the ILJ. As the liquid velocity is increased, the frequency was shown to increase [80]. The frequency was shown to increase with increasing gas velocity as well [80]. Engelbert et al. [67] showed the shedding frequency to increase with increasing gas velocity as well as decreasing liquid viscosity (via heating the fluid to higher temperatures). Raynal et al. [81] showed the frequency to increase with increasing gas velocity and liquid velocity, as was also shown by Marmottant and Villermaux [41] and Lasheras and Hopfinger [82]. Matas and Cartellier [68] showed that the shedding frequency increased with both increasing gas and liquid velocities. Tian et al. [71] propose a slightly modified version of the relations presented by previous studies [41, 80–82] to show the dependence of the frequency on the convective velocity and boundary layer thickness. They proposed that the distance at which the gas and liquid flows reattach past the atomizer is a function of the atomizer geometry [71]. Lasheras et al. [39] showed the frequency to increase with increasing gas velocity, but the correlation between frequency and gas velocity is dependent on whether the liquid velocity is greater than or less than 0.5 m/s.

#### 2.1.5 Surface Wavelengths

Eroglu and Chigier [80] reported that the jet surface wavelengths increase with distance from the atomizer, and they tend to decrease with increasing liquid jet velocity. However, in the case of laminar liquid jet flow, the average reported wavelengths first increase and then decrease with increasing liquid jet velocity. The wavelengths decrease with increasing

gas velocity. Marmottant and Villermaux [41] showed the primary wavelength (normalized by the gas boundary layer at the atomizer) to first increase, and then decrease as the gas velocity is increased. They also showed the primary wavelength to decrease with increasing liquid velocity.

### 2.1.6 Scaling

Previous studies have examined how the scaling of atomizers effects spray characteristics, but few have looked at the effect of atomizer scaling with a constant gas-to-liquid cross-sectional diameter. Yilmaz [22] lays out why scaling atomizers from the industrial scale to the lab scale is such a challenge, especially when considering pressure. If a 25 cm atomizer operating in a 7 MPag industrial-scale gasifier is to be scaled down to an atmospheric lab-scale at  $1/5^{th}$  the size, gas velocities at the lab-scale have to be supersonic in order to match the Reynolds and Weber numbers of the industrial-scale gas flow at only 3 m/s, which is significantly lower than what can be expected for the industrial gas velocity. Leroux et al. [44] looked at the effect of changing atomizer geometry on the spray SMD, but did not specifically evaluate changing the scale of an atomizer, keeping relative gas and liquid areas of flow constant. Thybo et al. [83] evaluated the effect of atomizer geometry on spray characteristics, but again, they did not specifically evaluate the scale of an atomizer while keeping the relative gas and liquid areas of flow constant. Engelbert et al. [67] also looked at a few different atomizer geometries, but did not draw any major conclusions on the effect of geometry, and did not look at scaling. Zhao et al. [69] looked at atomizers with a number of different liquid-to-gas cross-sectional area ratios and found that increasing the ratio will change the breakup morphology, but the resulting effect on the spray characteristics was not identified.

Practical concerns to be noted when changing the scale of an atomizer mainly cater to any possible values kept constant. For instance, reducing the liquid jet diameter while keeping a constant volumetric liquid flow can shift the flow regime from laminar to turbulent, which will change the some of the relations proposed between system inputs and the ILJ characteristics or spray-representative drop diameter. The same can be said for the gas, as increasing the gas annulus will reduce the gas velocity and can shift the flow regime from turbulent to laminar, which will decrease the ILJ length, increase the ILJ surface wavelengths, and increase the spray-representative drop diameter. Tian et al. [84] showed that increasing either the liquid tube thickness or the gas annular gap thickness will increase the distance past the atomizer at which the gas and liquid flows reattached, and thus will decrease the shedding frequency. Zhao et al. [69] show that increasing the gas-to-liquid

cross-sectional area correlates with a decrease in the ILJ length. What is not as well known is how the system behaves when all parameters are changed, or the general scale of the atomizer is increased while keeping the gas-to-liquid cross-sectional area relatively constant.

## 2.2 Stability Analysis

The more recent, mechanism-based approach described previously stems from the work of Hopfinger, Villermaux, Cartellier, and Lasheras, along with their PhD students Aliseda, Rehab, Raynal, Marmottant, Hong, and Varga [33, 39–41, 61, 81, 82, 85–89]. These studies explored the effect of flow rate, slight fluid property changes, and small geometry changes on the observed instability wavelengths, frequencies, and resulting spray characteristics. However, they do not extend the proposed breakup mechanism to a wide range of liquid physics properties or various atomizer scales.

### 2.2.1 Existing Studies

Hopfinger and Lasheras [85] explored the atomization of water with air using a single external-mixing, coaxial, two-stream atomizer. They evaluated liquid velocities between 0.22 and 1.5 m/s and gas velocities up to 270 m/s. They showed that an increase in the gas velocity correlated with a decrease in the spray SMD, and that an increase in the liquid velocity correlated with an increase in the spray SMD. The SMD was shown to be smallest along the center axis of the atomizer, and increase with radial position away from the center. Additionally, the difference between the maximum and minimum radial spray SMD increased with increasing distance past the atomizer [85].

Villermaux et al. [86] explored the oscillations of the ILJ jet for a external-mixing, coaxial, two-stream atomizer. They evaluated these fluctuations using seeded gas flow in either the outer annulus, the inner jet, or both. No liquids were used in there study.

Raynal et al. [81] explored the atomization of a liquid sheet with planar air flow and a water jet with air using an external-mixing, coaxial, two-stream atomizer. They evaluated liquid velocities between 0.1 and 5 m/s and gas velocities from 10 to 200 m/s. Only one atomizer geometry was used for either the two-dimensional case or the axisymmetric case. The convective velocity was measured using a hot-film and a Position Sensitive Detector (PSD), which is essentially a laser paired with a photodiode or photoresistor. Their measurements of the convective velocity for a gas-liquid system agreed with the proposed definition of Bernal and Roshko [90] (originally proposed by Brown and Roshko [91] and later verified by Dimotakis [92]) for a gas-gas system. They quantified and correlated the wave (or shedding) frequency with the gas and liquid velocity, and thus, the convective

velocity. They showed that the ILJ surface wavelength is independent of the liquid velocity. They also showed that the shedding frequency can be well defined by the convective velocity and the gas boundary layer thickness at the atomizer exit. They suggest that the primary instability observed is well-represented by the Kelvin-Helmholtz type instability.

Rehab et al. [87] explored the mixing of gases using an external-mixing, coaxial, two-stream atomizer. They explored the effect of the inner-to-outer velocity ratio on the formation of a recirculation region near the end of the gas-gas equivalent of the ILJ. While a gas-gas system has a significantly different density ratio than a gas-liquid system, the density ratio can easily be account for along with the velocity ratio (the driving parameter in their study) in the kinetic energy ratio. Villermaux [88] further built on the work of Rehab et al. [87] to suggest how the same system dynamic could lead to and be correlated with the formation of drops.

Lasheras et al. [39] explored the atomization of water and ethanol with air using a single external-mixing, coaxial, two-stream atomizer. They evaluated liquid velocities up to 1.5 m/s and gas velocities up to 250 m/s. They showed that the ILJ surface oscillation frequency increases with an increase in the gas velocity and the ILJ surface oscillation frequency is independent of the liquid velocity for small liquid Reynolds numbers. The proposed model qualitatively mimics the experimental observations. Lasheras et al. [39] propose an entrainment model to predict the ILJ length. They also show that the spray SMD first decreases before increasing as distance past the atomizer is increased.

Hong et al. [89] explored the atomization of water with air using an external-mixing, planar atomizer. They suggest (based upon the doctoral work of Marmottant, whose article [41] is discussed subsequently) that instead of the spray-representative drop diameter being dependent on the primary (or Kelvin-Helmholtz) instability wavelength, it is dependent on the transverse (or circumferential) instability wavelength. This instability is essentially a Rayleigh-Taylor instability wrapped around the circumference of the liquid jet, or in this case, along the planar liquid sheet surface. Hong et al. [89] showed that the transverse wavelength decreases with increasing gas velocity at a constant gas-to-liquid kinetic energy ratio.

Varga et al. [33, 40] explored the atomization of water and ethanol with air using two external-mixing, coaxial, two-stream atomizers of similar geometry. They evaluated liquid velocities up to 17 m/s and gas velocities up to 165 m/s. The measured primary drop sizes were shown to scale with the Rayleigh-Taylor instability wavelength, and the drop diameter dependence on gas velocity and and liquid surface tension was captured by the proposed

model. Varga et al. [40] showed many images of the various observed breakup regimes, reported centerline spray SMDs, and reported measured primary wavelengths and secondary Rayleigh-Taylor wavelengths (with no statistics). While evaluating both water and ethanol gives an idea of the effect of surface tension on the atomization mechanism ( $\sigma_{water} = 0.070$  N/m,  $\sigma_{ethanol} = 0.023$  N/m), the effect of viscosity is not known.

Marmottant and Villermaux [41] explored the atomization of water, ethanol, and a glycerol solution with air using a single external-mixing, coaxial, two-stream atomizer. They evaluated liquid velocities up to 2 m/s and gas velocities up to 90 m/s. They measured the velocity profile (somehow, not reported) in order to develop an equation for the vorticity layer thickness, normalized by the central tube thickness, as a function of the gaseous Reynolds number,  $Re_g$ . They reported the primary instability wavelength, normalized by the vorticity layer thickness, as a function of the gas velocity. The primary instability wavelength, normalized by the vorticity layer thickness, tends to decrease with an increase in the liquid velocity. The primary instability wavelength, normalized by the vorticity layer thickness, for a given liquid velocity first increases with increasing gas velocity, before decreasing. The gas velocity at which the peak in the primary instability wavelength-vorticity layer thickness ratio occurs increases with increasing liquid velocity. The liquid used in reporting these trends is not indicated [41]. Marmottant and Villermaux [41] report the ILJ surface oscillation frequency as a function of the gas and liquid velocities. The peak frequency increases with increasing gas velocity and increases with increasing liquid velocity, although this trend is less evident at high gas velocities. Marmottant and Villermaux [41] show a slightly different manifestation of the Rayleigh-Taylor instability. Whereas Varga et al. [40] show the Rayleigh-Taylor instability wavelengths developing in the radial direction away from the liquid jet axis, Marmottant and Villermaux [41] show the wavelengths developing in the azimuthal (or transverse, or circumferential) direction, around the surface of the jet. These transverse instabilities produce ligaments that are approximately evenly spaced. The spacing of the ligaments is shown to decrease with a decrease in surface tension and decrease with an increase in gas velocity. They show the ligaments stretching in the air stream, eventually breaking up via a capillary instability. This sequence of observed atomization dynamics is notably different than those reported elsewhere, and it likely represents a low-gas-velocity subregime of those regimes presented earlier [93].

Aliseda et al. [61] explored the atomization of six different fluids (of varying rheological properties) with air using a single external-mixing, coaxial, two-stream atomizer (from Spraying Systems). They evaluated liquid velocities up to 0.4 m/s and gas velocities up to

220 m/s. They report only drop sizes at multiple points along the central liquid jet axis, allowing for determination of the point at which atomization is complete. They compared their measurements with the two-stage instability mechanism proposed by Varga et al. [40], except they furthered the mechanism theoretically by including terms to partially represent the non-Newtonian behavior of the fluids used. In reality, they only modified the theory to include a viscosity value, via the Ohnesorge number ( $Oh = \frac{\mu}{\sqrt{\rho \sigma l}}$ ). While they explored non-Newtonian fluids, they assumed that the viscosity measured at the highest shear rate explored was representative of the fluid.

More recently, a few studies that followed the same two-stage instability mechanism development have been published. These studies often extend the two-stage instability mechanism, but with obvious limitations. A number of studies are from a research group at East China University of Science and Technology (ECUST).

Zhao et al. [72] explored the atomization of eight coal-water slurries with air using two atomizers of similar geometry. They evaluated liquid velocities up to 5.8 m/s and gas velocities up to 160 m/s. They made three major contributions. First, they propose a map to delineate breakup regimes as a function of  $We$  and  $Oh$ . This new map successfully identifies the Rayleigh-type regime, fiber-type regime, and atomization regime. Second, they modify and extend an existing equation (proposed by Lasheras et al. [39]) predicting the ILJ breakup length to include the fluid viscosity. They obtained a fairly good fit to data with the various coal-water slurries that they evaluated. Third, they proposed a method to quantify the pendular behavior of the ILJ. This method considers the ILJ to be a compound pendulum and develops a theoretical correlation to compare to their data. This pendular behavior has been identified in other studies, but this study [72] appears to be the first attempting to quantify it for the coaxial atomization of a liquid with a gas.

Tian et al. [71] explored the atomization of water with air using six different atomizers of similar geometry. They evaluated liquid velocities up to 1.6 m/s and gas velocities up to 83 m/s. They make one major contribution. In order to quantify the recirculation zone behind the central tube thickness, they dug up some studies evaluating flow over a backward-facing step or through a sudden expansion and flow separation and reattachment. Previous studies [41] showed the frequency of the primary instability to scale as a function of the vorticity layer thickness at the atomizer face. Tian et al. [71] show that a better prediction is made by using the vorticity layer thickness at the point of flow reattachment, which they show to be a function of the atomizer geometry.

Zhao et al. [73] explored the atomization of two different coal-water slurries with air

using two external-mixing, coaxial, two-stream atomizers of similar geometry, although one of the atomizers was the same as a previous study [72]. They evaluated liquid velocities up to 0.9 m/s and gas velocities up to 161 m/s. They make one major contribution. They modify and extend an existing equation (proposed by Lasheras et al. [39]) predicting ILJ breakup length to include normal stresses encompassing viscoelastic fluids. In addition, they propose equations for the pendular motion of the ILJ and for the oscillation frequency of the primary instability, but these have both been identified previously.

These studies all used the formulation of the two-stage instability mechanism to produce equations that are used to compare the system inputs to the primary instability frequency, the ILJ length, or a spray-representative drop diameter. Lasheras et al. [39], Varga et al. [40], and Marmottant and Villermaux [41] report some measured values of the instability wavelengths and their associated frequencies. However, Lasheras et al. [39] and Varga et al. [40] do not explore high viscosity fluids, and Marmottant and Villermaux [41] only explore the lower flow regimes. Aliseda et al. [61] apply this two-stage instability mechanism to a wide range of fluids, including high viscosity fluids, but they do not report any of the transition characteristics such as instability wavelengths and associated frequencies. Tian et al. [71] evaluate only the primary instability frequency for water. The studies by Zhao et al. [72,73] evaluate some of the transition ILJ characteristics for coal-water slurries, but do not report spray-representative drop diameters. Also, very few of these studies explore more than one atomizer geometry, or if more than one geometry is explored, the effect of changing geometry on this mechanism-based model is not evaluated. This provides ample opportunity to extend and verify hypothesized atomization models.

### 2.2.2 Breakup Mechanisms

There are two instabilities that are commonly associated with the coaxial breakup of a liquid jet by an annular gas stream: the Kelvin-Helmholtz instability (KHI) and the Rayleigh-Taylor instability (RTI). These instabilities are hypothesized to occur in sequence as a sort-of one-two punch, leading to the stripping of ligaments and drops from the ILJ. A few studies have explored their development, but none have sought to do so paying attention to a changing atomizer scale.

The KHI can occur when there exists a velocity difference across the interface between two fluids. For the case of laminar liquid flow and turbulent gas flow, it is hypothesized that a primary instability develops (KHI) on the surface of the ILJ. The most unstable wavelengths of this instability manifest and grow until they issue out past a hypothetical cylinder into the high-velocity gas stream. The KHI is illustrated in Figure 2.2, as reproduced from

Varga [33].

The RTI can occur on an interface between fluids of different densities when the lighter fluid is accelerated into the more dense fluid. At this point, a secondary instability develops (RTI). However, this secondary instability manifests in two distinct ways in the literature, perhaps dependent on the morphological regime or the relative fluid velocities of the system. The two manifestations of the Rayleigh-Taylor instability are shown in Figure 2.3 and Figure 2.4, as reproduced from Varga et al. [40] and Marmottant and Villermaux [41], respectively.

Figure 2.3 illustrates the first RTI manifestation. The instability wavelengths develops in the radial direction issuing away from the center axis of the liquid jet. In most cases, this is shown as the wavelength peaks of the primary instability issue far enough out into the high-velocity gas stream that they break from the central liquid jet and break multiple other times along the ligament length, likely dependent on the controlling parameters of the development of the RTI. The order in which the breakups occur is not entirely clear; the ligament may break apart from the central liquid jet before or after it breaks up itself. If it breaks apart from the central liquid jet first, it would then fall under the umbrella of secondary breakup. If the ligament itself breaks up before separating from the central liquid jet, it would fall under the umbrella of primary breakup, which is the main concern herein.

Figure 2.4 illustrates the second RTI manifestation. The instability wavelength develops in the azimuthal direction, along the circumference of the liquid jet. This case is not mutually exclusive with the last case, but it is not presented as such by Marmottant and Villermaux [41]. In the same fashion, the primary instability wavelengths develop such that their peaks issue out into the high-velocity gas stream. The high-velocity gas then provides the amplification needed for the RTI to manifest around the circumference of the central liquid jet. This leads to a distinct number of ligaments evenly separated around the axis that issue further into the gas stream as ligaments. Here, the ligaments pinch, shear, or pinch and shear into drops via stretching and/or capillary breakup (Rayleigh-Plateau instability).

A combined primary and secondary instability is suggested to lead to the end of primary atomization. While the ligaments and drops separated from the ILJ may undergo further atomization (secondary atomization), the focus herein is on primary atomization. No attempt to quantify the flow field to adequately ascertain the effects of secondary atomization are made, and secondary atomization is considered to be outside the scope for this work.

### 2.2.3 Atomization Regimes and Morphology

Some dimensionless numbers that are commonly used to describe atomization systems are the Reynolds number ( $Re = \frac{\rho_l u_i}{\mu_l}$ ), the relative Weber number ( $We = \frac{\rho_g l (u_g - u_l)^2}{\sigma}$ ), and

the gas-to-liquid kinetic energy ratio ( $M = \frac{\rho_g u_g^2}{\rho_l u_l^2}$ , also justifiably referred to as the dynamic pressure ratio and unjustifiably as the momentum flux ratio per unit volume).

A number of distinct morphological changes occur to the intact liquid jet (ILJ) as both the gas and liquid flow rates are changed. The flow conditions considered in this work are laminar liquid flow and a range of gas flows (but typically turbulent gas flow). These changes have been grouped into identified regimes of breakup for the atomizer types considered herein.

It is important to note some of the approximate absolute values that are used in this system. For instance, in all cases explored, the liquid flow regime is laminar. The liquid velocity is always below 1 m/s. This is important to note as it removes the contribution of cavitation to instability formation as the liquid jet leaves the atomizer, which can be a significant contribution at high enough velocities paired with certain atomizer geometries.

Faragó and Chigier [94] proposed regimes of atomization for external-mixing, coaxial, two-stream atomizers, Figure 2.5 [94], that are distinguished by the liquid Reynolds number,  $Re_l$  and the relative Weber number,  $We$ . These regimes were updated by Lasheras and Hopfinger [82], shown in Figure 2.6 [82], to include some effect of the gas-to-liquid kinetic energy ratio,  $M$ .

These regimes are associated with certain breakup morphologies. The Rayleigh regime (Figure 2.7 [94]), membrane-regime (Figure 2.8 [41]), fiber-type regime (Figure 2.9 [41]), and superpulsating submode (Figure 2.10 [94]) each correspond to different flow conditions. In this study, the focus lies mostly with high gas-to-liquid kinetic energy ratios, such that the regime of breakup explored is commonly of the membrane-type or higher.

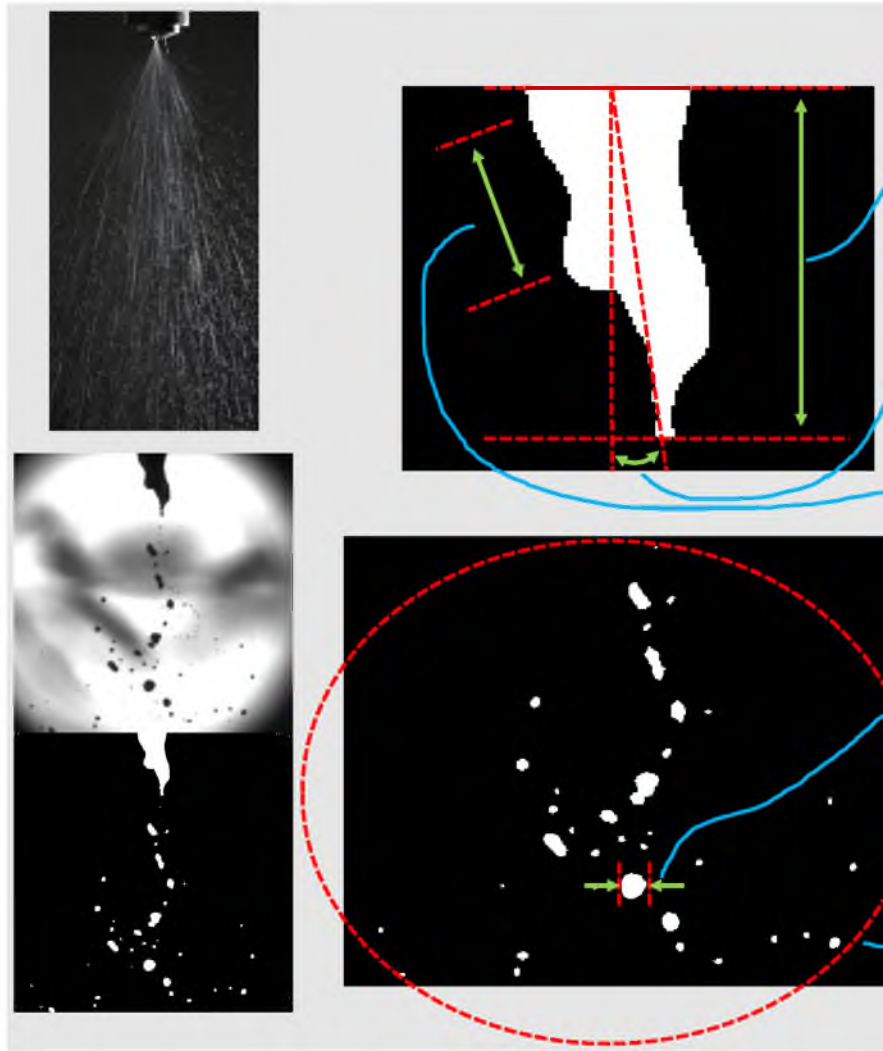
The regimes illustrated in Figures 2.7-2.10 serve to inform the rough geometric shapes that the ILJ takes. Conservation of mass dictates that as liquid drops and ligaments are stripped from the ILJ surface, more liquid takes its place. While the rate at which new liquid is supplied is relatively constant, the rate at which liquid is stripped from the ILJ oscillates around an average. This shedding of drops and transient characteristics of those drops are hypothesized to correspond to oscillations of the ILJ length and the pendular motion of the ILJ. In fact, the pendular motion (driven by the turbulent gas - laminar liquid interactions) can be seen to almost fling liquid ligaments or drops in some cases. In combustion or gasification applications, as the gaseous oxidant flow and liquid (typically solid-fuel-containing) drops mix, a flame front will develop. It does not take a leap of logic to see that this shape may dictate the resulting flame shape and propagation.

## 2.3 Gasificaton

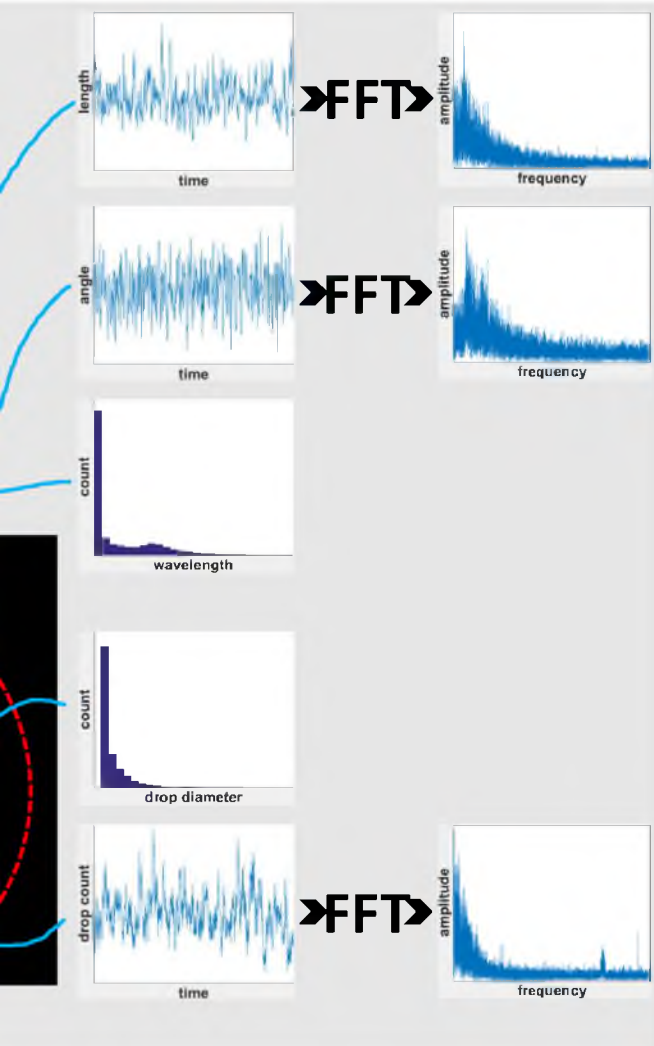
While coal and petroleum coke use in the United States is being slowly tempered, China and India will only increase their dependence in the coming years [1]. The use of these fossil fuels in China with inefficient, old technology has been suggested to decrease the life expectancy of those in close proximity by up to 5.5 years [95], and the pollutants formed in China are catching winds to the United States [96]. In China and India, and at a handful of locations in the United States, gasification facilities are being built to use both coal and petroleum coke more efficiently and with near-zero emissions [4]. Slurry-fed, entrained flow gasifiers are found in many of these facilities, and their operation relies heavily on the atomization of a high-viscosity, multiphase, fuel stream by a gas stream.

The performance of slurry-fed gasification systems is often dictated by the performance of the atomizer [4,18]. As previously shown in Table 2.2, an increase in the spray-representative drop diameter correlates with a decrease in the gas velocity. In a slurry-fed, entrained flow gasifier, this has been shown to lead to inefficient performance in the form of low conversion and a syngas that is rich in combustion products ( $\text{CO}_2$ ) as opposed to gasification products ( $\text{CO}$  and  $\text{H}_2$ ) [8]. This was also shown via the gasification of glycol [20]. Jakobs et al. [20] showed via numerical simulation that the fraction of drops with a diameter greater than or equal to 300 micron will significantly impact the performance of a gasifier. The increased size of these drops inhibits the beginning of gasification, as a larger period of time is required to evaporate the water contained in the drop. This additional time leads to the onset of gasification further through the reactor, and subsequently, many particles will leave the gasifier or impinge and stick to the gasifier wall before completely reacting. This leads to poor conversion, poor syngas quality, increased wear of the gasifier walls, and an increase in the carbon content of the produced slag (solid inorganic material), rendering it inadequate for sale [3,4].

Unfortunately, few studies explore the effect of atomizer design on the performance of an industrial gasification system. While this hinders the academic pursuit, it is not without reason. Most industrial gasifiers produce electricity or chemicals for profit, and any change that could lead to downtime is avoided at all costs. Additionally, as there are a number of companies with their own proprietary gasification technologies. Any significant advance by one single company is a significant capitalistic advantage. Sharing an insight into atomizer design for industrial gasification operation would reduce margin for the company having discovered that insight. As mentioned previously, this lends particular relevance to the work being done with the University of Utah's entrained flow gasifier [8–18].



**Figure 2.1.** Graphical illustration of analysis performed on image sets.



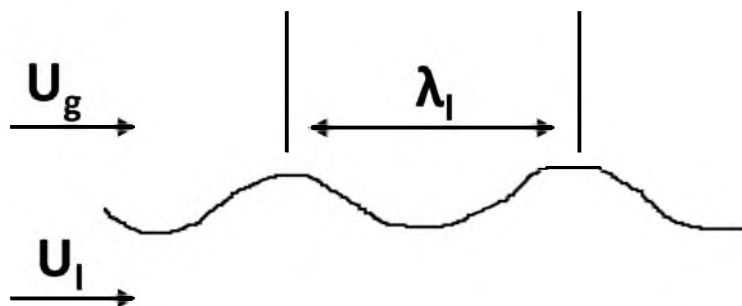


**Figure 2.2.** Kelvin-Helmholtz (or primary) instability wavelength, reproduced from Varga [33].

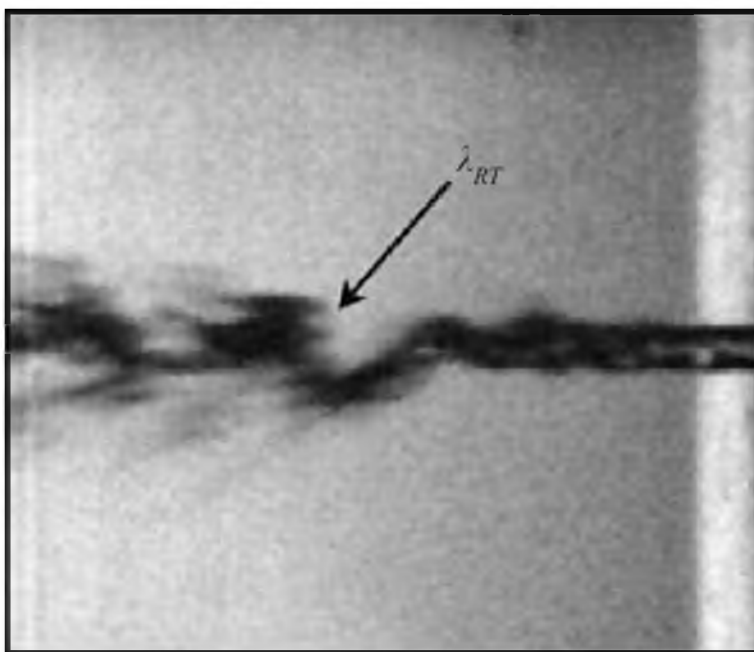


**Figure 2.3.** Rayleigh-Taylor instability wavelength manifestation one. © [40] The wavelength is seen to manifest in the radial direction, away from the center axis of the spray.

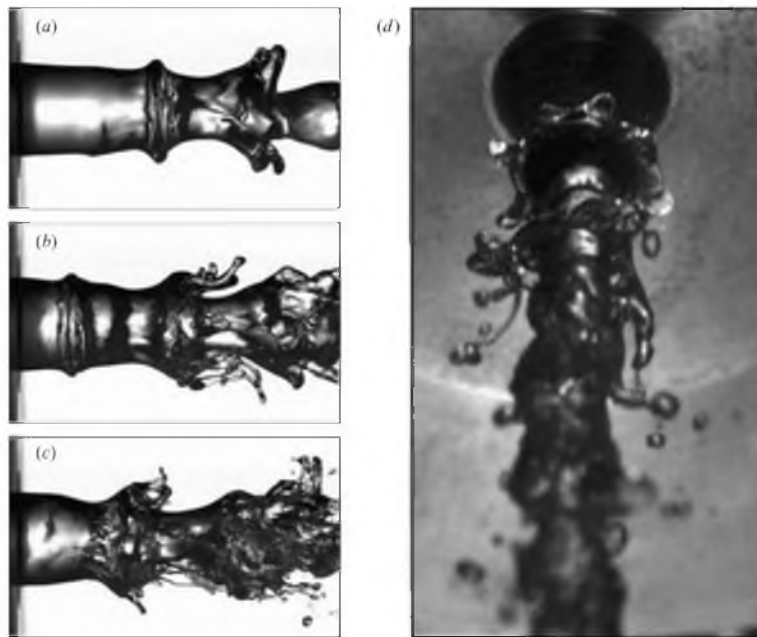


**Figure 2.4.** Rayleigh-Taylor instability wavelength manifestation two © [41]. The wavelength is seen to manifest in the azimuthal direction, around the circumference of the liquid jet.

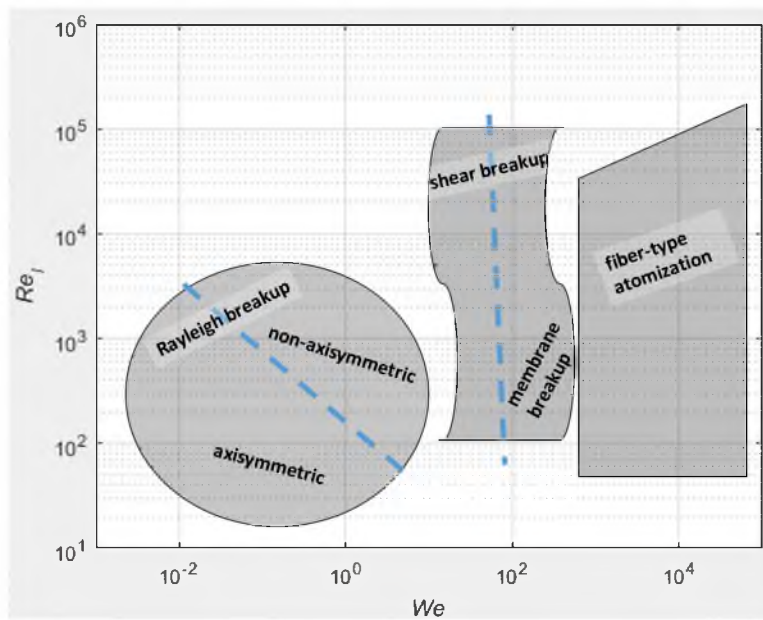


**Figure 2.5.** Faragó and Chigier's breakup regimes, reproduced from Faragó and Chigier [94].

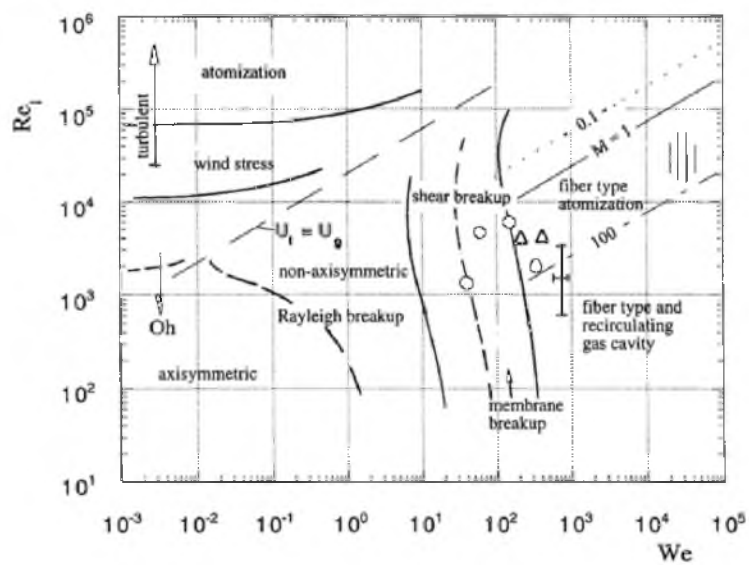


Figure 2.6. Lasheras and Hopfinger's breakup regimes © [82].

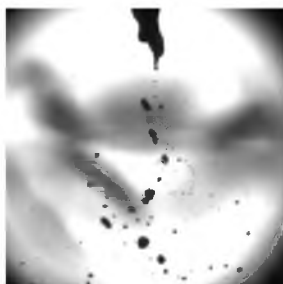


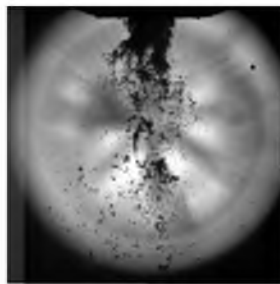
Figure 2.7. Rayleigh-type breakup morphology, reproduced from Faragó and Chigier [94].



Figure 2.8. Membrane-type breakup morphology © [41].



**Figure 2.9.** Fiber-type breakup morphology © [41].



**Figure 2.10.** Superpulsating submode breakup morphology.

**Table 2.1.** Identified trends with gas and liquid properties.

increasing...	$\mu_l$	$\rho_l$	$\sigma$	$\rho_g$	$P$
spray SMD	↑ [97–100]	↓* [97]	↑ ~ [97, 100]	na	↑ [20, 101]
ILJ length	~** [67]	↑ [39]	~** [67]	na	↓ [43]
pendular motion	na	↓ [72, 75]	na	na	↑ [72, 75]
spray angle	~ [99], ↓ [79]	↓ then ↑ [44]	↓ [100]	na	↓ [20, 101], ↑ [78], ↑ then ↓ [44]
wave $f$	na	↓ [39, 41, 71]	na	↑ [41, 71]	na
wavelength	na	na	na	na	na
wave amp.	na	na	na	na	na
breakup $f$	na	na	↓ [67]	na	na

\*Slight decrease for low gas velocity; little to no change for high gas velocity.

\*\*Liquid temperature increased.

**Table 2.2.** Identified trends with flows and geometry.

increasing...	$Q_l$	$u_g$	$d_0$	$a$	$b$	$A_g/A_l$
spray SMD	↑ [67, 97, 99, 100]	↓ [67, 97, 98]	~ ↑* [97, 102]	na	na	na
ILJ length	↑ [39, 42, 67–69]	↓ [39, 67, 68]	↑ [39]	↓ [44]	na	↓ [69]
pendular motion	↓ [72, 75]	↑ [72, 75]	na	na	na	na
spray angle	↓ [68, 77], ~ [99], ↓ then ↑ [44]	↑ [68, 77], ↑ then ↓ [44]	na	na	na	na
wave $f$	↓ then ↑** [39], ↑ [41, 71, 80–82]	↑ [39, 41, 67, 68, 71, 80–82]	na	↓ [71]	↓ [71]	na
wavelength	↑ then ↓*** [41, 80]	↓ [80], ↑ then ↓ [41]	na	na	na	na
wave amp.	↑ [67]	↓ [67]	na	na	na	na
breakup $f$	↓ [67]	↑ [67]	na	na	na	na

\*No change for low viscosity; increase for high viscosity.

\*\*Decrease for laminar liquid flow, increase for turbulent liquid flow.

\*\*\*For laminar flow. For turbulent flow, wavelengths decrease with increasing liquid jet velocity.

## CHAPTER 3

### EXPERIMENTAL METHODS

Predominantly, imaging was the method utilized to better understand the atomization systems explored. Some additional methods were used to both control and analyze the operation of the entrained flow gasifier. These are all detailed below.

#### 3.1 Small-Scale Atomizer Testing

The small-scale atomizer testing focused on two things in the near-field: the intact liquid jet (ILJ) and the produced drops. These were initially probed using a laser and photoresistor arrangement, such that oscillations in the ILJ surface cause the laser to fall out of direct alignment with the photoresistor, and the corresponding voltage measurement across the circuit containing the photoresistor could be correlated to ILJ surface oscillation frequencies. Luckily, a high-speed camera became available, which allows ILJ surface oscillation frequencies to be measured along the entire length of the ILJ in one test, whereas using the laser-photoresistor, multiple tests were needed to see the change in frequency and amplitude with increasing distance past the atomizer. While imaging has its limitations, it allows for the gathering of a very large quantity of data in a short amount of time, particularly for the relatively simple system being explored herein.

The aim of the small-scale atomizer testing is multifaceted. First, a verification of some of the mechanism-based atomization models (discussed in Chapter 2.2.2) is desired. The verification desired is both qualitative, in that the same visual steps should be seen, and quantitative, in that the correlations developed will be applied to the experimental results obtained herein. Second, an extension of those models is desired. As noted in Chapter 2, the studies proposing these mechanism-based models have not simultaneously covered a wide range of liquid properties, flow regimes, and atomizer geometry. With this verification, it is hoped that a better understanding is gained as to how scaling an atomizer effects the entire atomization process.

### 3.1.1 Equipment and Conditions

The atomizer geometry featured a central liquid jet with a coaxial, annular air flow, shown in Figure 3.1. The atomizers were from Spraying Systems [103] and have been used in other studies [61,104]. They are modular in design, allowing for quick changing of either the liquid or gas geometry. The geometries used in these experiments are given in Table 3.1. All experiments were conducted at atmospheric pressure and room temperature. The experimental conditions can be seen in Table 3.2.  $u_g$  is the gas velocity, while  $u_l$  is the liquid velocity.

Air was the atomizing gas, while water and silicone oils were the liquids being atomized. This provides a very large range of liquid viscosities being evaluated, although the liquids are all Newtonian. The fluid properties are shown in Table 3.3.

The liquid flow was measured with a rotameter, and calibrations of the flow were done before every condition explored. The liquid feed was supplied from a pressurized bladder tank. The use of a pump to feed the liquid was avoided as it would have unnecessarily added vibrations or pulsations to the system. The air pressure to the bladder tank was controlled with a regulator. The air flow was measured with a rotameter. A pressure gauge immediately after the rotameter was monitored and recorded to measure any pressure variation in order to accurately correct the gas flow.

The liquid jet was made visible by backwards illumination with a LED (HPLS-36DD182, Lightspeed Technologies, Inc.). A high-speed camera (Fastcam APX-RS, Photron Limited, CMOS sensor) was used to inspect the jet oscillations, ligament production, and breakup. Multiple extension tubes and a Tamron Macro Lens (Tamron AF 70-300mm f/4.0-5.6 Di LD Macro Lens) were used to better magnify the spray. The camera was operated at 10,000 frames per second (fps) in continuous mode, which allows measurement of frequencies up to 5,000 Hz according to the Nyquist criteria. As the highest measured frequency as reported by similar studies [39,41,71] was 4,000 Hz, the chosen frame rate should be appropriate. This also provided a frequency resolution of 1.0 Hz. Both the camera and LED were triggered externally using a pulse generator (Hewlett-Packard Model 8112A). For 10,000 fps, the period and width of the signal were 100 microseconds and 500 nanoseconds, respectively. The resolution of the images ranged from 512x544 to 512x480. By rear-illuminating the atomization process, shadows of the intact liquid jet and the resulting drops are captured in two-dimensional space, which in this case is assumed to be representative of three-dimensional behavior.

### 3.1.2 Image Processing

All images were processed and analyzed using either MATLAB<sup>®</sup> [105] or FIJI [106]. Other studies have reported using these programs for image processing [33,41,71–73,79,84,107–110], but oftentimes, little detail of the image processing method and threshold values chosen are reported. In this case, in addition to reporting drop characteristics, we are also reporting characteristics of the intact liquid jet, which has been characterized previously, but no image processing method has been presented. Here, a brief description of the methods used is given.

The image processing method for those images obtained via the high-speed camera can be reduced down to a few steps, outlined below.

- Import representative background image.
- Import object image.
- Register the object image with the background.
- Divide the object image with the background.
- Convert image to binary via auto-threshold.
- Creation of new image (from binary image) containing only the ILJ.
  - ILJ length and position (angle) are measured.
  - New image containing only the ILJ perimeter is created.
  - ILJ perimeter is indexed.
  - First and second derivatives of the ILJ perimeter column index are calculated.
  - Critical points are determined and reduced to identify and measure wavelengths.
- Creation of new image (from binary image) containing only the drops.
  - Drops are counted.
  - Drops are quantified.

For all cases, a minimum of 5,000 images were analyzed. For most cases, 10,000 images were analyzed. Duplicates of the air-water tests were performed, but the air-silicone oil tests were not repeated. Error bars were calculated for most figures. In almost all cases, particularly for the geometric mean and standard deviation measurements, the error bars

were insignificant. The only cases where the error bars were significant were for the drop diameter measurements at very low dynamic pressure ratios, essentially the cases where liquid was most like a dripping faucet. They have been left out here for readability.

The still images obtained were originally processed using MATLAB<sup>®</sup> [105] to convert the images to binary and overlay them on each other. Then, FIJI [106] was used to manually calculate the solid angle formed by the spray.

## **3.2 Pilot-Scale Atomizer Testing**

The pilot-scale atomizer testing focused largely on achieving better conversion in the University of Utah's entrained flow gasifier (EFG). However, the purpose of any testing on the EFG was never specifically to evaluate a particular atomizer design; operating the EFG is expensive, and there was often demand for specific testing to be done by industrial or academic clients during this graduate student's tenure. As such, the seemingly best performing atomizer design at any particular time was what was used for a particular set of EFG experiments. Occasionally, the EFG conditions sought after overlapped with tests utilizing another atomizer design, but this was not always the case. As such, there is some inclusion of EFG performance, but the focus largely falls on the cold-flow performance of a few of the atomizer designs used for EFG testing.

As most of the EFG testing performed occurred during the first two to three years of this graduate student's tenure, the pilot-scale atomizer design, evaluation, and testing occurred at a point where the methods used for evaluation were not as advanced as they were for the last one to two years. Imaging was used to evaluate the atomizers, but it was not high-speed. A digital single-lens reflex camera was used to capture a region of the spray, and a relatively small number of images was processed to obtain drop diameters when compared to the large image sets captured with the high-speed camera for the small-scale testing. Additionally, the atomizer designs, while always coaxial and external-mixing, were not always the simple concentric tube layout utilized for the small-scale testing. Due to these facts, the instability formation and growth could not be and was not quantified for the pilot-scale atomizers. Correlations are still established for spray-representative diameters.

### **3.2.1 Injector Design**

#### **3.2.1.1 Original Design**

The injector is a twin-fluid design. It allows coal-water slurry to flow down the inner tube, and the oxygen to flow down the outer tube. The injector neck is surrounded by a water jacket that keeps the injector from damage at the higher operating temperatures of

the EFG. An air or nitrogen purge is provided for the small gap between the water jacket and the slurry/oxygen tubes to prevent soot build-up and assist heat removal. A schematic of the injector is shown in Figure 3.2.

The injector has a removable nozzle that directs the oxygen flow into the coal slurry stream. Three nozzles have been constructed, with impingement angles of  $25^\circ$ ,  $45^\circ$ , and  $65^\circ$ . The angle of impingement is measured from the vertical. Each nozzle is denoted as an {angle}-nozzle representative of its impingement angle. A profile of the  $45^\circ$  nozzle is shown in Figure 3.3. The inner tube shown in Figure 3.3 is the coal slurry tube. The distance between the coal slurry tube and the nozzle is referred to as the gap width. By changing that distance, the oxygen or air pressure drop across the nozzle is changed by forcing the gas through a smaller or larger annulus.

### 3.2.1.2 Further Atomizer Development

The atomizers used in combustion or gasification systems are commonly twin fluid atomizers. A high-velocity gas stream is used to shear a low-velocity liquid stream. The difference in velocity between the two phases is often multiple orders of magnitude. Important spray characteristics are drop size, drop size distribution, spray pattern, and spray angle as these factors (along with the reactor geometry) will dictate the drop trajectory, flow recirculation, and, in a way, carbon conversion [34].

Many twin-fluid atomizer designs feature a gas annulus contacting a centered liquid jet. As the quality of atomization is largely dictated by the velocity of the gas stream relative the liquid stream for this design, the gas annulus is designed to provide a certain pressure drop (and equivalent velocity) for the target operating conditions (gas flow rate, system pressure). For most cases, performance is best if the pressure drop is maximized, although minimal returns are realized past a certain point.

The atomizers used with the University of Utah's EFG, while stemming initially from the literature, have slowly evolved in-house to meet the demands of the system. The two most evident (currently) pressing issues facing atomizer design are the scale of the gasifier and the cryogenic oxygen system.

The University of Utah's EFG is large in comparison to most facilities available to other gasification research groups in North America, but it is still somewhat small when compared to industrial facilities. The port available to house the injector is roughly 70.0 mm in diameter, and the cooling jacket that fits in this port leaves roughly a 25.4 mm diameter port with which to fit the injector tubing. This differs largely from the scale of injectors used in industrial gasifiers, which appear to be as large as 61.0 cm in diameter in pictures found

in the literature [3]. From surveying the patent literature, it is seen that current industrial slurry atomizers typically employ at least three streams: an inner gas jet, a center liquid annulus, and an outer gas annulus [111]. These prefilming atomizers (referred to herein as three-stream) offer better performance than the airblast design that features a central liquid jet surrounded by a gas annulus (referred to herein as two-stream). To use the three-stream design with the University of Utah's EFG, there are some practical complications to be overcome, particularly complications involving tight slurry passages where plugging is a major concern. Therefore, while a three-stream design that likely offers better performance and alleviates these complications is being furthered, the two-stream design is in use.

The other issue is the cryogenic oxygen system that supplies oxygen to the EFG. The maximum supply pressure from this system has been as high as 2.69 MPag, but the pressure swings. The lowest supply pressure seen from the system is 2.01 MPag, and this pressure is what can reliably be guaranteed to exist during the course of an EFG run. As is the case for all twin-fluid atomizer designs (both the three-stream and two-stream), higher gas velocities typically correspond to a smaller spray Sauter Mean Diameter (SMD). Maintaining a high gas pressure drop across the atomizer serves as a measure of the gas velocity and ensures proper atomization. Through EFG runs over the last few years, better performance has been seen for higher gas velocities. As system pressures of 1.72 MPag are often targeted, this leaves little working pressure with which to atomize. A span of more recent operations at 1.38 MPag have provided much more flexibility in the choice of atomizer with the increase working pressure, and performance has improved with the two-stream atomizer. For this reason, a better idea of the spray characteristics that govern operation of the EFG would help in diagnosing operational issues and improving performance.

This two-stream atomizer design has evolved over time as the constraints of fabrication and the limits of the EFG system itself have become more evident. Some of the atomizer design iterations are shown in Figure 3.4.

Initially, an adjustable design was used (shown in Figure 3.4, B and E), allowing for the gas velocity and subsequent gas pressure drop across the atomizer to be adjusted on the fly. These adjustable designs offered flexibility that was useful for start-up/shut-down conditions changes and even multiple experimental target conditions during the same run. Some of this work can be seen elsewhere [8]. However, due to the scale of the flow rates typical of the University of Utah's EFG system and small scale of the atomizer itself, the magnitude of the required adjustments became nearly impossible to achieve repeatedly. The atomizer designs quickly transitioned to something fixed.

The next designs sought to use spacers to set the target annular gap before welding separate pieces together. However, the scale of the system again made this difficult. This annulus had to be so small that reliably setting the gap could not be done in-house, and having it done elsewhere was difficult without having fabrication costs escalate dramatically. Attempts to do the work in-house proved futile, often leading to very nonconcentric sprays, as exhibited in Figure 3.5.

The next design iteration attempted to fix the desired gap by machining notches into the outside bevel of the inner slurry tubing (shown in Figure 3.4, C). The geometry of the notches was very simple and could easily and inexpensively be set to desired values. The thought was that the beveled inner slurry tubing and the outer tubing could be forced together and welded, resulting in the desired gap being maintained by the notches (Figure 3.4, C and D). It turned out that despite having the proper notch dimensions, the two tubes moved just enough while welding to cause the gap to change and the target design to be missed. This led to the most recent design iteration involving micro-holes.

The current injector iteration features two concentric tubes with slurry flowing in the center and oxygen flowing in the annulus. The injector tip, or atomizer, has micro-holes for gas flow (shown in Figure 3.4, A). The bottom face of the atomizer features an inner  $30^\circ$  bevel, and the micro-holes are machined in the bottom face perpendicular to the bevel. This bevel makes the gas impinge on the center slurry jet at a  $30^\circ$  angle. The diameter of these holes ranges from 0.254 mm to 0.787 mm depending on the target conditions in the EFG. The micro-hole atomizers explored herein had eight micro-holes evenly spaced around the center slurry line. They are approximately 0.245 mm away from the center slurry line, leading to contact between the oxygen and slurry approximately 1 mm away from the slurry exit orifice. The atomizer used in this study had micro-holes with a diameter of 0.584 mm.

### 3.2.2 Cold-Flow Testing

A system was constructed for atmospheric pressure cold-flow testing of the injector. Scaffolding was constructed to support the injector in a position far enough off the ground to allow visibility of the water spray and allow adjustments of the injector gap width. House air was connected to the injector through pressure regulator, a rotameter, and a pressure gauge. Water was also connected to the injector through a pressure regulator, a rotameter, and a pressure gauge. A schematic of the cold-flow set-up used for testing the injector on water and air is shown in Figure 3.6.

By suspending the injector and water jacket in the air, the plume from the injector was readily visible and photographed. Water and air lines were run to the injector as well as the

appropriate regulating devices in order to quantify the feed flow rates and pressures. The water and air flow rates and pressures were set to the desired values while simultaneously adjusting the gap width within the nozzle to achieve the desired pressure drop. Once the pressure drop and feed flow rates were set, photographs were taken to document the shape and profile of the water plume. This process was repeated with various flow rates, pressure drops, and impingement angles.

### 3.2.2.1 Rheology

Coal and petroleum coke are commonly mixed with water to form a suspension and used as a fuel. All slurries evaluated herein were made from preground coal or petroleum coke. Known weights of solid fuel and water were mixed together to approximate the desired solids weight loading. The loading was checked by heating a sample to 105°C, and holding it at that temperature until it stopped losing weight due to water evaporation. The difference between the initial and final weights leads to the solids loading. Then, more water or solid fuel was added until the desired loading was met.

The viscometer is an Advanced Rheometer AR-500. The geometry used was a 40.0 mm steel plate. The gap was typically set to 2.00 mm. Suspensions offer unique difficulties while attempting to identify rheological behavior. In order to ensure that the viscosity values obtained were representative, the range of shear stress applied to a sample was repeatedly ramped up and down. This was done for multiple samples until the viscosity values that were obtained converged upon themselves. The viscometer is shown in Figure 3.7.

### 3.2.2.2 Patternator

The patternator consists of a stand and test tubes. The stand was constructed so that gaps between cross-linked metal wires were large enough to allow the test tube body to pass through, but still small enough so that the lip on the top of the test tube would not fit. Thus, a five by five array of test tubes is placed in the stand, alternating gaps to place the test tubes so as to allow the spray to better flow through the patternator. Each gap is 25.4 mm wide and 25.4 mm long, and the metal wire is 3.18 mm in diameter. The patternator was positioned 40.6 cm below the bottom face of the atomizer. The patternator is shown in Figure 3.8.

The patternator is placed below the atomizer. A plum bob is used to align the center the patternator with the center axis of the atomizer. A level is used to ensure the patternator is perpendicular to the atomizer. A flat sheet is then inserted between the patternator and the atomizer, while the desired flow conditions are set. This deflector serves to prevent any slurry

from entering the patternator before the desired conditions are set. Once the flows are stable, the deflector is quickly removed and a stopwatch is started. The spray is collected until one of the tubes is almost full. Then the deflector is re-inserted, the stopwatch is stopped, and the flows are shut off. Next, the volume of slurry in each tube of the patternator is measured and logged.

### 3.2.2.3 PSV Equipment

Particle shadow velocimetry (PSV) utilizes a diffuse laser light source paired with a high-speed camera. The set-up and image analysis method has been described in detail elsewhere [109]. The object to be imaged (the spray) is positioned in-line between the light source and the camera. The light source is pulsed at a high frequency, allowing for the spray to appear to be stopped in the obtained images. The high frequency pulses (of a known time difference) allow for drop velocity and direction to be obtained relative the camera orientation. Figure 3.9 shows the orientation and set-up of the PSV equipment relative to the injector. For each condition, a minimum of 2,000 images were obtained. The average number of objects (drops) identified in each set of images was 43,803. Estimates of the standard error were calculated for each condition (based on the standard deviation of the data and the number of data points), and the maximum standard error was roughly 1.5 micron.

## 3.3 Entrained Flow Gasifier

The pressurized entrained-flow gasifier EFG is approximately 1.5 m (5 ft) tall and encompasses two sections: the reaction zone and the quench bath. The actual reaction zone inside the EFG is approximately 20 cm (8 in) in diameter. There are five thermocouples positioned in the reaction zone that provide a temperature profile and give an idea of the flame position. A cooling ring serves as a buffer between the reaction zone and the quench section. The reaction zone can approach temperatures around 1500°C (2700°F) at the refractory surface. Figure 3.10 shows the general lay of the entrained flow gasifier. Details of the EFG are given elsewhere [9].

The injector was evaluated during EFG operation over a multiple day period, discussed later in Section 5. For the first day of testing, the 45° nozzle was used in the injector. The EFG system pressure for this run was kept at 4.5 bar absolute pressure or bara (65 psia). Once the EFG had reached a steady-state on the coal slurry, the oxygen pressure drop across the injector was set to 2.1 bar (30 psi). The system was allowed time to move towards equilibrium before the pressure drop was changed again. This was done for pressure drops

of 2.1 bar (30 psi), 1.4 bar (20 psi), and approximately 1.0 bar (15 psi).

The 65° nozzle was used in the injector on the second day of testing. The EFG system pressure was kept at 4.5 bara (65 psia), similar to the first day's run. Once the EFG had reached a steady-state on the coal slurry, the pressure drop was set to 2.1 bar (30 psi). The system was allowed time to move towards equilibrium before the pressure drop was changed again. The pressure drop set points that were evaluated on the first day were repeated on the second day.

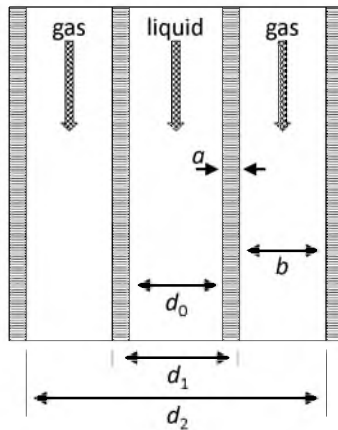


**Figure 3.1.** Atomizer schematic.

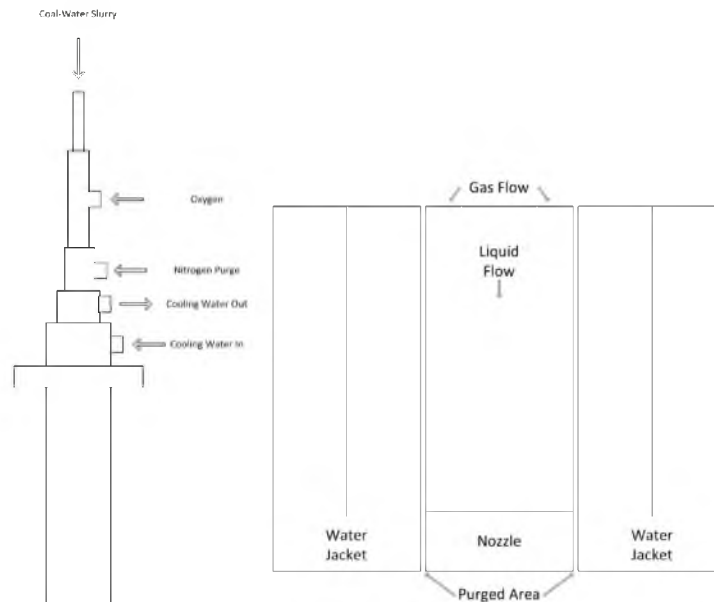


**Figure 3.2.** Above is a rough schematic of the coal-water slurry injector used for EFG testing at the University of Utah. The diagram on the left shows an overall view of the injector, while the diagram on the right shows some detail of inside the injector.

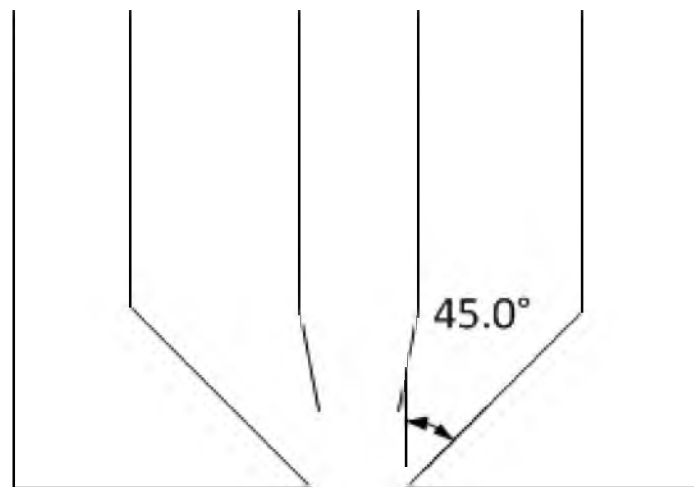


**Figure 3.3.** Schematic of the 45° nozzle that was used for testing. The angle is measured with the vertical as a reference.



**Figure 3.4.** Atomizer design iterations.





**Figure 3.5.** Old atomizer design showing a nonconcentric spray.

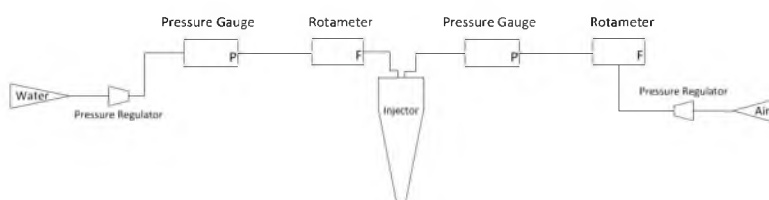


**Figure 3.6.** Above is the set-up of the cold-flow testing that was done on the injector. The injector was suspended on scaffolding so the water spray could be seen.

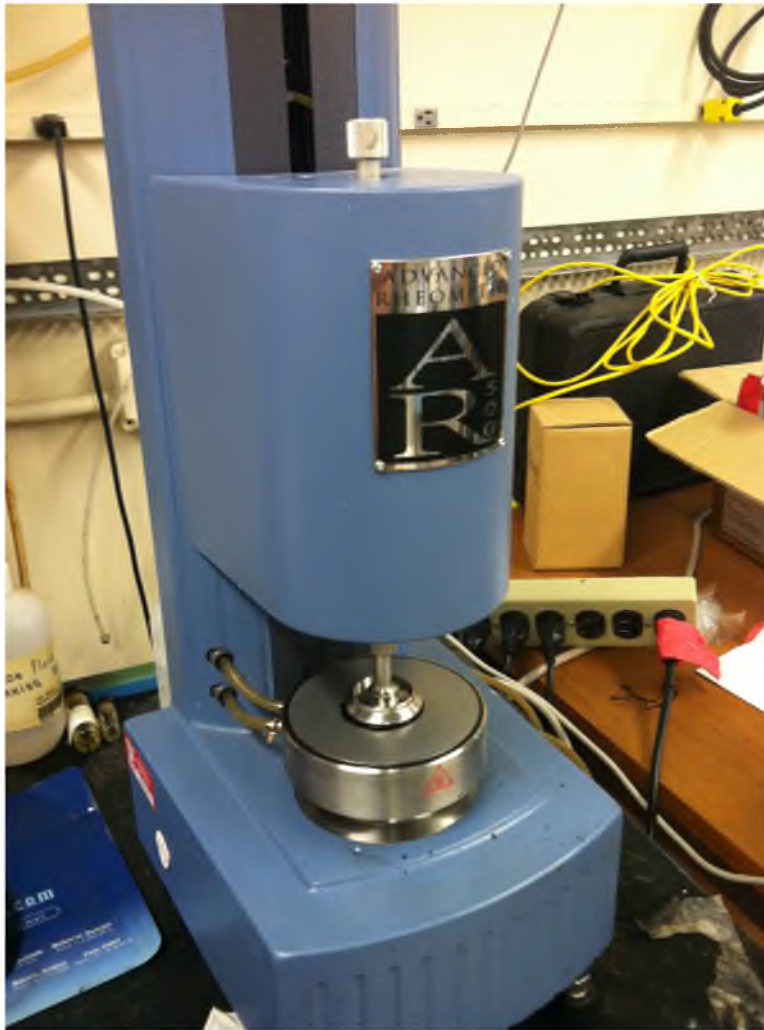
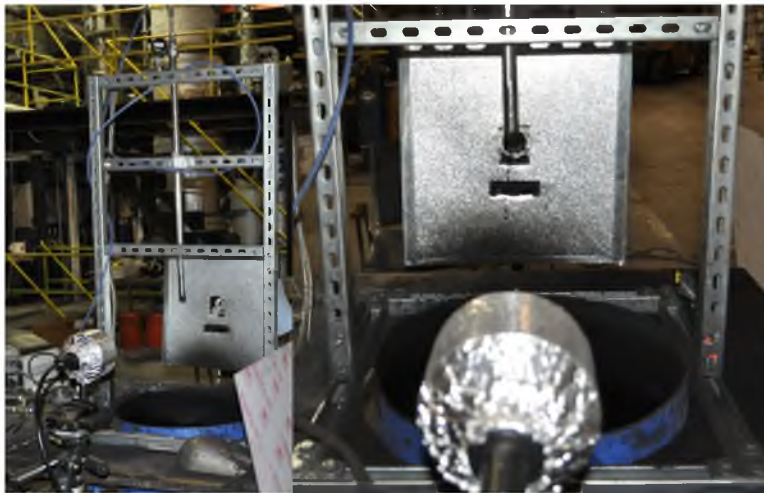


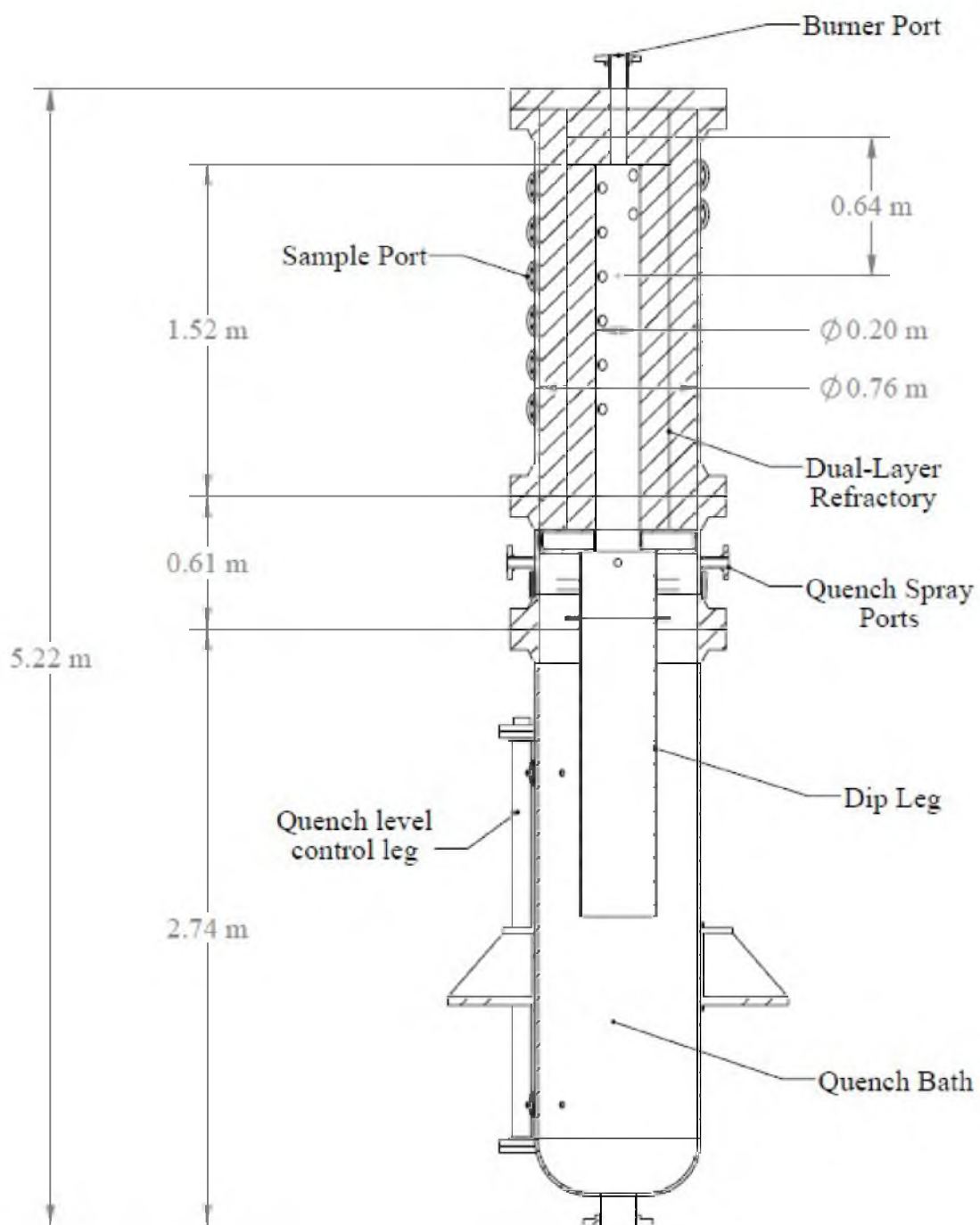
Figure 3.7. The AR-500 viscometer.



Figure 3.8. The patternator.



**Figure 3.9.** PSV equipment and injector alignment.



**Figure 3.10.** Schematic of the University of Utah's entrained flow gasifier © [112].

**Table 3.1.** Atomizer dimensions.

ID	$d_0$ (mm)	$d_1$ (mm)	$d_2$ (mm)	$A_g/A_l$	$d_0/d_0^*$
L1G1*	0.41	1.27	1.63	6.2	1.00
L2G2	0.51	1.27	1.78	6.0	1.25
L4G4	1.52	2.54	4.57	6.2	3.75
L2G1	0.51	1.27	1.63	4.0	na
L3G1	0.71	1.27	1.63	2.0	na
L3G2	0.71	1.27	1.78	3.1	na

**Table 3.2.** Experimental conditions.

Atomizer	$u_l$ (m/s)	$Re_l$	$u_g$ (m/s)	$Re_g$	$We$	$M$
L1G1	0.77-0.90	0.313-365.8	23.2-91.3	549-2,165	6.82-180	0.93-12.3
L2G2	0.74-0.86	0.376-437.7	23.1-87.0	783-2,948	7.82-212	0.89-13.4
L4G4	0.84-0.86	1.295-1,292	19.1-120	2,584-16,189	9.95-1,232	0.62-24.6
L2G1	0.74-0.86	0.376-437.7	30.1-87.3	714-2,068	8.52-202	1.51-13.5
L3G1	0.80-0.86	0.568-607.5	27.8-87.3	659-2,068	16.0-300	1.31-12.9
L3G2	0.80-0.86	0.568-607.5	24.7-86.7	835-2,937	8.81-301	1.03-12.8

**Table 3.3.** Fluid properties.

Fluid	Density ( $kg/m^3$ )	Viscosity ( $Pa * s$ )	Surface Tension ( $N/m$ )
Water	998.0	1.00e-3	0.070
Silicone Oil A	963.6	9.64e-2	0.021
Silicone Oil B	968.6	9.69e-1	0.021
Air	1.2	1.80e-5	na

## CHAPTER 4

### SMALL-SCALE ATOMIZER TESTING

#### 4.1 Morphology

A number of distinct morphological changes occur as the gas and liquid flow rates are changed. The flow conditions considered in this work are laminar liquid flows and a range of gas flows (but typically transition or turbulent gas flow). Using the dimensionless quantities defined for systems of this type ( $M$ ,  $Oh$ ,  $Re$ ,  $We$ , etc.), previous studies have developed maps used to predict the appearance of a given morphological breakup regime.

Faragó and Chigier [94] proposed regimes of atomization for external-mixing, coaxial, two-stream atomizers that are distinguished by the liquid Reynolds number ( $Re_l$ ) and the Weber number ( $We$ ). These regimes were updated by Lasheras and Hopfinger [82] (shown in Figure 4.1) to show the effect of the gas-to-liquid kinetic energy ratio ( $M$ ). Most recently, Zhao et al. [69] redrew the regime map and added a subdivision of the membrane regime, as a function of  $We_m = We/(1 + 1.4A_l/A_g)$  and  $M_m = M/(1 + 50A_l/A_g)$ , which are versions of  $We$  and  $M$  modified by the atomizer exit gas-to-liquid cross-sectional area ratio ( $A_g/A_l$ ).

These regimes are associated with certain breakup morphologies, which, while atomization is a very chaotic process, the specific regimes tend to represent a very similar sequence of breakup process that likely can be tied to similar spray characteristics. Figures 4.2-4.7 show some examples of the breakup morphology observed in this study.

The regimes present in this study, as illustrated in Figures 4.2-4.7, are the nonaxisymmetric Rayleigh regime, the membrane regime, the fiber regime, and the superpulsating regime. Merely changing the liquid viscosity is enough to facility a shift in the morphological regime. For instance, Figure 4.5 shows the superpulsating regime for the breakup of water, in which there are distinct regions of low and high liquid volume fractions among a fairly continuous spray area that has some minimum, non-zero liquid volume fraction. All atomization breakup regimes will have oscillations in the liquid volume fraction [94], but the lower regimes will have regions in the spray that have no liquid present, unlike the superpulsation regime.

By increasing the liquid viscosity (to Silicone Oil A), the superpululating regime shifts to the fiber breakup regime, shown in Figure 4.6. The fiber breakup regime is characterized by fibers rapidly being peeled off the main liquid core, and subsequently breaking into drops [94]. Due to the increased viscosity and reduced surface tension of Silicone Oil A, the fibers do not form drops as quickly as they would for fibrous breakup of water.

By increasing the liquid viscosity even further (to Silicone Oil B), the breakup regime shifts to membrane breakup, characterized by the formation of a membrane, shown here as the bursting of a bubble. These breakup regimes provide a broad stroke characterization of the atomization behavior that can be expected for given conditions. Similar behavior is seen for atomizer L2G1 in Figures 4.2-4.4, but the transitions are not as distinct for the smaller atomizer geometry.

## 4.2 Intact Liquid Jet Characteristics

The intact liquid jet (ILJ) is commonly referred to as the most important parameter characterizing near-field atomization [42–44]. It also houses, so to speak, all of the instability dynamics that have been predicted to cause the eventual ILJ breakup and ligament or drop formation. As such, it is quantified here.

### 4.2.1 Average ILJ Length

The ILJ length was measured for water and most Silicone Oil A cases. For Silicone Oil B, the viscosity was increased to a point that the end of the ILJ stretched past the frame of the image. As such, no ILJ lengths are reported for Silicone Oil B. Figure 4.8 shows the ILJ lengths for water and Silicone Oil A as a function of the gas-to-liquid kinetic energy ratio,  $M$ .  $M$  has been shown in the literature to likely be the factor that has the most control over the ILJ length [39, 42–44, 67–69, 73]. Figure 4.9 shows the effect of changing atomizer scale on the ILJ length. Figure 4.10 shows the effect of changing  $b$  on the ILJ length. Figure 4.11 shows the effect of changing  $d_0$  on the ILJ length.

The effect of changing the liquid from water to Silicone Oil A is not immediately evident from looking at Figure 4.8. For some cases, there appears to be an increase in ILJ length when changing to Silicone Oil A, but for other cases, there seems to be a slight decrease or no change at all. This will be discussed more further on.

The ILJ length seems to decrease with increasing  $M$  for all cases. For the smaller atomizers (which encompass a larger number of data points), the ILJ length appears to head towards an asymptote that is likely a function of the atomizer geometry. There do appear to be some clear trends in the ILJ length with changing atomizer geometry. Figure

4.9 shows that increasing the atomizer scale results in an increase in the ILJ length for either water or Silicone Oil A. But can this effect be isolated to a specific property of the atomizer geometry? Figure 4.10 shows what may be a modest increase in the ILJ length with an increase in  $b$ , but this increase is only seen for Silicone Oil A and not water. Figure 4.11 shows that an increase in  $d_0$  correlates with an increase in the ILJ length for both water and Silicone Oil A. While changing  $b$  may have a slight effect on the ILJ length for Silicone Oil A, the dominant geometric parameter appears to be  $d_0$ .

As Figure 4.11 showed that the ILJ length is very dependent on  $d_0$ , it would be wise to normalize the ILJ lengths by  $d_0$ . This is commonly done in the literature, and Equation 4.1 and Equation 4.2 represent the correlations for the ILJ length as proposed by Lasheras et al. [39] and Zhao et al. [73], respectively. Figure 4.12 shows the ILJ lengths normalized by  $d_0$  as a function of  $M$ .

$$\frac{L}{d_0} \approx \frac{6}{\sqrt{M}} \quad (4.1)$$

$$\frac{L}{d_0} = M^{-1/4} We^{-1/4} \left( \frac{-4.84 \times 10^{-10}}{3} We^{1/2} - \frac{-2.51 \times 10^{-11}}{3} Oh \sqrt{\frac{\rho_l}{\rho_g}} \right)^{-1/4} \quad (4.2)$$

The relative simple relation of Lasheras et al. [39], shown in Equation 4.1, predicts values much smaller than those measured here, and the more complex relation of Zhao et al. [73], shown in a slightly modified form in Equation 4.2, predicts values much larger than those measured here. The study by Zhao et al. [73] evaluated coal-water slurries, so their lengths were certainly larger; however, their correlation still corrects for fluid properties. The study by Lasheras et al. [39] evaluated the atomization of water with air, like the present study. The atomizer dimensions between the three studies were certainly different, with both Lasheras et al. [39] and Zhao et al. [73] using larger atomizer than used here. Atomizer L4G4 approaches the size of the atomizer used by Lasheras et al. [39], but the atomizers used by Zhao et al. [73] are roughly three times larger than atomizer L4G4. The atomizer used by Lasheras et al. [39] was of a similar geometry to the atomizer used here, with the exception of a slight expansion to the inner diameter of the liquid tube at the atomizer exit. This change in geometry could account for the difference in observed measurements.

It is interesting to note that Equation 4.2 predicts that Silicone Oil A will have a smaller  $d_0$ -normalized ILJ length than water for almost all cases shown in Figure 4.12. The experimental results indicate this to be the case for some of the experimental results reported

here, but not for all cases. Looking at Figure 4.8, most cases show the Silicone Oil A cases have shorter ILJ lengths than water, with the exception of L4G4.

The results shown in Figure 4.12 indicate that the liquid jet diameter ( $d_0$ ) is a good candidate for normalizing the ILJ length. However, while this study sought to evaluate modernly-hypothesized scaling factors, the range of atomizer scales only spans a factor of four, which may not tease out the limits of where the existing scaling factors break down. The clear displacement of atomizer L4G4 from the rest of the herd in Figure 4.12, or the notable difference between the literature predictions (Equation 4.1, Equation 4.2) and the experimental data in Figure 4.12 may indicate the need for a different scaling system length. However, the relationships proposed in Equation 4.1 and Equation 4.2 certainly capture the trend of the changing  $d_0$ -normalized ILJ length with  $M$ . When trying to scale an atomizer for larger system, this relationship can be used to predict what the new ILJ length will be. The data shown in Figure 4.12 indicate more than using a combination of the relations proposed in Equation 4.1 and Equation 4.2 will offer the proper parameter bounds at a minimum.

#### 4.2.2 ILJ Length Oscillations

The ILJ is not a static feature of near-field atomization; it is constantly evolving. One manner in which it is evolving is lengthwise. As drops are sheared or pinched off the end of the ILJ, the length oscillates. These oscillations will dictate, to some degree, the rate at which drops are issued into the system. As such, the ILJ length oscillations are quantified here.

In order to quantify the ILJ length oscillations for a given condition, the ILJ length was measured in each image captured via a high-speed camera. Oftentimes there were 10,000 images captured for a given condition. This provides a 10,000 point time-series of ILJ length measurements, which are then processed using a Fourier transform to obtain the oscillation amplitude as a function of oscillation frequency. To define a characteristic or dominant frequency, that frequency with the largest amplitude component was chosen. As such, the dominant frequency is often referred to as amplitude-defined. The amplitudes reported are then, obviously, that maximum amplitude.

Figure 4.13 shows the ILJ length oscillation frequency as a function of  $M$ . Figure 4.14 shows the effect of changing atomizer scale on the ILJ length oscillation frequency.

In general, the ILJ length oscillation frequency increases with increasing  $M$  (Figure 4.13). A few geometric trends are identified as well. Primarily, looking at the change in frequency between atomizers L1G1, L2G2, and L4G4 in Figure 4.14, it is seen that increasing the

atomizer scale reduces the sensitivity of ILJ length oscillation frequency on  $M$ , meaning as the atomizer scale is increased for a constant gas-to-liquid kinetic energy ratio, the rate at which the ILJ length oscillates decreases. This change is not so apparent between atomizer L1G1 and L2G2, but is clearly seen when looking at the difference between L1G1 and L4G4 or L2G2 and L4G4. Changes in the ILJ length oscillation frequency were evaluated with changes in  $b$  and  $d_0$  as well, but no significant trends were seen across all fluids. For Silicone Oil A, increasing  $d_0$  correlated with an increase in the ILJ length oscillation frequency. This is shown in Figure 4.15.

Figure 4.16 shows the ILJ length oscillation amplitude as a function of  $M$ . Figure 4.17 shows the  $d_0$ -normalized ILJ length oscillation amplitude as a function of  $M$ .

No clear trends are identified with changing geometry for the ILJ length oscillation amplitude. However, as shown in Figure 4.17, normalizing the ILJ length oscillation amplitude by  $d_0$  seems to collapse all of the data onto a single line, meaning that the bounds between which the ILJ length can be expected to oscillate can be estimated using just the liquid jet diameter and the gas-to-liquid kinetic energy ratio. In fact, for low- $M$ , it appears that the ILJ the  $d_0$ -normalized length oscillation amplitude approaches a value of one, meaning that the oscillation amplitude is roughly equal to the liquid jet diameter,  $d_0$ . This low- $M$  behavior likely represents the transition back into the Rayleigh-type breakup, where surface tension plays a destabilizing role. Akin to the dripping regime for pressure atomization (Figure 1.3), the typical drop diameter is roughly  $2d_0$ , meaning that as a drop separates from the ILJ, the  $d_0$ -normalized ILJ length oscillation amplitude should have an amplitude of roughly half a drop diameter, or  $2d_0/d_0 = 1$ .

As  $M$  is increased, the ILJ length oscillation amplitude decreases exponentially to a point, where an asymptote seems to exist. As there is no clear trend with geometry for the ILJ length oscillation amplitude, yet some geometric trends seem to exist for the ILJ length oscillation frequency, the overall ILJ length oscillation can be predicted. For a constant  $M$ , as the atomizer scale is increased, it can be expected that the average ILJ length will increase and will change at a slower rate, but the actual change will be larger than for smaller atomizers. Using the data in Figure 4.17, the maximum ILJ length can be approximated. If it is desired that primary atomization be largely complete by a certain distance into a system, these data can help design an atomizer.

### 4.2.3 Pendular Behavior

While the ILJ is oscillating lengthwise, it is also moving from side to side like a pendulum. In reality, the ILJ is not moving on a two-dimensional plane, but is moving in three

dimensions, pivoting on the base of the atomizer. Here, we assume that the nature of this pendular behavior can be understood by analyzing the motion along the two-dimensional plane that is imaged.

The pendular motions are not constant with time, and just like the ILJ length, the ILJ angle can be analyzed as a time series using a Fourier transform to get at the frequencies and their associated amplitudes. As was done for the ILJ length oscillations, the characteristic or dominant frequency of the ILJ angle oscillation is assumed to be that frequency that has the largest amplitude associated with it. This “dominant” frequency and the associated amplitude are quantified here. Figure 4.18 shows the ILJ angle oscillation frequency. Figure 4.19 shows the effect of changing  $d_0$  on the ILJ length for Silicone Oil A atomization.

The ILJ angle oscillation frequency shows very little variation for changes in geometry or the liquid being atomized, as seen in Figure 4.18. The data already seem to collapse on a single trend line. While the data shown in Figure 4.18 for atomizer L4G4-water, L2G1-water, and L3G1-water show some deviation from the main line, when averaged with their duplicates (also shown in Figure 4.18), the data fall along the trend line. Unfortunately, the tests with Silicone Oil A were not repeated to show whether or not the L4G4-Silicone Oil A point in Figure 4.18 falls along the same trend followed by the other data. However, all other tests with Silicone Oil A follow the trend, so while the L4G4-Silicone Oil A point is not removed, it is considered suspect. Figure 4.19 shows that an increase in  $d_0$  correlates with an increase in the ILJ angle oscillation frequency for Silicone Oil A. The effect of changing atomizer scale and  $b$  were evaluated, but no clear trends were seen. Additionally, no trend was seen with changing  $d_0$  for water.

Figure 4.20 shows the ILJ angle oscillation amplitude for water and Silicone Oil A as a function of the gas-to-liquid kinetic energy ratio,  $M$ . Figure 4.21 shows the effect of changing  $b$  on the ILJ angle oscillation amplitude for Silicone Oil A. Figure 4.22 shows the effect of changing  $d_0$  on the ILJ angle oscillation amplitude. No clear trend of ILJ angle oscillation amplitude is seen with changing the atomizer scale for water or Silicone Oil A, or with changing  $b$  for water, so these comparisons are not explicitly broken out into a figure here.

Much like the ILJ angle oscillation frequency, the ILJ angle oscillation amplitude largely follows a single trend line, as shown in Figure 4.20, but the fit is not as concise. The ILJ angle oscillation amplitude decreases as  $M$  is increased for all cases. Figure 4.21 shows that increasing  $b$  correlates with a decrease in the ILJ angle oscillation amplitude for Silicone Oil A. Figure 4.22 shows that increasing  $d_0$  correlates with an increase in the ILJ angle oscillation amplitude.

Why are these trends of ILJ angle oscillation important? To some degree, the ILJ angle oscillation will dictate the range of trajectories that can be taken by ligaments and drops as they are shed from the ILJ. This means that as the ILJ angle oscillation amplitude is changed, it will have a direct effect on the resulting spatial distribution of liquid within the spray. A means to better understand how to attain a particular liquid distribution within a spray is very crucial for designing atomizers for many industrial systems, particularly combustion or gasification systems. The results of Figures 4.18-4.19 and Figures 4.20-4.22 show trends that can help design atomizers for a controlled probably range of drop trajectories. For instance, it can be said that as  $d_0$  is increased for constant  $M$  and for a low viscosity fluid (such as water), the ILJ can be expected to swing to a wider angle but at a relatively constant frequency. For a higher viscosity fluid (such as Silicone Oil A), as  $d_0$  is increased for constant  $M$ , the ILJ can be expected to swing to a wider angle with a higher frequency. For a higher viscosity fluid (such as Silicone Oil A), as  $b$  is increased, the ILJ can be expected to swing to a shallower angle with a relatively constant frequency. The assumption here is that the ILJ angle is representative of or correlated to the eventual spray angle formed by the atomizer.

Another way the pendular behavior of the ILJ can be analyzed is by the dimensionless Strouhal number, defined in Equation 2.5, as has been done in the literature [72, 73]. Figure 4.23 shows the Strouhal number as a function of  $M$ .

$St$  is shown to increase with increasing  $M$ . A scaling effect is seen, in that increasing the atomizer scale increases  $St$ . This is clearly seen by comparing atomizer L4G4 to the other L1G1/L2G2 atomizers in Figure 4.23. Increasing the liquid jet diameter is shown to increase  $St$ , and no clear trend is seen by changing the gas annular thickness. The results of the present study are very similar to those reported in the literature. Other studies have been performed that report  $St$  as a function of  $M$  (such as the study by Carvalho et al. [75]), but all studies found, with the exception of Zhao et al. [72], evaluate a liquid sheet as opposed to a liquid jet. The correlations shown in Figure 4.23 from Carvalho et al. [75] and Zhao et al. [72] are those referred to in Equation 2.5. The data appear to trend the same with  $M$  as predicted by the literature, but the model fit produces slightly different coefficients. Fitting Equation 2.5 to the water data yields coefficients of 0.08 and 0.90 for  $c_a$  and  $c_b$ , respectively. Fitting Equation 2.5 to the Silicone Oil A data yields coefficients of 0.11 and 0.65 for  $c_a$  and  $c_b$ , respectively. These coefficients are very similar to those reported by Zhao et al. [72]: 0.17 and 0.5 for  $c_a$  and  $c_b$ , respectively. In fact, Zhao et al. [72] evaluated the pendular behavior of high-viscosity coal-water slurries, so it makes sense the the coefficients for the higher-viscosity Silicone Oil A would be closer to those reported by Zhao et al. [72] than the

coefficients for water.

While the coefficients obtained fitting Equation 2.5 to the experimental data are approximately the same as those from the literature, they do not capture the effect of geometry shown in the previous section.  $M$  takes the liquid density into account, but the liquid viscosity and surface tension are not included. This is not to say that they will significantly impact the oscillation of the ILJ, but Figure 4.20 shows that for a constant atomizer geometry and  $M$ , changing the liquid from water to Silicone Oil A will increase the ILJ angle oscillation amplitude. These studies do not independently evaluate a change in viscosity or surface tension, as Silicone Oil A has a higher viscosity than water, but also a much lower surface tension. However, a change in behavior is noted, even in the coefficients obtained fitting Equation 2.5 to the different data sets.

#### 4.2.4 Surface Oscillation

Deformations to the ILJ surface are hypothesized to precede breakup [39,41]. One way these deformations are quantified is by the oscillation of the ILJ surface. As was the case for the ILJ length and angle oscillations, here, the ILJ perimeter is indexed and tracked throughout the entire image sequence for a given experimental condition. This provides a time series for the ILJ perimeter, which can be subdivided into time series for the left and right side of the ILJ perimeter for each pixel-row. By processing the time series containing the perimeter location for a specific pixel row and ILJ side (left or right as the images contain a two-dimensional slice of the ILJ) with a Fourier transform, the frequencies and corresponding amplitudes of that pixel's perimeter location are obtained. In reporting these data, that frequency that has the largest associated amplitude is considered to be the characteristic or dominant frequency. In the case of ILJ surface oscillations, the choice of an amplitude-defined dominant frequency seems appropriate as the growth of that amplitude is what destabilizes the ILJ and leads to breakup.

A few studies have reported that the oscillation frequency along the length of the ILJ is constant [41, 71]. This has been shown here to be largely true, but not entirely. For some cases, there is a clear change in the surface oscillation frequency as distance past the atomizer is increased. This change typically occurs near the atomizer exit, and is attributed to the reattachment of the gas and liquid flows. Figure 4.24 shows the ILJ surface oscillation frequencies for all fluids as a function of the distance past the atomizer for atomizer L3G2. Figure 4.25 shows the ILJ surface oscillation amplitudes for all fluids as a function of distance past the atomizer for atomizer L3G2.

As shown in Figure 4.24, the ILJ surface oscillation frequency is roughly constant along

the length of the ILJ. There are a number of cases seen that the frequency very close to the atomizer is some arbitrary value, and as distance past the atomizer is increased, the frequency quickly rises to a much larger value. This is assumed to be the point at which the gas and liquid flows reattach, as noted in the literature [71]. Not all cases show a change in the assumed flow reattachment point. For instance, column one in Figure 4.24 shows no real change in the reattachment point as the gas velocity (or  $M$ ) is increased. A slight change is seen between the left and right sides of the ILJ for the largest  $M$  (row four), but this is assumed to be due to deviations from concentricity in the atomizer geometry. Column two (also air-water tests) in Figure 4.24 show that an increase in the gas velocity (or  $M$ ) correlates with a change in the assumed reattachment point to a point closer to the atomizer. This behavior is not as evident for the silicone oils (column three and four). This could be due to the increased viscosity, due to insufficient resolution near the atomizer tip, or some combination of these two factors.

Figure 4.25 generally shows a gradual increase in the oscillation amplitude with increasing distance past the atomizer. There are a few cases that show both increasing and decreasing amplitudes (subfigure c, g, and h), and this behavior cannot be fully explained. Initially, it was thought that the decrease in amplitude before the subsequent increase could represent the flow reattachment point. There likely exists a region before the reattachment point where surface oscillations typical of capillary breakup could be observed, as there is not a substantial shear supplied by the gas stream. The decrease in amplitude could be driven by the reattaching flows, and then the instabilities would be amplified by the gas shear. However, there does not appear to be a corresponding change in the oscillation frequency near this point, and it is thought that a regime shift such as that from capillary breakup to shear-driven breakup would result in a change in the surface oscillation frequency.

No other studies could be found that report either the ILJ surface oscillation frequency or amplitude as a function of distance past the atomizer, so there is no sufficient comparison to be made to in the literature. As the frequencies along the length of the ILJ surface are relatively constant, at least near the breakup region, they can be averaged and presented as a function of the system properties. These ILJ surface oscillation frequencies can be compared to the literature, which is useful in gauging the relevance of this work. Figure 4.26 shows the ILJ surface oscillation frequency as a function of  $Re_{g,hd}$ . Figure 4.27 shows the effect of changing atomizer scale on the ILJ surface oscillation frequency. Figure 4.28 shows the effect of changing  $b$  on the ILJ surface oscillation frequency. The effect of changing  $d_0$  was evaluated and the experimental data obtained showed a negligible effect, so that specific

trend is not broken out into a figure here.

Increasing  $Re_{g,hd}$  correlates with an increase in the ILJ surface oscillation frequency for all liquids evaluated. The data in Figure 4.26 follow seemingly two trend lines: one for atomizer L4G4 and one for the other atomizers. In Figure 4.27, it appears that for water, the ILJ surface oscillation frequency follows a single trend line. For Silicone Oil A, a similar trend exists, but a scaling effect can be seen, where increasing the atomizer scale correlates to a decrease in the ILJ surface oscillation frequency. For Silicone Oil B, increasing the atomizer scale correlates with an decrease in the ILJ surface oscillation frequency as well, and for Silicone Oil B, the decrease with increasing scale is larger than the decrease with increasing scale for Silicone Oil A. For the silicone oils, no repeat tests were performed. Additionally, as the reported frequencies are the result of processing the entire time series of images with a Fourier transform, standard deviation or error bars are not produced.

Figure 4.28 shows that an increase in  $b$  correlates with a decrease in the ILJ surface oscillation frequency for constant  $Re_{g,hd}$  for all liquids. This trend is very clear for both silicone oils. For water, the L2-atomizers do not show a trend of ILJ surface oscillation frequency with  $b$ , but the L3-atomizers show a decrease in ILJ surface oscillation frequency with increasing  $b$ . As the ILJ surface oscillation frequency is commonly tied to the rate at which drops are shed from the ILJ, this trend is very useful in designing an atomizer to control spray formation. For a constant  $Re_{g,hd}$ , increasing the gas annulus,  $b$ , will result in a decrease in the ILJ surface oscillation frequency. Intuitively, as the the liquid flow is constant, this should result in a larger average drop diameter. This provides a mechanism for why this change in atomizer geometry can likely be tied to a change in the representative drop diameter.

The ILJ surface oscillation frequencies can be roughly compared to studies in the literature. Studies by Marmottant and Villermaux [41] and Tian et al. [71] proposed relationships for the ILJ surface oscillation frequency  $f$ . These relationships are shown in Equation 4.3 and Equation 4.4, respectively.

$$f \propto \frac{u_c}{\delta_0} \left( \frac{\rho_g}{\rho_l} \right)^{1/2} \quad (4.3)$$

$$f \propto \frac{u_c}{\delta_r} \left( \frac{\rho_g}{\rho_l} \right)^{1/2} \quad (4.4)$$

The difference between Equation 4.3 and Equation 4.4 lies in the choice of the gas boundary layer thickness used. Marmottant and Villermaux [41] used the gas boundary

layer thickness at the atomizer's exit ( $\delta_0 = 5.6bRe_g^{-1/2}$ ) to define the ILJ surface oscillation frequency, while Tian et al. [71] used the gas boundary layer thickness at the estimated point of flow reattachment past the atomizer ( $\delta_r = \delta_0 + 0.071a$ ). The predictions of Equation 4.3 and Equation 4.4 are shown in Figure 4.29 compared to the measured ILJ surface oscillation frequencies.

Both Equation 4.3 and Equation 4.4 can be seen in Figure 4.29 to capture the trend of the ILJ surface oscillation frequency, but Equation 4.4 does a better job of collapsing the data. The studies by Marmottant and Villermaux [41] and Tian et al. [71] do not report their respective coefficients to fit the proportional relationships defined in Equation 4.3 and Equation 4.4. Here, the best fit using Equation 4.4 to the experimental data is given in Equation 4.5.

$$f \approx 0.25 \frac{u_c}{\delta_r} \left( \frac{\rho_g}{\rho_l} \right)^{1/2} \quad (4.5)$$

#### 4.2.5 Wavelengths

Figure 4.30 shows the primary wavelength as a function of  $Re_{g,hd}$ . Figure 4.31 shows the effect of changing atomizer scale on the primary wavelength. Figure 4.32 shows the effect of changing  $b$  on the primary wavelength. Little affect was seen by changing  $d_0$ , so it is not included here.

Figure 4.30 shows that an increase in  $Re_{g,hd}$  correlates with a decrease in the primary wavelength. As the atomizer scale is increased for water in Figure 4.31, there does not appear to be any change in the primary wavelength. All atomizer scales appear to collapse along one trend line for water. For Silicone Oil A, Figure 4.31 shows an increase in the primary wavelength with increasing atomizer scale. For Silicone Oil B, Figure 4.31 also shows an increase in the primary wavelength with increasing atomizer scale, and the increase appears larger than that for Silicone Oil A. The primary wavelength is commonly directly correlated with a spray representative drop diameter. This suggests that changing the atomizer scale for a low viscosity fluid such as water may have little effect on the  $Re_{g,hd}$ -tunability of the drop diameter, and an equivalent scale change for a higher viscosity fluid may limit the effect of changing  $Re_{g,hd}$ .

Figure 4.32 shows that increasing  $b$  has little effect for water, correlates with a slight wavelength increase for Silicone Oil A, and correlates with a slightly larger wavelength increase for Silicone Oil B. This again suggests that changing an atomizer geometry has a much greater impact for a high-viscosity fluid than for a low-viscosity fluid.

The primary wavelength has been measured in a few existing studies, and a correlation proposed by Varga et al. [40] is shown in Equation 4.6. The comparison between the predicted primary wavelengths of Equation 4.6 and the measured primary wavelengths can be seen in Figure 4.33.

$$\lambda \approx 0.055 \left( \frac{\rho_l}{\rho_g} \right)^{1/2} \left( \frac{\mu_l}{\rho_g u_g} \right)^{1/2} \quad (4.6)$$

The measured primary wavelengths fit the prediction of Varga et al. [40] moderately well. They seem to predict the Silicone Oil A wavelengths very well, predict too large wavelengths for water, and too small wavelengths for Silicone Oil B. This indicates an opportunity for improving the relation between these fluid properties, atomizer geometries, and the produced wavelengths.

## 4.3 Spray-Representative Drop Diameters

### 4.3.1 Buckingham-II Theorem Application

There are a large number of dimensionless quantities that are used in the existing literature to explain atomization phenomena. There are far too many to keep track of both practically and intuitively. In an attempt to reduce the dimensionless quantities to those that are most appropriate, Buckingham-II theorem is used [54].

Here, this process is repeated for three quantities deemed to be representative of the atomization process: the geometric mean drop diameter ( $\mu_{GM}$ ), the geometric standard deviation of the drop diameter ( $\sigma_{GM}$ ), and the SMD (in order to compare to existing literature), although only the case for  $\mu_{dd}$  is worked out. The following parameters are those considered to affect the previously listed drop diameter characteristics: liquid jet diameter ( $d_0$ ), the central tube thickness ( $a$ ), annular gas jet thickness ( $b$ ), the liquid velocity ( $u_l$ ), the gas velocity ( $u_g$ ), surface tension ( $\sigma$ ), liquid density ( $\rho_l$ ), gas density ( $\rho_g$ ), liquid viscosity ( $\mu_l$ ), and gas viscosity ( $\mu_g$ ). This provides a functional relationship between the geometric mean drop diameter (for example) of the form shown in Equation 4.7.

$$\mu_{dd} = f(d_0, b, a, u_g, u_l, \sigma, \rho_l, \rho_g, \mu_l, \mu_g) \quad (4.7)$$

So, there are eleven physical variables involved ( $m = 11$ ) and those eleven physical variables have three dimensional units ( $n = 3$ ), leaving eight II-groups ( $p = n - k$ ). This leaves Equation 4.7 in the form shown in Equation 4.8, where the II-groups are given in Equation 4.9.

$$f(\Pi_1, \Pi_2, \Pi_3, \Pi_4, \Pi_5, \Pi_6, \Pi_7, \Pi_8) = 0 \quad (4.8)$$

$$\Pi_1 = d_0^{a_1} u_g^{b_1} \sigma^{c_1} \mu_{dd} \quad (4.9a)$$

$$\Pi_2 = d_0^{a_2} u_g^{b_2} \sigma^{c_2} b \quad (4.9b)$$

$$\Pi_3 = d_0^{a_3} u_g^{b_3} \sigma^{c_3} a \quad (4.9c)$$

$$\Pi_4 = d_0^{a_4} u_g^{b_4} \sigma^{c_4} u_l \quad (4.9d)$$

$$\Pi_5 = d_0^{a_5} u_g^{b_5} \sigma^{c_5} \rho_l \quad (4.9e)$$

$$\Pi_6 = d_0^{a_6} u_g^{b_6} \sigma^{c_6} \rho_g \quad (4.9f)$$

$$\Pi_7 = d_0^{a_7} u_g^{b_7} \sigma^{c_7} \mu_l \quad (4.9g)$$

$$\Pi_8 = d_0^{a_8} u_g^{b_8} \sigma^{c_8} \mu_g \quad (4.9h)$$

The condition that the  $\Pi$ -groups are dimensionless allows for the determination of the coefficients on the right-hand sides of Equation 4.9. By substituting in the appropriate dimensional units and solving for the coefficients, the  $\Pi$ -groups are obtained. They are shown in Equation 4.10.

$$\Pi_1 = \frac{\mu_{dd}}{d_0} \quad (4.10a)$$

$$\Pi_2 = \frac{b}{d_0} \quad (4.10b)$$

$$\Pi_3 = \frac{a}{d_0} \quad (4.10c)$$

$$\Pi_4 = \frac{u_l}{u_g} \quad (4.10d)$$

$$\Pi_5 = \frac{d_0 u_g^2 \rho_l}{\sigma} \quad (4.10e)$$

$$\Pi_6 = \frac{d_0 u_g^2 \rho_g}{\sigma} \quad (4.10f)$$

$$\Pi_7 = \frac{u_g \mu_l}{\sigma} \quad (4.10g)$$

$$\Pi_8 = \frac{u_g \mu_g}{\sigma} \quad (4.10h)$$

The  $\Pi$ -groups can be shuffled around and redefined as functions of each other. So  $\Pi_1' = \Pi_1/\Pi_2 = \mu_{dd}/b$ ,  $\Pi_3' = \Pi_3/\Pi_2 = a/b$ ,  $\Pi_5' = \Pi_5/\Pi_6 = \rho_l/\rho_g$ ,  $\Pi_7' = \Pi_5/\Pi_7^2 = d_0 \sigma \rho_l / \mu_l^2$ , and

$\Pi_8' = \Pi_7/\Pi_8 = \mu_l/\mu_g$ . Substituting these into Equation 4.8 leads to the relation shown in Equation 4.11, which is equivalent to Equation 4.12.

$$\frac{\mu_{dd}}{b} = f\left(\frac{b}{d_0}, \frac{a}{b}, \frac{u_l}{u_g}, \frac{\rho_l}{\rho_g}, \frac{d_0 u_g^2 \rho_l}{\sigma}, \frac{d_0 \sigma \rho_l}{\mu_l^2}, \frac{\mu_l}{\mu_g}\right) \quad (4.11)$$

$$\frac{\mu_{dd}}{b} = f(A, D, E, B, We, Lp, C) \quad (4.12)$$

In Equation 4.12,  $A = b/d_0$ ,  $D = a/b$ ,  $E = u_l/u_g$ ,  $B = \rho_l/\rho_g$ ,  $We = d_0 u_g^2 \rho_g/\sigma$ ,  $Lp = Oh^2 = d_0 \sigma \rho_l/\mu_l^2$ , and  $C = \mu_l/\mu_g$ . Also, as the main property being changed for a given atomizer and liquid selection is the gas flow, the gaseous Reynolds number ( $Re_g = \rho_g d_0 u_r/\mu_g$ ) is used to evaluate performance.  $Re_g$  is directly used to assess the turbulent length scales that interact with the formed drops that are being measured, and will dictate the degree to which secondary atomization may occur.  $Re_g$  can be described as a function of the determined  $\Pi$ -groups ( $Re_g = \sqrt{WeLpC/B}$ ). Additionally, the gas-to-liquid kinetic energy ratio ( $M = \rho_g u_g^2/\rho_l u_l^2$ ) is evaluated for relevance in the system. It can also be described as a function of the determined  $\Pi$ -groups ( $M = 1/BE^2$ ). These quantities are considered to be the appropriate quantities with which the atomization systems are analyzed in the subsequent section. Also, an identical method is used for preparing correlations for  $\mu_{GM}$ ,  $\sigma_{GM}$ , and the SMD.

### 4.3.2 Geometric Mean Drop Diameter

Drop diameter distributions can often be described as log-normal. In order to verify that this is an appropriate choice of distribution with which to describe these results, some of the conditions explored are evaluated on a probability plot, compared against a standard log-normal distribution probability. Figures 4.34-4.37 show the distribution of drop diameters for atomizer L1G1 and L4G4, for  $Re_g = 1,637$  and  $12,022$ , respectively.

As shown in Figures 4.34-4.37, the distribution of drop diameters is log-normal, meaning when the logarithm of the drop diameter values are computed and plotted, the resulting distribution appears normal. The falling tails on the left side of Figures 4.34-4.37 represent the smallest measured drop diameter for each condition. Of the conditions shown in Figures 4.34-4.37, the distribution that appears least log-normal, still fits the log-normal distribution for approximately 95% of its data. As such, all conditions explored will be assumed to have a log-normal drop diameter distribution.

As the measured drop size distributions appear to be log-normal, they can be quantified using log-normal distributions statistics, which are comprised of location and scale parameters,

better known as the geometric mean ( $\mu_{dd}$ ) and standard deviation ( $\sigma_{dd}$ ), respectively. These parameters offer detail into the average drop values as well as the spread of the distributions, as the geometric standard deviation ( $\sigma_{dd}$ ) roughly represents the ratio of the diameter cumulatively comprising 15% of the drops versus the diameter cumulatively comprising 50% of the drops. This means that as  $\sigma_{dd}$  approaches a value of one, all drop diameters have the same diameter.

Figures 4.38-4.41 show the geometric average drop diameters as a function of the Reynolds number, defined using the gas hydraulic diameter as the length scale.

Some distinct geometric trends can be identified by examining Figures 4.38-4.41. In Figure 4.39, it is clear that increasing the atomizer scale results in an increase in the resulting drop diameter. For Silicone Oil A, this trend is not as apparent, as the data for L1G1 and L2G2 are nearly identical, and while the data for L4G4 appears to indicate a larger drop diameter than the data for L1G1 and L2G2, there is not enough overlap between the explored  $Re_{g,hd}$ -values to indicate this trend with confidence. For water, there appears to be a clear increase in the measured drop diameter with every increase in atomizer scale from L1G1 to L2G2 to L4G4.

Is the trend of increasing drop diameters with increasing atomizer scale related to increases in both  $d_0$  and  $b$ , or can it be isolated to one specific geometric property? In Figure 4.40, the gas annular gap,  $b$ , appears to have an effect. Looking at the change from L2G1 to L2G1 for the water spray, a decrease in drop diameter correlates with a decrease in  $b$ . Additionally, looking at the change from L3G1 to L3G2 for either the water or Silicone Oil A spray, a decrease in drop diameter correlates with a decrease in  $b$ .

In Figure 4.41, the liquid jet diameter,  $d_0$ , appears to have an effect as well, although it is only apparent for Silicone Oil A at  $Re_{g,hd} < 1,500$ . This trend can be seen by looking at the difference between L1G1, L2G1, and L3G1. For Silicone Oil A and  $Re_{g,hd} < 1,500$ , increasing  $d_0$  correlates with an increase in the drop diameter. However, there is no clear trend seen between the drop diameter and  $d_0$  for  $Re_{g,hd} > 1,500$  or for the water data at any value of  $Re_{g,hd}$ . Similar behavior is seen looking at atomizer L2G2 and atomizer L3G2. When  $Re_{g,hd} < 1,500$ , approximately, increasing the liquid jet diameter for Silicone Oil A correlates with an increase in the measured drop diameter. However, for  $Re_{g,hd} > 1,500$  and Silicone Oil A, or water and any value of  $Re_{g,hd}$ , there is no correlation between  $d_0$  and the measured drop diameter. This agrees with the results of Varga et al. [40], who showed that the measured drop diameter is insensitive to the liquid jet diameter for low viscosity fluids such as water or ethanol. This indicates that for a particular range of flow rates and

high viscosity fluids, the drop diameter may be a function of the liquid jet diameter ( $d_0$ ).

The change in behavior at  $Re_{g,hd} \approx 1,500$  seems to follow theory. Aliseda et al. [61] report that in order for the primary instability to develop rapidly, it is necessary that the Reynolds number of the liquid shear layer be sufficiently large, such that  $Re_{\lambda_l} = \frac{(u_c - u_l)\lambda_l \rho_l}{\mu_l} > 10$ . This happens to overlap quite well with the  $Re_{g,hd}$  threshold seen in Figure 4.41. As such, it can be suggested that in following the mechanistic model of Aliseda et al. [61], if the primary instability does not develop fast enough such that  $Re_{\lambda_l} > 10$ , the measured characteristic drop diameter can be a function of the liquid jet diameter.

As there are ranges of  $Re_{g,hg}$  where increasing either  $d_0$  or  $b$  results in an increase in the measured drop diameter, the trend of increasing drop diameter with increasing atomizer scale cannot be isolated to one geometric property. However, for high values of  $Re_{g,hd}$ , changes in  $d_0$  did not appear to affect the measured drop diameter. So, changing  $b$  appears to be more important to the resulting drop diameter as  $Re_{g,hd}$  is increased.

The average diameter for the Silicone Oil A spray is noticeably smaller than the average diameter for the water spray, particularly for smaller gas velocities. This seems to be counterintuitive, as increasing the fluid viscosity commonly correlates with an increase in the average drop diameter [40,62], and the liquid viscosity is increased from  $1.00\text{e-}3$  to  $9.64\text{e-}2$ , which is nearly a one-hundred-fold increase. However, a decrease in the surface tension was also shown to reduce the average drop diameter [40,62], and moving from water to Silicone Oil A results in the surface tension dropping from  $0.070\text{ N/m}$  to  $0.021\text{ N/m}$ , a 70% reduction (as shown in Table 3.3). Additionally, as mentioned previously, the regions in which the drops are being measured varies from the water tests to the Silicone Oil A tests. As shown in Figure 4.2 and Figure 4.5, drops are almost immediately generated past the atomizer. However, for Silicone Oil A, hardly a single drop is generated in the same frame, as shown in Figure 4.3 and Figure 4.6. As such, imaging was performed at a distance of  $70d_0$  downstream the atomizer to capture drops of Silicone Oil A. Figure 4.42 shows an example of a downstream image appearance.

Changing the imaging location will certainly affect the concentration of drops in the frame. It may also affect the range of drop sizes that pass through the particular region being imaged. For the water tests, all generated drops are captured in the image as the generation of drops is entirely in the frame, but atomization may not be complete as indicated by larger drops or ligaments that likely undergo secondary atomization, as can be seen in Figure 4.5. For the Silicone Oil A tests, atomization should be practically complete, with maybe a few exceptions (see the long ligament in Figure 4.42). Additionally, all

drops are certainly not captured as their trajectories lead to a much wider region than can be captured by a single camera framing at a distance of  $70d_0$  downstream the atomizer. In fact, Hopfinger and Lasheras [85] showed that for a similar atomizer geometry (at a distance of  $30d_0$ ,  $45d_0$ , and  $60d_0$  downstream) the relative minimum SMD of a radial spray profile always lies along the atomizer center axis. Additionally, as the distance past the atomizer is increased, the difference between the relative maximum and minimum spray SMD increases [85]. As such, caution is used when making direct comparisons on the effect of the atomized fluid on the resulting drop characteristics. The study of Aliseda et al. [61] suggests that the atomization of most liquids is complete at a distance of  $70d_0$  past the atomizer. However, the difference shown between the complete atomization of water and the complete atomization of a high-viscosity non-Newtonian liquid insofar as the change in SMD is quite different, with the absolute change in water SMD from not complete to complete being much smaller than that for the high-viscosity non-Newtonian liquid. This suggests that comparing the atomization of water and Silicone Oil A as measured from two different locations is appropriate.

### 4.3.3 Drop Size Distribution

Figures 4.43-4.46 show the change in the drop diameter geometric standard deviation as a function of  $Re_{g,hd}$ .

The trends for  $\sigma_{dd}$  are much the same as the trends for  $\mu_{dd}$  and SMD with changing  $Re_{g,hd}$ . Increasing the atomizer scale correlates with an increase in  $\sigma_{dd}$ . Increasing  $b$  correlates with an increase in  $\sigma_{dd}$ . Increasing  $d_0$  correlates with an increase in  $\sigma_{dd}$ , but only for Silicone Oil A. The nature of  $\sigma_{dd}$  means that as  $Re_{g,hd}$  is increased further,  $\sigma_{dd}$  will asymptote at a value of one.

### 4.3.4 Spray Sauter Mean Diameter

The Sauter mean diameter is commonly reported in the literature, particularly for applications that rely on mass and heat transfer as the SMD is meant to represent the a drop with the same volume-to-area ratio as the entire spray. The method for calculating the SMD is distinctly different than the method for calculating the geometric mean diameter, leading to some shifts in the data as compared to the geometric mean drop diameter results. Figures 4.47-4.50 show the SMDs.

The trends of the measured SMDs versus  $Re_{g,hd}$  look distinctly different than the same trends for  $\mu_{dd}$ , yet the trends with changes in geometry remain approximately the same. Figure 4.48 shows that increasing the atomizer scale correlates with an increase in the spray

SMD for both water and Silicone Oil A. As the inclusion of even a small quantity of large drops can significantly increase the SMD, the drastic increase in SMD for L4G4 as  $Re_{g,hd}$  is increased can likely be explained by errant ligaments. It is believed that increasing  $Re_{g,hd}$  correlates with a decrease in spray SMD across the board. However, increasing  $Re_{g,hd}$  could lead to a larger fraction of any large ligaments to pass along the atomizer's center axis as opposed to following a trajectory away from the centerline, which would then lead to an increase as shown in Figure 4.48. Figure 4.49 shows that increasing  $b$  correlates with an increase in the measured spray SMD for all conditions explored. Figure 4.50 shows that increasing  $d_0$  correlates with an increase in the measured spray SMD. The trend is only distinctly seen for  $Re_{g,hd} < 1,500$  for Silicone Oil A, as was the case for the geometric mean drop diameters. However, for the water tests with G1-atomizers (or  $b = 0.18mm$ ), increasing  $d_0$  seems to correlate with an increase in the spray SMD for all values of  $Re_{g,hd}$  explored.

Unfortunately, few studies report geometric mean drop diameters. Luckily, the SMD trends with respect to both  $Re_{g,hd}$  and geometry can be compared to the correlations presented by previous studies in Equations 2.1-2.3 [40, 55–61]. Figure 4.51 shows the measured SMDs for all cases explored versus the calculated SMDs using the correlations of Nukiyama and Tanasawa [55–60], Varga et al. [40], and Aliseda et al. [61], shown in Equations 2.1-2.3, respectively.

There are noticeable differences in the measured SMD values and the calculated SMD values for the correlations presented, but some do better than others. Nukiyama and Tanasawa's (Equation 2.1) prediction for the water SMDs shows the most discrepancy between measured and calculated SMDs, particularly for their prediction for the Silicone Oil A SMDs, which are substantially higher than what was measured. Their predictions for the water spray SMDs are reasonably close. The Varga et al. [40] prediction for both water and Silicone Oil A is smaller than what was measured, but their prediction suggests that the SMDs of Silicone Oil A should be smaller than that of water, which is seen in this study. The Aliseda et al. [61] prediction is fairly close to what was measured for the water SMDs, and they predict that the SMDs for Silicone Oil A should be larger than that of water, which is the opposite of what was measured.

It is useful (and reassuring to us, the authors!) to note that Nukiyama and Tanasawa's [55–60] prediction (Equation 2.1) is based solely on an empirical comparison between the inputs and the resulting drop diameter. The viscosity of Silicone Oil A is far outside the range of liquid viscosities evaluated by Nukiyama and Tanasawa [55–60], meaning that applying their correlation is not appropriate. Additionally, their methods of measuring the

drop diameters were fairly rudimentary compared to the high-tech methods available to modern researchers. The predictions of Varga et al. [40] and Aliseda et al. [61] are both based upon a mechanistic model that suggests breakup occurs due to quantifiable physical phenomena, leading the authors to believe they are of more value than the prediction of Nukiyama and Tanasawa [55–60].

The prediction of Varga et al. [40] accurately described the SMD dependence on surface tension in their studies, but they did not explore fluids with significant differences in viscosity as the present study does. In fact, their prediction (Equation 2.2) does not include a dependence on the liquid viscosity at all. Aliseda et al. [61] evaluated fluids with both a wide range of viscosity and surface tension, although they did not set up their experiments to independently evaluate those parameters. Their study reports spray SMDs for various fluids as a function of only one set of flow rates, but at multiple locations downstream the atomizer. Aliseda et al. [61] also note that a seemingly small reduction in surface tension will have a much greater effect than an equivalent increase in viscosity.

While the present study, the study by Varga et al. [40], and the study by Aliseda et al. [61] all use a similar atomizer geometry, the atomizer geometries are not completely identical. The atomizers used in the present study and by Aliseda et al. [61] are both from Spraying Systems [103] and employ a short length in which the gas flow could develop, providing a higher degree of turbulence to the gas flow. The atomizers used by Varga et al. [40] have smooth, convergent gas channels allowing the flow to become fully developed before leaving the atomizer. This difference is assumed to explain why the measured SMDs are smaller than the predictions of Varga et al. [40] in Equation 2.2. While Aliseda et al. [61] evaluated a range of liquid viscosities that encompasses the fluids evaluated herein, the Newtonian fluids evaluated by Aliseda et al. [61] had viscosities less than Silicone Oil A. Non-Newtonian fluids will offer different behavior during atomization than Newtonian fluids, and it cannot be assumed that comparing the two is appropriate.

#### 4.3.5 Characteristic Drop Correlations

In order to predict drop diameters for the system explored herein, Buckingham-II theorem was employed. The relevant parameters were reduced previously, leaving the following parameters:  $A = b/d_0$ ,  $D = a/d_0$ ,  $M$ , and  $Re_{g,hd}$ . From these parameters, a nonlinear model was fit to the various characteristic drop diameters:  $\mu_{dd}$  and SMD. The method used to find the nonlinear model coefficients was the *fitnlm*-function in MATLAB<sup>®</sup> [105], which employs an iterative least squares estimation.

The correlations for  $\mu_{dd}$ , SMD, and  $\sigma_{dd}$  are shown in Equation 4.13, Equation 4.14, and Equation 4.15, respectively.

$$\frac{\mu_{dd}}{b} = 17.5A^{-0.76}D^{0.39}M^{0.09}Re_{g,hd}^{-0.61} \quad (4.13)$$

$$\sigma_{dd} = 5.89A^{0.11}D^{-0.14}M^{-0.06}Re_{g,hd}^{-0.13} \quad (4.14)$$

$$\frac{SMD}{b} = 25.8A^{-0.77}D^{-0.08}M^{-0.28}Re_{g,hd}^{0.42} \quad (4.15)$$

The predictions based upon Equations 4.13-4.15 are shown in Figures 4.52-4.54.

The empirically-derived correlations fit the data quite well, but are very different than the mechanistic correlations presented in Equation 2.2 and Equation 2.3, via Varga et al. [40] and Aliseda et al. [61], respectively.

#### 4.4 Comparing Instabilities and the Resulting Spray

The proposal made in the literature is that the instability characteristics can be correlated to a spray-representative drop diameter. The goal here is to verify the existing relationships and extend them to other fluids and atomizer geometries, so these comparisons are included. Figure 4.55 shows the measured primary wavelengths versus the measured Sauter mean diameters.

As shown in Figure 4.55, the data collapse well when normalizing both the primary wavelength and the spray SMD by  $b$ . In the previous sections,  $b$  is noted to more commonly have an effect on both the ILJ surface instabilities and the resulting spray SMD. Additionally,  $Re_{g,hd}$  seemingly best characterized the behavior of the system, and  $Re_{g,hd}$  itself is a function of the atomizer gas hydraulic diameter.

#### 4.5 Conclusions

Numerous trends were identified to the dynamic characteristics of the intact liquid jet (ILJ) and the formation and growth of instabilities existing on the ILJ. Changing the atomizer scale was shown to significantly impact the ILJ length, the ILJ length oscillation frequency, the ILJ surface oscillation frequency, and the primary wavelength. The dependence of the ILJ surface oscillation frequency and the primary wavelength were shown to be very dependent on the fluid being atomized, which is important to understand when trying to scale an atomizer for fluids other than water. Changing only the gas annular thickness ( $b$ ) was shown to effect the ILJ length, the ILJ angle oscillation amplitude, the ILJ surface

oscillation frequency, and the primary wavelength. The ILJ angle oscillation amplitude was shown to be unchanged for changes in  $b$  for the atomization of water, but for Silicone Oil A, increasing  $b$  was shown to increase the ILJ angle oscillation amplitude. Changing the liquid jet diameter ( $d_0$ ) was shown to effect the the ILJ length, the ILJ length oscillation frequency, the ILJ angle oscillation frequency, and the ILJ angle oscillation amplitude.

Existing empirical and mechanistic correlations prediction spray characteristics were compared to the measured spray characteristics for multiple atomizer geometries and three different fluids. Additionally, Buckingham-II theorem was used to develop dimensionless correlations predicting spray characteristics. These developed correlations were shown to predict the spray characteristics well over the range of variables explored.

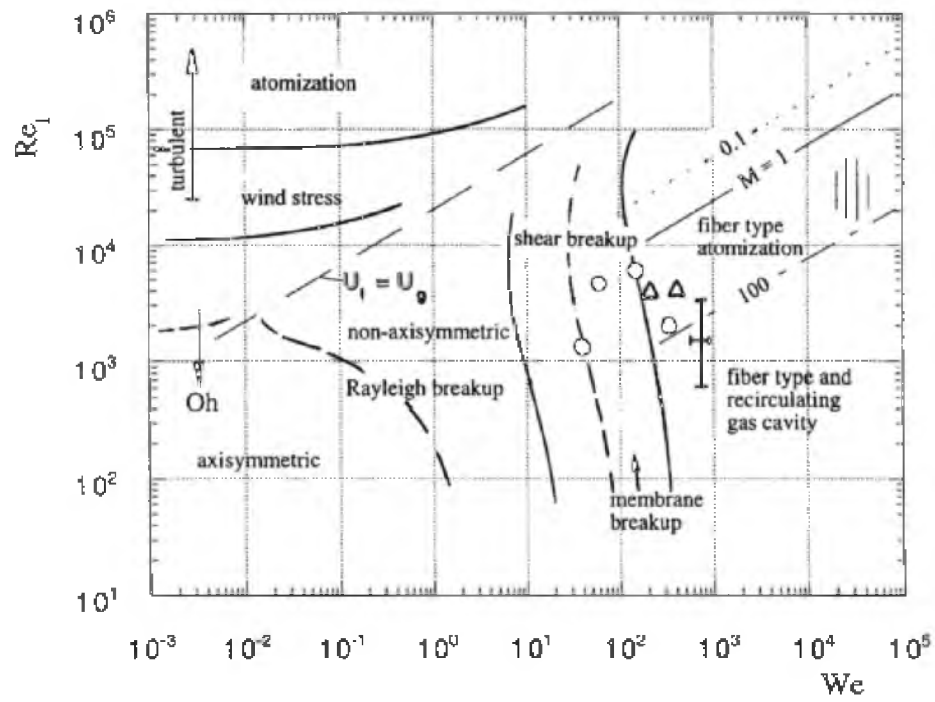


Figure 4.1. Morphological breakup regimes of Lasheras and Hopfinger © [82].



Figure 4.2. L2G1 water.



**Figure 4.3.** L2G1 Silicone Oil A.



**Figure 4.4.** L2G1 Silicone Oil B.

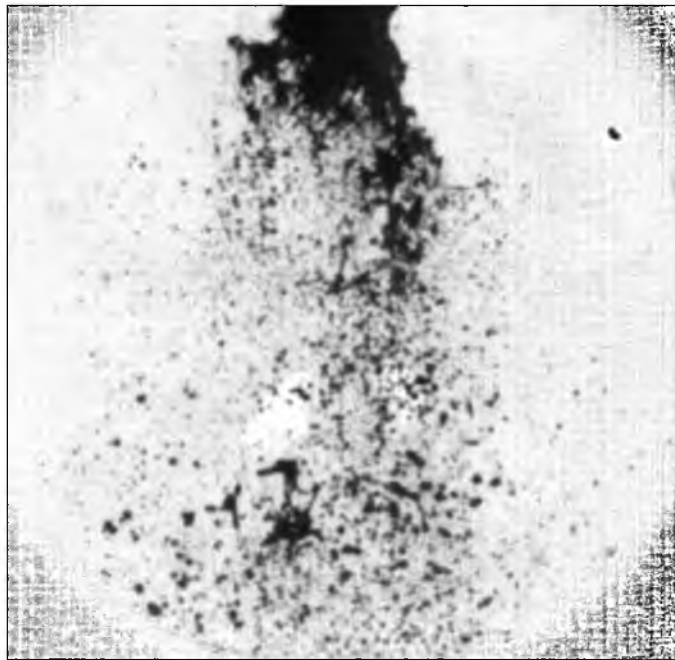


Figure 4.5. L4G4 water.

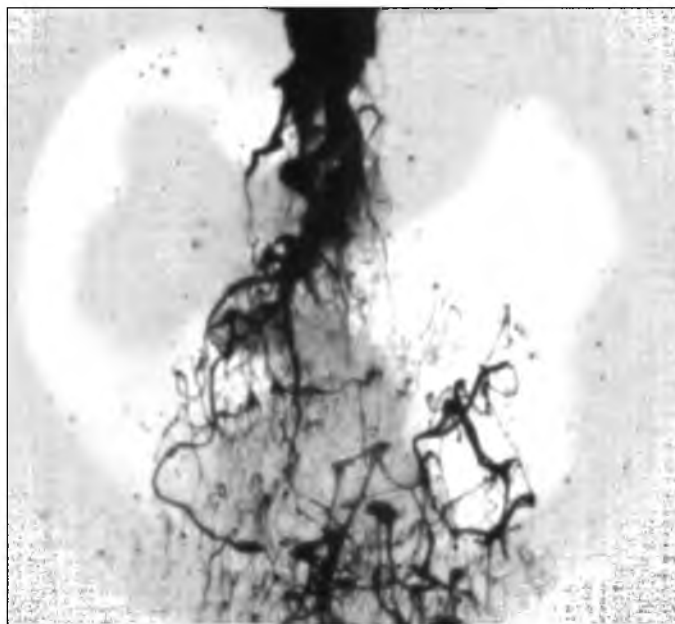


Figure 4.6. L4G4 Silicone Oil A.

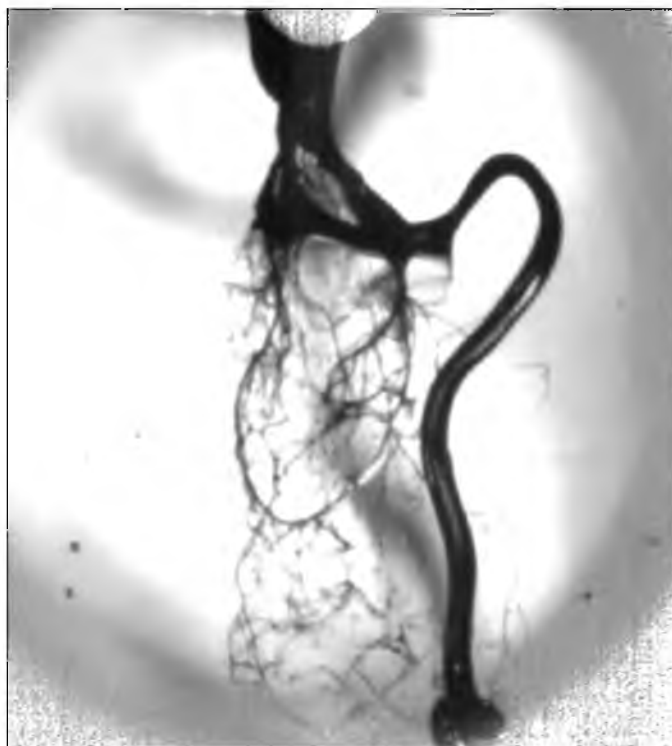


Figure 4.7. L4G4 Silicone Oil B.

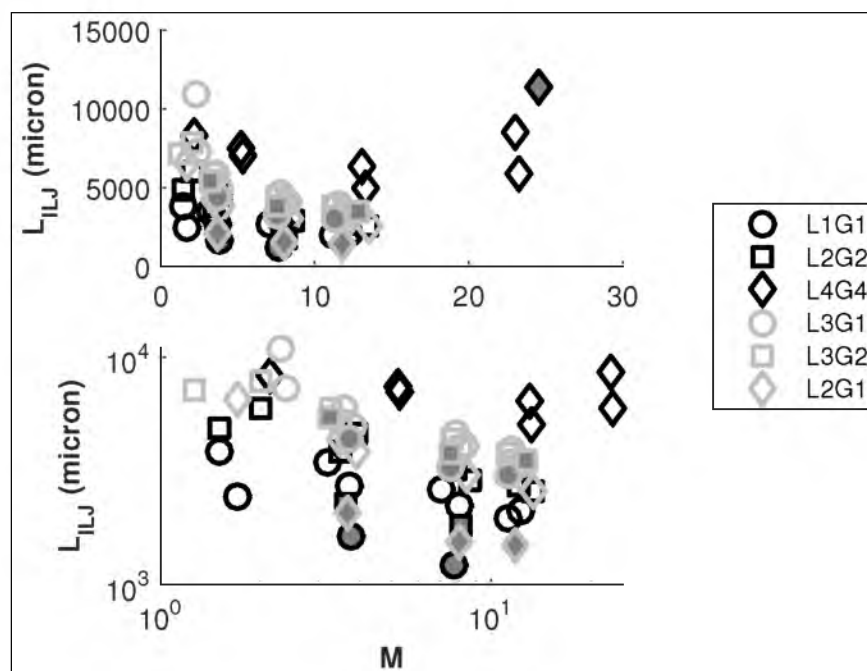
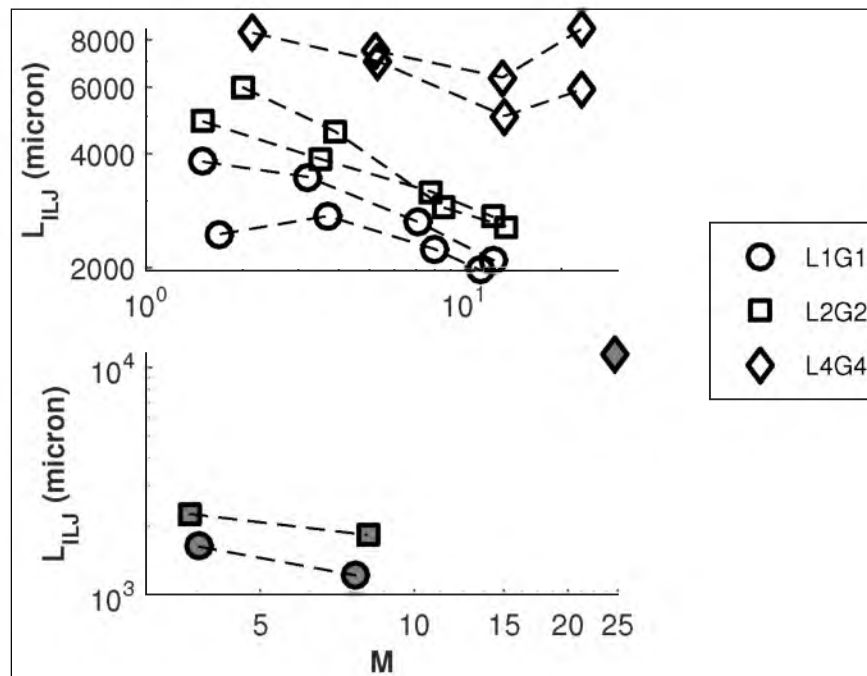
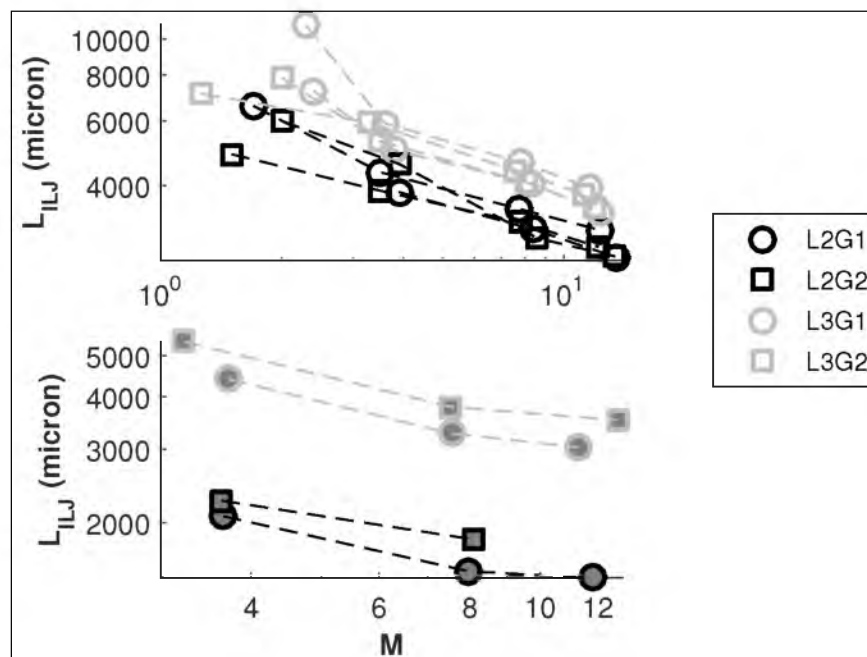


Figure 4.8.  $M$  versus the ILJ length. Filled markers represent Silicone Oil A. All data.



**Figure 4.9.**  $M$  versus the ILJ length. Filled markers represent Silicone Oil A. Scale-able atomizers only. All have  $A_g/A_l \approx 6$ . Dashed lines indicate similar tests and serve to better identify geometric trends between conditions.



**Figure 4.10.**  $M$  versus the ILJ length. Filled markers represent Silicone Oil A. Constant  $d_0$  by marker edge color, changing  $b$ . Dashed lines indicate similar tests and serve to better identify geometric trends between conditions.

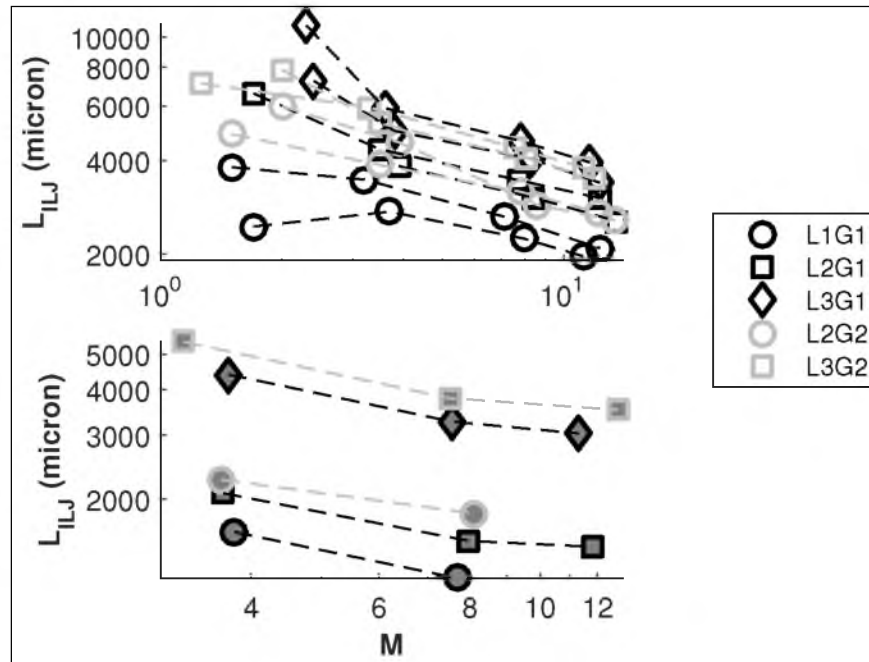


**Figure 4.11.**  $M$  versus the ILJ length. Filled markers represent Silicone Oil A. Constant  $b$  by marker edge color, changing  $d_0$ . Dashed lines indicate similar tests and serve to better identify geometric trends between conditions.

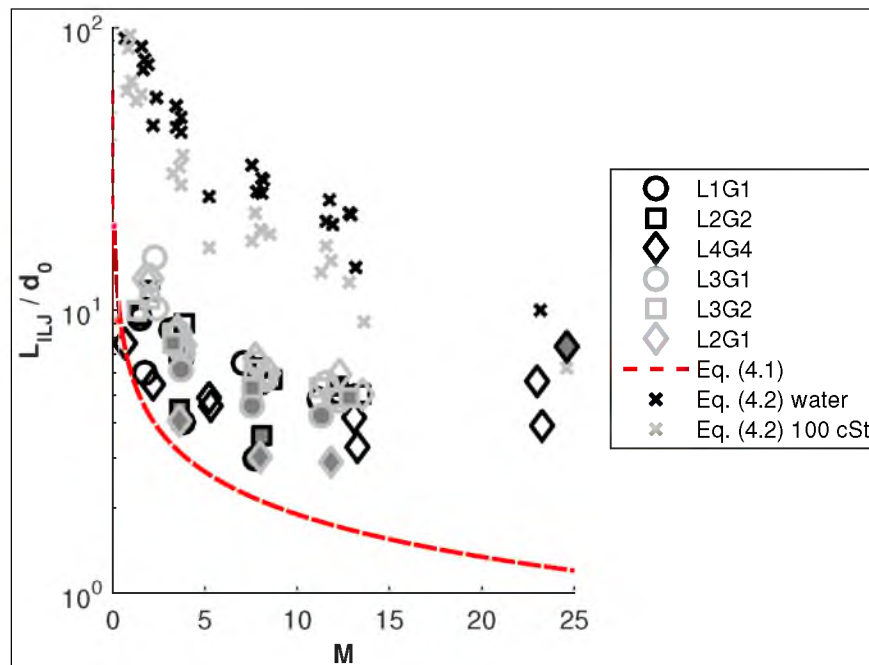


**Figure 4.12.**  $M$  versus the  $d_0$ -normalized ILJ length. Filled markers represent Silicone Oil A. Dashed line represents the prediction of Lasheras et al. [39], shown in Equation 4.1.  $x$ 's represent the predictions of Zhao et al. [73], shown in Equation 4.2.

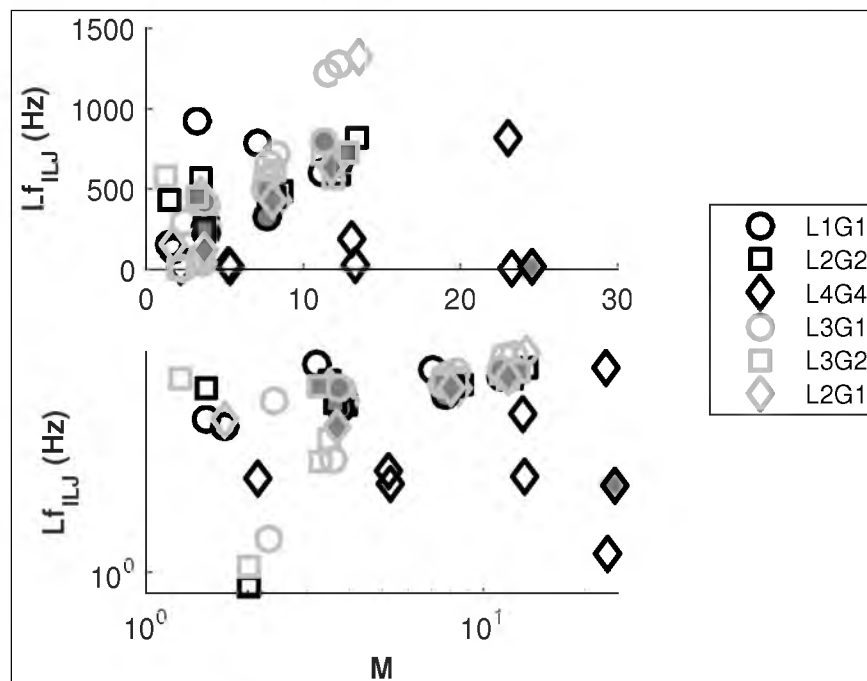


**Figure 4.13.**  $M$  versus the ILJ length oscillation frequency. Filled markers represent Silicone Oil A. All data.

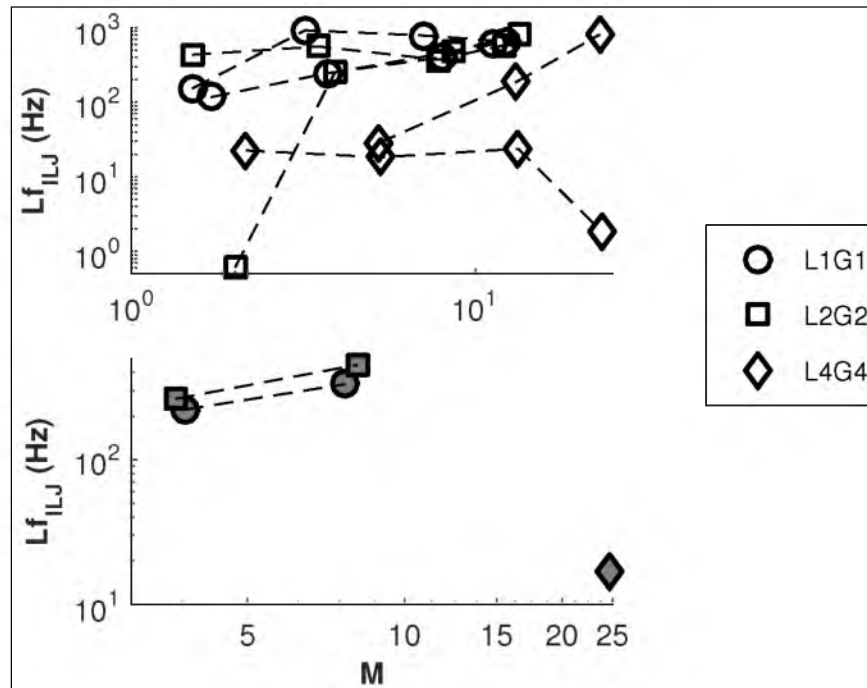


**Figure 4.14.**  $M$  versus the ILJ length oscillation frequency. Filled markers represent Silicone Oil A. Scale-able atomizers only. All have  $A_g/A_l \approx 6$ . Dashed lines indicate similar tests and serve to better identify geometric trends between conditions.

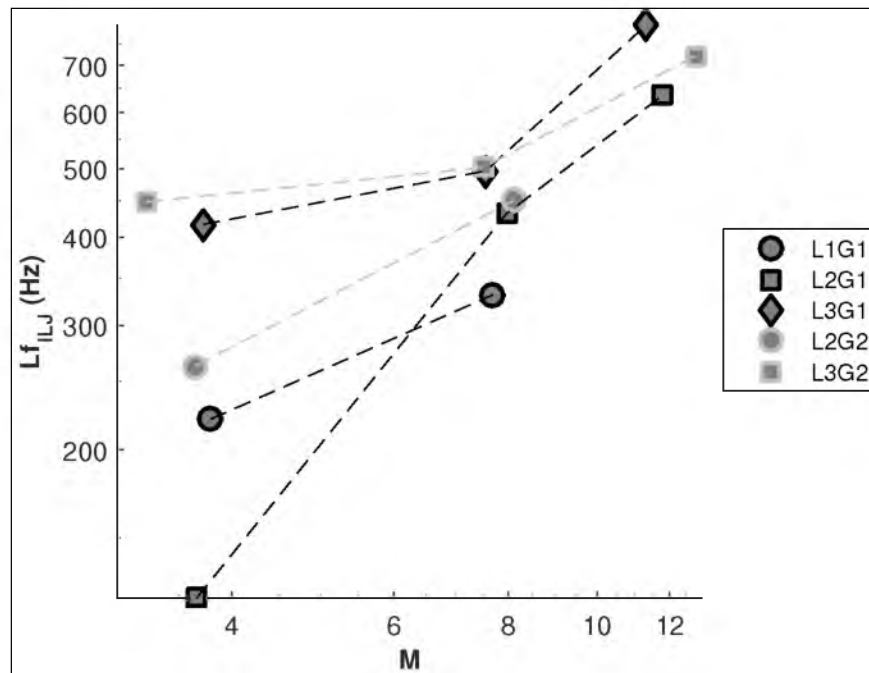


**Figure 4.15.**  $M$  versus the ILJ length oscillation frequency. Filled markers represent Silicone Oil A. Constant  $b$  by marker edge color, changing  $d_0$ . Dashed lines indicate similar tests and serve to better identify geometric trends between conditions.

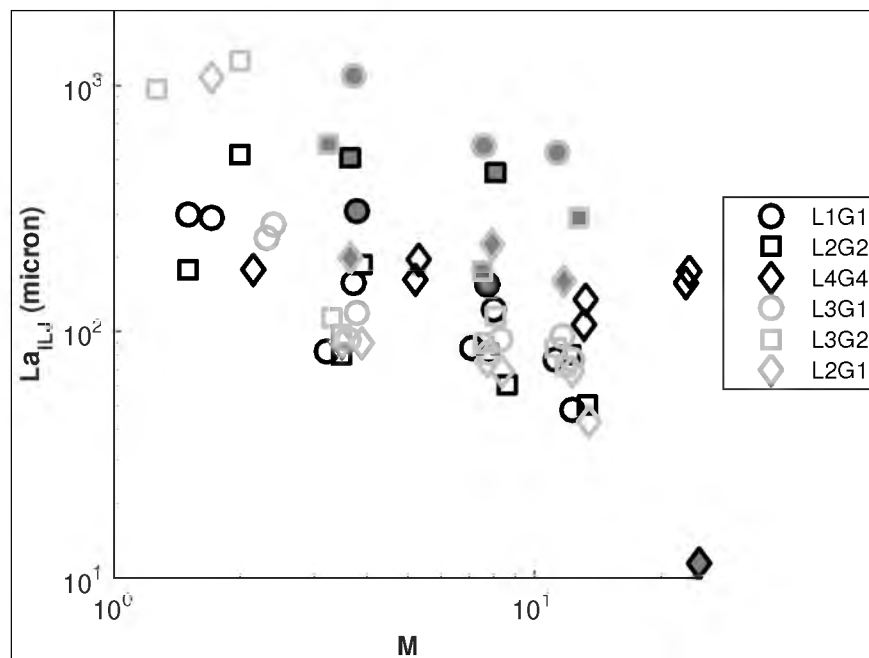


**Figure 4.16.**  $M$  versus the ILJ length oscillation amplitude. Filled markers represent Silicone Oil A. All data.

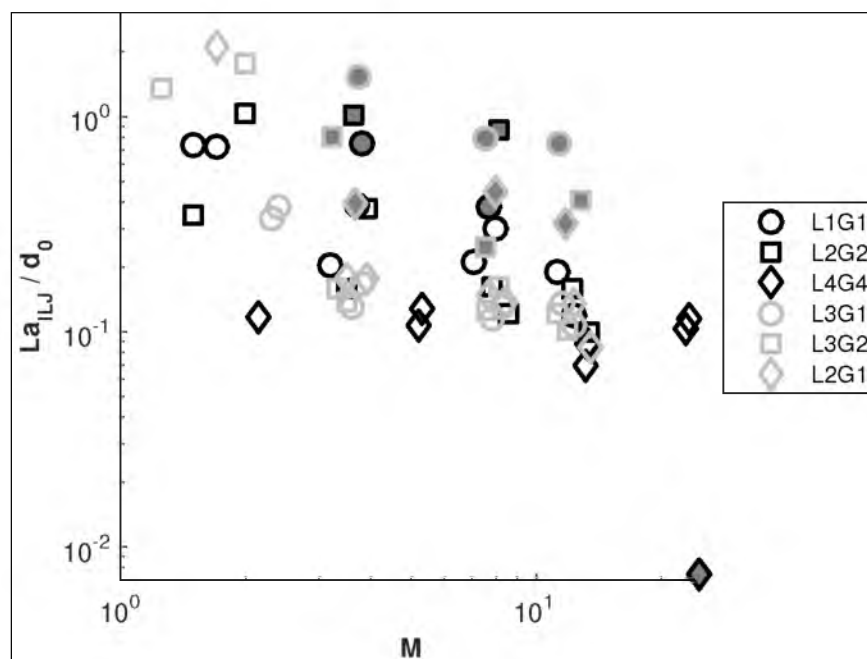


**Figure 4.17.**  $M$  versus the ILJ length oscillation amplitude. Filled markers represent Silicone Oil A. All data.

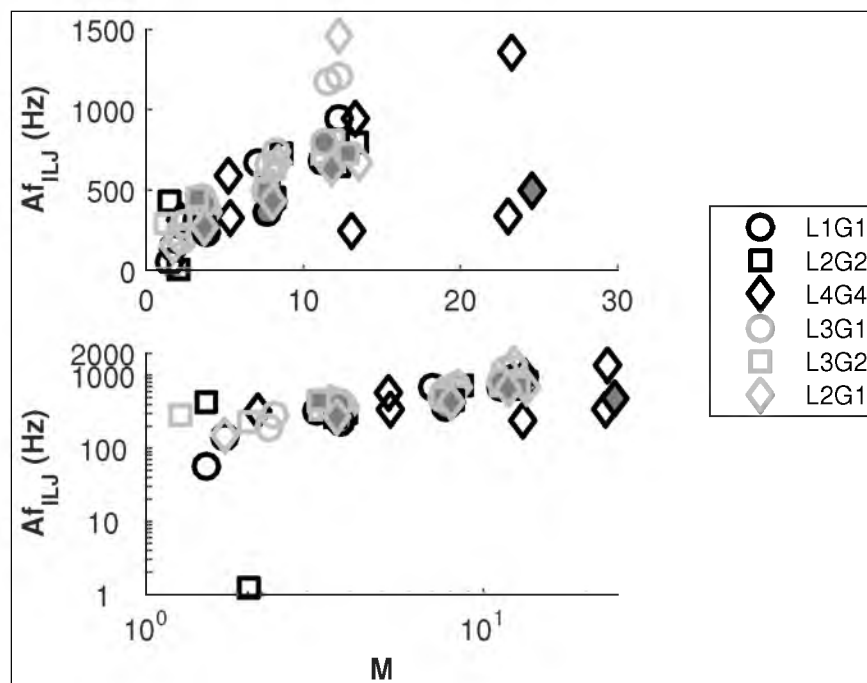


**Figure 4.18.**  $M$  versus the ILJ angle oscillation frequency. Filled markers represent Silicone Oil A. All data.

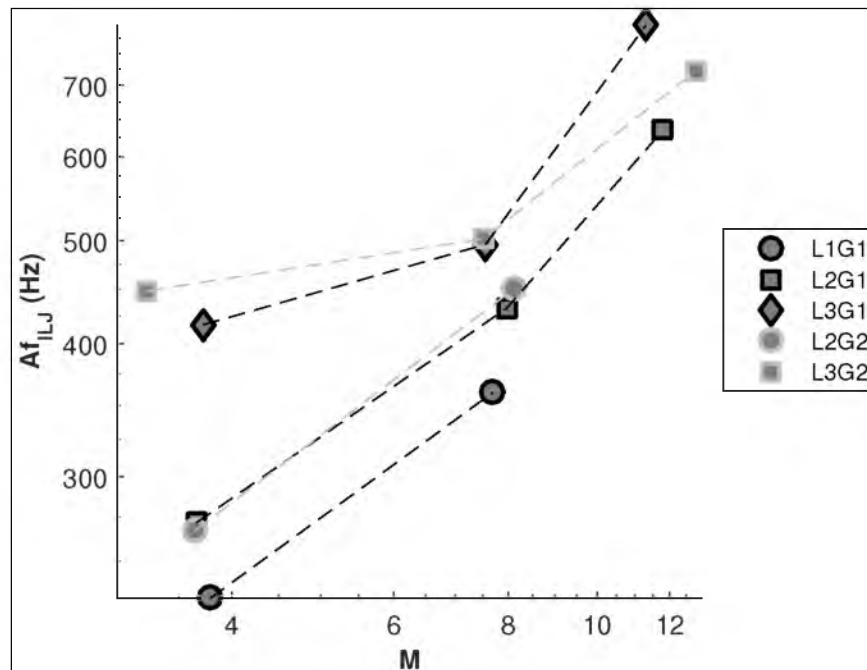


**Figure 4.19.**  $M$  versus the ILJ angle oscillation frequency. Filled markers represent Silicone Oil A. Constant  $b$  by marker edge color, changing  $d_0$ . Dashed lines indicate similar tests and serve to better identify geometric trends between conditions.

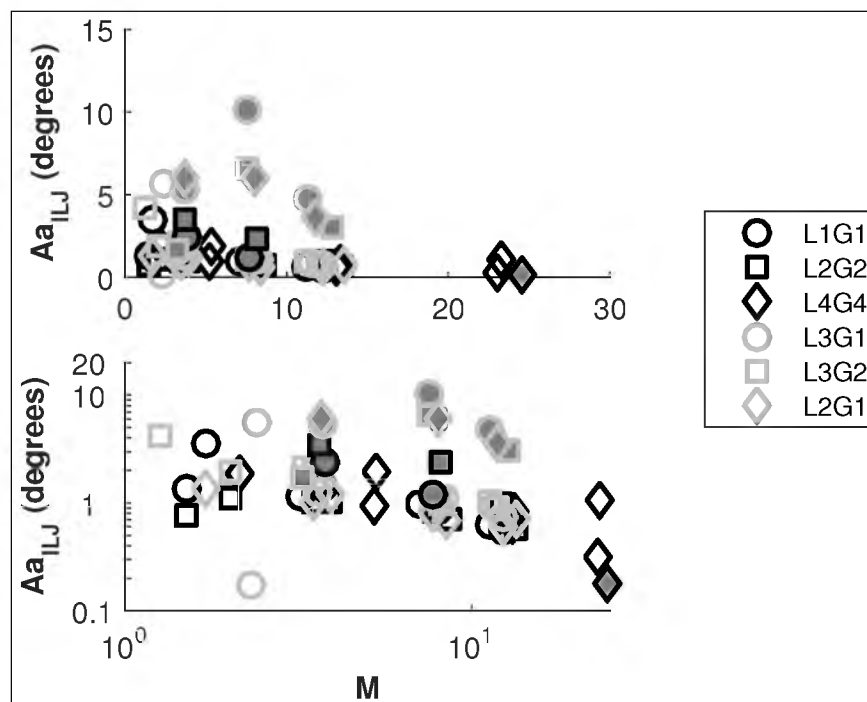


**Figure 4.20.**  $M$  versus the ILJ angle oscillation amplitude. Filled markers represent Silicone Oil A. All data.

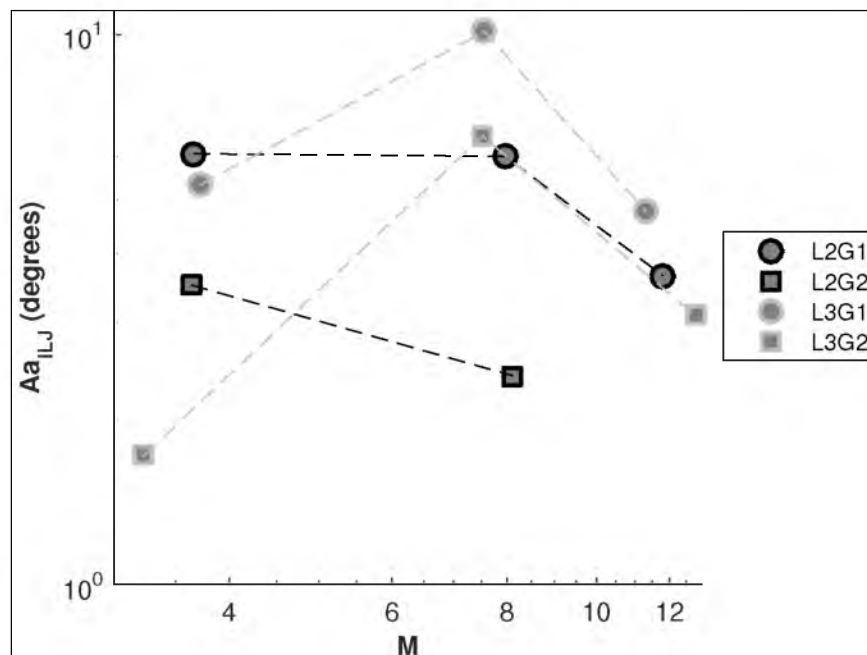


**Figure 4.21.**  $M$  versus the ILJ angle oscillation amplitude. Filled markers represent Silicone Oil A. Constant  $d_0$  by marker edge color, changing  $b$ . Dashed lines indicate similar tests and serve to better identify geometric trends between conditions.

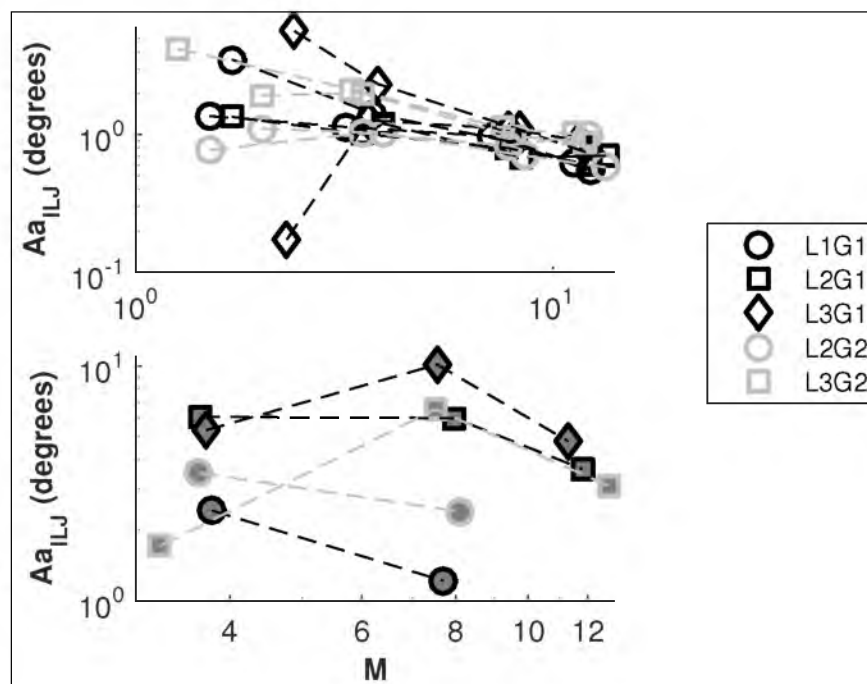


**Figure 4.22.**  $M$  versus the ILJ angle oscillation amplitude. Filled markers represent Silicone Oil A. Constant  $b$  by marker edge color, changing  $d_0$ . Dashed lines indicate similar tests and serve to better identify geometric trends between conditions.

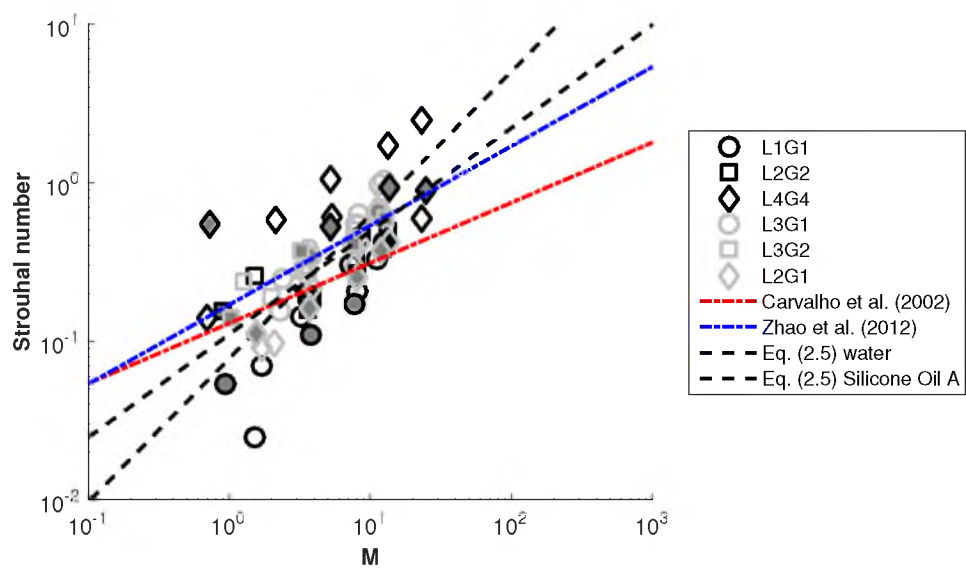


**Figure 4.23.** Average Strouhal number as a function of  $M$ .

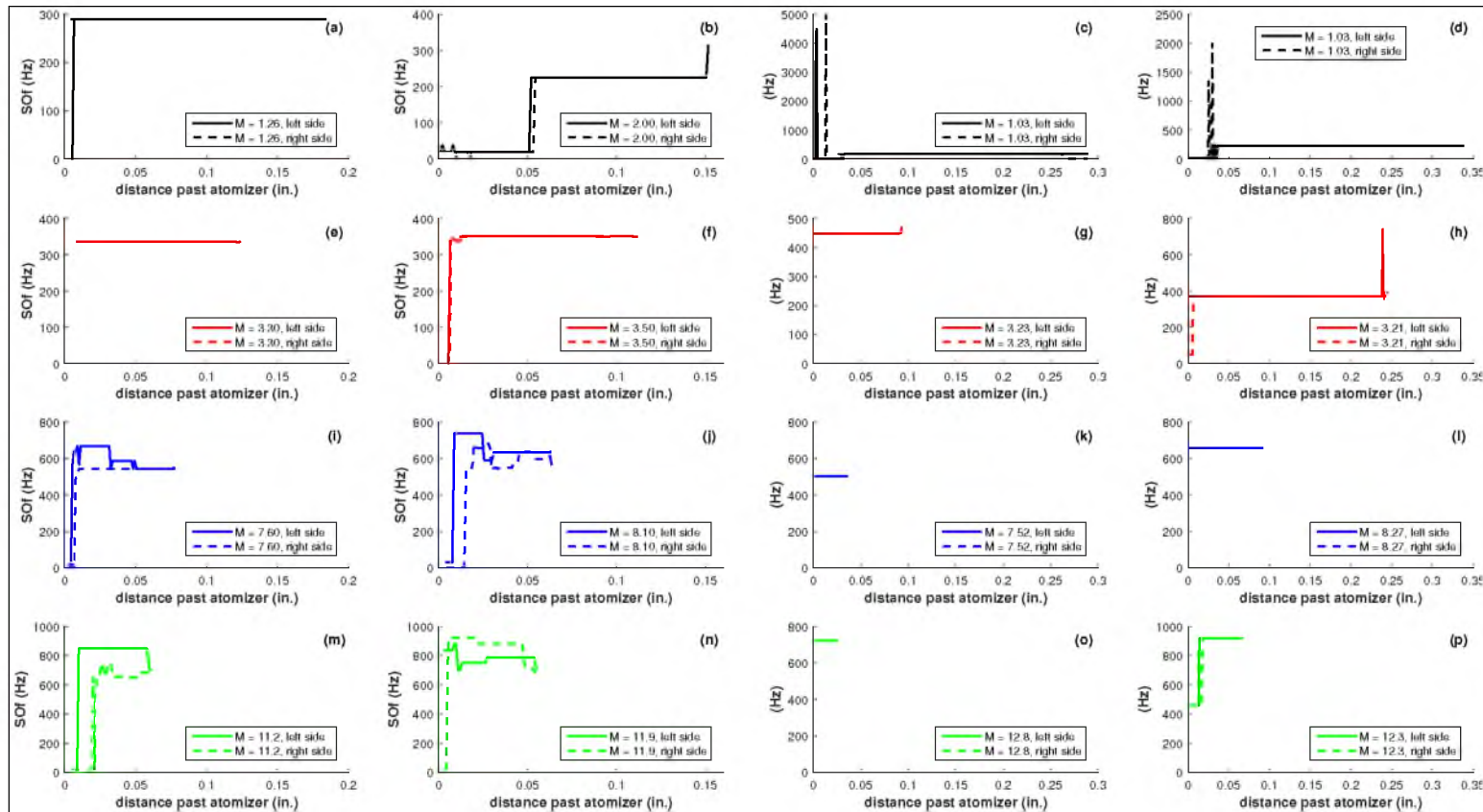


**Figure 4.24.** ILJ surface oscillation frequency (SOI) as a function of distance past the atomizer. Atomizer L3G2. Column one and two (from left to right) are water tests (subfigures a, b, e, f, i, j, m, n), column three is Silicone Oil A (subfigures c, g, k, o), and column four is Silicone Oil B (subfigures d, h, l, p). From top to bottom, gas velocity is increased, corresponding to an increase in  $M$ .

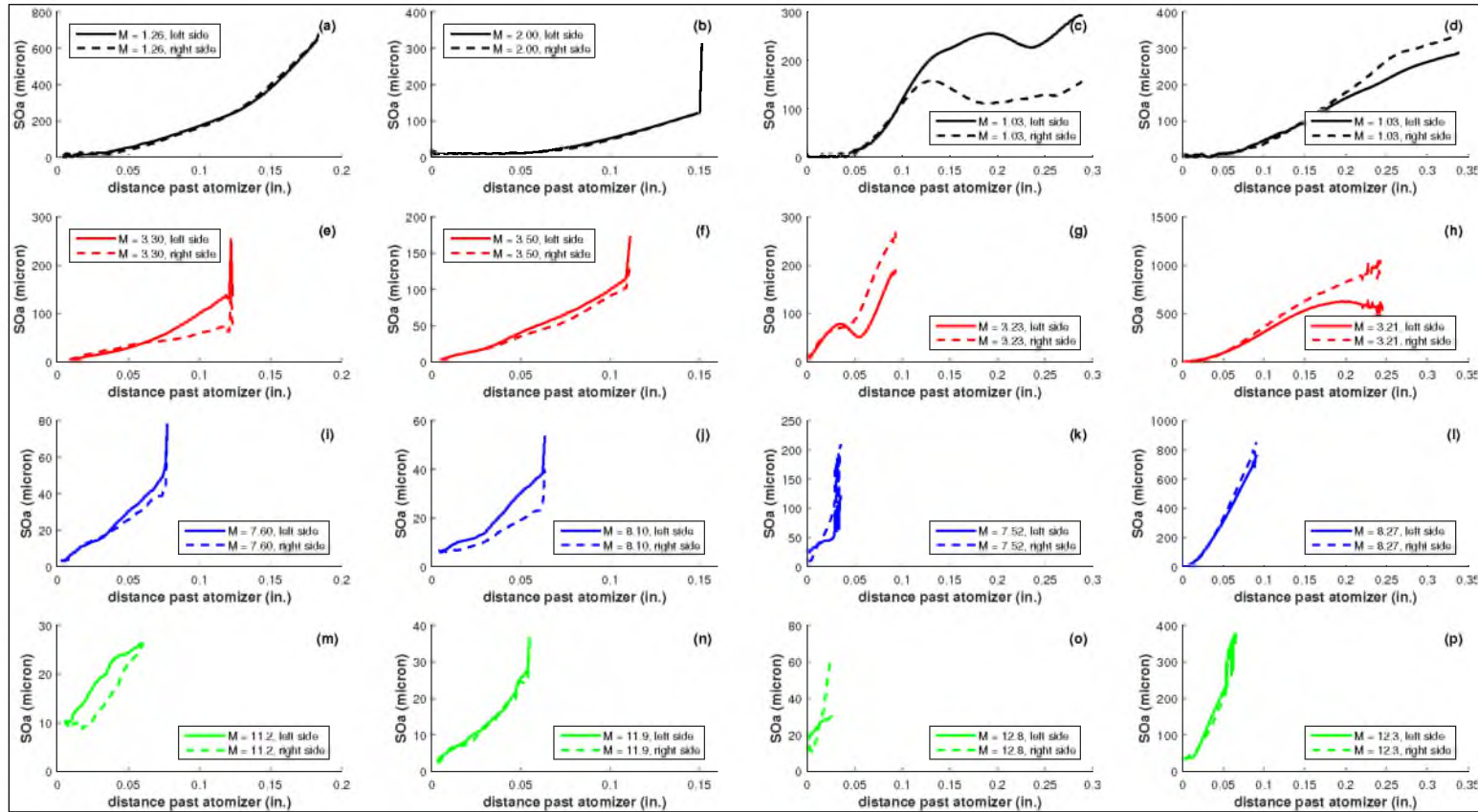


**Figure 4.25.** ILJ surface oscillation amplitude (SOa) as a function of distance past the atomizer. Atomizer L3G2. Column one and two (from left to right) are water tests (subfigures a, b, e, f, i, j, m, n), column three is Silicone Oil A (subfigures c, g, k, o), and column four is Silicone Oil B (subfigures d, h, l, p). From top to bottom, gas velocity is increased, corresponding to an increase in  $M$ .

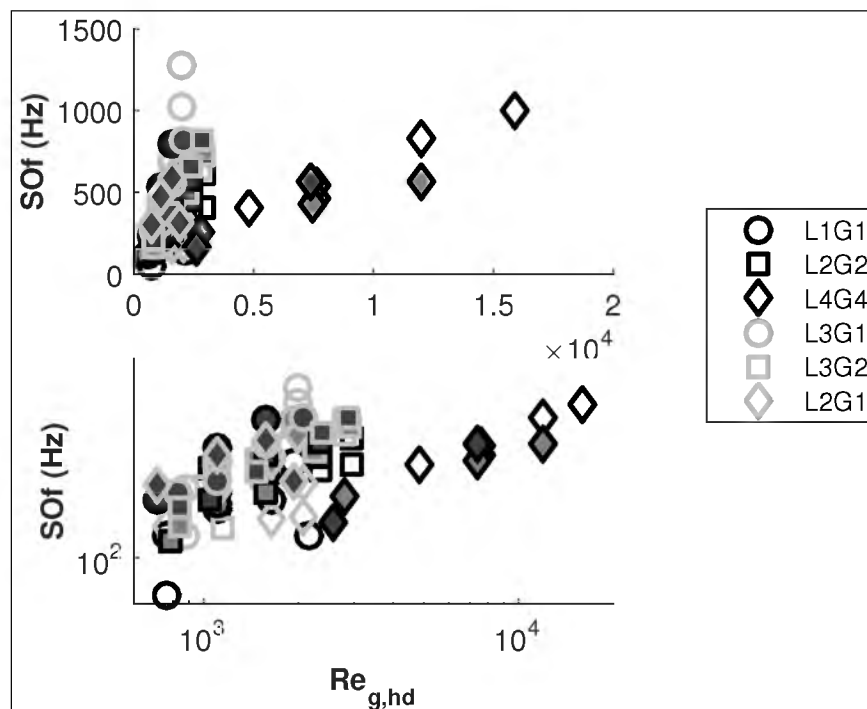


**Figure 4.26.**  $Re_{g,hd}$  versus the ILJ surface oscillation frequency. Light-filled markers represent Silicone Oil A. Dark-filled markers represent Silicone Oil B. All data.

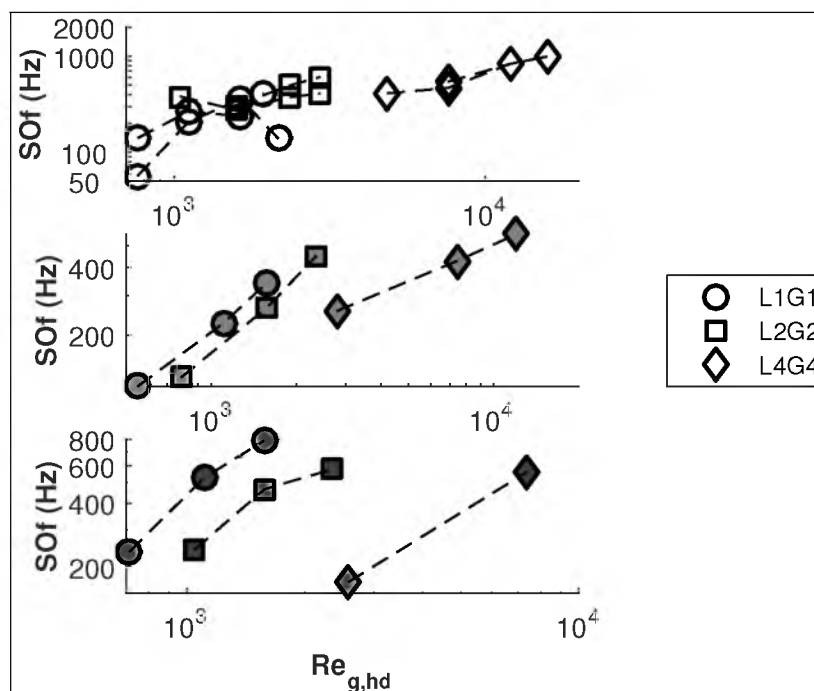


**Figure 4.27.**  $Re_{g,hd}$  versus the ILJ surface oscillation frequency. Light-filled markers represent Silicone Oil A. Dark-filled markers represent Silicone Oil B. Scale-able atomizers only. All have  $A_g/A_l \approx 6$ . Dashed lines indicate similar tests and serve to better identify geometric trends between conditions.

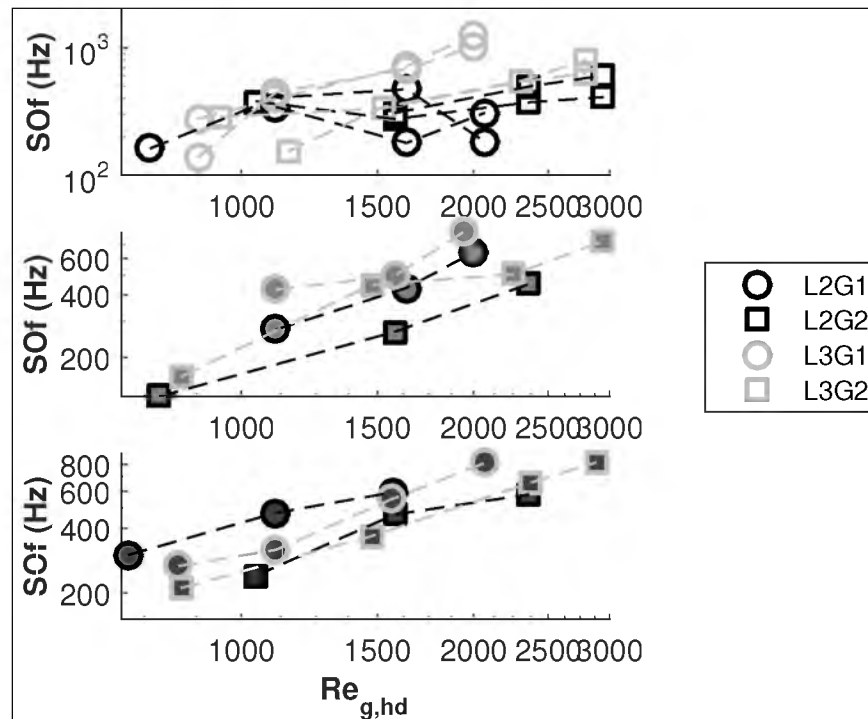


**Figure 4.28.**  $Re_{g,hd}$  versus the ILJ surface oscillation frequency. Light-filled markers represent Silicone Oil A. Dark-filled markers represent Silicone Oil B. Constant  $d_0$  by marker edge color, changing  $b$ . Dashed lines indicate similar tests and serve to better identify geometric trends between conditions.

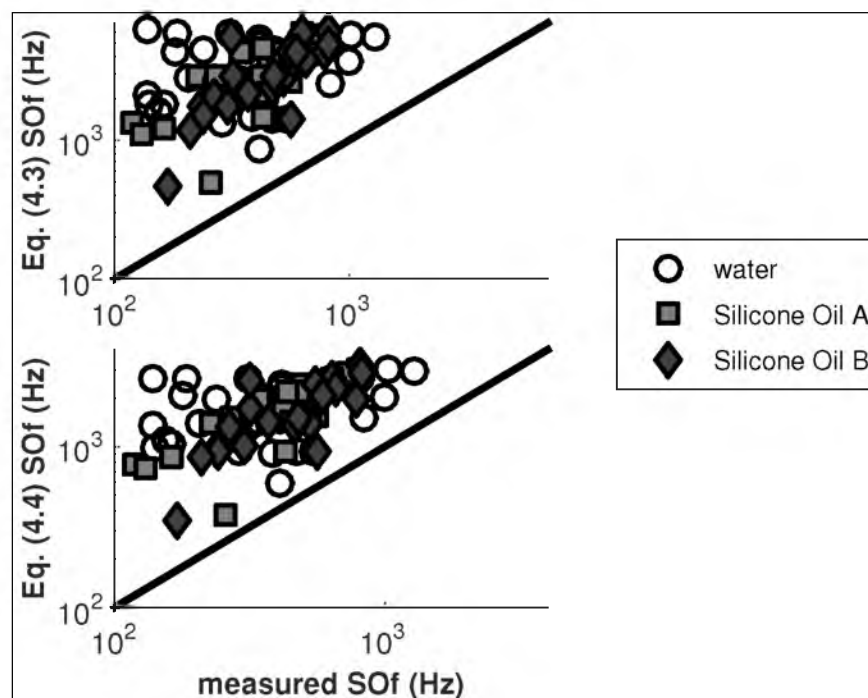


**Figure 4.29.** Measured versus calculated ILJ surface oscillation frequencies.

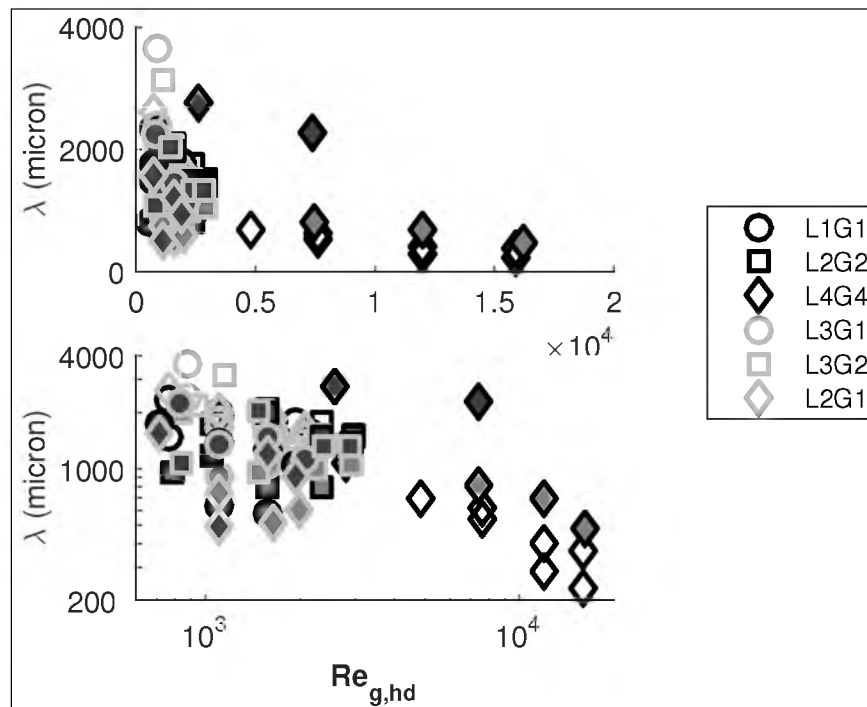


**Figure 4.30.**  $Re_{g,hd}$  versus the primary wavelength. Light-filled markers represent Silicone Oil A. Dark-filled markers represent Silicone Oil B. All data.

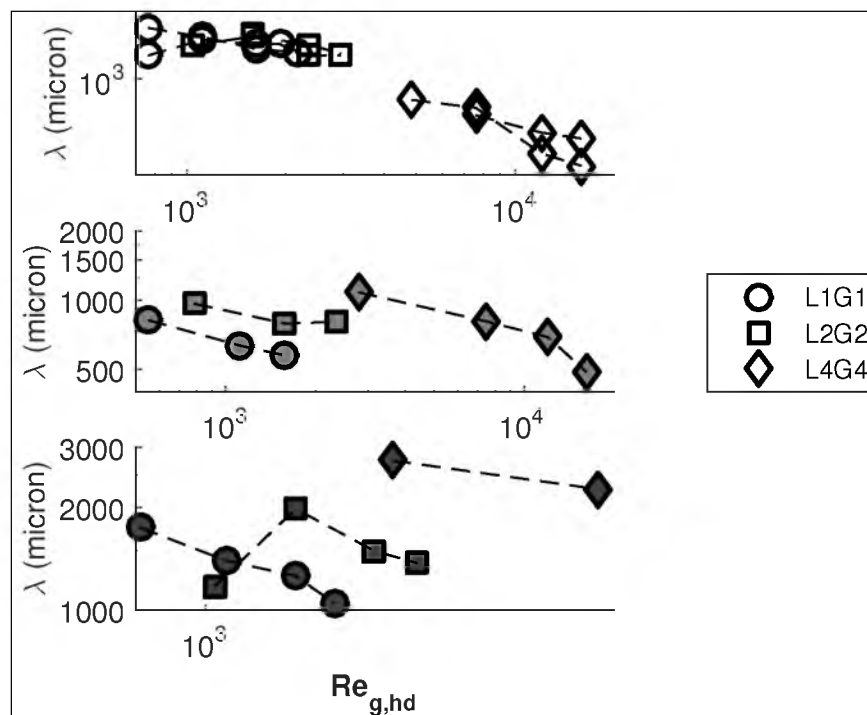


**Figure 4.31.**  $Re_{g,hd}$  versus the primary wavelength. Light-filled markers represent Silicone Oil A. Dark-filled markers represent Silicone Oil B. Scale-able atomizers only. All have  $A_g/A_l \approx 6$ . Dashed lines indicate similar tests and serve to better identify geometric trends between conditions.

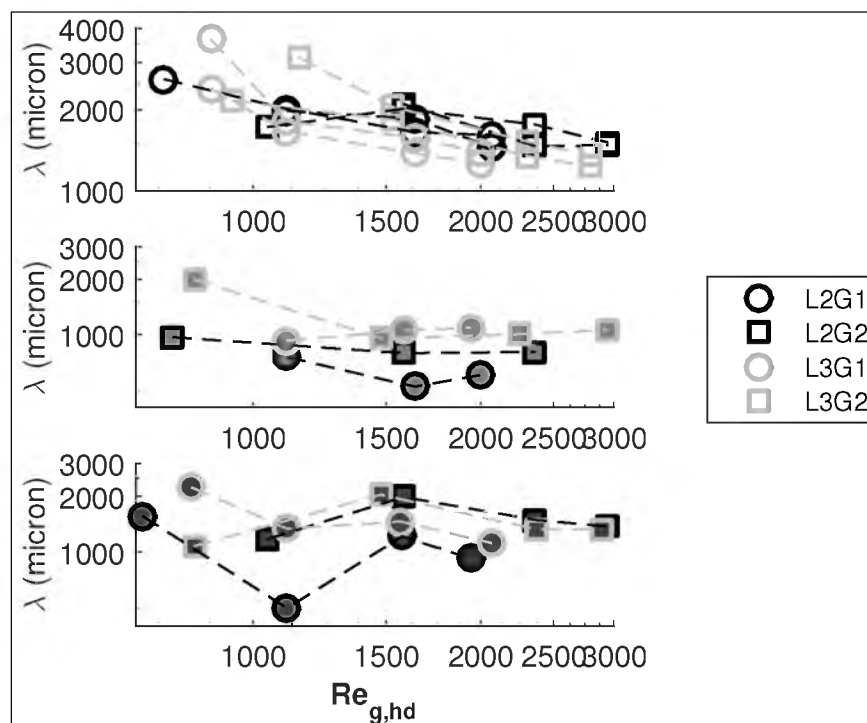


**Figure 4.32.**  $Re_{g,hd}$  versus the primary wavelength. Light-filled markers represent Silicone Oil A. Dark-filled markers represent Silicone Oil B. Constant  $d_0$  by marker edge color, changing  $b$ . Dashed lines indicate similar tests and serve to better identify geometric trends between conditions.

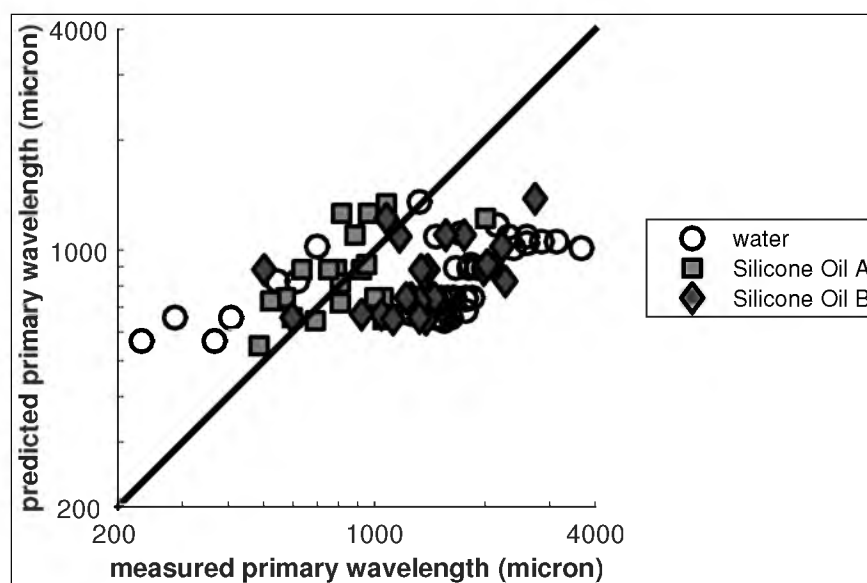


**Figure 4.33.** Measured versus calculated ILJ surface primary wavelengths.

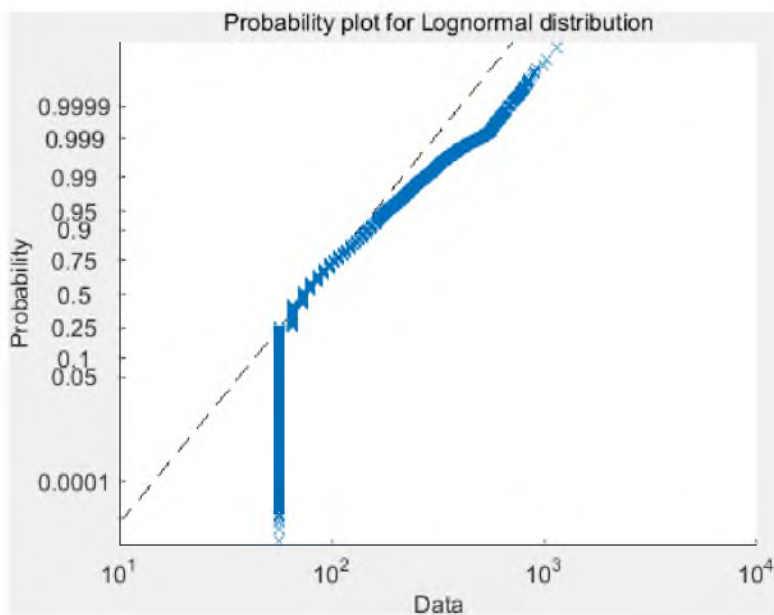


**Figure 4.34.** Drop diameter distribution comparison to a log-normal distribution. Water, L1G1-1,  $Re_g = 1,637$ .

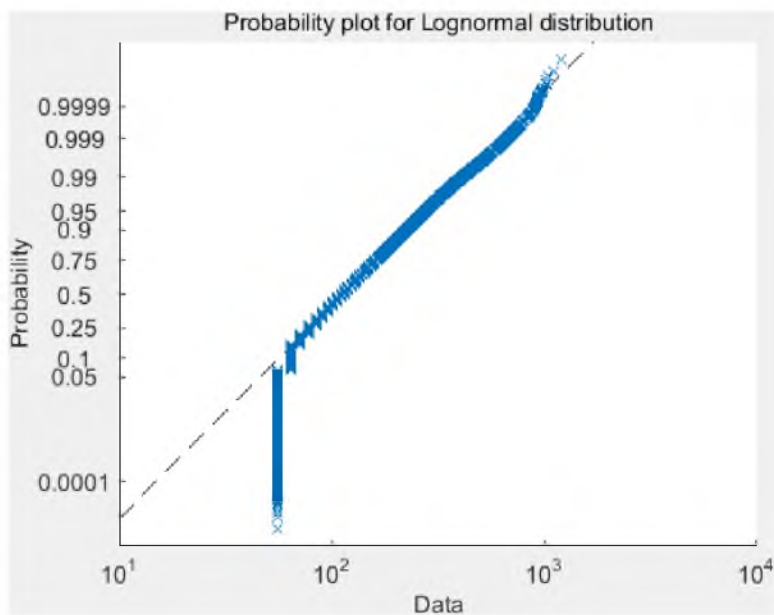


**Figure 4.35.** Drop diameter distribution comparison to a log-normal distribution. Water, L1G1-2,  $Re_g = 1,638$ .

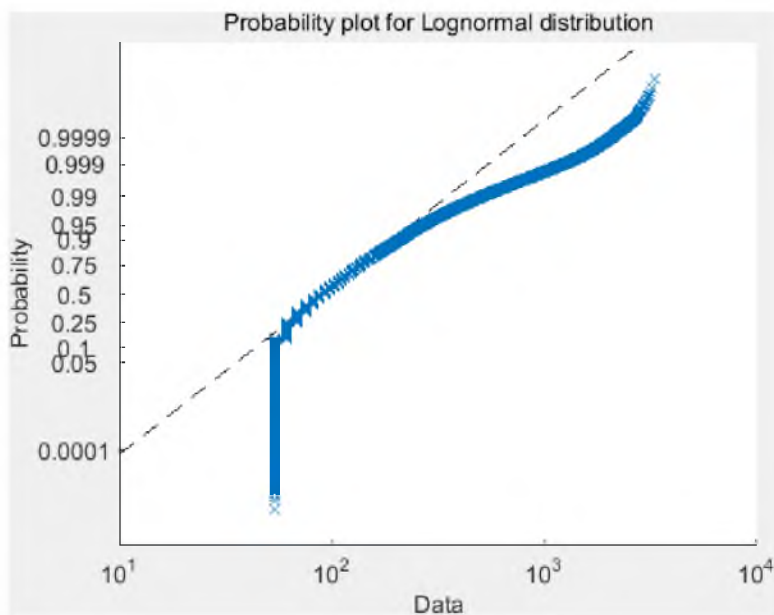


**Figure 4.36.** Drop diameter distribution comparison to a log-normal distribution. Water, L4G4-1,  $Re_g = 12,022$ .

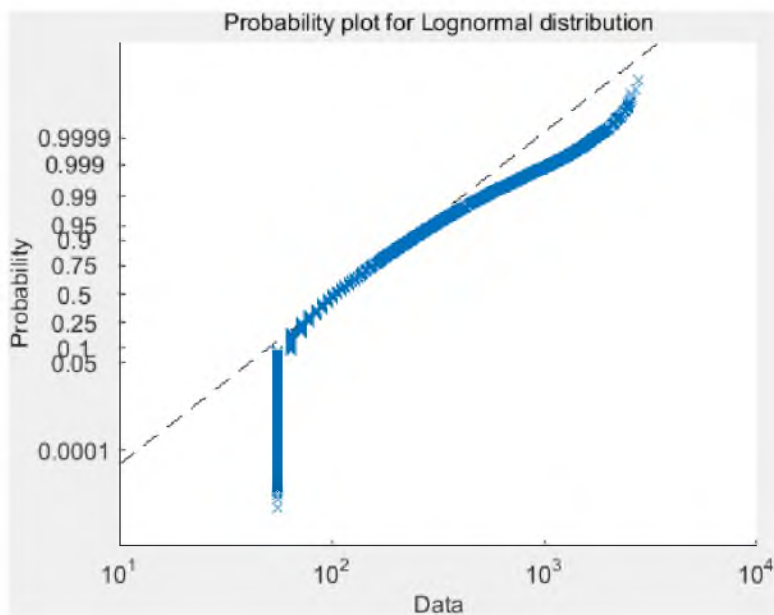


**Figure 4.37.** Drop diameter distribution comparison to a log-normal distribution. Water, L4G4-2,  $Re_g = 12,022$ .

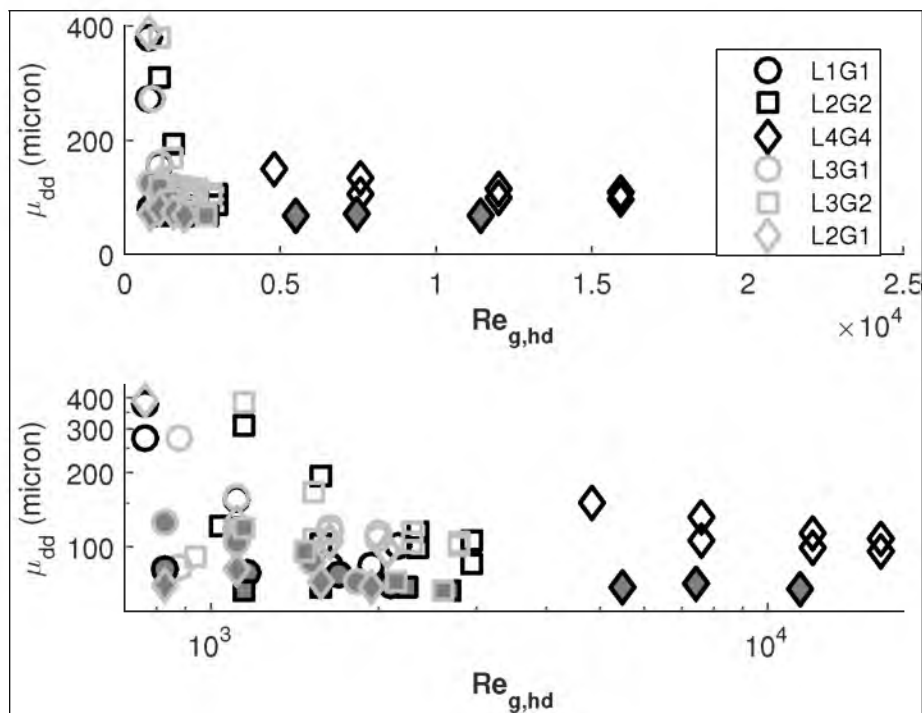


**Figure 4.38.**  $Re_{g,hd}$  versus the geometric mean drop diameter. Filled markers represent Silicone Oil A. All data. Dashed lines indicate similar tests and serve to better identify geometric trends between conditions.

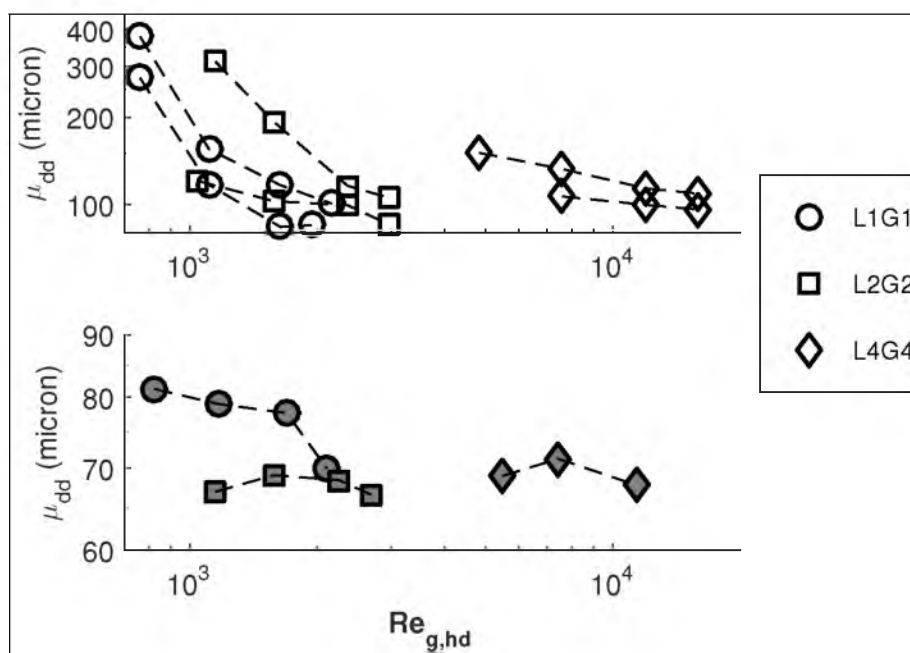


**Figure 4.39.**  $Re_{g,hd}$  versus the geometric mean drop diameter. Filled markers represent Silicone Oil A. Scale-able atomizers only. All have  $A_g/A_l \approx 6$ . Dashed lines indicate similar tests and serve to better identify geometric trends between conditions.

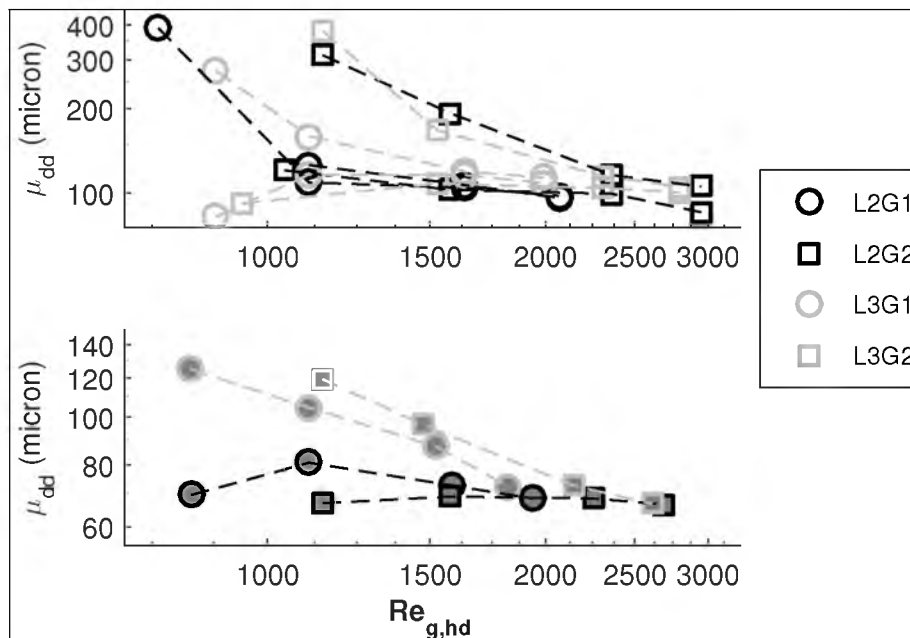


**Figure 4.40.**  $Re_{g,hd}$  versus the geometric mean drop diameter. Filled markers represent Silicone Oil A. Constant  $d_0$  by marker edge color, changing  $b$ . Dashed lines indicate similar tests and serve to better identify geometric trends between conditions.

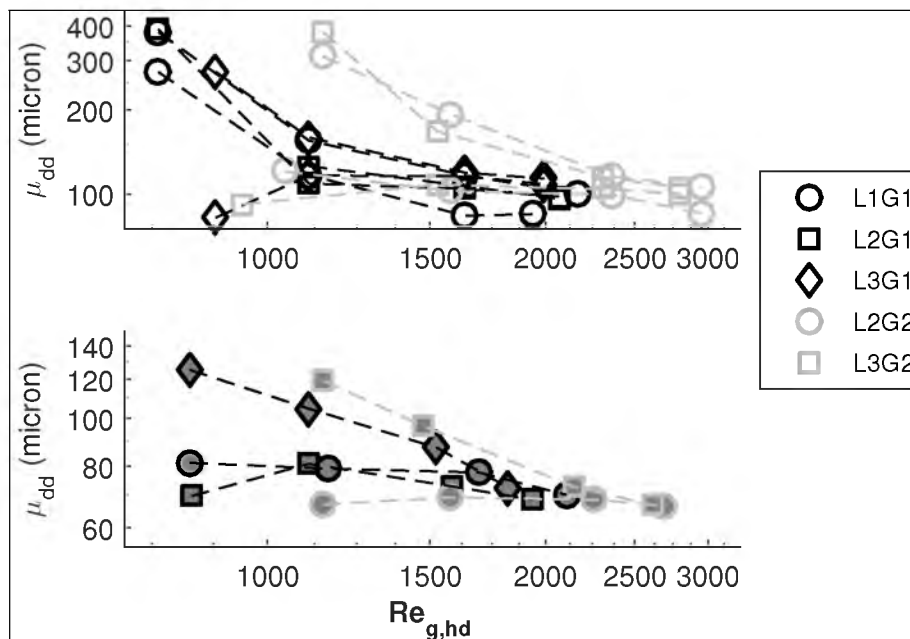


**Figure 4.41.**  $Re_{g,hd}$  versus the geometric mean drop diameter. Filled markers represent Silicone Oil A. Constant  $b$  by marker edge color, changing  $d_0$ . Dashed lines indicate similar tests and serve to better identify geometric trends between conditions.

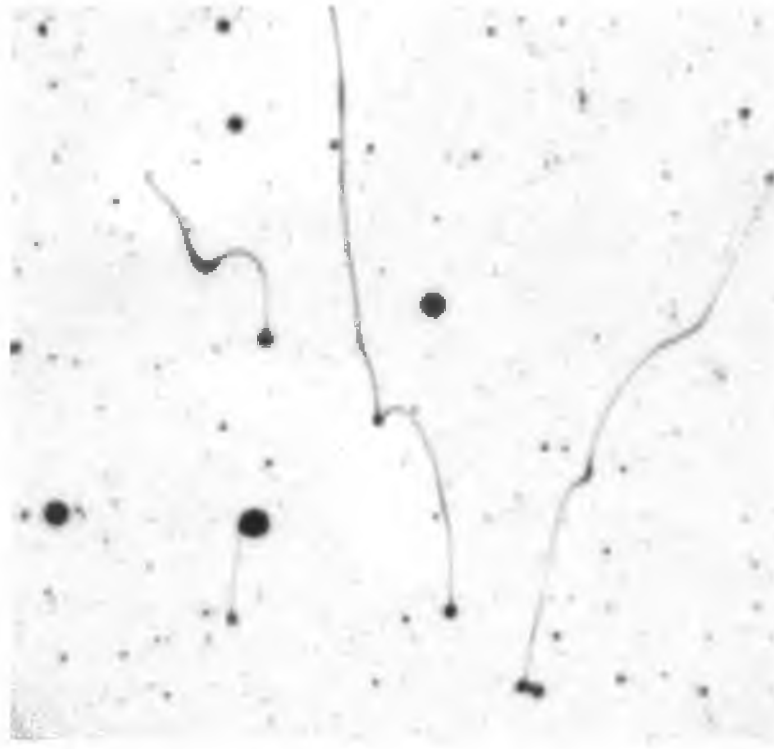


**Figure 4.42.** Downstream Silicone Oil A spray of L2G1 for  $M = 11.5$ .

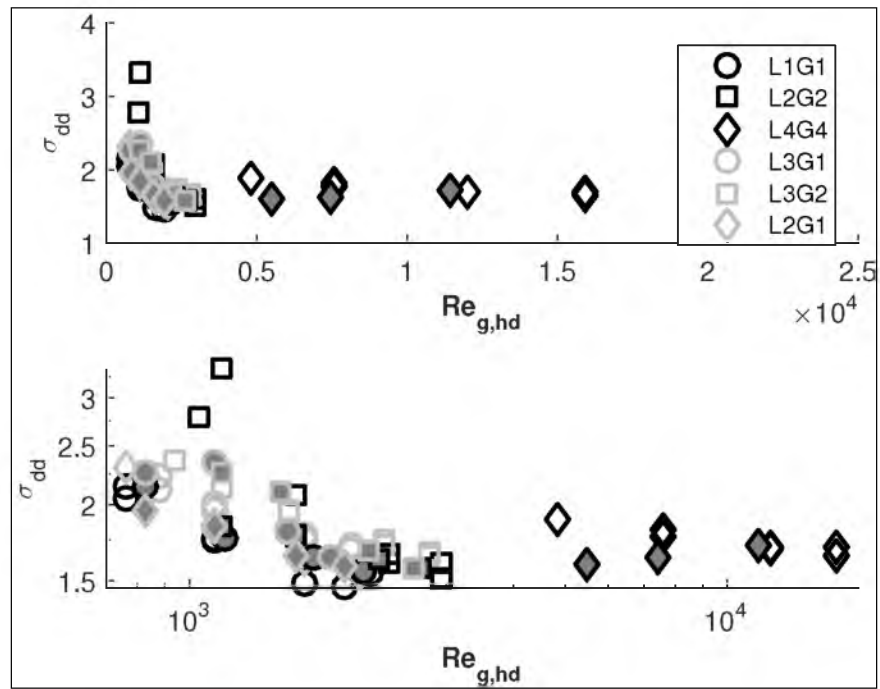


**Figure 4.43.**  $Re_{g,hd}$  versus the geometric standard deviation of the drop diameter. Filled markers represent Silicone Oil A. All data. Dashed lines indicate similar tests and serve to better identify geometric trends between conditions.

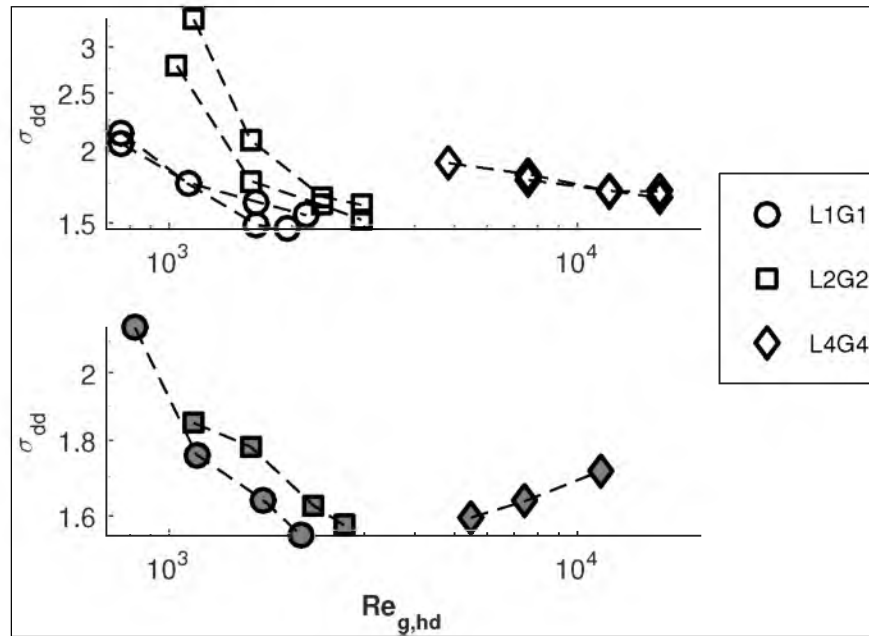


**Figure 4.44.**  $Re_{g,hd}$  versus the geometric standard deviation of the drop diameter. Filled markers represent Silicone Oil A. Scale-able atomizers only. All have  $A_g/A_t \approx 6$ . Dashed lines indicate similar tests and serve to better identify geometric trends between conditions.

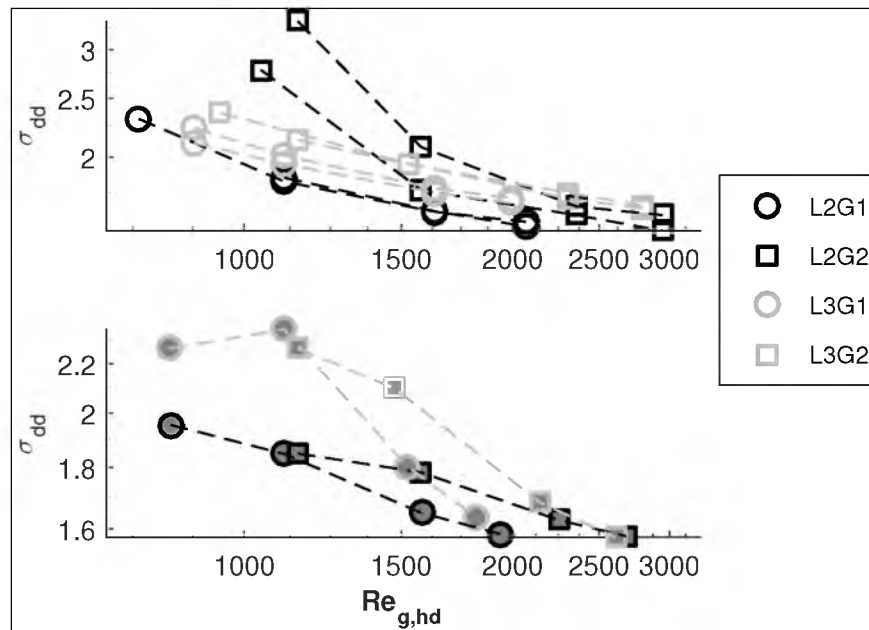


**Figure 4.45.**  $Re_{g,hd}$  versus the geometric standard deviation of the drop diameter. Filled markers represent Silicone Oil A. Constant  $d_0$  by marker edge color, changing  $b$ . Dashed lines indicate similar tests and serve to better identify geometric trends between conditions.

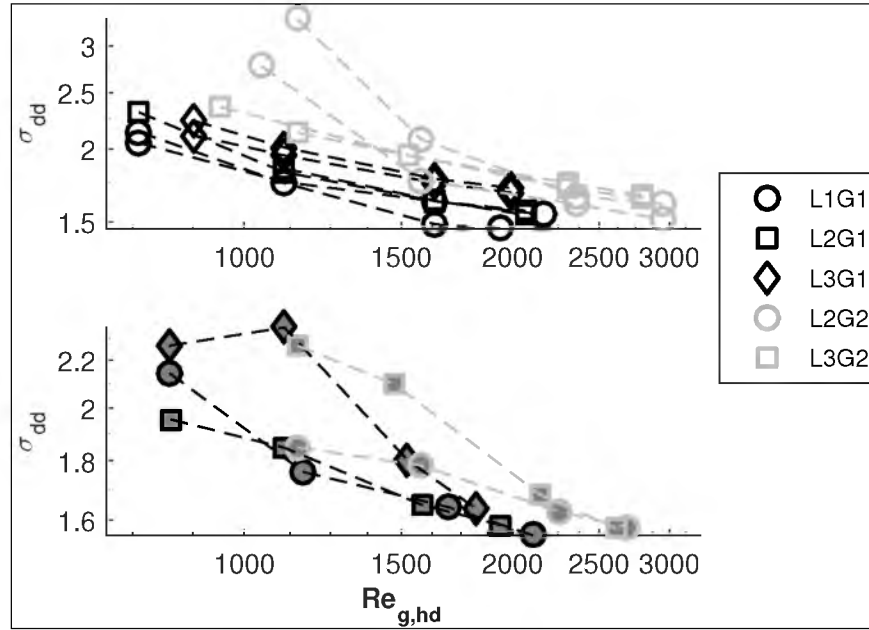


**Figure 4.46.**  $Re_{g,hd}$  versus the geometric standard deviation of the drop diameter. Filled markers represent Silicone Oil A. Constant  $b$  by marker edge color, changing  $d_0$ . Dashed lines indicate similar tests and serve to better identify geometric trends between conditions.

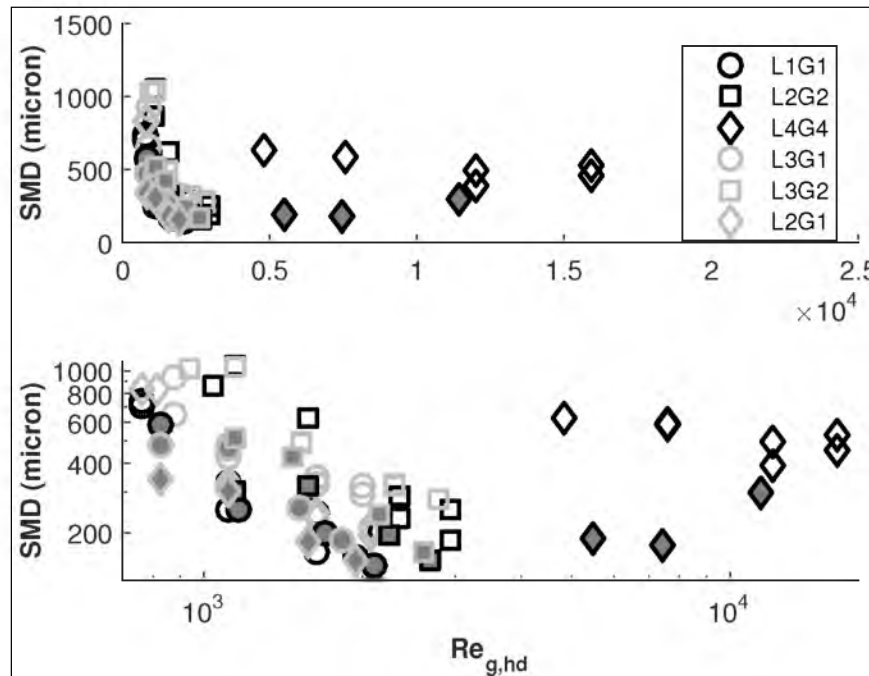


**Figure 4.47.**  $Re_{g,hd}$  versus the spray Sauter mean diameter. Filled markers represent Silicone Oil A. All data. Dashed lines indicate similar tests and serve to better identify geometric trends between conditions.

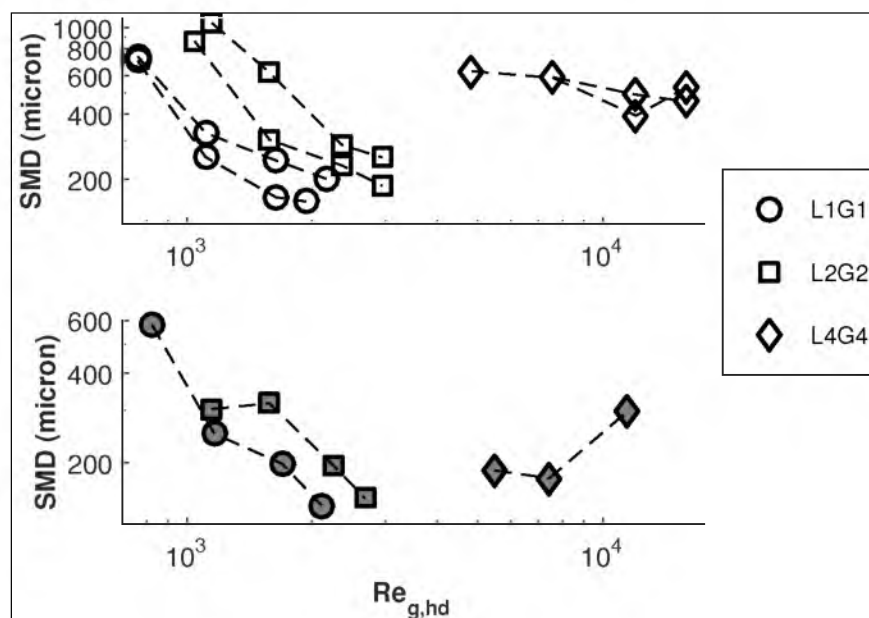


**Figure 4.48.**  $Re_{g,hd}$  versus the spray Sauter mean diameter. Filled markers represent Silicone Oil A. Scale-able atomizers only. All have  $A_g/A_l \approx 6$ . Dashed lines indicate similar tests and serve to better identify geometric trends between conditions.

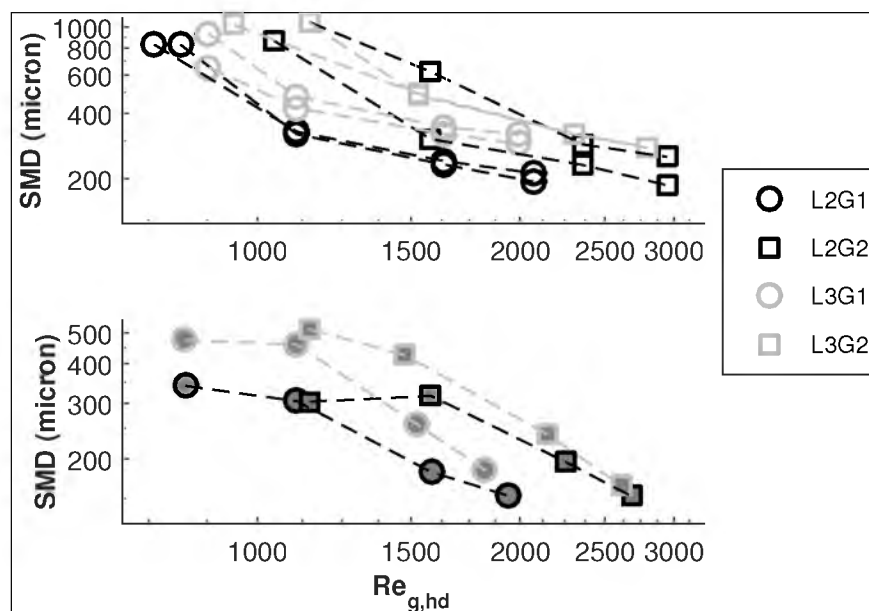


**Figure 4.49.**  $Re_{g,hd}$  versus the spray Sauter mean diameter. Filled markers represent Silicone Oil A. Constant  $d_0$  by marker edge color, changing  $b$ . Dashed lines indicate similar tests and serve to better identify geometric trends between conditions.

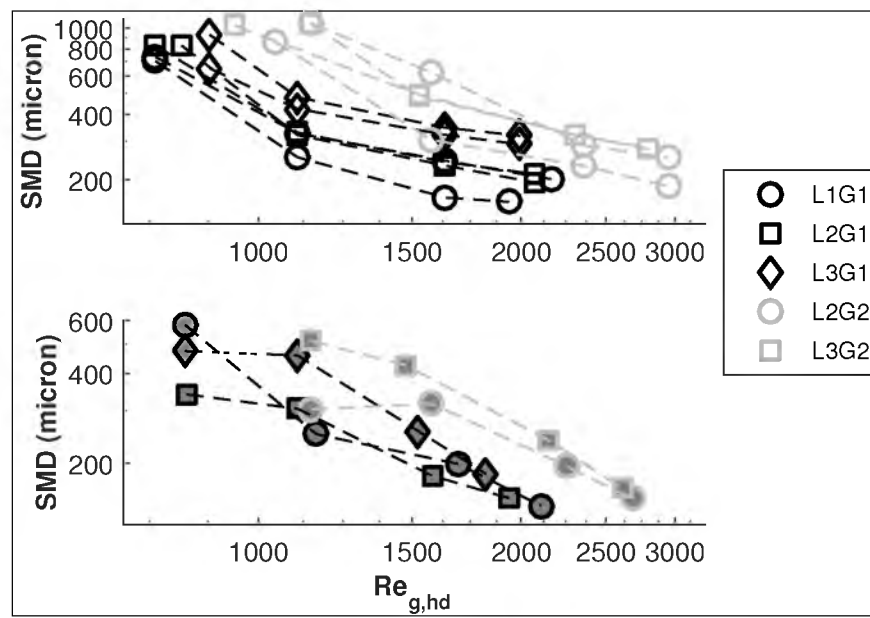


**Figure 4.50.**  $Re_{g,hd}$  versus the spray Sauter mean diameter. Filled markers represent Silicone Oil A. Constant  $b$  by marker edge color, changing  $d_0$ . Dashed lines indicate similar tests and serve to better identify geometric trends between conditions.

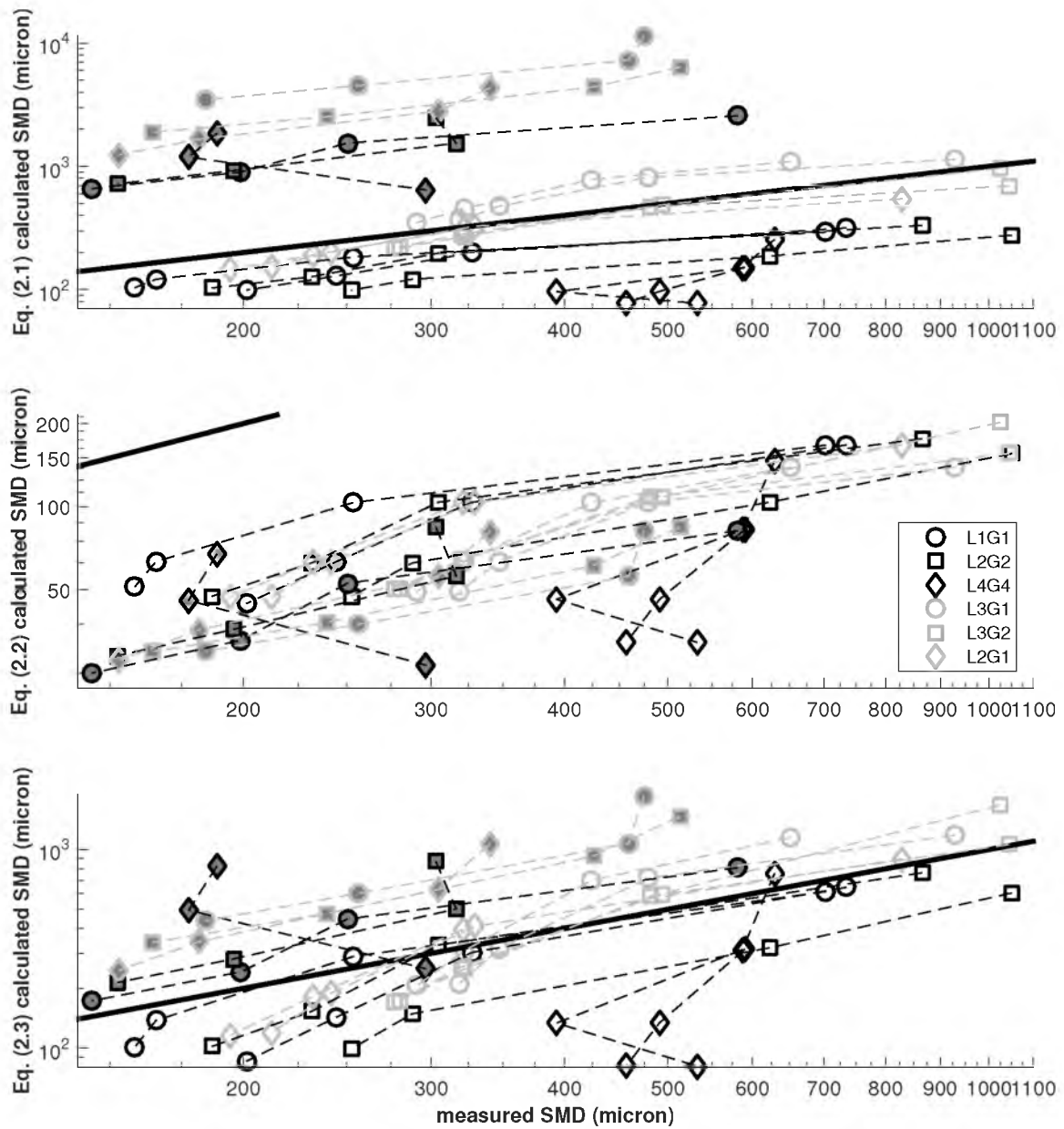


**Figure 4.51.** Measured drop SMDs versus calculated drop SMDs. Solid black line represents the one-to-one, where the measured and calculated values are identical.

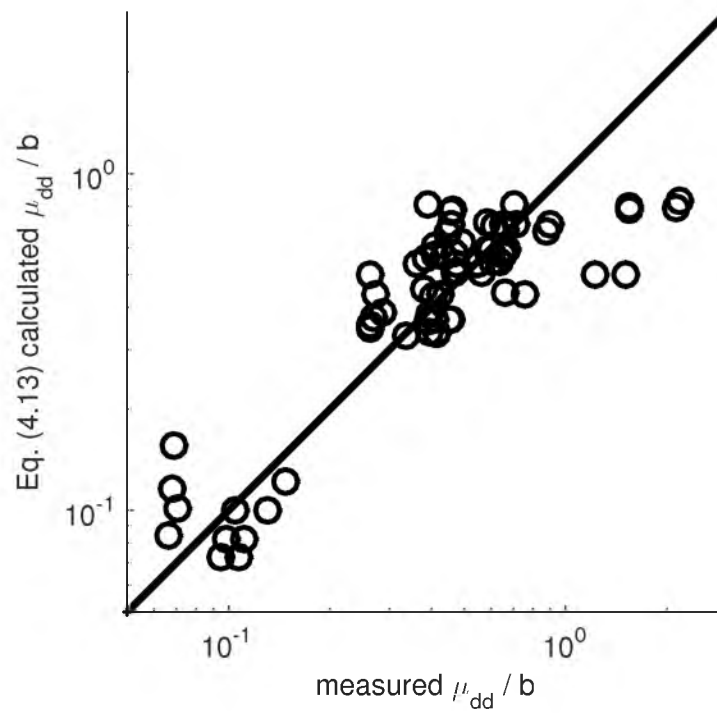


**Figure 4.52.**  $\mu_{dd}$  correlation comparison to measured values. Solid black line represents the one-to-one, where the measured and calculated values are identical.

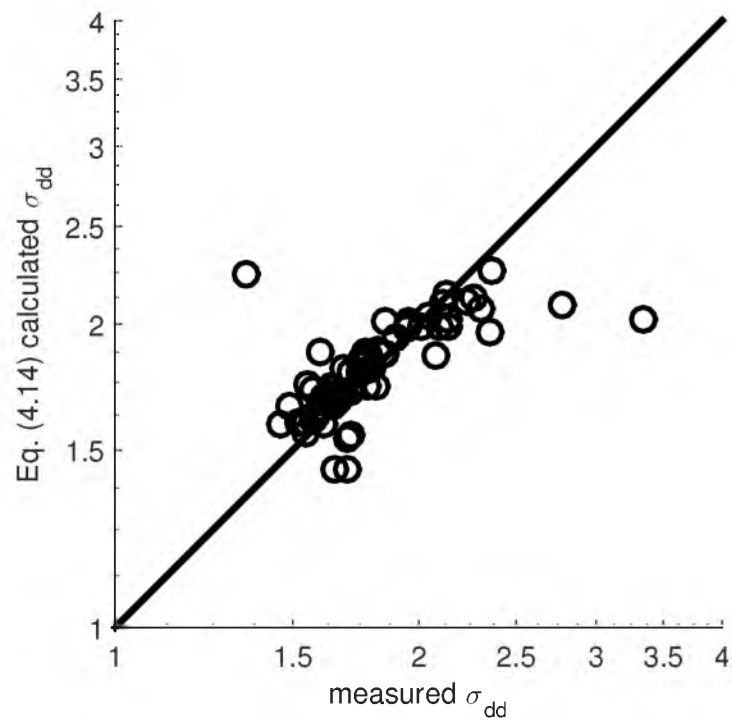


**Figure 4.53.**  $\sigma_{dd}$  correlation comparison to measured values. Solid black line represents the one-to-one, where the measured and calculated values are identical.

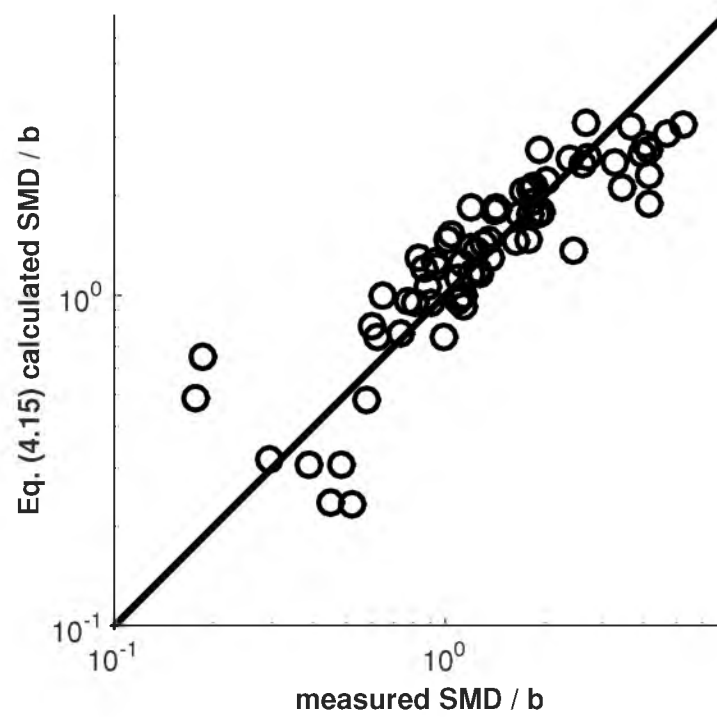


**Figure 4.54.** SMD correlation comparison to measured values. Solid black line represents the one-to-one, where the measured and calculated values are identical.

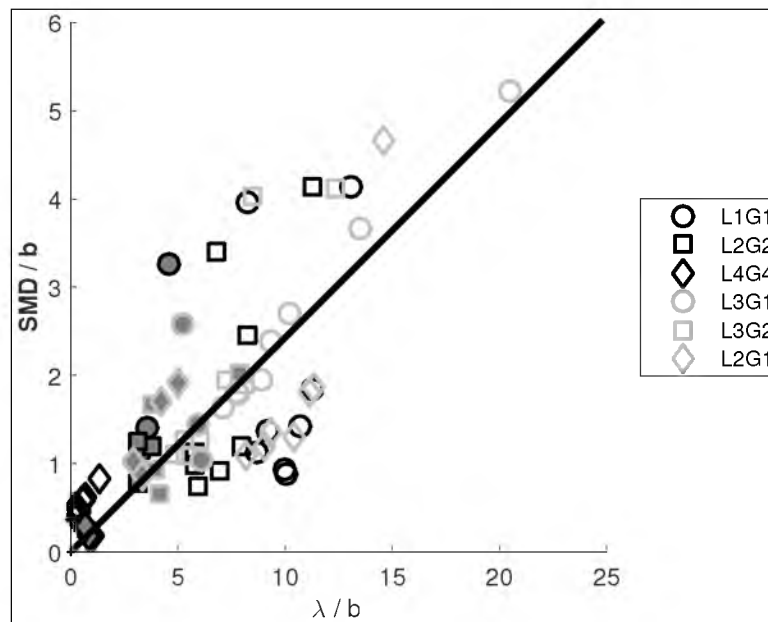


**Figure 4.55.**  $b$ -normalized primary wavelength versus the  $b$ -normalized spray Sauter mean diameter. Filled markers represent Silicone Oil A.

## CHAPTER 5

### ATOMIZER DESIGN SCOPING

#### 5.1 Introduction

Injector performance is important for gasification. An efficient injector design will provide the proper atomization of a coal-water slurry mixture so that the fuel can completely devolatilize into the gasification products. Improper injector design can lead to unreactant fuel and a loss in efficiency. An efficient injector will also ensure stable flame operation for the system [23].

The University of Utah operates a 1 ton/day pressurized, slurry-fed, oxygen-blown entrained-flow coal gasifier. During poorly-controlled operation, the temperature profile of an EFG can often be the opposite of what would be expected. If the flame from the injector is pushed too far into the reactor, a myriad of problems can occur. Downtime and repairs can be expected from problems such as excessive refractory erosion, erratic syngas composition, overheating of the EFG body, or others.

If the flame is pushed too far into the reactor, the cause can most likely be identified as the injector, assuming that feed flow rates are correct. The injector geometries might be such that the oxygen stream does not interact enough with the coal-water slurry stream to provide proper atomization at a distance that is not down inside the reactor. In order to determine which factors affect the position of the flame inside the EFG, several tests were performed involving injector settings, and hot and cold operation of the injector.

The goal in operating the gasifier is to acquire a thorough characterization of this particular EFG. By achieving some degree of repeatability, error will be able to be quantified in such a way to develop a working numerical model of the gasification process. The injector testing provides an important facet to this model. Because oxygen and coal-water slurry enter the EFG through the injector, the injector becomes a boundary condition defining the behavior of these two substances as they enter the EFG.

## 5.2 Theory

The nozzle used for testing directs the gas stream into the liquid stream as they exit the nozzle's tip. The gas stream velocity is orders of magnitude faster than the liquid stream. This velocity difference provides the energy needed for a thorough atomization of the liquid stream. However, as the droplets move away from the injector, they will begin to coalesce [113]. This type of atomization is known as gas-assist atomization because the high-velocity gas stream provides the energy to break apart the coal-water slurry [114].

Gas-assist atomization is enhanced in this injector due to design. Because the space that the gas stream flows through is decreased as it impinges on the liquid stream and exits the nozzle, the velocity of the gas stream is greatly increased by the Venturi effect. The increased velocity gives the stream a higher kinetic energy. This increase in kinetic energy provides better atomization. However, the increased velocity is at the expense of a pressure drop due to Bernoulli's principle. That fact is of little concern, as the fluids have reached their destination. In fact, this pressure drop is exploited to achieve the velocity increase and atomization.

## 5.3 Results

### 5.3.1 Cold-Flow Testing

Cold-flow analysis was performed on the injector in order to evaluate the spray profile of the various nozzles at various flow rates and pressure drops. The three factors that were evaluated during the cold-flow analysis were (1) the impingement angle, (2) the flow rates of oxygen and water, and (3) the pressure drop across the nozzle.

#### 5.3.1.1 Influence of Impingement Angle

Three nozzles were available for analysis. The angles of the three nozzles were 25°, 45°, and 65°. A schematic of the 45° nozzle is shown in Figure 3.3. For evaluating the effect of the impingement angle, each nozzle was run at a set flow rate (corresponding to the appropriate flow rates into the EFG at 4.5 bara, 65 psia) and pressure drop. For the case shown in Figure 5.1, the air pressure drop chosen was 1.4 bar (20 psi). The nozzle resulting spray profile was photographed, and the nozzle was changed out.

Figure 5.1 shows a comparison of the three nozzles operating at the same pressure drop and flow rates (air and water). The 45° and 65° nozzles had similar spray patterns, while the 25° nozzle produced a notably narrower spray. The bulk spray from each nozzle is highlighted by the dark blue lines that encapsulate the majority of the spray. Both the 65° nozzle and the 45° nozzle have a somewhat uniform fine mist surrounding the bulk spray

as shown by the mist outside of the blue lines. The 25° nozzle produced larger droplets in addition to the fine mist, presumably due to less aggressive atomization due to the shallower impingement angle. The streams of mist coming from the 65° nozzle appear to be fairly controlled. They appear to be symmetric around the bulk spray, and careful inspection of the photographs indicates that the streams of mist have the same relative size water drop on each side of the bulk spray. The streams of mist coming from the 45° nozzle also appear to be symmetric with slightly more diversity in the droplet size. The 25° nozzle seems to randomly scatter water droplets, and the droplets do not appear to be any constant size.

The green grid shown in Figure 5.1 is in place to gauge the dimensions of the water plume. Each green square represents an area that is approximately 1.27 cm (0.5 in) by 1.27 cm (0.5 in). The width of each nozzle is 2.54 cm (1.0 in). The plume from the 65° nozzle travels approximately 7 cm (2.75 in) to achieve a width of approximately 1.91 cm (0.75 in). This gives the plume from the 65° nozzle an angle of approximately 15.5° from one blue line to the other. The plume from the 45° nozzle achieves a width of approximately 2.41 cm (0.95 in) over the same distance. This gives the plume from the 45° nozzle an angle of approximately 19.6°. The plume from the 25° nozzle achieves a width of approximately 0.76 cm (0.30 in) at the same distance from the nozzle. This gives the plume from the 25° nozzle an angle of approximately 6.2°. It should be noted that the spray angle for coal-water slurry atomization will be larger than that of water atomization [115]. The water spray angles comparisons are useful to determine the change due to impingement angle, but the spray angle will not be the same for coal-water slurry atomization in the EFG [115].

Each nozzle's spray profile appears to have a pinch point or neck just below the exit point of the injector. The smallest neck of the three nozzles is in the spray profile from the 25° nozzle. The next smallest neck is from the 65° nozzle. The largest neck is from the 45° nozzle. This is surprising. One would expect that as the angle of the nozzle increased, the resulting spray profile's neck would decrease from the higher radial momentum of the gas stream. The 45° nozzle appears to be the median at which the impacting air streams and water stream maintain the proper balance that gives a large neck in the spray profile. The sharp angle of impingement on the 65° nozzle inherently creates the small neck in its spray profile. The neck in the 25° nozzles spray profile is far less pronounced than the other two nozzles because the impingement angle is less normal to the water stream.

### 5.3.1.2 Influence of Flow Rates

The gas and liquid flow rates were also evaluated. The injector's spray profile was evaluated at flow rates corresponding to the appropriate flow rates into the EFG at pressures

ranging from 1 bara (15 psia) to 7.9 bara (115 psia). These flow rates are calculated based on some assumptions. The assumptions are that the product gas flow has a residence time of five seconds, the coal-water slurry is 60 weight percent solids, the stoichiometric ratio is 0.6, and that the EFG is operating at 1400°C (2600°F). For evaluating the effect of flow rate, a nozzle and a pressure drop were chosen. In the case shown in Figure 5.2, the 45° nozzle and a 2.8 bar (40 psi) air pressure drop were chosen. The flow rates were then set. The resulting spray profile was photographed, and the flow rates were changed.

Figure 5.2 shows a comparison of two nozzles operating with different flow rates. Both nozzles are the 45° nozzles. Both nozzles have an air pressure drop of 2.8 bar (40 psi). The flow rates of water and air in the photograph on the left correspond to an EFG system pressure of 1.7 bara (25 psia). The flow rates of the nozzle on the right correspond to an EFG system pressure of 7.9 bara (115 psia). There does not appear to be many differences between the two nozzles. The higher flow rates of the nozzle on the right are apparent in the increased density of water droplets shown in Figure 5.2. However, the size of the water droplets coming from the left injector appears to be approximately the same as the water droplets coming from the right injector. The gap width between the nozzle and the inner water tube is larger for the injector on the right than that of the injector on the left. Without changing that gap width, a flow rate increase alone would increase the air pressure drop across the nozzle. Therefore, in order to maintain the 2.8 bar (40 psi) air pressure drop, the gap width must be increased to allow more through flow.

The angles of the water plumes from each nozzle in Figure 5.2 appear to have the same angle. There seems to be no noticeable difference between the spray profiles when the flow rates are increased. Of course, EFG operation would surely change with the increase flow rate as residence time of the resulting syngas would change. This could lead a different syngas composition. Considering the cold-flow testing, the only difference between the two flow rates is the operational change of increasing the gap width of the injector to maintain the same air pressure drop.

### 5.3.1.3 Influence of Pressure Drop

The influence of pressure drop across the nozzle was also evaluated. The injector's spray profile was evaluated at pressure drops of 0.7 bar (10 psi), 1.4 bar (20 psi), 2.1 bar (30 psi), 2.8 bar (40 psi), and 3.5 bar (50 psi). For evaluating each pressure drop, a nozzle was chosen and the water and air flow rates were set (corresponding to the appropriate flow rates into the EFG at 4.5 bara, 65 psia). In the case shown in Figure 5.2, the 45° nozzle was chosen. In Figure 5.3, a comparison is shown between a 25° nozzle operating at a 0.7 bar (10 psi)

drop and the same nozzle operating at a 3.5 bar (50 psi) drop. The resulting spray profile was photographed, and the pressure drop was changed.

By increasing the pressure drop across a nozzle, a noticeable change occurs. The spray profile on the left, 0.7 bar (10 psi) drop, of Figure 5.3 appears to contain much larger water droplets than that of the spray profile on the right, 3.5 bar (50 psi) drop. The spray profile on the right, 3.5 bar (50 psi) drop, appears to be more forceful, or the overall velocity of the spray appears larger. The angles of the plumes appear to be the same for both pressure drops. However, the higher pressure drop, 3.5 bar (50 psi) drop, appears to produce fewer large droplets surrounding the bulk spray.

As described above, the pressure drop is increased across the nozzle by decreasing the size of the annulus that the air flows through. This decrease in size and corresponding increase in pressure create an increase in velocity at the nozzle's exit. This velocity increase is the cause of the smaller water droplets coming from the left injector shown in Figure 5.3. The increased velocity provides a higher kinetic energy that shears the water droplets from the water stream coming from the injector. The large droplets shown on the left of Figure 5.3 are due to smaller velocities of air, and thus, a smaller shearing kinetic energy.

### 5.3.2 Entrained-Flow Gasifier Reactor Operation

In addition to the cold-flow testing, the operation of the EFG was analyzed with various injector settings. The 65° nozzle and 45° nozzle were both used. Also, the pressure drop across the injector was varied from approximately 0.7 bar (10 psi) to 2.1 bar (30 psi) at 0.7 bar (10 psi) intervals. To evaluate the effect the injector settings had, the resulting temperature profile and syngas composition were analyzed. The coal slurry contained 56% pulverized coal by weight and was fed at 20 kg/hr. The oxygen flow rate during testing was approximately 15 kg/hr.

The pressure drop with respect to time is shown in Figure 5.4 for the first day of testing on the EFG. The temperature profiles from the five thermocouples in the reaction zone are shown with respect to time in Figure 5.5. The syngas composition for each pressure drop is shown in Table 5.1. Figure 5.4, Figure 5.5, and Table 5.1 all are the result of the 45° nozzle.

The oxygen pressure drop is shown in Figure 5.4 for the EFG testing with the 45° nozzle. Three distinct pressure drops were targeted: 2.1 bar (30 psi), 1.4 bar (20 psi), and 0.7 bar (10 psi). As seen on the right in Figure 5.4, an oxygen pressure drop of 0.7 bar (10 psi) was not achievable, so 0.8 bar (12 psi) was targeted instead. The respective oxygen pressure drops were maintained for an average of 35 minutes. This amount of time is not enough to

ensure the EFG has reached an operational equilibrium. However, a general trend can be made by looking at the decreasing oxygen pressure drop over time.

Figure 5.5 shows the average temperature profile throughout the reaction zone of the EFG for testing with the 45° nozzle for injector oxygen pressure drops of 2.1 bar (30 psi), 1.4 bar (20 psi), and 0.8 bar (12 psi). The temperature of every thermocouple increased as the pressure drop decreased, with the exception of TC4.

Figure 5.5 shows the temperatures generally increasing with the decreasing oxygen pressure drop. The time allowed for each respective pressure drop was not adequate to allow the EFG to completely reach equilibrium. However, the data show the temperature increasing with the decreasing pressure drop. The flame is thought to be closest to TC2 for all pressure drops shown in Figure 5.5. It was thought that the flame position might change as the pressure drop was changed, but this was not observed.

Table 5.1 shows the average syngas composition for each targeted pressure drop during EFG testing with the 45° nozzle. The carbon monoxide and hydrogen appear to change proportionally to the pressure drop, whereas the carbon dioxide appears to be inversely proportional. The decrease in pressure drop worsens the degree to which the coal slurry is atomized (see Figure 5.3), likely allowing some of the slurry to fall through the EFG without reacting and resulting in an effecting increase in the oxygen/fuel ratio. This would explain the slight increase in CO<sub>2</sub> at the expense of CO in Table 5.1 and the slight increase in temperature shown in Figure 5.5.

During the second day of testing, the 65° was not used. Figure 5.6 shows the pressure drop with respect to time for the second day of testing on the EFG. Figure 5.7 shows the temperature profiles from the five thermocouples in the reaction zone. Table 5.2 shows the syngas composition. Figure 5.6, Figure 5.7, and Table 5.2 are all the result of the 65° nozzle.

The oxygen pressure drop is shown in Figure 5.6 for the EFG testing with the 65° nozzle. Three distinct pressure drops were targeted: 2.1 bar (30 psi), 1.4 bar (20 psi), and 0.7 bar (10 psi). As seen on the right in Figure 5.6, an oxygen pressure drop of 0.7 bar (10 psi) was not achievable, so 1.0 bar (15 psi) was targeted instead. The respective oxygen pressure drops were maintained for an average of 36 minutes. This amount of time is not enough to ensure the EFG has reached an operational equilibrium. However, a general trend can be made by looking at the decreasing oxygen pressure drop over time.

Figure 5.7 shows the average temperature profiles throughout the reaction zone of the EFG for testing with the 65° nozzle for injector oxygen pressure drops of 2.1 bar (30 psi), 1.4 bar (20 psi), and 1.1 bar (15 psi). The temperature of every thermocouple increased as the pressure drop decreased.

As seen in Figure 5.7, performance versus pressure drop was similar to that observed on day one with the 45° nozzle. TC2 indicated the highest temperature, and temperatures overall increased with decreasing pressure drop.

Table 5.2 shows the average syngas composition for each targeted pressure drop during EFG testing with the 65° nozzle. The carbon monoxide and hydrogen increase with pressure drop while CO<sub>2</sub> is highest at the lowest pressure drop. As with the 45° nozzle, the suspicion is that low pressure drops result in poor atomization, allowing more of the fuel to pass through the reactor without reacting, resulting in an effective increase of the oxygen/fuel ratio.

Comparing the cold-flow and gasification tests, there are notable similarities, such as the worse atomization that results at low oxygen pressure drops. One must be cautious drawing too many conclusions, as there is a definite physical difference between water and coal-water slurry. The coal-water slurry has significantly different rheological properties, most notably viscosity and surface tension [116]. The coal-water slurry requires much more energy to thoroughly atomize. The spray from coal slurry will have a larger spray angle than that of just water. The drop size from coal slurry atomization will be larger than that of water with the same injector conditions. Considering the fact that coal-water slurry requires much more energy to thoroughly atomize than water and considering that lower pressure drops seem to favor combustion more than higher pressure drops, it is not difficult to deduce that a lower limit exists for efficient pressure drop over an injector nozzle during gasification.

Figure 5.1, shows a comparison of the 65° nozzle, the 45° nozzle, and the 25° nozzle. Theoretically, the 25° nozzle provides a much higher axial velocity. This high velocity could be enough to cause some of the coal-water slurry to rapidly flow through the reaction zone without fully undergoing conversion.

By quantifying droplet size, the degree of atomization for each injector setting can be quantified numerically instead of visually. By making the injector tubes more concentric, an easily repeatable spray pattern is possible. Also, an idea of the quench water contents would help in re-affirming the results shown from these preliminary tests. If any unreactant coal is found in the quench water, a lower limit on oxygen pressure drop and impingement angle can be set. A method of sampling the quench bath, or dumping it completely, would have to be established to allow a check for coal while the EFG is idling at atmospheric pressure.

## 5.4 Conclusions

By performing cold-flow tests with the coal slurry injector, a good visualization of the resulting atomized water plume was established. This allowed for a better understanding of

what is happening inside the EFG during operation, despite a coal slurry spray being wider than a water spray. The change in spray characteristics with changes in injector factors was able to be seen. By making changes to the injector, operation of the EFG can hopefully be improved and optimized.

The gasification products, CO and H<sub>2</sub>, were increased by both a higher impingement angle and a higher oxygen pressure drop across the nozzle. From the cold-flow testing, it was shown that these factors (high impingement angle and high gas pressure drop) both provide a more complete atomization per visual analysis. This suggests that by increasing the impingement angle and oxygen pressure drop, the coal-slurry was able to more thoroughly devolatilize in the EFG, although the water spray and coal slurry spray will behave differently.

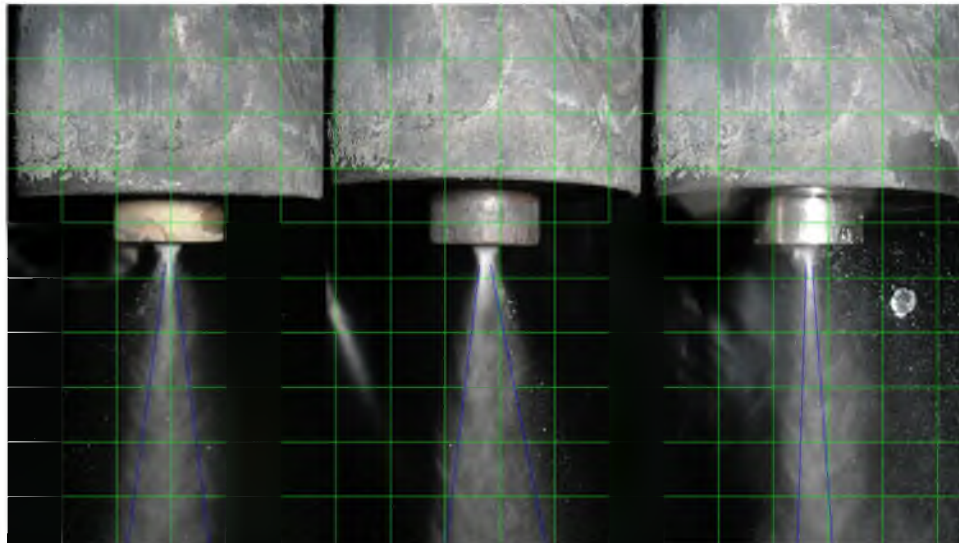


**Figure 5.1.** The injector on the left has the 65° nozzle. The injector in the middle has the 45° nozzle. The injector on the right has the 25° nozzle. Each green square represents an area that is approximately 1.27 cm (0.5 in) by 1.27 cm (0.5 in).

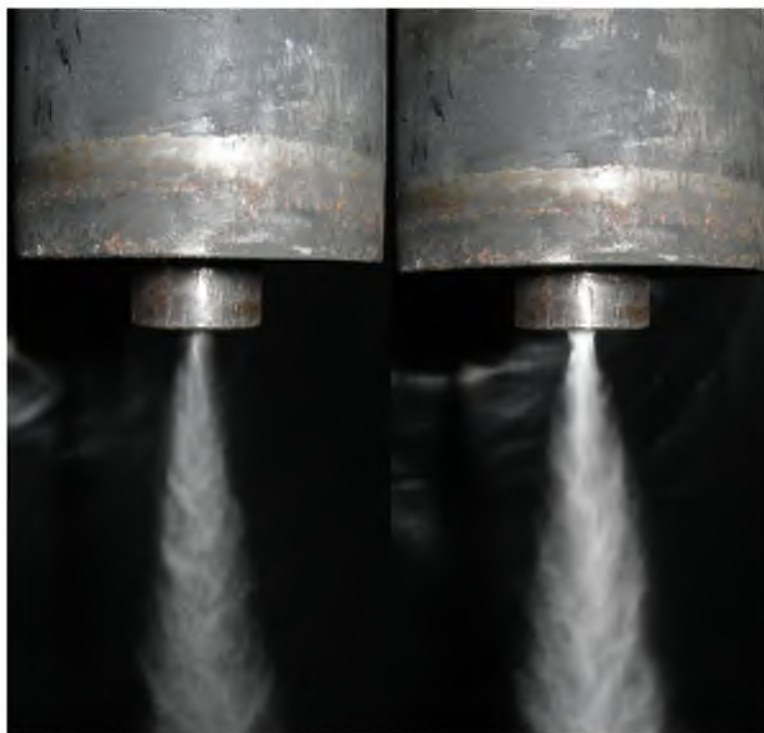


**Figure 5.2.** Both injectors have the 45° nozzle. The injector on the left has a flow rate corresponding to an EFG system pressure of 1.7 bara (25 psia). The injector on the right has a flow rate corresponding to an EFG system pressure of 7.9 bara (115 psia). Both injectors are operating at a 2.8 bar (40 psi) air pressure drop.

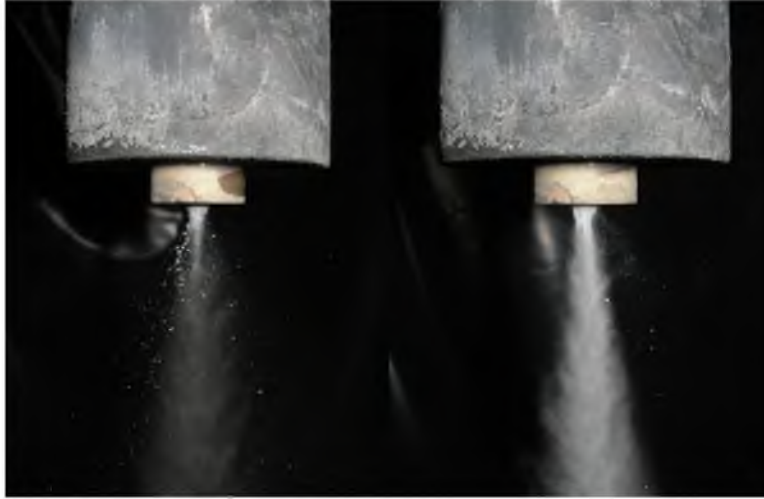


**Figure 5.3.** Both injectors shown have the 65° nozzle. The injector on the left is operating at a 0.7 bar (10 psi) pressure drop, whereas the injector on the right is operating at a 3.5 bar (50 psi) pressure drop. Water and air flows are the same for both cases.

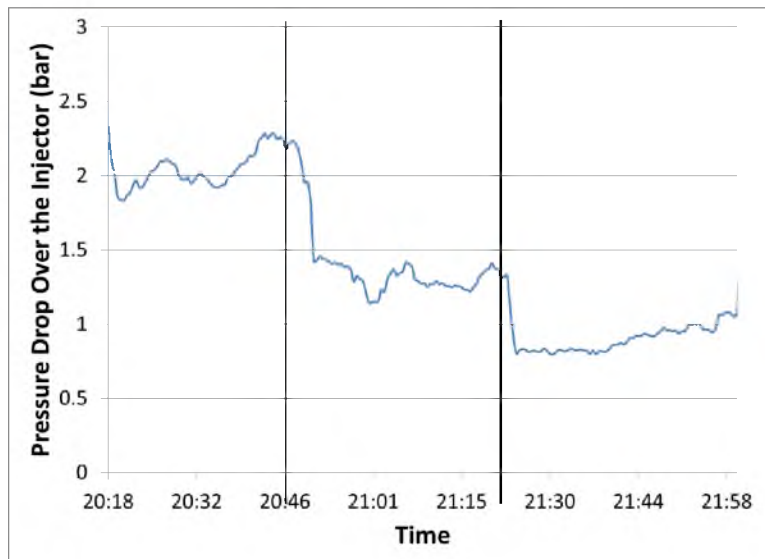


**Figure 5.4.** Oxygen pressure drop over the injector versus time.

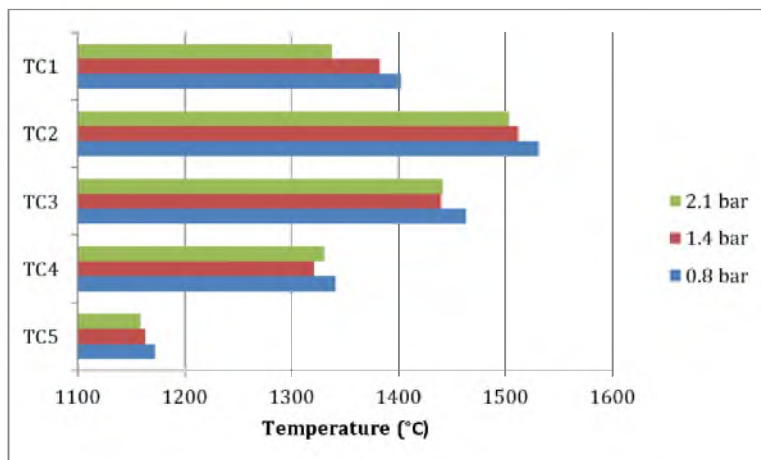


**Figure 5.5.** Reactor temperature profiles during operation with the 45° nozzle at specific injector oxygen pressure drops. The thermocouples are numbered in order of their position from the top of the reaction zone, so TC1 is closest to the injector and TC5 is furthest away. The thermocouples are 29 cm (11 in) from the adjacent thermocouple.

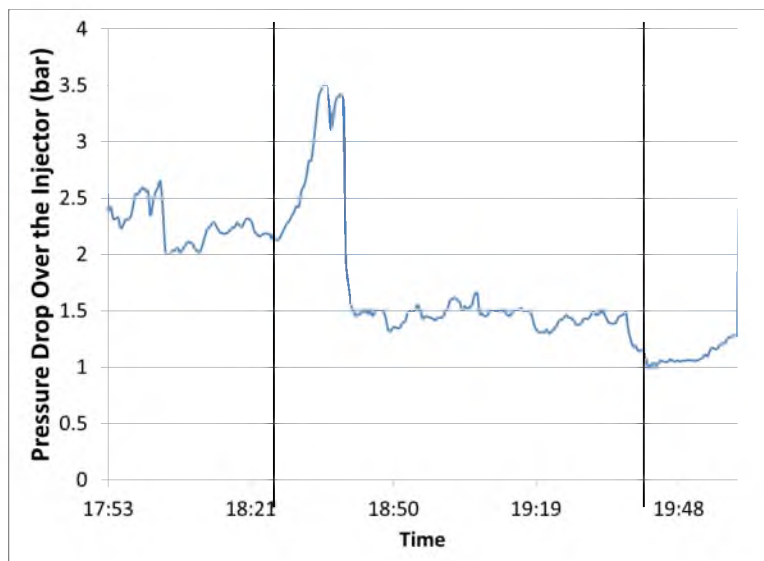


**Figure 5.6.** Oxygen pressure drop over the injector during the second day of testing.

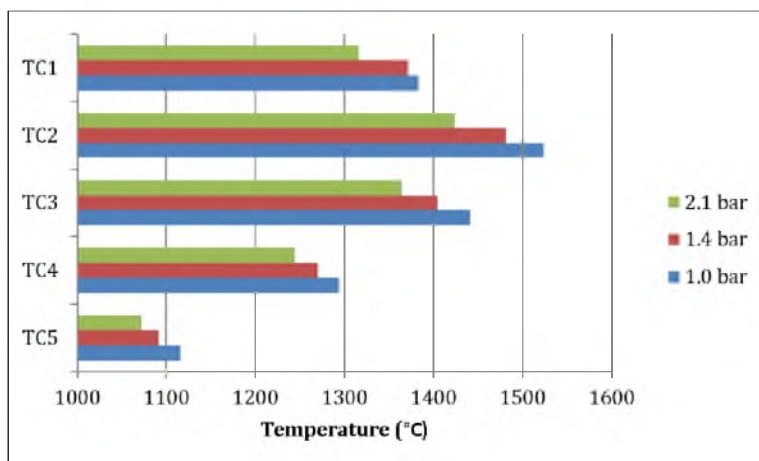


**Figure 5.7.** Reactor temperature profiles during operation with the 65° nozzle at specific injector oxygen pressure drops. The thermocouples are numbered in order of their position from the top of the reaction zone, so TC1 is closest to the injector and TC5 is furthest away. The thermocouples are 29 cm (11 in) from the adjacent thermocouple.

**Table 5.1.** Syngas composition (mol %, dry, normalized nitrogen-free) from EFG testing on 8/18/10.

Pressure Drop, bar (psi)	H <sub>2</sub>	CO	CO <sub>2</sub>
0.8 (12)	25.9%	35.7%	38.2%
1.4 (20)	27.1%	37.3%	35.4%
2.1 (30)	27.9%	38.3%	33.6%

**Table 5.2.** Syngas composition (mol %, dry, normalized nitrogen-free) from EFG testing on 8/19/10.

Pressure Drop, bar (psi)	H <sub>2</sub>	CO	CO <sub>2</sub>
1.0 (12)	27.8%	39.7%	32.4%
1.4 (20)	28.6%	40.3%	30.9%
2.1 (30)	30.0%	41.5%	28.3%

## CHAPTER 6

### ITERATING PILOT-SCALE ATOMIZERS

#### 6.1 Introduction

The University of Utah operates a 1 ton/day slurry-fed, oxygen-blown, pressurized, entrained flow gasifier (EFG). These systems have many input variables that will effect operation (fuel type, fuel slurry solids loading, test conditions), but during operation, there are typically only two inputs that can be changed, oxygen flow and fuel slurry flow. These feeds are often set by the test conditions being explored, so improvements in operation are often left to improvements in atomization.

#### 6.2 Theory

Slurries, or solid fuel suspensions, often have unique rheological properties, as the solid loading of the suspensions is often maximized so as to increase the energy density. These highly loaded suspensions exhibit shear dependent behavior, and the shear rate imposed within an atomizer has been shown to be as high as  $10^4$  to  $10^5$   $\text{s}^{-1}$  [117]. Atomization quality has been shown to be inversely proportional to the viscosity of the suspension [118], so knowing the viscosity of a suspension being used can help explain the spray atomization quality. Suspension viscosity has been shown to be a function of solid concentration, solid average particle size, and the physiochemical properties associated with the fuel [119–121]. Typically, decreasing the average particle size leads to an increase in viscosity, and an increase in solid loading increases the viscosity. Roh et al. [119] suggest that the more hydrophobic a fuel particle is, the lower the viscosity will be for comparably high solids loadings. Fuel suspensions have been shown to have a minimum viscosity at maximum solids loading if the particle size distribution is set to provide the maximum bulk density [122].

These rheological data are presented to offer a benchmark for spray behavior. The details for why certain suspensions have certain rheological properties were not evaluated, yet certain trends can be identified from both the literature and the experimental results. The relevant physiochemical properties of the fuels explored herein are not available. Additionally, all

the fuels explored are preground and no attempt to change the solid particle distribution to meet the maximum bulk density was made. The particle size distributions reported are representative of those making up the slurries fed to the University of Utah's entrained flow gasifier.

A good primer on the experimental work done on two-stream airblast atomizers (and most other atomizer types) can be found in Lefebvre [34]. While the liquids being explored in the studies summarized in Lefebvre [34] do not typically include fuel suspensions, a wide range of pure liquids are covered, and some discussion is given towards non-Newtonian liquid atomization. There is some work done on the atomization of suspensions and non-Newtonian liquids [77, 79, 115, 121, 123, 124], but only a few studies used an externally mixed, two-stream atomizer [72, 125–127]. Spray characteristics are often tied to the air-to-fuel ratio (AFR), which can also be thought of as the air-to-liquid ratio. The AFR is typically set on a mass basis, which does not account for atomizer geometry and the resulting velocities of each specific feed. The spray Sauter Mean Diameter (SMD) has been shown to decrease with an increase in the AFR [121, 128]. The area of highest mass flux of a coal-water suspension spray was shown to decrease with an increase in the AFR. There are not clear distinctions for the behavior of the drop size distribution for changing flow rates or liquid properties. Many definitions of the drop size distribution exist, and often, they differ from one study to the next. Some common mathematical and empirical distribution functions are the normal, log-normal, Nukiyama-Tanasawa [59], Rosin-Rammler [129], and upper-limit distributions [34].

Atomizer design can dictate whether gasifier performance sinks or swims. It has been shown to have a significant effect of both combustion and gasification systems [4, 117, 130]. The slurried fuel needs to be atomized into sufficiently small droplets to allow complete evaporation of the water along with conversion of carbon from solid to gas before the droplets impact on the reactor walls or leave the reaction zone [20]. In-situ (high-pressure, high-temperature) spray characteristics are more difficult to come by, so ex-situ characterization has to be performed and translated as best as possible.

## 6.3 Results

### 6.3.1 Rheology

The liquids evaluated in this study are listed in Table 6.1. For comparison, the particle size distribution as a function of weight and surface area is given in Figure 6.1. Assumptions about the fuel particles sphericity and density were made in calculating the surface area

averaged particle diameter in Table 6.1 and the surface area fractions listed in Figure 6.1.

I evaluated the shear dependent viscosity for all of the suspensions evaluated with PSV in order to see how they behave relative to one another. The suspensions evaluated were listed in Table 6.1. These suspensions were evaluated using the viscometer described in the Experimental section. The shear rate dependent viscosities of the suspensions evaluated are shown in Figure 6.2.

The solid lines in Figure 6.2 represent power law fits of the obtained data, which are shown as the black-bordered data points. All suspensions exhibited non-Newtonian behavior. The petcoke suspensions seemed to be shear thinning, while all coal suspensions seemed to be shear thickening with the exception of 57\_Coal.

The most uncertainty in the viscosity measurements likely lies at lower values of the shear rate. Oftentimes, small shear stresses were initially applied to determine the value needed for the sample to flow. This small shear stress typically corresponded to the lower shear rates. As the shear stress was ramped up and down multiple times for multiple samples of the same suspension, a seemingly representative viscosity was identified. As shown in Figure 6.2, the data for all slurries converged well, with the only exception being 53\_Coal. Yet even still, a clear trend can be seen in the data for 53\_Coal.

The solid fuels used to prepare the slurries had a slightly different particle size distributions (PSDs), as shown in Table 6.1. However, for shear rates above  $10 \text{ s}^{-1}$ , the viscosity of the slurries increases with increased loading, regardless of the solid particle type. When considering a spray produced from a given slurry, knowing the behavior of the liquid while undergoing changing shear rates is important, as even a change in the degree of shear thinning between two liquids could change the spray behavior.

### 6.3.2 Patternator

The patterning tests offer a very simple means of identifying the general form of the spray and the spatial distribution of liquid within the spray. Common spray forms are flat fan, full cone, and hollow cone. The atomizer design being explored issues a full cone spray for all conditions.

Some of the suspensions offered little to no change in liquid distribution within the spray with respect to liquid and/or gas flow rate. Others changed quite significantly.

The baseline is the atomization of water. The patterning results for water are shown in Figure 6.3.

As shown in Figure 6.3, the spatial distribution of water within the spray is rather insensitive to either air or water flow. For a liquid flow of  $3.79\text{e-}2 \text{ m}^3/\text{hr}$ , the increase in

airflow does seem to increase the fraction of the spray that falls along the spray's center axis. For a liquid flow of  $4.54\text{e-}2 \text{ m}^3/\text{hr}$ , there is almost no change in the spray patterning as the airflow is increased. There is some slight change in the boundary representing the 0.1 fraction of water, but that is small enough to be just slight spray variation.

Figure 6.4 shows the patterning results of the coal suspensions. Figure 6.5 shows the patterning results of the petcoke suspensions.

The coal suspensions shown in Figure 6.4 have significantly different responses to changes in air or liquid flow. 31\_Coal patterning shows almost no sensitivity to air or liquid flow, definitely less sensitivity than the water patterning shown in Figure 6.3. 53\_Coal patterning is far more sensitive to both air and liquid flow than the water patterning. As the liquid flow is increased, a more defined center of the spray is seen in the patterning of 53\_Coal. For the  $3.79\text{e-}2 \text{ m}^3/\text{hr}$  case, increasing the airflow leads to a very poorly defined spray center, which could also be described as a more constant flux along a larger portion of the spray's center. The liquid is much better distributed with the increase in airflow, although little difference is seen between the two highest airflow rates. For the  $4.54\text{e-}2 \text{ m}^3/\text{hr}$  case, as the airflow is increased, the position of largest liquid flux is first seen to move, and the liquid becomes better dispersed.

As shown in Figure 6.5, 37\_Petcoke patterning is more sensitive to both air and liquid flow than the water patterning, shown in Figure 6.3. The increase in liquid flow, for all cases of airflow, seems to increase the fraction of liquid along the center axis of the spray. Increasing the airflow seems to center the spray for the  $3.79\text{e-}2 \text{ m}^3/\text{hr}$  case, while it seems to do the opposite for the  $4.54\text{e-}2 \text{ m}^3/\text{hr}$  case. 43\_Petcoke patterning is also more sensitive to both air and liquid flow than the water patterning. Again, as the liquid flow is increased for all airflows, the fraction of liquid along the center axis of the spray seems to increase. However, in this case, a better way to phrase the result of increasing the liquid flow may be that a spray center is more defined. For both liquid flow rates, as the air is increased, the position representing the largest liquid flux moves more off-center. This effect is likely exacerbated with higher viscosity liquids and could possibly be explained by slight deviations from symmetry in the atomizer design.

For the higher viscosity suspensions evaluated (43\_Petcoke, 53\_Coal), increases in the atomizing airflow tend to correspond to the disappearance or shrinking of a high fraction location (0.5) anywhere in the spray. It also corresponds to an increase in the areas of the lower fractions, or a larger portion of the spray that has a relatively constant liquid flux. This behavior is not seen for the lower viscosity liquids (water, 37\_Petcoke). In fact, for

water and 37\_Petcoke, the opposite trend is seen, where increasing the airflow leads to an area of a higher fraction than was seen for lower airflow rates. For 31\_Coal and the  $4.54\text{e-}2 \text{ m}^3/\text{hr}$  - water case, no trend is seen with changing airflow other than slight variation in the contour lines for each fraction.

### 6.3.3 PSV Results

#### 6.3.3.1 Drop Size and Distribution

The average drop diameter in the center of the spray and along the edge of the spray are shown in Figure 6.6 and Figure 6.7, respectively.

Across the board, the effect of gas flow tends to decrease the drop diameter in the center of the spray, as shown in Figure 3.41. There were three instances where this was not the case. For the coal slurries, both liquid flow rates of 31\_Coal and the  $4.54\text{e-}2 \text{ m}^3/\text{hr}$  case for 57\_Coal show slight increases in the average drop diameter as the airflow is increased. For the petcoke slurries, both liquid flow rates of 37\_Petcoke show slight increases in the average drop diameter as the airflow is increased. It seems the lower loadings of both fuels show this behavior, yet the water cases do not. Both water cases show a decrease in the average drop diameter as the airflow is increased. Additionally, both liquid flow rates of 37\_Petcoke and the  $3.79\text{e-}2 \text{ m}^3/\text{hr}$  57\_Coal case show a decrease in average drop diameter with an increase in airflow.

A proposed qualitative explanation for the slight increases in average drop diameter with airflow for the lower slurry loadings could be tied to the physical properties of the slurries and the atomizer geometry. The atomizer has an inner bevel, which sometimes allows the atomized liquid to adhere to the atomizer's face. This is seen more for slurries than for water, both because the slurry is more visible and likely because the slurry can dry out, leaving a solid fuel residue. The higher slurry loadings may be viscous enough that as they exit the atomizer, they are thick enough to only be propelled down by the atomizing air. The lower slurry loadings may adhere enough to the atomizer's bottom face to form drops, which as the airflow is increases, are more prone becoming entrained with the airflow. These drops would cause the average drop diameter to increase as they are not subject to the same magnitude of atomizing air as the slurry not adhering to the atomizer's bottom face.

For almost every case along the center of the spray, as the liquid flow rate is increased, the average drop diameter increases. The only case where this does not happen is for 57\_Coal and an airflow of  $0.65 \text{ kg/hr}$ . In this case, the difference between the average diameters is approximately 3 micron, which is within the standard error of the measurements.

At the edge of the spray, the relation between airflow and drop diameter is less predictable. Most of the cases in Figure 3.42 showed a slight reduction in drop diameter with an increase in airflow. The exceptions are both liquid flows of 43\_Petcoke, the  $3.79\text{e-}2 \text{ m}^3/\text{hr}$  flow of 53\_Coal, the  $4.54\text{e-}2 \text{ m}^3/\text{hr}$  37\_Petcoke case, and the  $4.54\text{e-}2 \text{ m}^3/\text{hr}$  water case. The  $4.54\text{e-}2 \text{ m}^3/\text{hr}$  37\_Petcoke case is the only one of these that increases in average diameter with every increase in airflow, and the increase is approximately 6 micron. The other cases listed show either an increase followed by a decrease in average drop diameter with increasing airflow, or vice versa. I would suspect that this is also a function of liquid adhering to the bottom face of the atomizer. In the 43\_Petcoke case, the initial increase in average drop diameter could be explained by an increase in the entrainment of these drop forming on the edge of the atomizer's bottom face. The then subsequent decrease in average drop diameter with increasing airflow could be explained by better atomization of those entrained drops. In the 53\_Coal case, a similar explanation could be offered, except the steps are shifted by the increased slurry viscosity.

Drop size distributions are shown in Figure 6.8 and Figure 6.9. Figure 6.8 shows what should seemingly be the best atomization case, lowest liquid flow paired with the highest gas flow ( $0.93 \text{ kg/hr}$  air,  $3.79\text{e-}2 \text{ m}^3/\text{hr}$ ). Figure 6.9 shows what should be the worst atomization case ( $0.65 \text{ kg/hr}$  air,  $4.54\text{e-}2 \text{ m}^3/\text{hr}$ ). When comparing these data sets, know indicators are the quantity of drops with a diameter equal to or larger than 300 micron ( $0.0003 \text{ m}$ ). These large drops take much more time to evaporate, devolatilize, and burn out than smaller drops. The presence of these large drops typically indicates poor performance.

Figure 6.8 shows drop diameter number distributions for all liquids explored for the  $0.93 \text{ kg/hr}$  air and  $3.79\text{e-}2 \text{ m}^3/\text{hr}$  case. The first thing that is evident is that more larger drops exist in the center of the spray than at the edge. This is shown by the higher fraction for all liquids at the center position versus the edge position. Considering the edge position, when looking at the 300 micron limit, all liquids except the petcoke slurries have a fraction less than 0.01 of drops that are 300 micron in diameter. The petcoke slurries have almost exactly a fraction of 0.01 of drops that are 300 micron in diameter. Considering the center position, all liquids have a fraction greater than or equal to 0.01 of drops that are 300 micron in diameter, with the maximum fraction being 0.02 for 37\_Petcoke.

Figure 6.9 shows drop diameter number distributions for all liquids explored for the  $0.65 \text{ kg/hr}$  air and  $4.54\text{e-}2 \text{ m}^3/\text{hr}$  case. When comparing Figure 6.8 and Figure 6.9, the distributions shift towards higher fractions of larger drops for all liquids in both spray positions as the airflow is decreased and the liquid flow is increased, which is to be expected.

The distributions move around the 300-micron point as well. Considering the edge position, all liquids have a fraction greater than or equal to 0.01 of drops that are 300 micron in diameter. Considering the center position, the distributions for all liquids move closer to the 0.02 fraction for 300-micron diameter drops. While this fraction may seem trivial, other studies have shown that for certain reactor geometries and test conditions, drops that are 300 micron in diameter are often trapped at a reactor wall or pass through the reactor without completely converting [20]. While the fractions discussed herein are 0.01-0.02, they amount to a large number of drops. Consider the 0.93 kg/hr air and  $3.79\text{e-}2 \text{ m}^3/\text{hr}$  case. The average drop diameter for both the center and edge of the spray (taken as the average of the two averages) is 82.7 micron. For this representative drop diameter, approximately 120,000 drops are produced every minute, of which, between 1,200 and 2,400 drops will be 300 micron in diameter. For both cases, all sprays had a majority of drop diameters fall below approximately 50 micron.

Predicting the dynamics of drop size distributions has always posed a challenge [131], as tying the behavior to physical properties is difficult. When comparing an individual slurry viscosity with the resulting drop size distribution, no real trend is seen. As shown in Figure 6.2, as the loading increases, so does the slurry viscosity, regardless of the solid particle type. It would seem that increasing the slurry viscosity would lead to a higher fraction of large diameter drops and a lower fraction of small diameter drops. In Figure 6.8 for the edge distributions, the order seems to be 31\_Coal, 57\_Coal, water, 43\_Petcoke, and 37\_Petcoke, from lowest fraction of large diameter drops to highest fraction of large diameter drops. For the center distributions, it is more difficult to say in what order the liquids fall, as there is much crossover from one diameter to the next. In Figure 6.9, for either the edge or the center positions, the same lack of trend is seen with slurry viscosity. More work is need to flush out the relation between the liquid properties and the drop size distribution.

### 6.3.3.2 Spray Velocity and Direction

Figure 6.10 shows the average spray direction along the center of the spray. Figure 6.11 shows the average spray direction along the edge of the spray. In Figure 6.10 and Figure 6.11,  $270^\circ$  is straight down along the center axis of the injector.  $180^\circ$  is horizontal to the left.

The spray direction is measured in degrees, where when looking directly at the spray,  $0^\circ$  is the positive horizontal axis,  $90^\circ$  is the positive vertical axis,  $180^\circ$  is the negative horizontal axis, and  $270^\circ$  is the negative vertical axis. The injector's center axis points along the  $270^\circ$  line, so for a  $270^\circ$  spray direction, the spray is moving straight down. For comparison,  $0^\circ$  corresponds to a line from the center to the left of any of the subplots in Figure 6.3, Figure

6.4, or Figure 3.40, as well as to the right in the images shown in Figure 6.10. There is little variation in the direction of the spray in the center of the spray. As shown in Figure 6.10, along the center of the spray, increasing the airflow serves to move the spray direction closer to  $270^\circ$  degrees, regardless of liquid flow rate, fuel type, or fuel loading.

At the edge of the spray, the spray direction is more erratic, as shown in Figure 6.11. As the left edge of the spray was imaged, it would be expected that if a trend in direction exists, it would be to the left, or towards  $180^\circ$ . For almost all cases, increasing the airflow results in either no significant change in the average spray direction, or the average spray direction moves more to the left, towards  $180^\circ$ . The only case not following this trend is the  $3.79\text{e-}2 \text{ m}^3/\text{hr}$  53\_Coal case. It shows little change in direction for the first airflow increase, and a movement back towards center for the second airflow increase. This could help explain the behavior of the average drop diameter for the same case in Figure 3.42. Figure 3.42 shows an increase in the average drop diameter for the second airflow increase. The increased mass of these larger drops is going to require more force to propel them in a direction other than straight down. The increased prevalence of these larger drops likely moves the average spray direction towards  $270^\circ$ . This logic dictates that the same behavior would be seen with the first airflow increase for both liquid flow rates of 43\_Petcoke. As the average drop diameter increases with the first airflow increase, it stands to reason that the larger drops would move the average spray direction towards  $270^\circ$ , just as with the 53 wt% coal slurry. 43\_Petcoke is less viscous than 53\_Coal, and the drops could be more easily atomized leading to no substantial change in the average spray direction.

When comparing the direction of 53\_Coal in Figure 6.11 with the patterning results in Figure 6.4, some agreement is found. For the  $4.54\text{e-}2 \text{ m}^3/\text{hr}$  case, as the air flow is increased, the direction of the drops at the edge of the spray tends more towards horizontal. This can be seen as increased area of the 0.3-0.4 fraction in the patterning results. For the  $3.79\text{e-}2 \text{ m}^3/\text{hr}$  case with respect to increasing airflow, there is an initial change in direction towards horizontal, before another change back towards the downward direction. In the patterning results with respect to increasing airflow, dispersion initially increases, which should lead to an increase in flow in the horizontal direction. Then, oscillation is seen in the dispersion area, which could lead to a change in flow towards the downward direction. These effects are not exactly clear, but some relation can be seen.

While these condition-averaged spray directions offer some insight into the spray behavior, looking at the nuances within a condition better illuminate changes from condition to condition. Figure 6.12 shows the relation between spray direction and drop velocity for all

liquids evaluated. The flow condition explored in Figure 6.12 is  $3.79\text{e-}2$  m<sup>3</sup>/hr liquid flow and 0.93 kg/hr airflow.

The  $3.79\text{e-}2$  m<sup>3</sup>/hr (liquid) 0.93 kg/hr (air) case was chosen, as this should provide the best atomization of all the conditions explored having the highest airflow and the lowest liquid flow. One thing to note about Figure 6.12, the color bars are identical for each specific subplot. They represent a normalized drop count for the given conditions. Red represents one, and blue represents zero.

For all liquids evaluated in Figure 6.12, the velocity range encountered is wider at the edge of the spray than at the center of the spray. Additionally, for all cases, the maximum velocity in the center of the spray is higher than the maximum in the edge of the spray. The range of spray direction is much higher at the edge of the spray than at the center of the spray. For 31\_Coal and 53\_Coal, the edge spray has a count of at least one drop for all possible directions. The highest velocity drops appear to be moving in the 270°-direction at the center of the spray. At the edge of the spray, the highest velocity drops are moving in the 250°-direction, which corresponds to moving slightly to the left of straight down. The slower moving drops along the edge of the spray have a stronger tendency to move straight down, as indicated by the tails for all liquid sprays shown in Figure 6.12. The average velocity along the center of the spray for all liquids is between 5-10 *m/s*. Along the edge of the spray, the average velocity is closer to 1 *m/s*, as most of the edge sprays have a group of approximately 3 *m/s* drops and a group of approximately 0.7 *m/s* drops.

### 6.3.4 High-Speed Imaging Results

In addition to the cold-flow slurry testing performed, high-speed imaging was performed with three different atomizers used for operating the University of Utah's entrained flow gasifier. Two of these atomizers, MH013 and MH031, were of the micro-hole type illustrated previously in Figure 3.4-A, with micro-hole diameters of 0.33 mm and 0.79 mm, respectively. The third atomizer (referred to herein as atomizer S) was an impinging, concentric two-stream atomizer illustrated previously in Figure 3.4-E and Figure 3.5. The micro-hole atomizers used in this study were chosen as they represent the extreme geometries for the micro-hole atomizers used for EFG testing. Atomizer S was chosen as it was one of the original atomizers used for EFG operation, and when new atomizer designs underperformed, it was chosen for operation. These atomizers and their general features are noted in Table 6.2.

The atomizers listed in Table 6.2 were evaluated over a range of gas and liquid flows. Table 6.3 shows the ranges of conditions explored.

The gas was air. The liquid was water. The fluid properties were listed previously in Table 3.3. All experiments were performed at atmospheric pressure and temperature.

As was shown in Section 4.3, the range of drop diameter in a spray is commonly log-normally distributed. For the properties of a log-normal distribution to be accurately applied here, we must first ensure that the drop diameters are indeed log-normally distributed. Figures 6.13-6.15 show the drop diameter distributions for atomizer MH013, MH031, and Atomizer S, respectively.

As can be seen in Figures 6.13-6.15, the drop diameter distributions for all atomizers are well captured by a log-normal distribution. The tails on the the low end of the axes in Figures 6.13-6.15 represent the smallest measured drop diameter for a given test. As Figures 6.13-6.15 represent cumulative functions, there can be no probability of obtaining a measurement below the minimum measurable diameter for the tests. Log-normal distributions lends themselves to characterization by log-normal distribution statistics, which are comprised of location and scale parameters, better known as the geometric mean ( $\mu_{dd}$ ) and standard deviation ( $\sigma_{dd}$ ), respectively. These parameters will be evaluated further into the chapter. As most spray analysis targets a direct application and an understanding between the system conditions and a spray-representative drop diameter, first we evaluate the spray Sauter mean diameters (SMDs) produced for these atomizers.

The main variables changed, other than the atomizer geometry itself, were the gas and liquid velocities. For MH013 and Atomizer S, as the gas exit cross-sectional area is so small, most of the flows approached sonic velocities with under-expanded gas at the atomizer exit. Per the discussion in Section 4.3, the main factor considered here to influence the resulting drop diameters is  $Re_{g,hd}$ . Figure 6.16 shows the spray SMD as a function of  $Re_{g,hd}$ .

As was shown in Section 4.3, the spray SMD was shown to decrease with an increase in  $Re_{g,hd}$ . This trend is seen in Figure 6.16, with the very noticeable exception of Atomizer S. While this trend seems very prominent and counter to theory, it can be explained. The trends of any representative drop diameter are only as valid as the region being imaged. For all cases, the region being imaged is the immediate region past the end of the atomizer. This is a very similar region to what was imaged for the water results in Chapter 4. However, for the atomizers evaluated here, a clear intact liquid jet (ILJ) is not formed, at least not in the form that an ILJ is formed for the small-scale atomizers. Here, for MH013 and MH031, atomizer is mostly axisymmetric, with no clear deviations from concentricity. For Atomizer S, there is a clear deviation from concentricity, as was shown in Figure 3.5. As such, the images contain a prominent liquid jet being diverted directly to one side, through the entire

frame. This behavior is seen in Figure 6.17.

As is immediately evident upon looking at Figure 6.17, the spray SMDs reported in Figure 6.16 for Atomizer S are artificially small. As the annular gap is drastically nonconcentric, most of the liquid is directed in the form of a jet through the frame; the only drops being measured are the small drops peeling off the larger jet. As the gas flow is increased, the jet itself begins to break up periodically, which in turn leads to the increase in spray SMD shown in Figure 6.16 for Atomizer S. A higher- $Re_{g,hd}$  case for Atomizer S is shown in Figure 6.18.

There is no noticeable difference in performance between MH013 and MH031. While the range of gas velocities explored for MH013 and MH031 were similar (Table 6.3), the decrease gas cross-sectional area of MH013 results in larger values of  $Re_{g,hd}$ . The measured spray SMDs for both MH013 and MH031 fall along the same trend line, indicating that a change in micro-hole diameter does not effect the resulting spray to any measurable degree. This is a useful conclusion to establish, particularly when taken in the context of operation of the University of Utah's entrained flow gasifier. Oftentimes the choice of micro-hole atomizer fell on the desired operating conditions. As the oxygen feed has an upper limit on pressure delivered, the gas cross-sectional area must be chosen appropriately so as to allow the desired oxygen flow rate at the desired operating pressure. The results for MH013 and MH031 in Figure 6.16 indicate that aside from any change operating pressure may have on the atomization dynamics, the spray SMD can be assumed to be relatively constant if  $Re_{g,hd}$  is kept constant.

In addition to varying the gas flow, the liquid flow was also changed. Figure 6.19 shows the spray SMD as a function of  $Re_l$ .

Here, the same strange behavior is seen for Atomizer S. The effect of liquid flow on a spray-representative drop diameter depends on the regime of atomization taking place, as there are instances of pressure atomization where increasing the liquid flow can result in a decrease in drop size. But generally, as liquid flow is increased, the spray-representative drop diameter will increase. This is shown in Figure 6.19 for MH013 and MH031. However, for Atomizer S, as  $Re_l$  is increased, the drop diameter clearly decreases. However, as previously mentioned, image framing and the nonconcentricity of Atomizer S leads to strange behavior. For large liquid flows (or large  $Re_l$ ), the liquid is pushed to one side, and jets through the image are unbroken. As the liquid flow (or  $Re_l$ ) is decreased, the jet does not make it through the entire image. It breaks up within the image frame, leaving a much larger volume of liquid in the form of drops than the high- $Re_l$  case and resulting in a smaller SMD.

To illustrate this phenomena, Figure 6.20 shows the low- $Re_l$  case for Atomizer S, and Figure 6.21 shows the high- $Re_l$  case for Atomizer S.

While Figure 6.21 has a much large liquid structure present in the image, the drop sizing algorithm will ignore any structure that exists on the image border, which the prominent liquid jet does for all images captured. As such, the only drops measured in Figure 6.21 are those small drops shed from the edge of the liquid jet. Figure 6.20 clearly shows better atomization than Figure 6.21, but as the volume of liquid put in a form that can be identified as a drop is larger than the same volume in Figure 6.21, the measured spray SMD is larger for Figure 6.20. This behavior indicates the need to have a good general understanding of the overall spray structure. In the case of Atomizer S, if drops were being measured along the atomizer's center axis at some position downstream with no knowledge of the near-field behavior, Atomizer S may be viewed as superior to either of the micro-hole atomizers as it provides a smaller spray SMD. In reality, the extreme liquid jetting that takes place would cause issues for almost any practical system that can be thought of to need an atomizer. In the case of a slurry-fed combustion or gasification system (if the assumption is made that a slurried fuel shows a similar behavior to the water explored here), the behavior shown in Figure 6.21 would result in a large majority of the slurried fuel ending up on the wall of the reactor. Additionally, it can be speculated that the small drops formed would be largely comprised of water, as studies have shown that drop distributions for solid-liquid suspension tend to be bimodal, with the smaller diameter peak representing a pure liquid drop [132]. At any rate, while the solid fuel in the slurry would have a range of particle sizes and the small drops would possibly contain some of the smaller solid particles, the large majority of the solid fuel would be contained in the liquid jet, and the largest solid fuel particles are those that will offer the most resistance to complete fuel conversion.

As mentioned previously, the drop size distributions of these tests can be characterized using the geometric mean ( $\mu_{dd}$ ) and standard deviation ( $\sigma_{dd}$ ). First, we will explore the trends of  $\mu_{dd}$ . Figure 6.22 shows  $\mu_{dd}$  as a function of  $Re_{g,hd}$ .

Figure 6.22 shows the same representative diameter trends with  $Re_{g,hd}$  as were shown in Figure 6.16 for the micro-hole atomizers. The trend of decreasing  $\mu_{dd}$  with increasing  $Re_{g,hd}$  is the opposite of what was seen for the spray SMD. The SMD has a tendency to be significantly shifted by the existence of a relatively small number of large diameter drops. So while some large diameter drops significantly effect the SMD measurement, it has less of an effect on  $\mu_{dd}$ . As was shown for the SMD as well, the results for the micro-hole atomizers fall along the same trend line. While the  $\mu_{dds}$  shown in Figure 6.22 for Atomizer

S are significantly less than those for the micro-hole atomizers, the Atomizer S data cannot be directly compared to the data from the micro-hole atomizers, due to the liquid jetting previously discussed. As such, the Atomizer S data will be disregarded from here on out.

Figure 6.23 shows  $\sigma_{dd}$  as a function of  $Re_{g,hd}$  for a constant liquid velocity.

Both MH013 and MH031 show that an increase in  $Re_{g,hd}$  correlates with a decrease in  $\sigma_{dd}$ , showing that the drop diameter distribution narrows with increasing gas flow. Here, the results do not seem to fall along the same trend line like they did for  $\mu_{dd}$  in Figure 6.22. MH031 shows a fairly consistent, almost linear, decrease in  $\sigma_{dd}$  with increasing  $Re_{g,hd}$ , where  $\sigma_{dd}$  for MH013 seems insensitive to changes in  $Re_{g,hd}$  over the range of approximately  $700 < Re_{g,hd} < 1,500$ .  $\sigma_{dd}$  for MH013 is seen to decrease for increasing  $Re_{g,hd}$  above  $Re_{g,hd} > 1,500$ , approximately.

In order to better control systems utilizing these atomizers, correlations need to exist that can predict behavior for target operating conditions. Before new correlations are generated for this unique atomizer design, the predictions of the correlations developed in Section 4.3 are compared to the data here, to see if they accurately predict the spray characteristics, despite being developed for a significantly different atomizer geometry. The correlations for spray SMD,  $\mu_{dd}$ , and  $\sigma_{dd}$  were given in Equation 4.14, Equation 4.13, and Equation 4.15, respectively. Figure 6.24, Figure 6.25, and Figure 6.26 show the measured versus prediction results for the spray SMD,  $\mu_{dd}$ , and  $\sigma_{dd}$ , respectively.

As the micro-hole atomizers have a different geometry than the small-scale atomizers previously explored, they do not have a  $b$ -value, or a gas annular thickness. In order to approximate this value, as Equation 4.14 and Equation 4.13 normalize with  $b$ , an annular gap with the same gas cross-sectional area as the micro-holes is assumed. This artificial  $b$  is used in the correlations and predictions shown in Figures 6.24-6.26.

It is difficult to say that the correlations of Equations 4.14-4.13 predict the micro-hole behavior well. Not a measured value matches the predicted value, as seen in Figures 6.24-6.26, although the trends seem to be captured well, as indicated by the slope of the data points approaching that of the one-to-one line. In order to better predict the spray properties of these micro-hole atomizers, Buckingham-II theorem is again used, as it was in Section 4.3. The minutia is not repeated here. Only the developed correlations are presented. Correlations for the spray SMD,  $\mu_{dd}$ , and  $\sigma_{dd}$  are presented in Equation 6.1, Equation 6.2, and Equation 6.3, respectively. The variables considered were  $A = \text{artificial-}b/d_0$ ,  $D = a/d_0$ ,  $M$ , and  $Re_{g,hd}$ . The spray representative diameters were normalized by artificial- $b$ . The predictions based upon Equations 6.1-6.3 are shown in Figures 6.27-6.29.

$$\frac{SMD}{b} = 1.90A^{-0.65}B^{-0.62}M^{-0.04}Re_{g,hd}^{-0.32} \quad (6.1)$$

$$\frac{\mu_{dd}}{b} = 0.07A^{-0.79}B^{-0.43}M^{-0.05}Re_{g,hd}^{-0.11} \quad (6.2)$$

$$\sigma_{dd} = 3.06A^{-0.02}B^{0.01}M^{-0.02}Re_{g,hd}^{-0.05} \quad (6.3)$$

The dependence on  $M$  in Equations 6.1-6.3 is shown to be quite small, which is likely due to the majority of tests having a constant liquid velocity.  $M$  is the only parameter that incorporates the liquid velocity, and while changing either the gas density or velocity will impact  $M$ , the largest change seems to come through the few tests that change the liquid velocity. Equation 6.1, Equation 6.2, and Equation 6.3 are shown to predict the measured spray properties quite well in Figure 6.27, Figure 6.28, and Figure 6.29, respectively.

## 6.4 Conclusions

The sprays produced from atomizing solid fuel water suspensions were characterized using patterning and PSV. The dynamic viscosities of the suspensions were also obtained. For shear rates above approximately  $10 \text{ s}^{-1}$ , increases in viscosity were seen for an increase in solid particle loading, regardless of the solid particle type. The petcoke suspensions were found to be shear thinning, while the coal suspensions, with the exception of 57\_Coal, were shown to be shear thickening. All liquids evaluated were shown to issue a full cone spray profile.

For the higher viscosity suspensions evaluated (43\_Petcoke, 53\_Coal) with patterning, increasing the airflow corresponded to the disappearance or shrinking of a high fraction region anywhere in the spray. The areas of the lower fraction regions also increased. This shows that the sprays were better dispersed with increases in the airflow. Almost the opposite trend is seen for the lower viscosity suspensions evaluated (water, 37\_Petcoke). For these liquids, increases in airflow correspond to a slight increase in area of the high fraction regions. For all liquids, increasing the liquid flow rate typically resulted in an increase in the area of a high fraction center region.

Increasing the airflow decreased the average drop diameter for practically all cases along the center of the spray. Increasing the liquid flow showed an increase in the average drop diameter for practically all cases along the center of the spray. Along the edge of the spray, a clear trend is not identified. The drop size distributions show a trend with changes in the

air and liquid flow rates. Increasing the air-to-liquid ratio shows an increase in the fraction of small diameter drops and a decrease in the fraction of large diameter drops.

The average direction of the produced drops along the center of the spray is largely unaffected by changes in flow rates or liquid atomized. Along the edge of the spray, increasing the airflow results in either no significant change in the spray direction or a shift towards  $180^\circ$ . Increases in the liquid flow rate tended to move the spray direction slightly more towards  $270^\circ$ . Along the edge of the spray (for  $0.93 \text{ kg/hr}$  air and  $3.79\text{e-}2 \text{ m}^3/\text{hr}$  liquid), two predominant drop velocity groups were seen. One group was moving  $250^\circ$  at approximately  $3 \text{ m/s}$ , while the other group was moving  $270^\circ$  at approximately  $0.7 \text{ m/s}$ .

The spray characteristics correlations developed in Chapter 4 were compared to the spray characteristics measured for two micro-hole atomizer and an impinging, coaxial, two-stream atomizer and found to not accurately predict the representative drop diameters, likely due to the geometry change. New correlations were developed using Buckingham-II theorem to predict the geometry average drop diameter ( $\mu_{dd}$ ), the geometric standard deviation of the drop diameter ( $\sigma_{dd}$ ), and the spray Sauter mean diameter. These correlations were shown to accurately predict behavior over the range of variables explored.

While the dynamics behind the spray behavior have yet to be fully clarified, the characterization of these various liquid sprays can assist in understanding why a slurry-fed gasifier behaves the way that it does, as well as offer representative inputs into any gasification model.

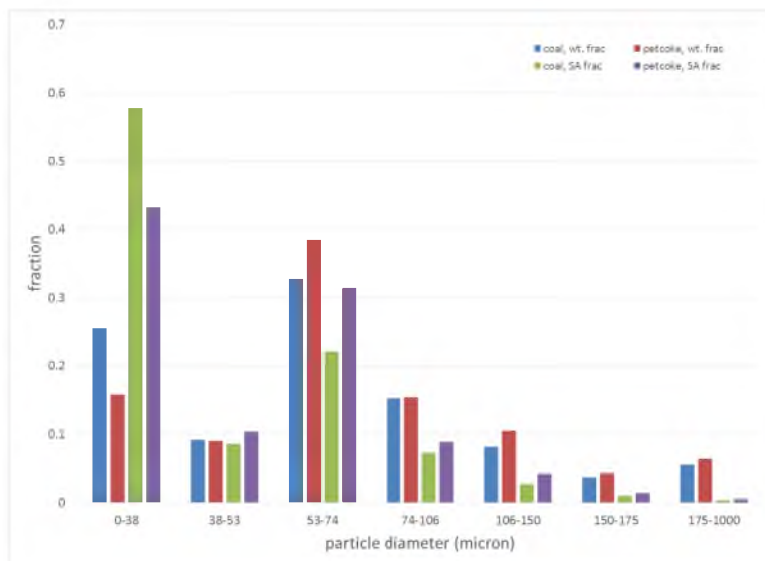


**Figure 6.1.** Particle size distribution for both the coal and petcoke evaluated.

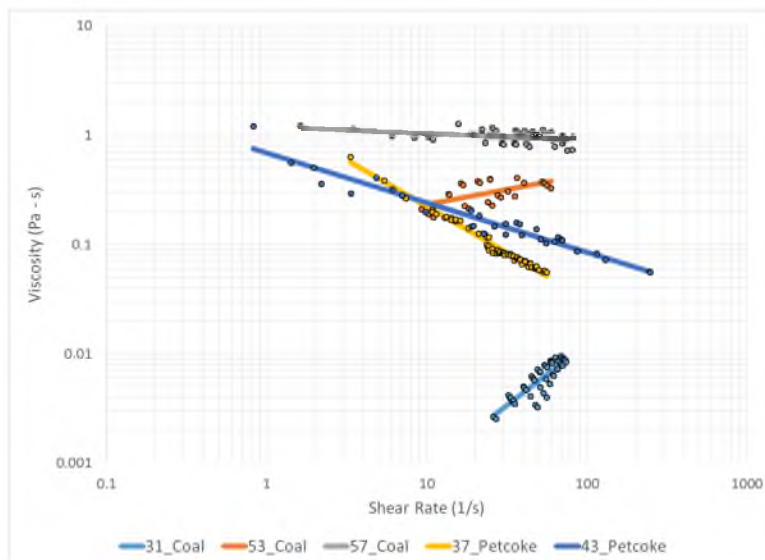


**Figure 6.2.** Shear-dependent viscosity of various fuel slurries.

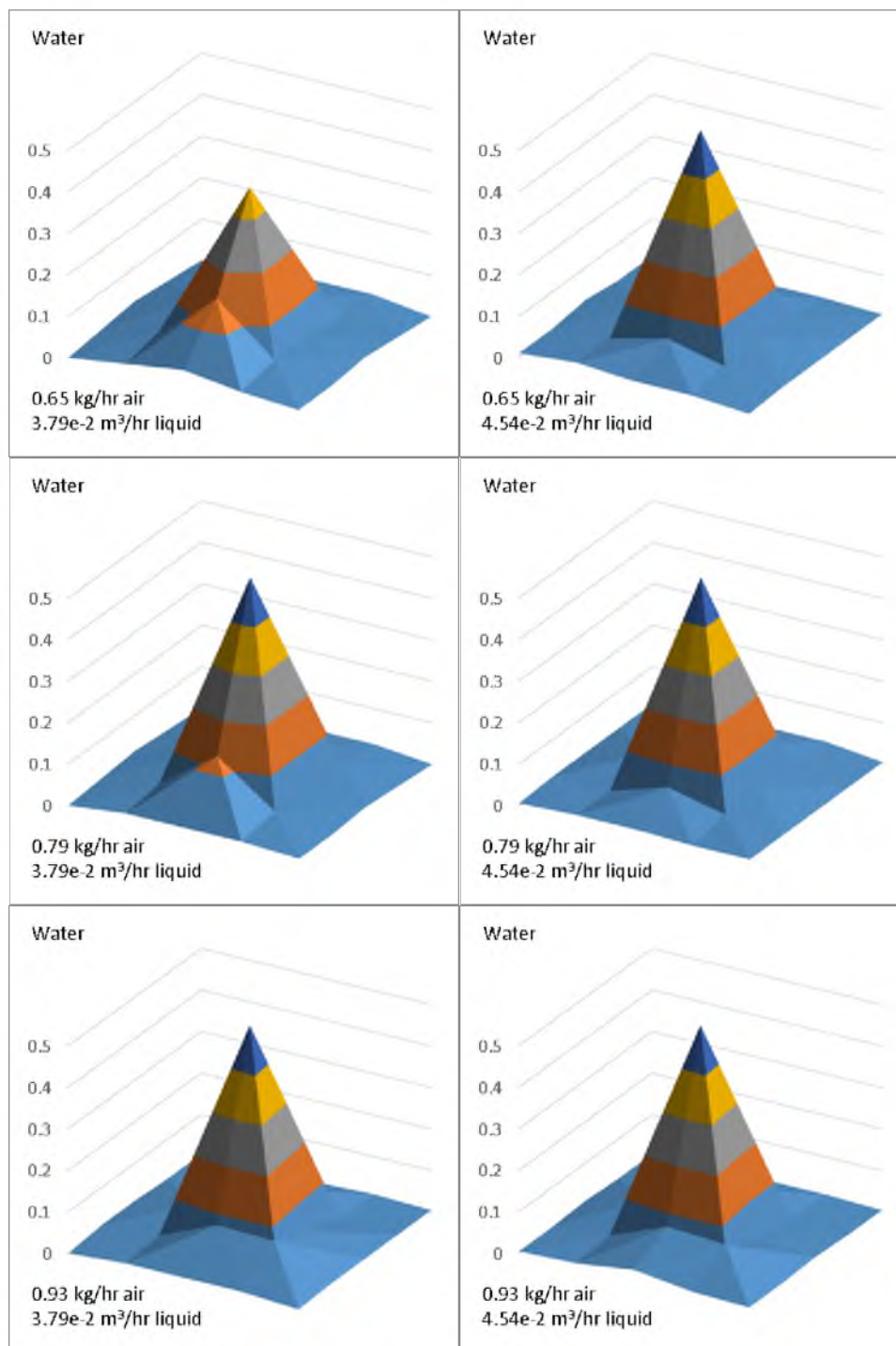


Figure 6.3. Patternation results of water.

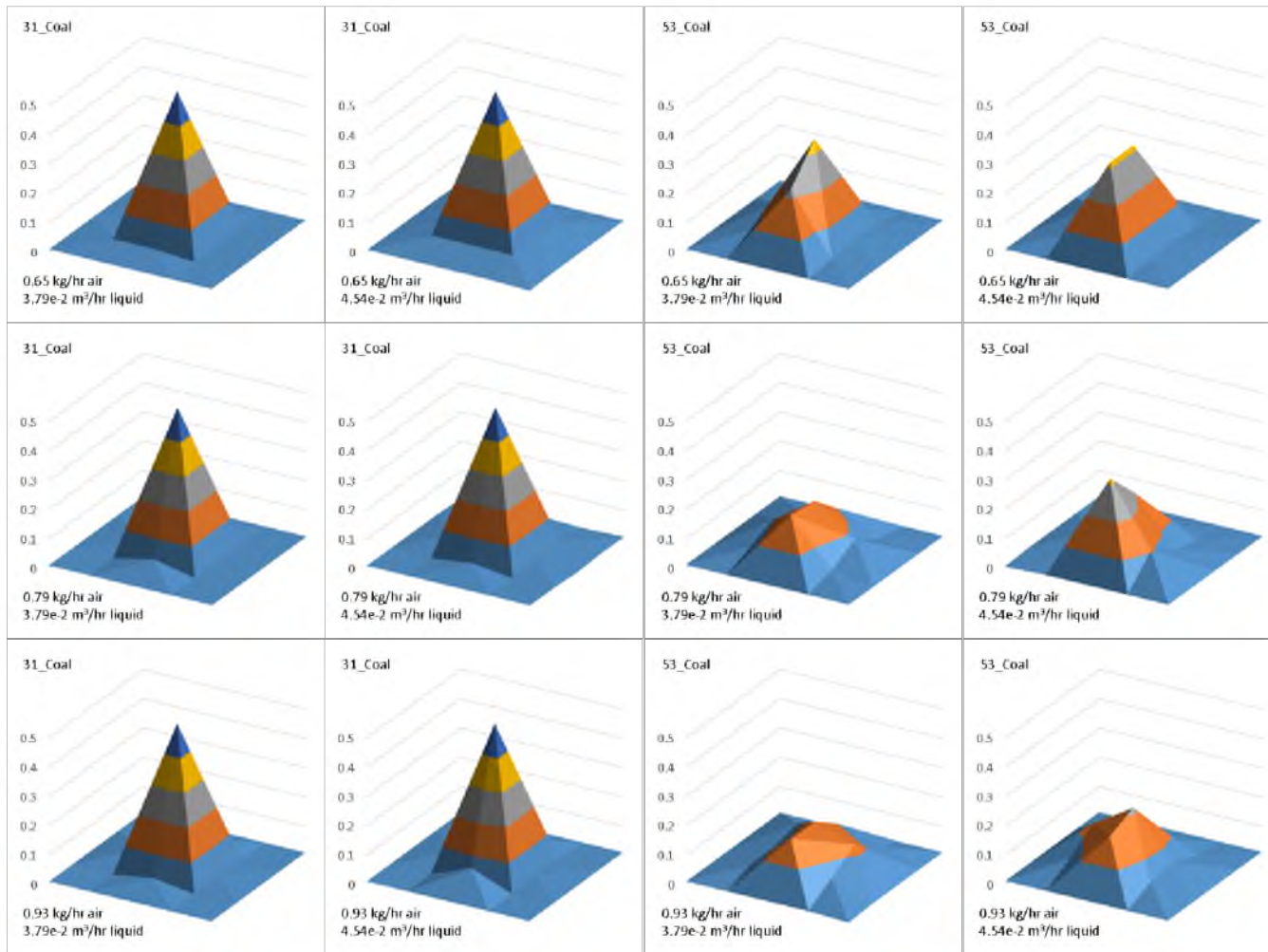


Figure 6.4. Patternation results of 31\_Coal (left) and 53\_Coal (right).

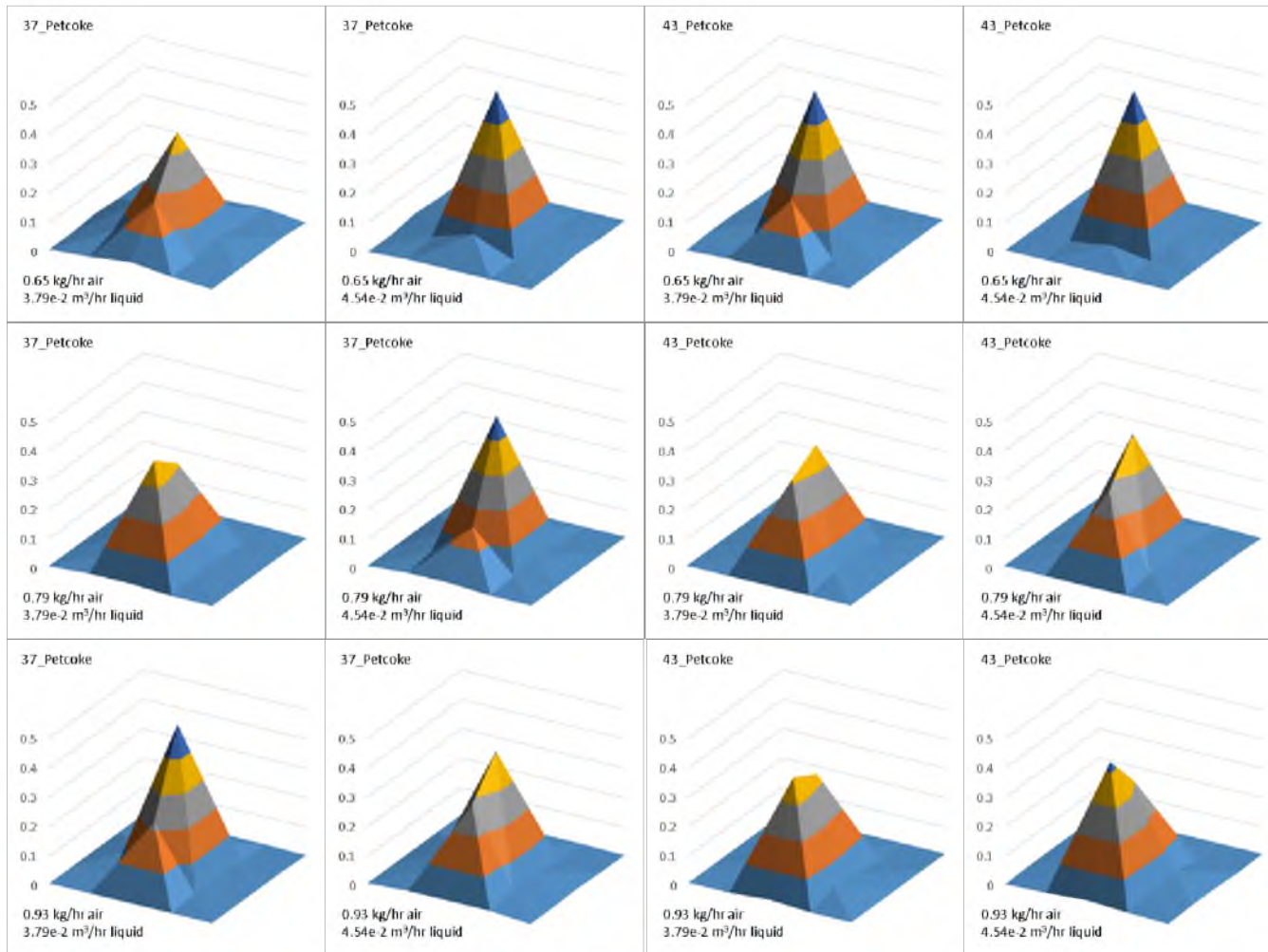
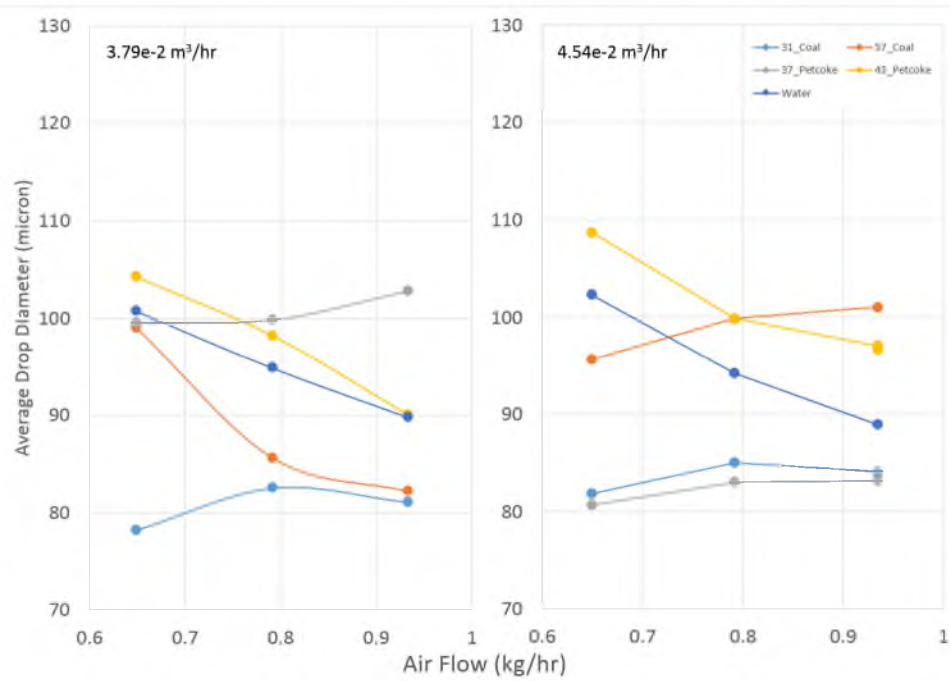
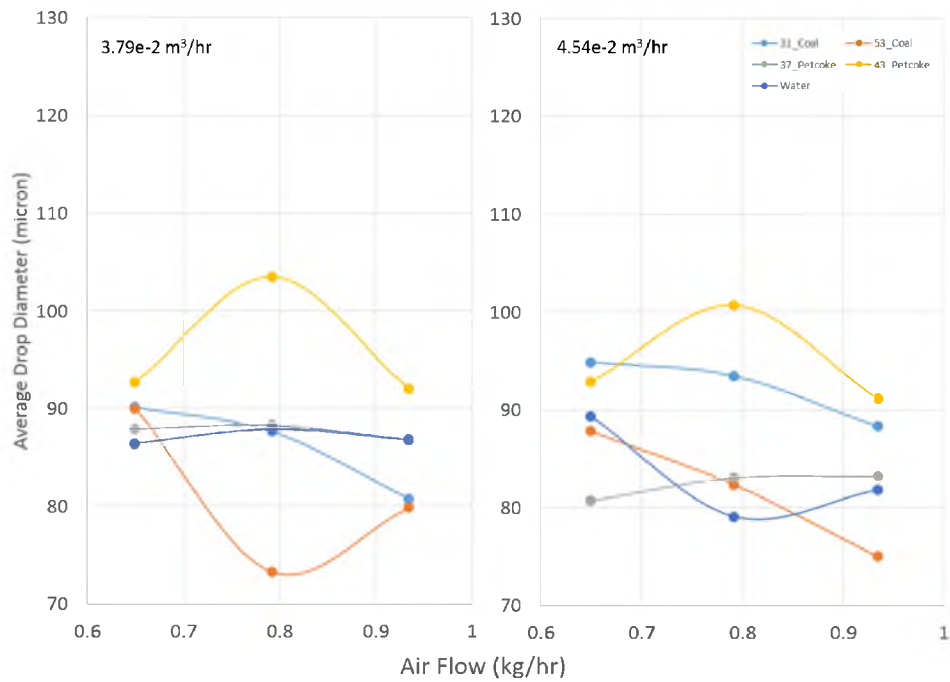


Figure 6.5. Patternation results of 37\_Petcoke (left) and 43\_Petcoke (right).



**Figure 6.6.** Effect of gas and liquid flow on the average drop diameter along the spray's center axis.



**Figure 6.7.** Effect of gas and liquid flow on the average drop diameter along the spray's edge.

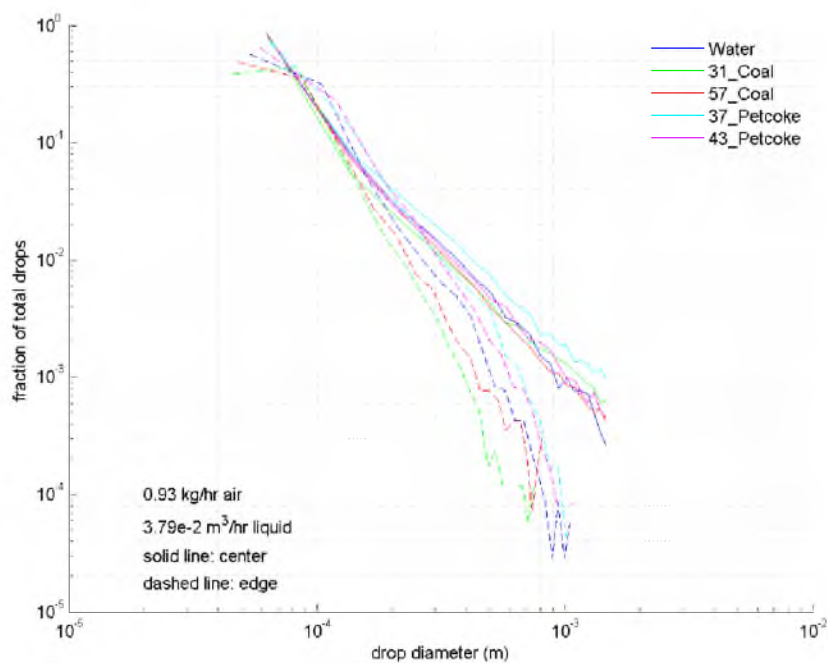


**Figure 6.8.** Drop diameter number distribution for all liquids and the 0.93 kg/hr air,  $3.79 \times 10^{-2} \text{ m}^3/\text{hr}$  case.

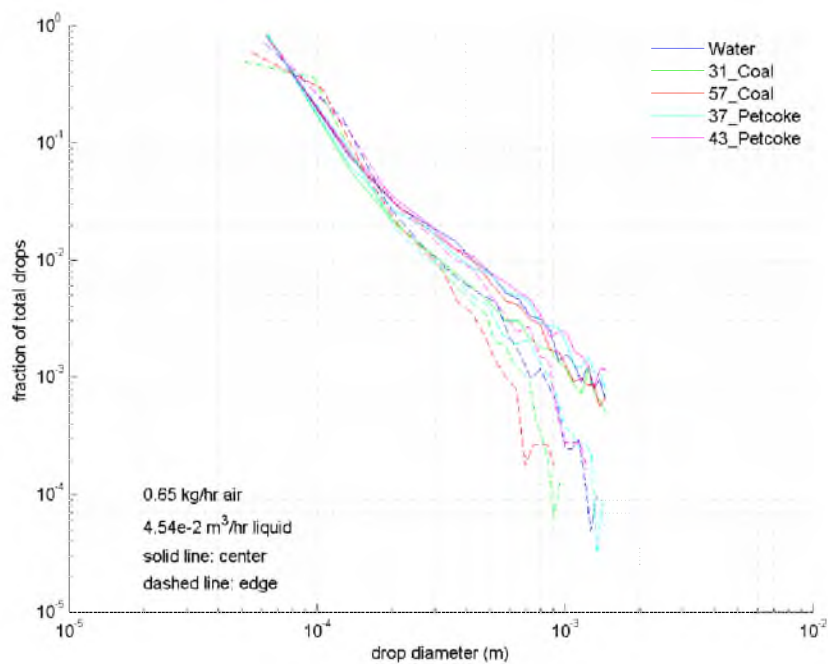


**Figure 6.9.** Drop diameter number distribution for all liquids and the 0.65 kg/hr air,  $4.54 \times 10^{-2} \text{ m}^3/\text{hr}$  case.

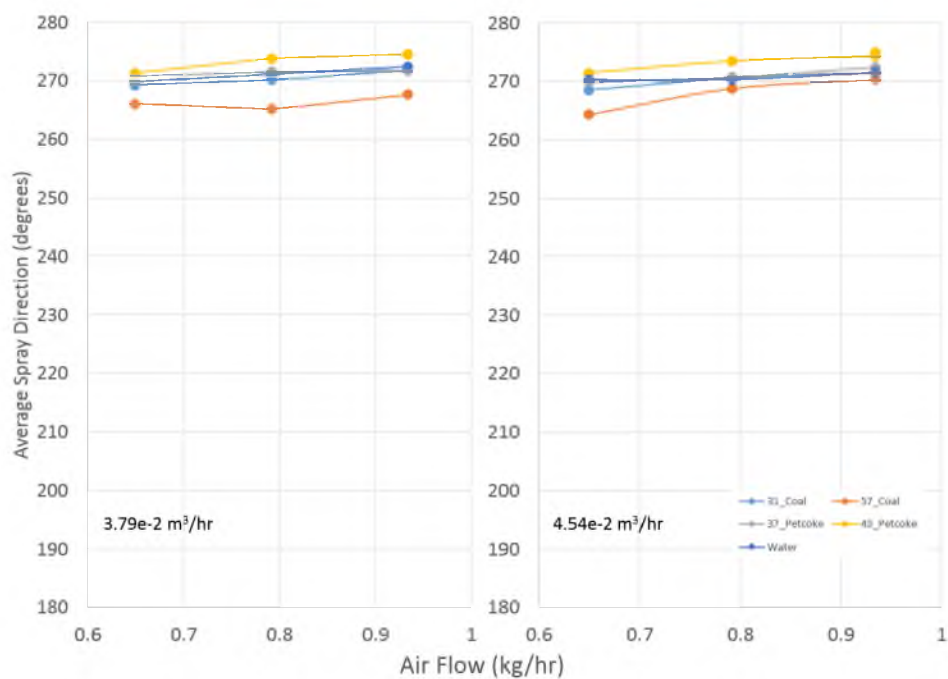


**Figure 6.10.** Effect of gas and liquid flow on the average spray direction along the center of the spray.

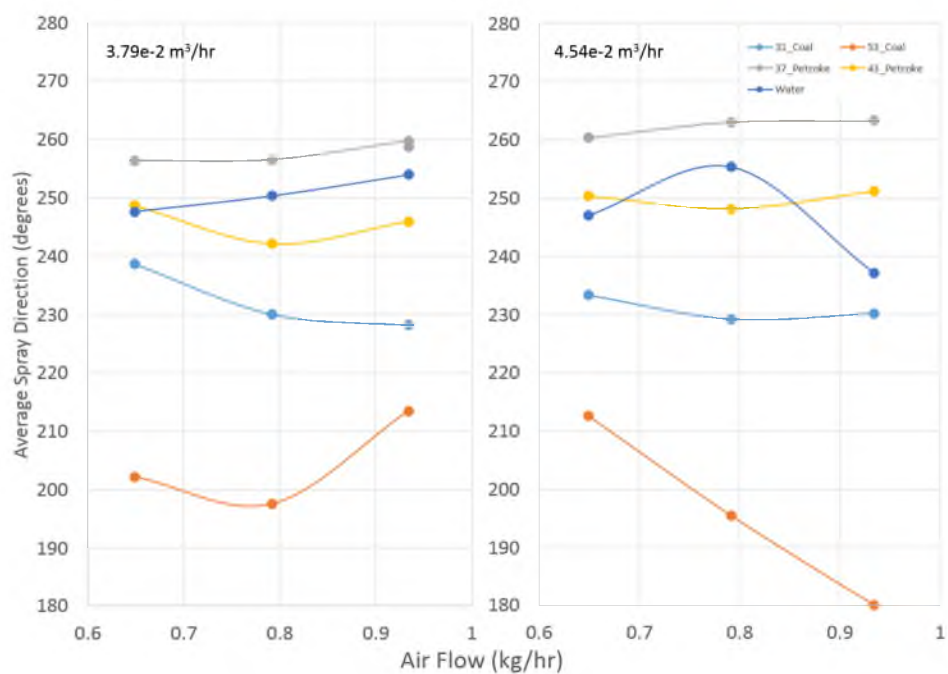


**Figure 6.11.** Effect of gas and liquid flow on the average spray direction along the edge of the spray.

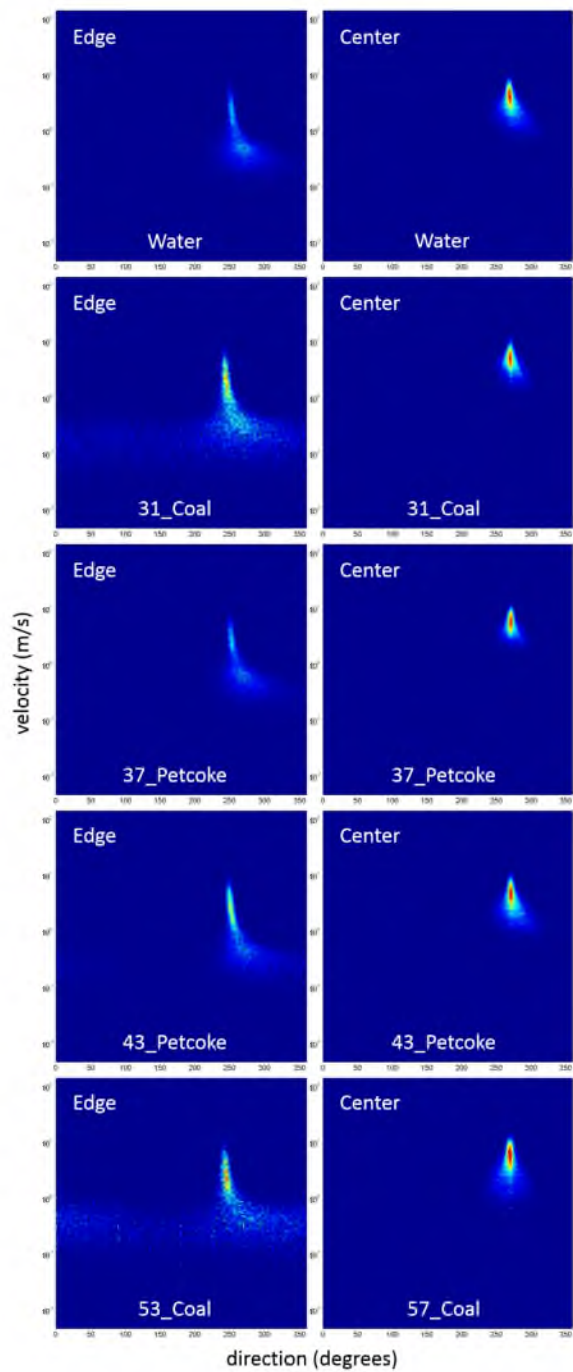


**Figure 6.12.** Relation between spray direction and drop velocity for all liquids. Flow rates were  $3.79 \times 10^{-2}$  m<sup>3</sup>/hr (12 gph) and 0.93 kg/hr, liquid and air, respectively.

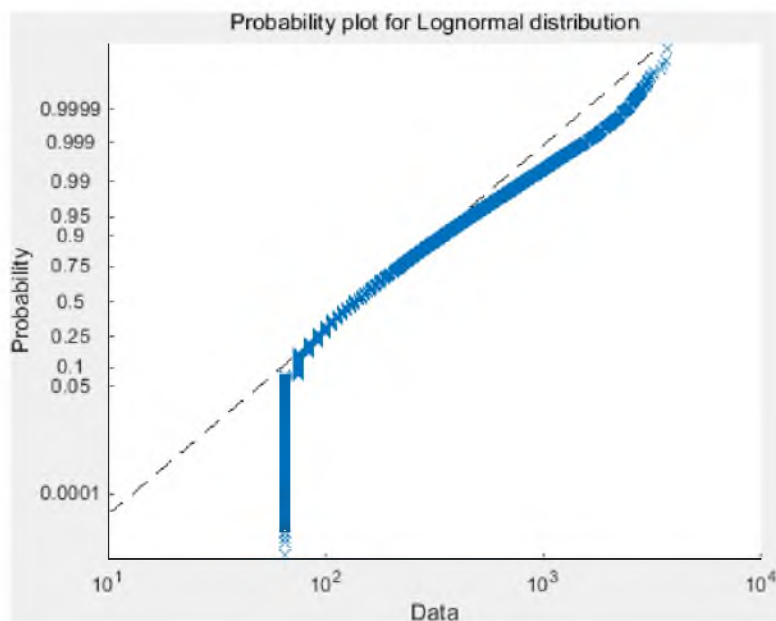


**Figure 6.13.** Drop diameter distribution comparison to a log-normal distribution. Water, MH013,  $u_g = 330$  m/s,  $u_l = 0.35$  m/s.

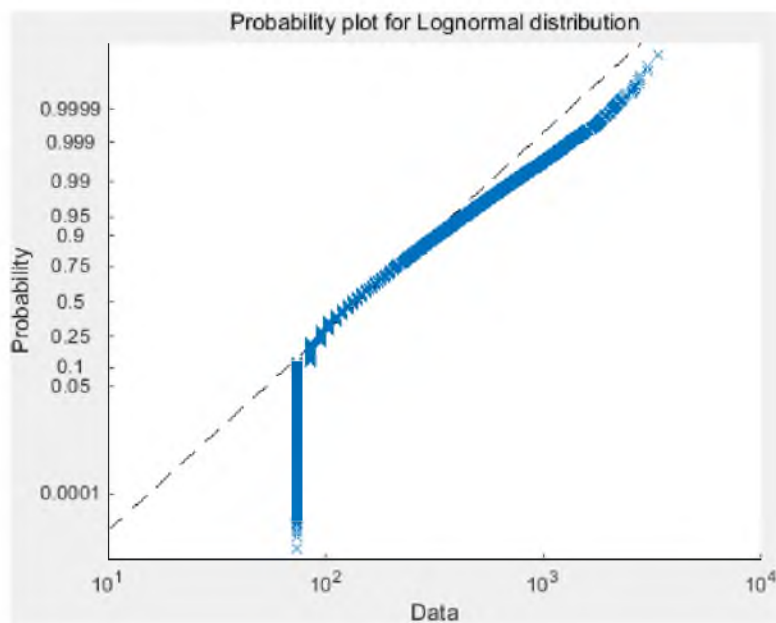


**Figure 6.14.** Drop diameter distribution comparison to a log-normal distribution. Water, MH031,  $u_g = 332$  m/s,  $u_l = 0.35$  m/s.

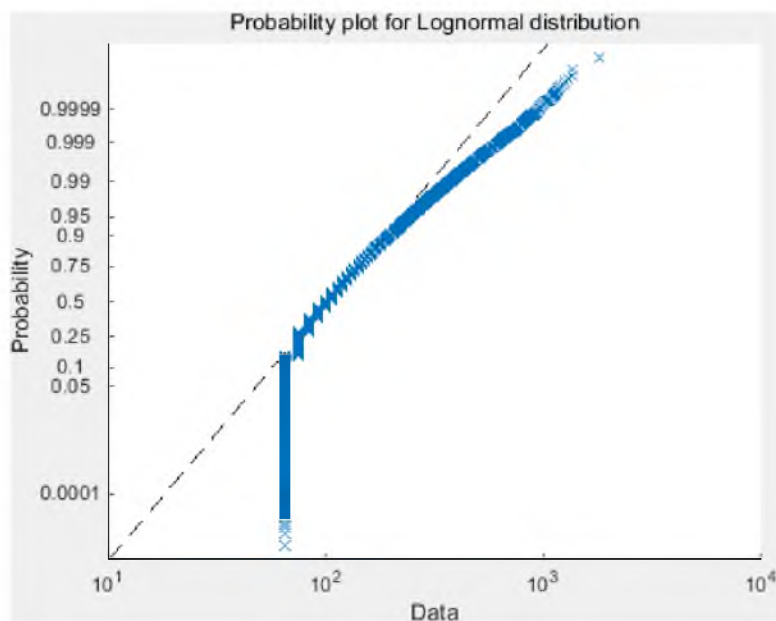


**Figure 6.15.** Drop diameter distribution comparison to a log-normal distribution. Water, Atomizer S,  $u_g = 332 \text{ m/s}$ ,  $u_l = 0.35 \text{ m/s}$ .

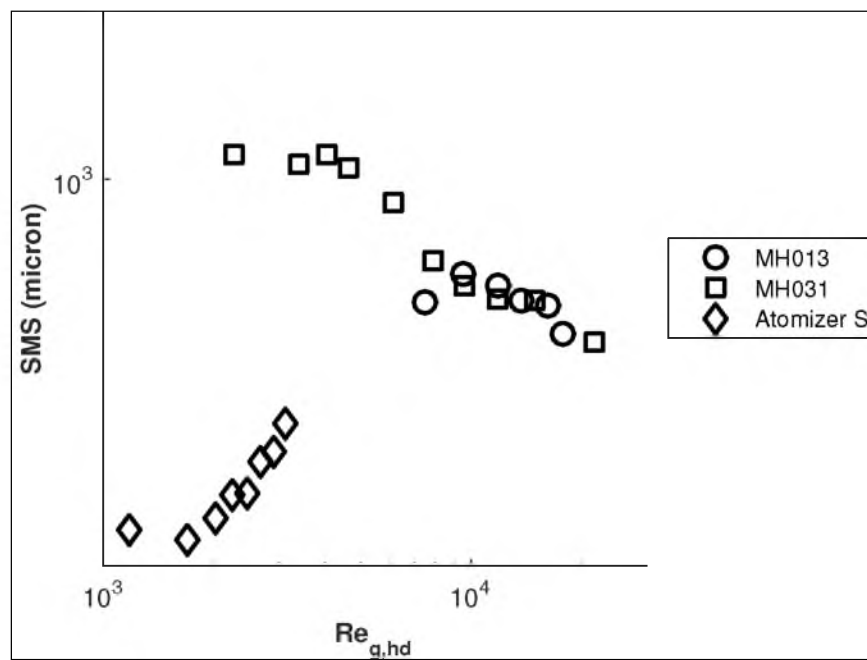


**Figure 6.16.**  $Re_{g,hd}$  versus the spray SMD.  $u_l = 0.35 \text{ m/s}$ .

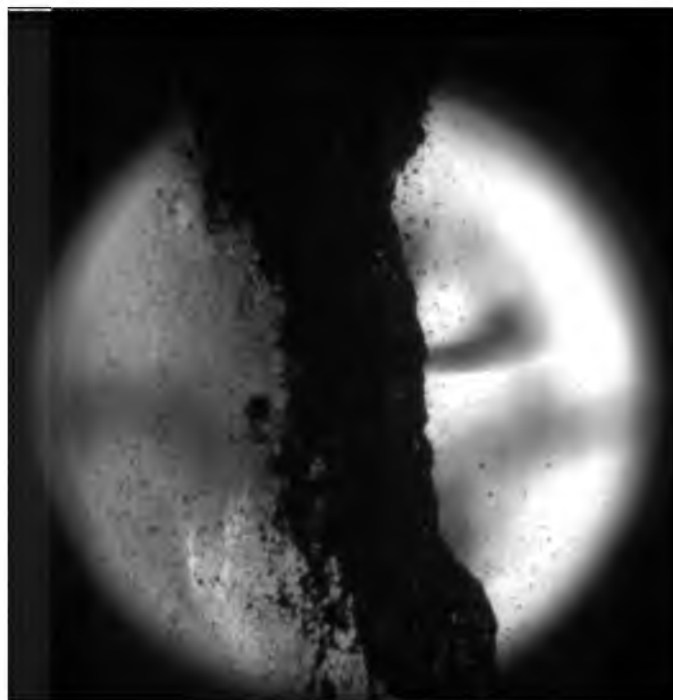


**Figure 6.17.** Image of breakup for Atomizer S.  $u_g = 344 \text{ m/s}$ ,  $u_l = 0.35 \text{ m/s}$ , and  $Re_{g,hd} = 2,236$ .

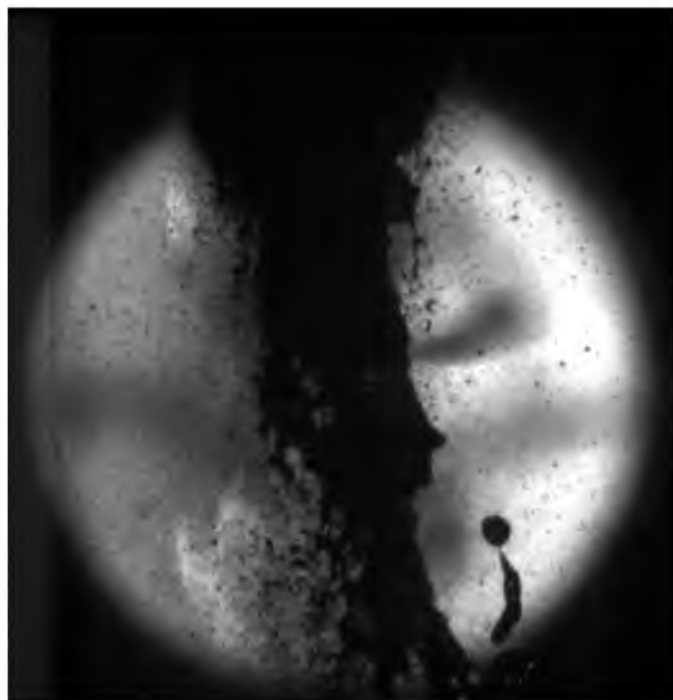


**Figure 6.18.** Image of breakup for Atomizer S.  $u_g = 344 \text{ m/s}$ ,  $u_l = 0.35 \text{ m/s}$ , and  $Re_{g,hd} = 3,122$ .

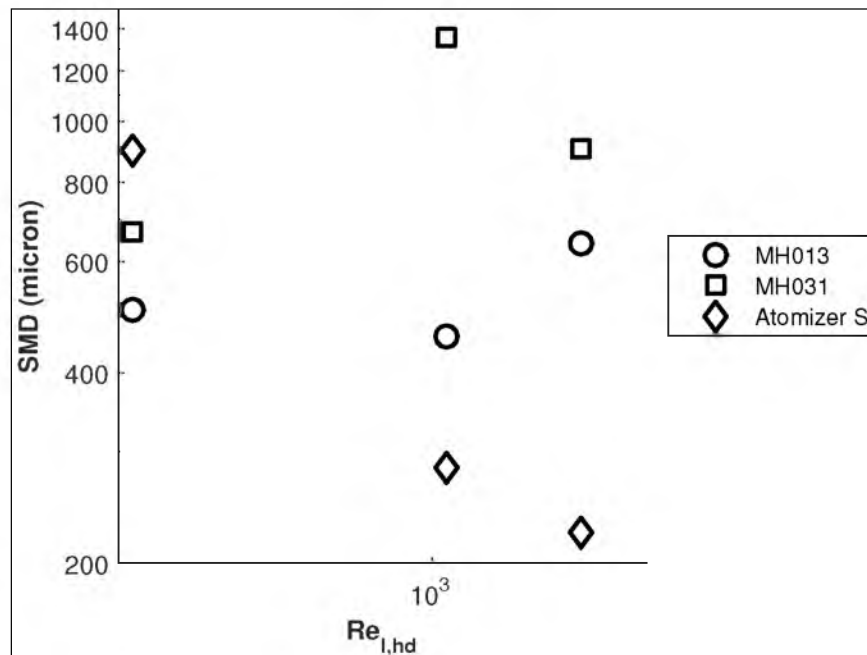


**Figure 6.19.**  $Re_l$  versus the spray SMD.  $u_g = 313 \text{ m/s}$  for MH013.  $u_g = 117 \text{ m/s}$  for MH031.  $u_g = 332 \text{ m/s}$  for Atomizer S.

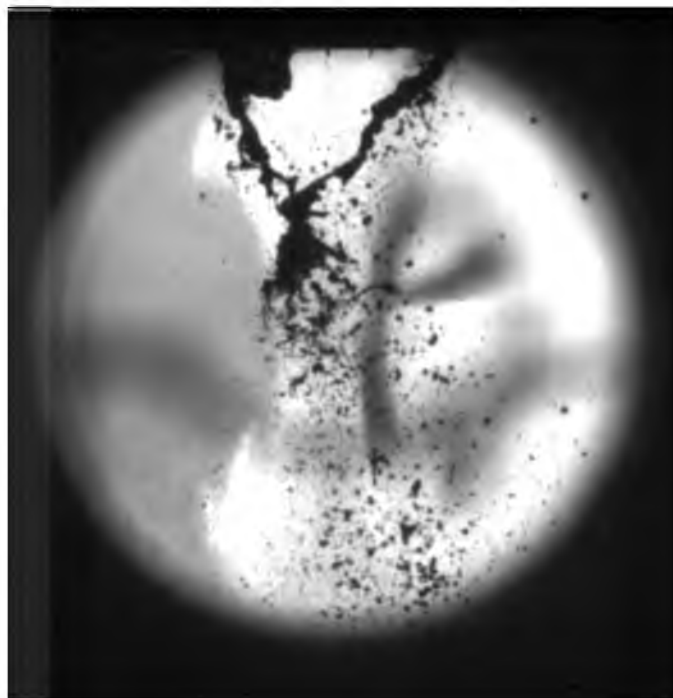


**Figure 6.20.** Image of breakup for Atomizer S.  $u_g = 332 \text{ m/s}$ ,  $u_l = 0.03 \text{ m/s}$ , and  $Re_{g,hd} = 1,733$ .

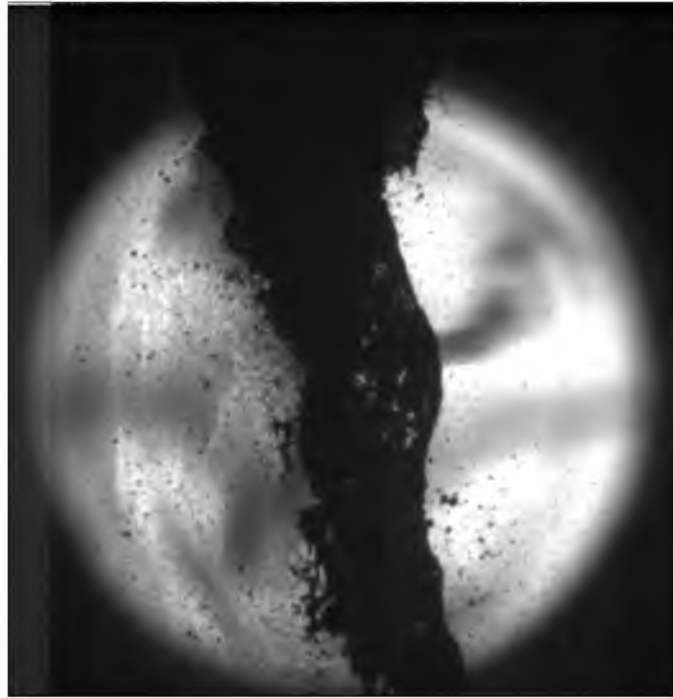


**Figure 6.21.** Image of breakup for Atomizer S.  $u_g = 332 \text{ m/s}$ ,  $u_l = 0.35 \text{ m/s}$ , and  $Re_{g,hd} = 1,690$ .

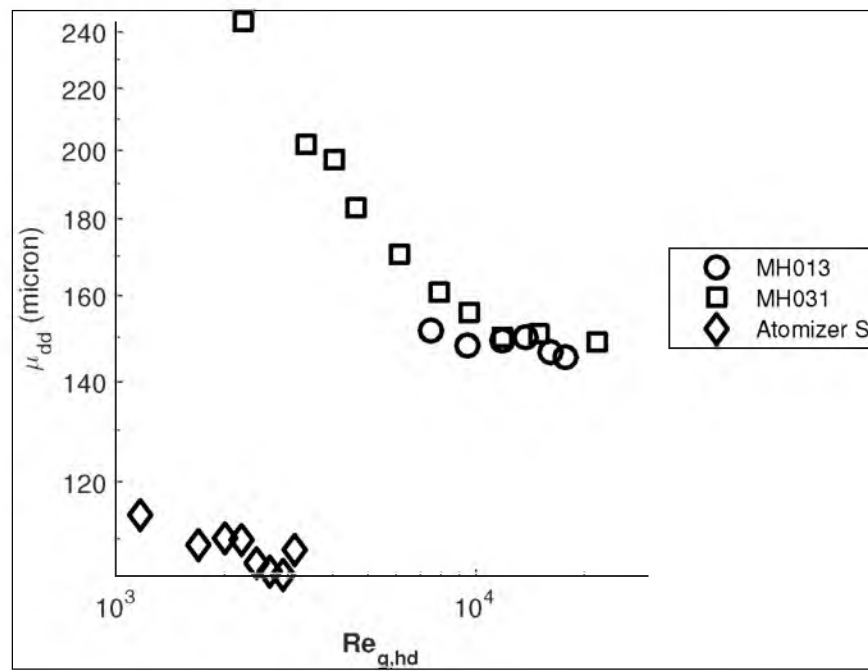


**Figure 6.22.**  $Re_{g,hd}$  versus the geometric mean drop diameter,  $\mu_{dd}$ .  $u_l = 0.35 \text{ m/s}$  for all cases shown.

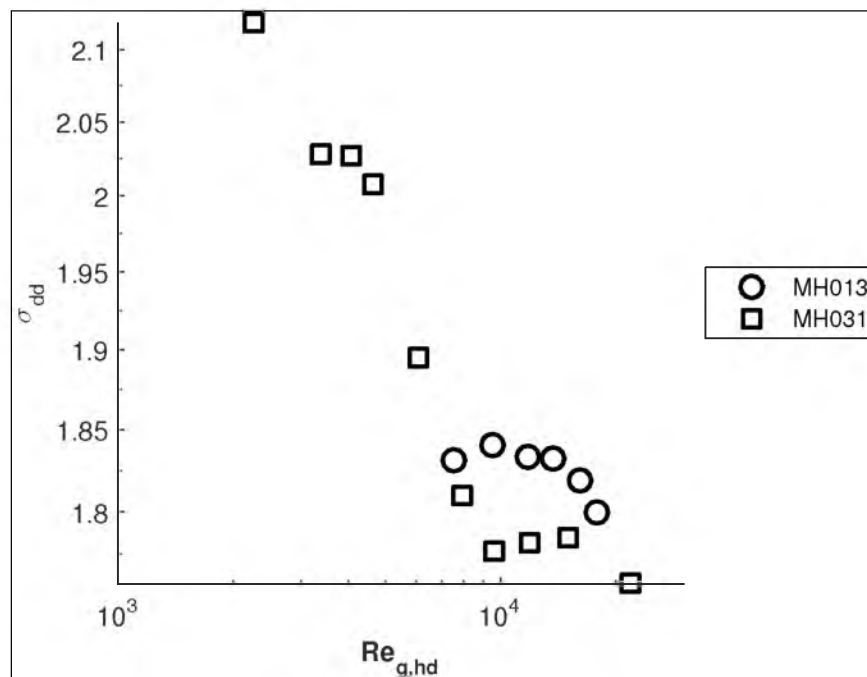


**Figure 6.23.**  $Re_{g,hd}$  versus the geometric mean standard deviation of the drop diameter,  $\sigma_{dd}$ .  $u_l = 0.35 \text{ m/s}$  for all cases shown.

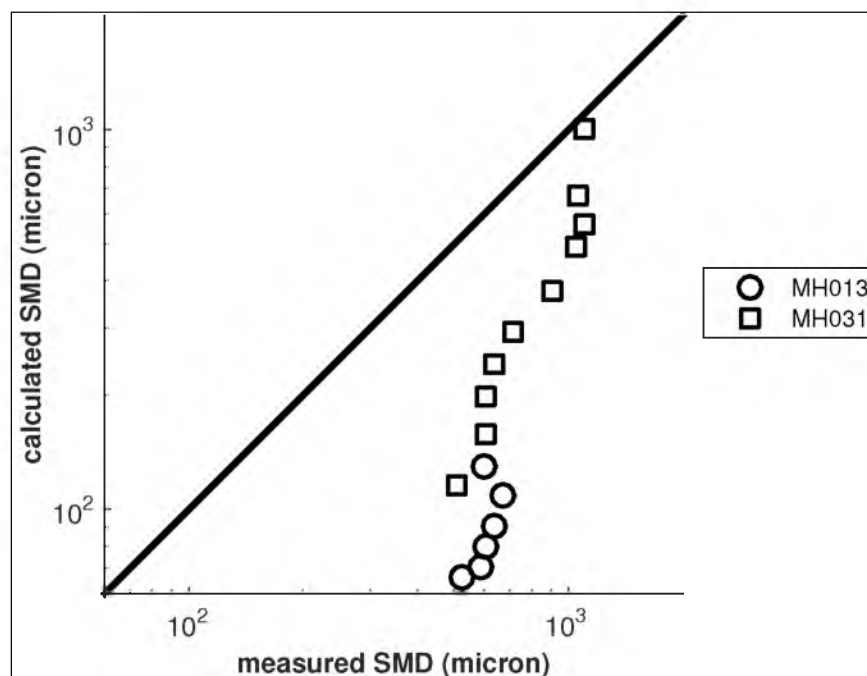


**Figure 6.24.** SMD correlation of Equation 4.14 compared to the measured SMD values for the micro-hole atomizers. Solid black line represents the one-to-one, where the measured and calculated values are identical.

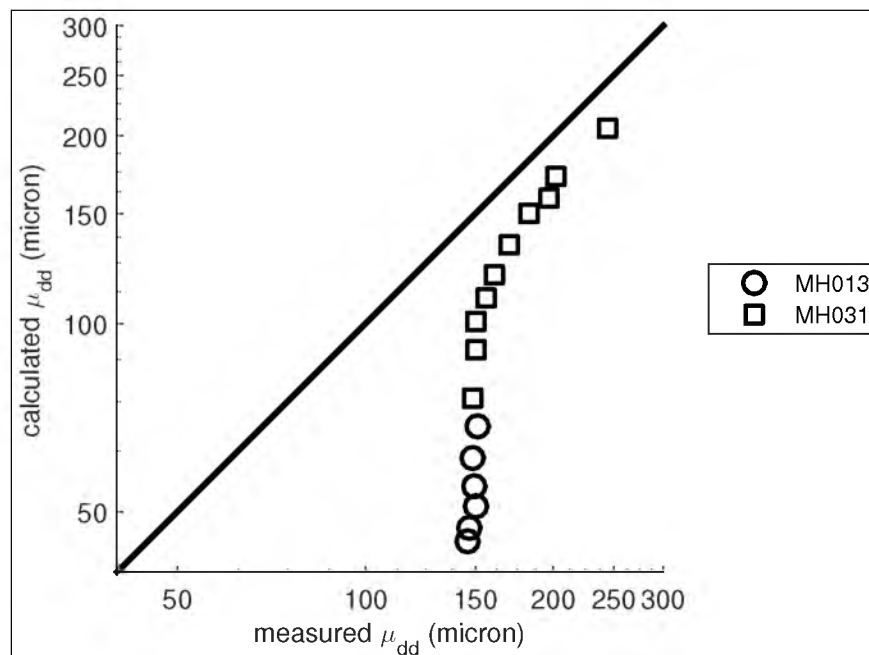


**Figure 6.25.**  $\mu_{dd}$  correlation of Equation 4.13 compared to the measured  $\mu_{dd}$  for the micro-hole atomizers. Solid black line represents the one-to-one, where the measured and calculated values are identical.

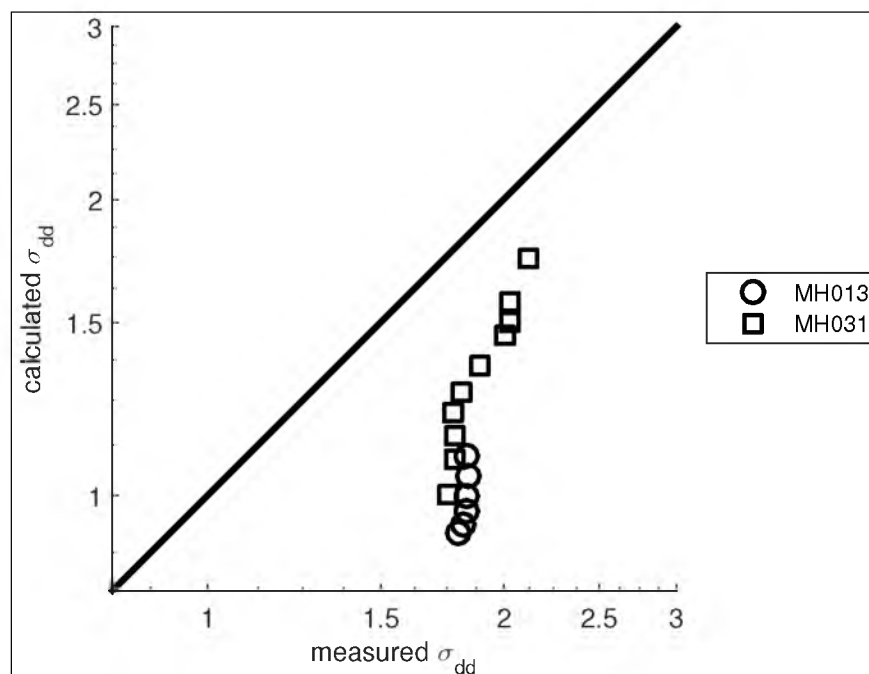


**Figure 6.26.**  $\sigma_{dd}$  correlation of Equation 4.15 compared to the measured  $\sigma_{dd}$  for the micro-hole atomizers. Solid black line represents the one-to-one, where the measured and calculated values are identical.

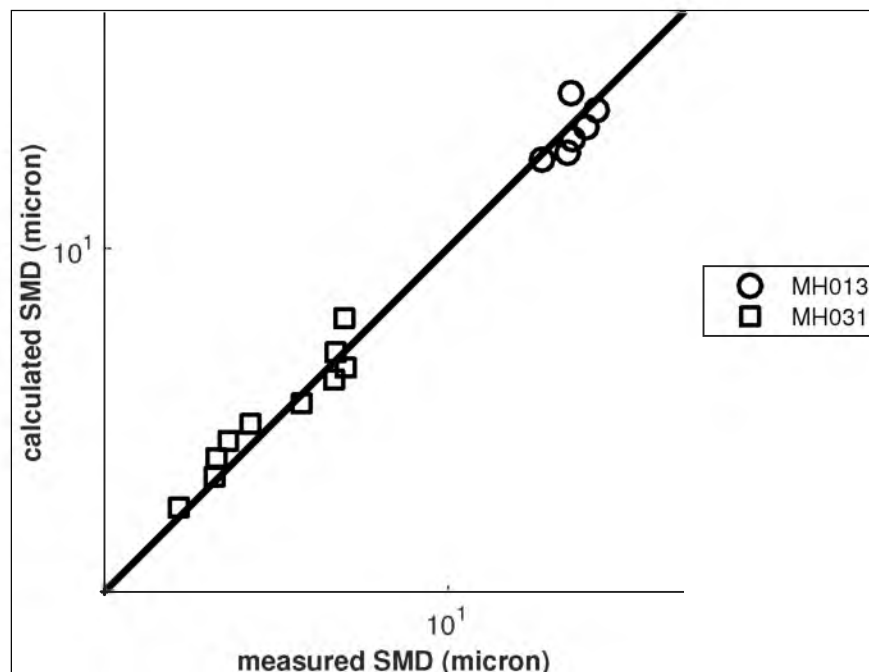


**Figure 6.27.** SMD correlation of Equation 6.1 compared to the measured SMD values for the micro-hole atomizers. Solid black line represents the one-to-one, where the measured and calculated values are identical.

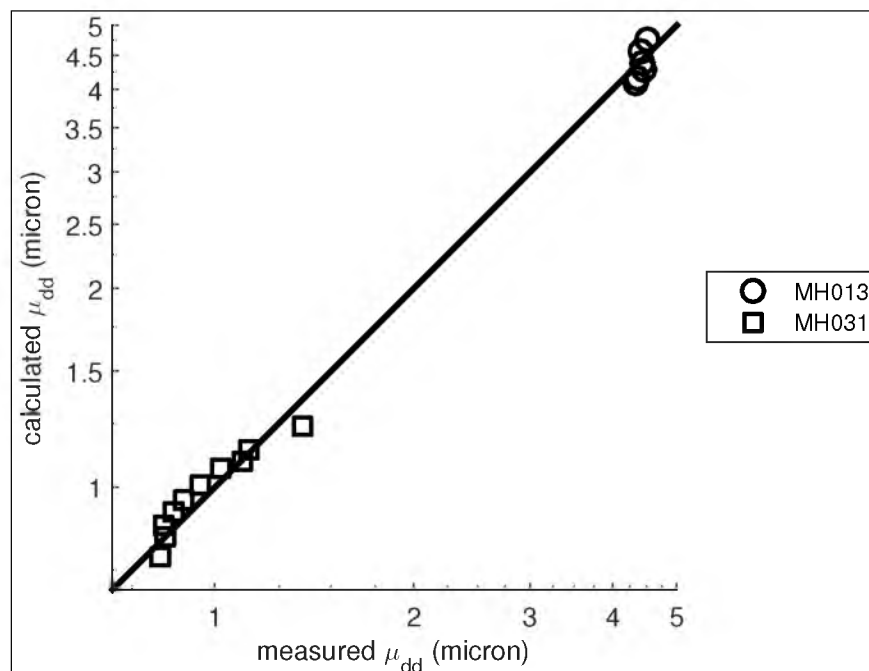


**Figure 6.28.**  $\mu_{dd}$  correlation of Equation 6.2 compared to the measured  $\mu_{dd}$  for the micro-hole atomizers. Solid black line represents the one-to-one, where the measured and calculated values are identical.

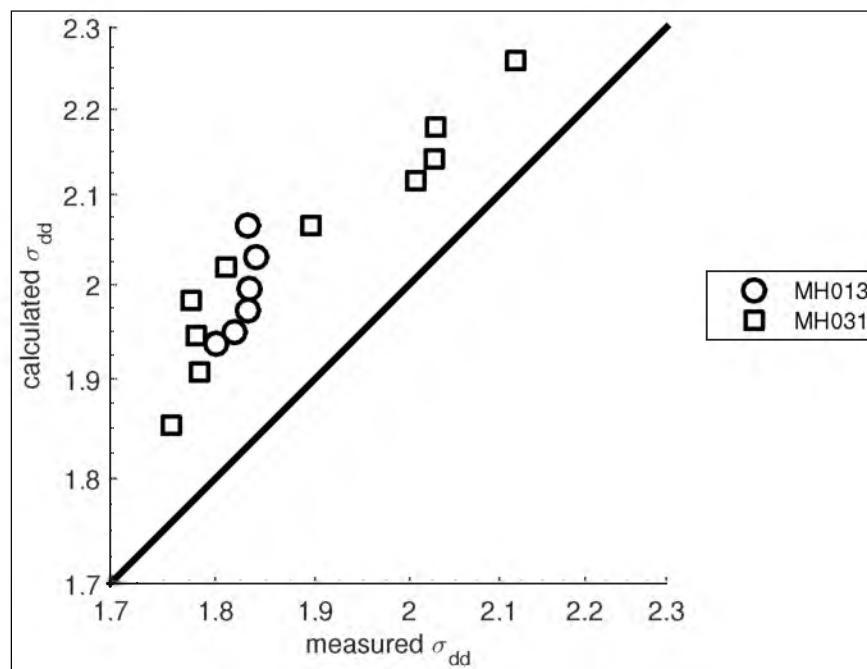


**Figure 6.29.**  $\sigma_{dd}$  correlation of Equation 6.3 compared to the measured  $\sigma_{dd}$  for the micro-hole atomizers. Solid black line represents the one-to-one, where the measured and calculated values are identical.

**Table 6.1.** Description of the liquids being evaluated.

Designation	Solid	Liquid	Solid Wt.%	Ave. Particle Size: Mass/Surface Area (micron)	Viscosity @ 50 s <sup>-1</sup> (Pa*s)
Water	na	water	0	0 / 0	88.8e-4
31_Coal	coal	water	31	92.5 / 43.0	5.79e-3
53_Coal	coal	water	53	92.5 / 43.0	0.374
57_Coal	coal	water	57	92.5 / 43.0	1.03
37_Petcoke	petcoke	water	37	104 / 51.8	6.06e-2
43_Petcoke	petcoke	water	43	104 / 51.8	0.125

**Table 6.2.** Atomizer dimensions.

ID	$d_0$ (mm)	$d_1$ (mm)	$d_2$ (mm)	$A_g/A_l$	#MH*	MH diameter (mm)
MH013	6.22	6.45	1.63**	0.02	8	0.33
MH031	6.22	6.73	1.78**	0.13	8	0.79
Atomizer S	6.22	9.53	9.57	0.02	na	na

\*micro-hole (MH)

\*\*equivalent diameter

**Table 6.3.** Experimental conditions.

Atomizer	$u_l$ (m/s)	$Re_l$	$u_g$ (m/s)	$Re_g$	$We$	$M$
MH013	0.03-0.35	214.7-2,147	264-344	5,817-7,569	7,431-12,588	702.6-98,419
MH031	0.03-0.35	214.7-2,147	42.9-332	2,253-17,399	193.4-11,696	18.5-13,676
Atomizer S	0.03-0.35	214.7-2,147	272-344	828-1,047	7,861-12,588	743.2-111,105

## CHAPTER 7

### CONCLUSIONS

Scaling atomizers is a notoriously difficult problem whose solution would have a positive impact on a number of industries. Here we used high-speed imaging and a novel image processing method to explore the atomization of water with air using coaxial atomizers of various scales. By using atomizers with a relatively constant gas-to-liquid cross-sectional area ratio but different scales, we were able to observe some issues that can be expected when trying to scale an atomizer.

#### 7.1 Main Conclusions

Numerous trends were identified to the dynamic characteristics of the intact liquid jet (ILJ) and the formation and growth of instabilities existing on the ILJ. Changing the atomizer scale and geometry was shown to significantly impact characteristics of both the intact liquid jet and the resulting drops. The primary wavelengths were shown to correlate well with the spray Sauter mean diameter. Buckingham-II theorem was used to develop dimensionless correlations predicting spray characteristics, which fit the measured data well.

By performing cold-flow tests with the coal slurry injector, a good visualization of the resulting atomized water plume was established. This allowed for a better understanding of what is happening inside the entrained flow gasifier (EFG) during operation, despite a coal slurry spray being wider than a water spray. It was shown that a lower limit on acceptable atomization must be enforced during operation of the EFG, as improper atomization leads to noticeable conversion decreases.

Sprays produced from atomizing solid fuel water suspensions were characterized using patternation and PSV. While the viscosities of the various suspensions were evaluated, the observed trends with viscosity were not always clear. For the higher viscosity suspensions evaluated with patternation, increasing the airflow corresponded to the disappearance or shrinking of a high fraction region anywhere in the spray. The areas of the lower fraction regions also increased. This shows that the sprays were better dispersed with increases in the

airflow. Almost the opposite trend is seen for the lower viscosity suspensions evaluated. For these liquids, increases in airflow correspond to a slight increase in area of the high fraction regions. For all liquids, increasing the liquid flow rate typically resulted in an increase in the area of a high fraction center region. Increasing the airflow decreased the average drop diameter for practically all cases along the center of the spray. Increasing the liquid flow showed an increase in the average drop diameter for practically all cases along the center of the spray. Along the edge of the spray, a clear trend is not identified. Increasing the air-to-liquid ratio shows an increase in the fraction of small diameter drops and a decrease in the fraction of large diameter drops. The average direction of the produced drops along the center of the spray is largely unaffected by changes in flow rates or liquid atomized. Along the edge of the spray, increasing the airflow results in either no significant change in the spray direction or a shift towards  $180^\circ$ . Increases in the liquid flow rate tended to move the spray direction slightly more towards  $270^\circ$ . Along the edge of the spray (for 0.93 kg/hr air and  $3.79\text{e-}2$  m<sup>3</sup>/hr liquid), two predominant drop velocity groups were seen. One group was moving  $250^\circ$  at approximately 3 m/s, while the other group was moving  $270^\circ$  at approximately 0.7 m/s.

The spray characteristics correlations developed in Chapter 4 were compared to the spray characteristics measured for two micro-hole atomizer and an impinging, coaxial, two-stream atomizer in Chapter 6 and found to not accurately predict the representative drop diameters, likely due to the geometry change. New correlations were developed using Buckingham-II theorem to predict the geometry average drop diameter ( $\mu_{dd}$ ), the geometric standard deviation of the drop diameter ( $\sigma_{dd}$ ), and the spray Sauter mean diameter. These correlations were shown to accurately predict behavior over the range of variables explored.

## 7.2 Surface Tension vs. Viscosity Effect

The tests performed here are not sufficient to isolate the effect of changing surface tension. This is because there is not a constant viscosity between any of the liquids used in experiments, as was shown in Table 3.3. There is a constant surface tension between Silicone Oil A and Silicone Oil B, allowing for a visual examination of the effect of changing viscosity on atomization.

The relationship between viscosity and surface tension in atomizations systems is difficult to separate. While increasing either liquid viscosity or surface tension has been shown to increase an average drop diameter in the literature, the degree of each property's effect is difficult to quantify. From the results here, we show that little change in the measured

drop diameter can be seen between the water spray and the Silicone Oil spray (increase in viscosity and decrease in surface tension, from water to Silicone Oil A). However, the frame used to image each respective fluid had to be different (due to the substantial increase in breakup length for the higher viscosity fluid), and thus could obfuscate the true average drop diameter. It was clearly seen that increasing the liquid viscosity leads to a substantially longer breakup length for most cases. This effect was seen between with an increase in viscosity along with a decrease in surface tension. Also, increasing the viscosity while keeping the surface tension constant resulted in a substantial lengthening of the ILJ breakup length, which suggests that surface tension likely plays a lesser effect than viscosity in dictating the intact liquid jet breakup length. This conclusion suggests that the driving instability mechanism for this regime of atomization is not the Rayleigh-Plateau instability, which says that surface tension is the driving force behind the breakup of a liquid jet. Additionally, for the Rayleigh-Plateau instability, increasing the surface tension would result in a smaller drop diameter, which is the opposite effect seen in coaxial atomization systems.

Viscosity seems to be the driving factor in these atomization systems driven by a high-velocity gas flow. Increasing viscosity can be seen to increase the surface oscillation frequency and increase the average ILJ primary wavelength. The surface oscillation frequency has been shown to be negatively correlated with an average drop diameter, and the ILJ primary wavelength has been shown to be positively correlated with an average drop diameter.

### 7.3 Hypothesized Mechanism(s) Observed

It has been suggested in the literature that coaxial atomization occurs via a two-step instability mechanism, as was discussed in Chapter 2.2.2. This mechanism involved the sequential observation (or manifestation) of the Kelvin-Helmholtz instability (KHI) followed by the Rayleigh-Taylor instability (RTI). These are assumed to encompass the initial instability formulation and amplification, often leading to the formation of drops encompassed by primary atomization. Additionally, the KHI and RTI are assumed to be the dominant drivers of the approximate drop size, even though the Rayleigh-Plateau instability (RPI) or capillary pinching can be seen to occur along some of the longer ligaments that are formed. This is verified here, as the drops formed and measured are significantly smaller than those predicted by RPI-induced breakup of a liquid jet. However, the dynamic nature of the high-speed atomization process does not allow for clear delineation between the driving instabilities hypothesized; they can often be considered to be occurring all at once.

The breakup mechanisms best supported by the data contained in this work suggest that

the dominant mechanism at any given moment in time or space is entirely dependent on the existing local conditions, which are often also dependent on the previous conditions to which a particular volume of liquid was subjected.

## 7.4 Future Work

The sets of high-speed camera images offer up a number of further studies that would be interesting to pursue. From the existing sets alone, it would be interesting to evaluate oscillation frequencies on a single pixel basis, which would give an idea of the frequency at which drops exist on a given pixel. This ideally could be tied to the angular, length, and surface oscillations of the intact liquid jet to provide a better fundamental understanding of drop trajectory as a function of conditions.

Obvious extensions are for the atomization of suspensions with a simple atomizer geometry, such as those used in Chapter 4. While instability characteristics have been reported for Newtonian fluids, there are few published studies applying the same mechanisms to suspensions. Additionally, while the liquids evaluated here in Chapter 4 provided a range of viscosities and surface tensions, being able to separate the effect of viscosity and surface tension would be useful, as it could not be done here.

It would be useful to extend to image processing methods to attempt to automatically measure the manifestation of the secondary instability discussed in Chapter 2. This would provide further validation to the mechanism-based models proposed in the literature. Additionally, extending the image processing method to identify the occurrence of secondary breakup in the near-field would be useful, as then a correlation to the primary breakup drop characteristics could be made, and the degree to which secondary breakup occurs for the explored conditions could be tracked.

Evaluating the effect of ambient temperature and pressure on the hypothesized breakup mechanisms would be worth exploring, particularly in a reacting environment. The small-scale tests in Chapter 4 provided a good characterization of a number of atomizer geometries and the dynamic characteristics of their produced sprays. If the gas and liquid fed were forced to combust, it would be interesting to quantify the dynamics of the resulting flame over a range of stoichiometric ratios and atomizer geometries. While the pure fluid dynamic oscillations studied in this document can certainly be assumed to affect the spatial and temporal distributions of fuel inside a reactor, it cannot be said that the high-frequency flame oscillations would also be controllable, although it would be fun to try.

## REFERENCES

- [1] J. Conti and P. Holtberg, “International Energy Outlook 2011,” U.S. Energy Information Agency, Tech. Rep., 2011.
- [2] “International Data Base, World Population: 1950-2050,” 2012. [Online]. Available: <http://www.census.gov/population/international/data/idb/worldpopgraph.php>
- [3] R. A. Dowd, “Wabash River Coal Gasification Repowering Project: Final Technical Report,” Wabash River Energy Ltd., Tech. Rep., August 2000.
- [4] M. J. Hornick and J. E. McDaniel, “Tampa Electric Polk Power Station Integrated Gasification Combined Cycle Project: Final Technical Report,” Tampa Electric Company, Polk Power Station, Tech. Rep., August 2002.
- [5] J. Zhang, Z. Zhou, L. Ma, Z. Li, and W. Ni, “Efficiency of wet feed IGCC (integrated gasification combined cycle) systems with coal-water slurry preheating vaporization technology,” *Energy*, pp. 1–9, 2013.
- [6] L. M. Abadie and J. M. Chamorro, “Valuing flexibility: the case of an integrated gasification combined cycle power plant,” *Energy Economics*, vol. 30, no. 4, pp. 1850–1881, 2008.
- [7] “World Gasification Database,” 2013. [Online]. Available: <http://www.gasification.org>
- [8] T. Waind and K. J. Whitty, “Characterization of a small scale slurry-fed, oxygen-blown entrained flow gasifier: How injector geometry affects flame stability and performance,” in *27th Annual International Pittsburgh Coal Conference*, Istanbul, Turkey, 2010, pp. 1341–1353.
- [9] K. J. Whitty, R. J. Pummill, D. R. Wagner, T. Waind, and D. A. Wagner, “Performance of a 500 kwth pressurized entrained-flow coal gasifier,” in *27th Annual International Pittsburgh Coal Conference*, Istanbul, Turkey, 2010, pp. 1333–1340.
- [10] K. J. Whitty, T. Waind, and D. A. Wagner, “Initial Experience with a 500 kWth Pressurized Entrained Flow Coal Gasifier,” in *International Advanced Coal Technologies Conference*, Laramie, Wyoming, 2010.
- [11] K. J. Whitty, T. Waind, and D. R. Wagner, “Commissioning of a 500 KW pressurized entrained-flow coal gasifier,” in *AIChE Annual Meeting*, Salt Lake City, Utah, 2010.
- [12] —, “Pressurized entrained-flow coal gasifier performance: A parametric study,” in *28th Annual International Pittsburgh Coal Conference*, Pittsburgh, Pennsylvania, 2011, pp. 831–846.

- [13] K. Sun, R. Sur, X. Chao, J. B. Jeffries, R. K. Hanson, R. J. Pummill, and K. J. Whitty, "TDL absorption sensors for gas temperature and concentrations in a high-pressure entrained-flow coal gasifier," *Proceedings of the Combustion Institute*, vol. 34, no. 2, pp. 3593–3601, 2012.
- [14] M. C. Celebi and K. J. Whitty, "Characterization of fine particulate material in syngas from a pilot scale entrained flow coal gasifier," in *The Clearwater Coal Conference: The 38th International Technical Conference on Clean Coal & Fuel Systems*, 2013.
- [15] R. Sur, K. Sun, J. B. Jeffries, R. K. Hanson, R. J. Pummill, T. Waind, D. R. Wagner, and K. J. Whitty, "TDLAS-based sensors for in situ measurement of syngas composition in a pressurized, oxygen-blown, entrained flow coal gasifier," *Applied Physics B*, 2013.
- [16] D. R. Wagner, "Coal Conversion Experimental Methods for Validation of Pressurized Entraind-Flow Gasifier Simulation," Doctor of Philosophy, University of Utah, 2013.
- [17] D. R. Wagner and K. J. Whitty, "Gas-phase measurements of a bituminous coal in a pressurized entrained-flow gasifier," in *The 8th US National Combustion Meeting*, Park City, Utah, 2013, pp. 070CO–0385.
- [18] T. Waind, P. Tóth, and K. J. Whitty, "Performance of a small-scale injector for atomization of coal-water and petcoke-water slurries," in *30th Annual International Pittsburgh Coal Conference*, Beijing, China, 2013.
- [19] A.-G. Collot, "Matching gasification technologies to coal properties," *International Journal of Coal Geology*, vol. 65, no. 3-4, pp. 191–212, 2006.
- [20] T. Jakobs, N. Djordjevic, S. Fleck, M. Mancini, R. Weber, and T. Kolb, "Gasification of high viscous slurry R&D on atomization and numerical simulation," *Applied Energy*, vol. 93, pp. 449–456, May 2012.
- [21] C.-J. Chen, C.-I. Hung, and W.-H. Chen, "Numerical investigation on performance of coal gasification under various injection patterns in an entrained flow gasifier," *Applied Energy*, vol. 100, pp. 218–228, 2012.
- [22] E. Yilmaz, K. Venkatesan, A. Ergut, B. Steinhaus, C. T. Brown, U. Mondragon, and V. McDonnell, "Coal slurry atomization: applications, scaling and unanswered questions," in *ILASS Americas*, Ventura, California, 2011.
- [23] J. Pohl, J. Sepulveda, and L. Rothfeld, "Correlation of the spray characteristics of coal-water fuels," in *7th International Symposium on Coal Slurry Fuels Preparation and Utilization*, New Orleans, Louisiana, 1985, pp. 357–376.
- [24] J. Plateau, *Statique expérimentale et théorique des liquides soumis aux seules forces moléculaires*, volume 2 ed. Paris, France: Gauthier-Villars, 1873.
- [25] L. Rayleigh, "On the instability of jets," *Proceedings of the London Mathematical Society*, vol. s1-10, no. 1, pp. 4–13, 1878.
- [26] C. Weber, "Disintegration of liquid jets," *Zeitschrift für Angewandte Mathematik und Mechanik*, vol. 11, no. 2, pp. 136–154, 1931.
- [27] A. Haenlein, "Disintegration of a liquid jet," NACA, Tech. Rep., 1932.

- [28] W. von. Ohnesorge, "Formation of drops by nozzles and the breakup of liquid jets," *Zeitschrift für Angewandte Mathematik und Mechanik*, vol. 16, no. 6, pp. 355–358, 1936.
- [29] N. A. Chigier and R. D. Reitz, "Regimes of Jet Breakup and Breakup Mechanisms (Physical Aspects)," in *Recent Advances in Spray Combustion: Spray Atomization and Drop Burning Phenomena Volume I*, K. K. Kuo, Ed. Reston, Virginia: American Institute of Aeronautics and Astronautics, Inc., 1996, ch. 4, pp. 109–135.
- [30] S. Leroux, C. Dumouchel, and M. Ledoux, "The break-up length of laminar cylindrical liquid jets. Modification of Weber's theory," *Fluid Mechanics Research*, vol. 24, no. 1-3, pp. 428–438, 1997.
- [31] S. P. Lin and R. D. Reitz, "Drop and spray formation from a liquid jet," *Annual Review of Fluid Mechanics*, vol. 30, no. 1, pp. 85–105, 1998.
- [32] C. Dumouchel, "On the experimental investigation on primary atomization of liquid streams," *Experiments in Fluids*, vol. 45, no. 3, pp. 371–422, 2008.
- [33] C. M. Varga, "Atomization of a small-diameter liquid jet by a high-speed gas stream," Doctor of Philosophy, University of California, San Diego, 2002.
- [34] A. H. Lefebvre, *Atomization and Sprays*. New York City, New York: Hemisphere Pub. Corp., 1989.
- [35] J. Taylor and J. Hoyt, "Water jet photography - techniques and methods," *Experiments in Fluids*, vol. 1, no. 3, pp. 113–120, 1983.
- [36] N. A. Chigier, "Challenges for future research in atomization and spray technology: Arthur Lefebvre memorial lecture," *Atomization and Sprays*, vol. 16, no. 7, pp. 727–736, 2006.
- [37] J. P. Hecht and A. E. Bayly, "Atomization for spray drying: unanswered questions and industrial needs," in *ICLASS*, Vail, Colorado, 2009, p. 6.
- [38] W. Sowa, "The effect of injector design on the performance of the Brigham Young University Gasifier," Doctor of Philosophy, Brigham Young University, 1987.
- [39] J. C. Lasheras, E. Villermaux, and E. J. Hopfinger, "Break-up and atomization of a round water jet by a high-speed annular air jet," *Journal of Fluid Mechanics*, vol. 357, no. 1, pp. 351–379, 1998.
- [40] C. M. Varga, J. C. Lasheras, and E. J. Hopfinger, "Initial breakup of a small-diameter liquid jet by a high-speed gas stream," *Journal of Fluid Mechanics*, vol. 497, pp. 405–434, 2003.
- [41] P. H. Marmottant and E. Villermaux, "On spray formation," *Journal of Fluid Mechanics*, vol. 498, no. 1, pp. 73–111, 2004.
- [42] H. Eroglu, N. A. Chigier, and Z. Faragó, "Coaxial atomizer liquid intact lengths," *Physics of Fluids A: Fluid Dynamics*, vol. 3, no. 2, pp. 303–308, 1991.
- [43] E. Porcheron, J.-L. Carreau, D. L. Visage, and F. Roger, "Effect of injection gas density on coaxial liquid jet atomization," *Atomization and Sprays*, vol. 12, no. 1-3, pp. 209–228, 2002.

- [44] B. Leroux, O. Delebroy, and F. Lacas, “Experimental study of coaxial atomizers scaling. Part I: dense core zone,” *Atomization and Sprays*, vol. 17, no. 5, pp. 381–407, 2007.
- [45] S. Chandrasekhar, *Hydrodynamic and Hydromagnetic Stability*. Mineola, New York: Dover Publications, Inc., 1981.
- [46] C. Godrèche and P. Manneville, Eds., *Hydrodynamics and Nonlinear Instabilities*, 1st ed. Cambridge, United Kingdom: Cambridge University Press, 1998.
- [47] G. Batchelor, H. Moffatt, and M. Worster, Eds., *Perspectives in Fluid Dynamics*, 1st ed. Cambridge, United Kingdom: Cambridge University Press, 2000.
- [48] P. Drazin and W. Reid, *Hydrodynamic Stability*, 2nd ed., G. Batchelor and J. Miles, Eds., Cambridge, United Kingdom, 2004.
- [49] P. Manneville, *Instabilities, Chaos and Turbulence*, 1st ed. London, England: Imperial College Press, 2004.
- [50] F. Charru and P. de Forcrand-Millard, *Hydrodynamic Instabilities*, 1st ed. Cambridge University Press, 2011.
- [51] M. A. Gorokhovski and M. Herrmann, “Modeling primary atomization,” *Annual Review of Fluid Mechanics*, vol. 40, no. 1, pp. 343–366, 2008.
- [52] S. P. Lin, *Breakup of Liquid Sheets and Jets*, 1st ed. Cambridge, United Kingdom: Cambridge University Press, 2003.
- [53] N. Ashgriz, *Handbook of Atomization and Sprays: Theory and Applications*, 1st ed. Springer, 2011.
- [54] L. P. Bayvel and Z. Orzechowski, *Liquid Atomization*. Taylor & Francis, 1993.
- [55] S. Nukiyama and Y. Tanasawa, “An experiment on the atomization of liquid by means of an air stream (1. Report),” *Transactions of the Japan Society of Mechanical Engineers*, vol. 4, no. 14, pp. 128–135, 1938.
- [56] —, “An experiment on the atomization of liquid by means of an air stream (the 2nd Report).” *Transactions of the Japan Society of Mechanical Engineers*, vol. 4, no. 15, pp. 138–143, 1938.
- [57] —, “An experiment on the atomization of liquid : 3rd Report, on the distribution of the size of droplets.” *Transactions of the Japan Society of Mechanical Engineers*, vol. 5, no. 18, pp. 131–135, 1939.
- [58] —, “An experiment on the atomization of liquid. : 4th Report, the effect of the properties of liquid on the size of drops.” *Transactions of the Japan Society of Mechanical Engineers*, vol. 5, no. 18, pp. 136–143, 1939.
- [59] —, “An experiment on the atomization of liquid : 5th Report the atomization pattern of liquid by means of an air stream,” *Transactions of the Japan Society of Mechanical Engineers*, vol. 6, no. 22-2, pp. 7–15, 1940.
- [60] Y. Tanasawa, “An experiment on the atomization of liquid by means of an air stream : 6th Report, characteristics of crossed nozzles,” *Transactions of the Japan Society of Mechanical Engineers*, vol. 6, no. 23-2, pp. 18–28, 1940.

- [61] A. Aliseda, E. J. Hopfinger, J. C. Lasheras, D. M. Kremer, A. Berchielli, and E. K. Connolly, "Atomization of viscous and non-newtonian liquids by a coaxial, high-speed gas jet. Experiments and droplet size modeling," *International Journal of Multiphase Flow*, vol. 34, no. 2, pp. 161–175, 2008.
- [62] A. H. Lefebvre, "Airblast atomization," *Progress in Energy and Combustion Science*, vol. 6, no. 3, pp. 233–261, 1980.
- [63] ———, *Gas Turbine Combustion*, 2nd ed. Ann Arbor, Michigan: Taylor & Francis, 1999.
- [64] N. A. Chigier, *Energy, Combustion, and Environment*, 1st ed. McGraw-Hill, 1981.
- [65] H. Liu, *Science and Engineering of Droplets: Fundamentals and Applications*, Knovel, Ed. Park Ridge, New Jersey: Norwich, New York: William Andrew, 2000.
- [66] G. G. Nasr, A. J. Yule, and L. Bendig, *Industrial Sprays and Atomization: Design, Analysis and Applications*, 1st ed. London, England: Springer, 2002.
- [67] C. Engelbert, Y. Hardalupas, and J. Whitelaw, "Breakup phenomena in coaxial airblast atomizers," *Proceedings of the Royal Society A: Mathematical, Physical and Engineering Sciences*, vol. 451, no. 1941, pp. 189–229, 1995.
- [68] J.-P. Matas and A. Cartellier, "Flapping instability of an atomized liquid jet," in *Proceeding of the ASME 3rd Joint US-European Fluids Engineering Summer Meeting and 8th International Conference on Nanochannels, Microchannels, and Minichannels*, Montreal, Canada, 2010, pp. 1–6.
- [69] H. Zhao, H.-F. Liu, X.-S. Tian, J.-L. Xu, W.-F. Li, and K.-F. Lin, "Influence of atomizer exit area ratio on the breakup morphology of coaxial air and round water jets," *AIChE Journal*, vol. 60, no. 6, pp. 2335–2345, 2014.
- [70] R. Woodward, R. Burch, K. K. Kuo, and F. Cheung, "Correlation of intact-liquid core length for coaxial injectors," in *ICLASS*, Rouen, France, 1994, pp. 105–112.
- [71] X.-S. Tian, H. Zhao, H.-F. Liu, W.-F. Li, and J.-L. Xu, "Effect of central tube thickness on wave frequency of coaxial liquid jet," *Fuel Processing Technology*, vol. 119, pp. 190–197, 2014.
- [72] H. Zhao, H.-F. Liu, J.-L. Xu, W.-F. Li, and W. Cheng, "Breakup and atomization of a round coal water slurry jet by an annular air jet," *Chemical Engineering Science*, vol. 78, pp. 63–74, 2012.
- [73] H. Zhao, Y. B. Hou, H. F. Liu, X. S. Tian, J. L. Xu, W. F. Li, Y. Liu, F. Y. Wu, J. Zhang, and K. F. Lin, "Influence of rheological properties on air-blast atomization of coal water slurry," *Journal of Non-Newtonian Fluid Mechanics*, vol. 211, no. 6, pp. 1–15, 2014.
- [74] T. Arai and H. Hashimoto, "Disintegration of a thin liquid sheet in a cocurrent gas stream," in *ICLASS*, London, England, 1985, pp. 1–7.
- [75] I. S. Carvalho, M. V. Heitor, and D. Santos, "Liquid film disintegration regimes and proposed correlations," *International Journal of Multiphase Flow*, vol. 28, no. 5, pp. 773–789, 2002.

- [76] R. A. Nelson and M. Olsson, "The pendulum-rich physics from a simple system," *American Journal of Physics*, vol. 54, no. 2, pp. 112–121, 1986.
- [77] F. Boylu and G. Ateok, "Atomization properties of Turkish coal having different structures in coal-water slurry," *Madencilik*, vol. 44, no. 3, pp. 3–12, 2005.
- [78] Q. Zheng, A. K. Jasuja, and A. H. Lefebvre, "Structure of airblast sprays under high ambient pressure conditions," *Journal of Engineering for Gas Turbines and Power*, vol. 119, no. 3, pp. 512–518, 1997.
- [79] S. G. Daviault, O. B. Ramadan, E. A. Matida, P. M. Hughes, and R. W. Hughes, "Atomization performance of petroleum coke and coal water slurries from a twin fluid atomizer," *Fuel*, vol. 98, pp. 183–193, 2012.
- [80] H. Eroglu and N. A. Chigier, "Wave characteristics of liquid jets from airblast coaxial atomizers," *Atomization and Sprays*, vol. 1, no. 4, pp. 349–366, 1991.
- [81] L. Raynal, E. Villermaux, J. C. Lasheras, and E. J. Hopfinger, "Primary instability in liquid-gas shear layers," in *11th Symposium on Turbulent Shear Flows*, Grenoble, France, 1997, pp. 1–5.
- [82] J. C. Lasheras and E. J. Hopfinger, "Liquid jet instability and atomization in a coaxial gas stream," *Annual Review of Fluid Mechanics*, vol. 32, no. 1, pp. 275–308, 2000.
- [83] P. Thybo, L. Hovgaard, S. K. Andersen, and J. S. Lindeløv, "Droplet size measurements for spray dryer scale-up," *Pharmaceutical Development and Technology*, vol. 13, no. 2, pp. 93–104, 2008.
- [84] X.-S. Tian, H. Zhao, H.-F. Liu, W.-F. Li, and J.-L. Xu, "Liquid entrainment behavior at the nozzle exit in coaxial gas-liquid jets," *Chemical Engineering Science*, vol. 107, pp. 93–101, 2014.
- [85] E. J. Hopfinger and J. C. Lasheras, "Breakup of a water jet in high velocity co-flowing air," in *ICLASS*, Rouen, France, 1994, pp. 110–117.
- [86] E. Villermaux, H. Rehab, and E. J. Hopfinger, "Breakup regimes and self-sustained pulsations in coaxial jets," *Meccanica*, vol. 29, pp. 393–401, 1994.
- [87] H. Rehab, E. Villermaux, and E. J. Hopfinger, "Flow regimes of large-velocity-ratio coaxial jets," *Journal of Fluid Mechanics*, vol. 345, pp. 357–381, 1997.
- [88] E. Villermaux, "Mixing and spray formation in coaxial jets," *Journal of Propulsion and Power*, vol. 14, no. 5, pp. 807–817, 1998.
- [89] M. Hong, A. Cartellier, and E. J. Hopfinger, "Atomisation and mixing in coaxial injection," in *4th International Conference on Launcher Technology, Liquid Propulsion*, 2002.
- [90] L. Bernal and A. Roshko, "Streamwise vortex structure in plane mixing layers," *Journal of Fluid Mechanics*, vol. 170, pp. 499–525, 1986.
- [91] G. L. Brown and A. Roshko, "On density effects and large structure in turbulent mixing layers," *Journal of Fluid Mechanics*, vol. 64, no. 4, pp. 775–816, 1974.
- [92] P. E. Dimotakis, "Two-dimensional shear-layer entrainment," *AIAA Journal*, vol. 24, no. 11, pp. 1791–1796, 1986.

- [93] Y. Wang, K.-S. Im, and K. Fezzaa, "Similarity between the primary and secondary air-assisted liquid jet breakup mechanisms," *Physical Review Letters*, vol. 100, no. 15, p. 154502, apr 2008.
- [94] Z. Faragó and N. A. Chigier, "Morphological classification of disintegration of round liquid jets in a coaxial air stream," *Atomization and Sprays*, vol. 2, no. 2, pp. 137–153, 1992.
- [95] Y. Chen, A. Ebenstein, M. Greenstone, and H. Li, "Evidence on the impact of sustained exposure to air pollution on life expectancy from China's Huai River policy," *Proceedings of the National Academy of Sciences of the United States of America*, vol. 110, no. 32, pp. 12936–41, aug 2013.
- [96] M. Lin, A. M. Fiore, L. W. Horowitz, O. R. Cooper, V. Naik, J. Holloway, B. J. Johnson, A. M. Middlebrook, S. J. Oltmans, I. B. Pollack, T. B. Ryerson, J. X. Warner, C. Wiedinmyer, J. Wilson, and B. Wyman, "Transport of Asian ozone pollution into surface air over the western United States in spring," *Journal of Geophysical Research: Atmospheres*, vol. 117, no. D21, p. D00V07, 2012.
- [97] G. Lorenzetto and A. H. Lefebvre, "Measurements of drop size on a plain-jet airblast atomizer," *AIAA Journal*, vol. 15, no. 7, pp. 1006–1010, 1977.
- [98] M. Risberg and M. Marklund, "Visualizations of gas-assisted atomization of black liquor and syrup/water mixtures at elevated ambient pressures," *Atomization and Sprays*, vol. 19, no. 10, pp. 957–967, 2009.
- [99] L. K. Li, D. M. Dressler, S. I. Green, M. H. Davy, and D. T. Eadie, "Experiments on air-blast atomization of viscoelastic liquids, Part 1: quiescent conditions," *Atomization and Sprays*, vol. 19, no. 2, pp. 157–190, 2009.
- [100] P. D. Hede, P. Bach, and A. D. Jensen, "Two-fluid spray atomisation and pneumatic nozzles for fluid bed coating/agglomeration purposes: A review," *Chemical Engineering Science*, vol. 63, no. 14, pp. 3821–3842, 2008.
- [101] T. Jakobs, N. Djordjevic, S. Fleck, N. Zarzalis, and T. Kolb, "Influence of ambient pressure on twin fluid atomization R&D work for high pressure entrained flow gasification," in *ICLASS*, Heidelberg, Germany, 2012.
- [102] H.-F. Liu, W.-F. Li, X. Gong, X.-K. Cao, J.-L. Xu, X.-L. Chen, Y.-F. Wang, G.-S. Yu, F.-C. Wang, and Z.-H. Yu, "Effect of liquid jet diameter on performance of coaxial two-fluid airblast atomizers," *Chemical Engineering and Processing: Process Intensification*, vol. 45, no. 4, pp. 240–245, apr 2006.
- [103] "Spraying Systems Co." 2014. [Online]. Available: <http://www.spray.com/>
- [104] A. J. Mackrory, "Characterization of Black Liquor Sprays for Application to Entrained-Flow Processes," Master of Science, Brigham Young University, 2006.
- [105] "MATLAB," 2014.
- [106] J. Schindelin, I. Arganda-Carreras, E. Frise, V. Kaynig, M. Longair, T. Pietzsch, S. Preibisch, C. Rueden, S. Saalfeld, B. Schmid, J.-Y. Tinevez, D. J. White, V. Hartenstein, K. Eliceiri, P. Tomancak, and A. Cardona, "Fiji: an open-source platform for biological-image analysis," *Nature Methods*, vol. 9, pp. 676–682, 2012.

- [107] H. Lu, H.-F. Liu, W.-F. Li, and J.-L. Xu, "Bubble formation in an annular granular jet dispersed by a central air round jet," *AIChE Journal*, vol. 59, no. 6, pp. 1882–1893, 2013.
- [108] H.-F. Liu, W. Cao, J.-L. Xu, W.-F. Li, and Z.-G. Sun, "Dispersion mode of granular jet in a coaxial air jet," *Powder Technology*, vol. 217, pp. 566–573, 2012.
- [109] P. Tóth, Á. B. Palotás, T. A. Ring, and E. G. Eddings, "A robust method for the quantitative shadow imaging of dense reacting particulate flows," in *The 8th US National Combustion Meeting*, Park City, Utah, 2013.
- [110] R. J. Furbank and J. F. Morris, "An experimental study of particle effects on drop formation," *Physics of Fluids*, vol. 16, no. 5, p. 1777, 2004.
- [111] C. Y. Guo, J. S. Stevenson, D. W. Davis, and A. J. Avagliano, "Methods and Systems for Mixing Reactor Feed," 2013.
- [112] D. R. Wagner and K. J. Whitty, "Extractive gas-phase sampling of the reaction zone of a pressurized entrained-flow coal gasifier," *Fuel Processing Technology*, vol. 137, pp. 157–163, September 2015.
- [113] A. Hedley and J. Yiu, "Droplet size distribution changes during the atomization of a coal water slurry," in *7th International Symposium on Coal Slurry Fuels Preparation and Utilization*, New Orleans, Louisiana, May 1985, pp. 377–391.
- [114] A. H. Lefebvre, "Energy considerations in twin-fluid atomization," *Journal of Engineering for Gas Turbines and Power*, vol. 114, no. 1, pp. 89–96, 1992.
- [115] P. Meyer and N. A. Chigier, "Photographic and malvern analysis of coal-water slurry atomization," in *7th International Symposium on Coal Slurry Fuels Preparation and Utilization*, New Orleans, Louisiana, May 1985, pp. 402–429.
- [116] N. A. Chigier and P. Meyer, "The atomization process in coal-water slurry sprays," in *8th International Symposium on Coal Slurry Fuels Preparation and Utilization*, Orlando, Florida, May 1986, pp. 144–161.
- [117] T.-U. Yu, S.-W. Kang, J. M. Beér, A. F. Sarofim, and J. Teare, "Atomization quality and high shear rate viscosity of coal water fuels," in *Proceedings of the 12th International Conference on Slurry Technology*, New Orleans, Louisiana, 1987, pp. 99–105.
- [118] S. F. Ahmed and A. R. Hasan, "Rheology of low-rank coal-water slurries at both high and low shear rates," *Fuel*, vol. 72, no. 6, pp. 763–769, 1993.
- [119] N.-S. Roh, D.-H. Shin, D.-C. Kim, and J.-D. Kim, "Rheological behaviour of coal-water mixtures. 1. Effects of coal type, loading and particle size," *Fuel*, vol. 74, no. 8, pp. 1220–1225, 1995.
- [120] A. R. Hasan, D. Baria, and A. Rao, "Rheological behavior of low-rank coal-water slurries," *Chemical Engineering Communications*, vol. 46, no. 4-6, pp. 227–240, 1986.
- [121] S. Son and K. D. Kihm, "Effect of coal particle size on coal-water slurry (CWS) atomization," *Atomization and Sprays*, vol. 8, no. 5, pp. 503–519, 1998.

- [122] G. Ateok, F. Boylu, A. A. Sirkeci, and H. Dincer, "The effect of coal properties on the viscosity of coalwater slurries," *Fuel*, vol. 81, no. 14, pp. 1855–1858, 2002.
- [123] T. Rosfjord, "Atomization of coal water mixtures: Evaluation of fuel nozzles and cellulose gun simulant," in *Gas Turbine Conference and Exhibit*, Houston, Texas, 1985, pp. 1–8.
- [124] H. T. Sommer and Y. Matsuzaki, "Mechanisms of effective coal/water slurry atomization," in *American Flame Research Committee*, Akron, Ohio, 1983, pp. 1–16.
- [125] C. Smith, P. E. Sojka, and J. Thames, "The influence of fluid physical properties on coal-water slurry atomization," *Journal of Engineering for Gas Turbines and Power*, vol. 112, no. 1, p. 15, 1990.
- [126] S. C. Tsai, K. Ghazimorad, and B. Viers, "Airblast atomization of micronized coal slurries using a twin-fluid jet atomizer," *Fuel*, vol. 70, no. 4, pp. 483–490, 1991.
- [127] S. C. Tsai and T. Vu, "Atomization of coal-water slurry using twin-fluid jet atomizer," *Fuel*, vol. 66, no. 11, pp. 1596–1602, 1987.
- [128] R. LaFlesh, M. Rini, Y. Lachowicz, and A. Levasseur, "Comparison of the performance of a cross-section of commercial CWF burners," in *7th International Symposium on Coal Slurry Fuels Preparation and Utilization*, New Orleans, Louisiana, 1985, pp. 596–606.
- [129] P. Rosin and E. Rammler, "The laws governing the fineness of powdered coal," *The Institute of Fuel*, vol. 7, pp. 29–36, 1933.
- [130] W. F. Farmayan, S. Srinivasachar, L. Monroe, F. DiTaranto, J. Teare, and J. M. Beér, "NOX and carbon emission control in coal-water slurry combustion," in *6th International Symposium on Coal Slurry Combustion and Technology*, Orlando, Florida, 1984, pp. 165–184.
- [131] E. Babinsky and P. E. Sojka, "Modeling drop size distributions," *Progress in Energy and Combustion Science*, vol. 28, no. 4, pp. 303–329, 2002.
- [132] B. Mulhem, G. B. Schulte, and U. Fritsching, "Solid-liquid separation in suspension atomization," *Chemical Engineering Science*, vol. 61, no. 8, pp. 2582–2589, apr 2006.